6-18-2012

Mass Spectrometry-Based Strategies for Protein Biophysics: Effects of Modification, Structure, and Interactions

Richard Yu-Cheng Huang
Washington University in St. Louis

WASHINGTON UNIVERSITY IN ST. LOUIS

Department of Chemistry

Dissertation Examination Committee:
Michael L. Gross, Chair
Robert Blankenship
Carl Frieden
Liviu Mirica
Gary Patti
Kathryn A. Yamada

Mass Spectrometry-Based Strategies for Protein Biophysics: Effects of Modification, Structure, and Interactions

by

Richard Yu-Cheng Huang

A dissertation presented to the
Graduate School of Arts and Sciences
of Washington University in
partial fulfillment of the
requirements for the degree
of Doctor of Philosophy

August 2012

Saint Louis, Missouri

Abstract

Two important biophysical characteristics of proteins, their interaction with ligands and their post-translational modifications, modulate various biological processes including signal transduction, chemical synthesis, and cell function. Protein-ligand interactions include the interactions with protein, peptide, DNA, and metal. Characterization of the physical properties of these interactions (binding interfaces, binding affinities, and the protein conformational changes due to the binding) is essential in understanding the mechanism of related diseases and, more importantly, in future drug design.

Mass spectrometry, with its own revolution and improvement, becomes a powerful tool in protein and peptide analysis. In this thesis, we applied two mass spectrometry-based strategies, proteomics and protein footprinting, to characterize these biophysical properties of three disease-related proteins, connexin 43 (Cx43), troponin, and apolipoprotein E (ApoE), and Fenna-Matthews-Olson protein (FMO), which is the key factor in energy transfer of the photosynthetic system of green sulfur bacteria.

By the combination of standard proteomics workflow and two fragmentation methods, collision-induced dissociation (CID) and electron transfer dissociation (ETD), we successfully identified 15 serine residues, including one novel site, in the Cx43-CT

that are phosphorylated by CaMKII, the activity of which may be important in regulating Cx43 in normal and diseased hearts.

We further utilized hydrogen/deuterium exchange (H/DX), one mass spectrometry-based protein footprinting strategy, to examine the binding affinities of troponin C (TnC), a cardiac disease-related protein, with its four metal binding ligands (Ca^{2+}), and their binding order. We then expanded this approach to elucidate the dynamics of TnC within the complex and its interactions with other subunits (TnT and TnI) at peptide-level resolution. This same approach was also applied to two protein-ligand complexes: (1) the interaction of FMO and its binding partner, CsmA baseplate protein, in which the orientation of FMO between chlorosome and membrane can be confirmed, and (2) the interaction of ApoE and Aβ40, which are both key factors in Alzheimer's disease. Moreover, we improved the spatial resolution of H/DX to residue-level by conducting ETD fragmentation in the study of ApoE oligomerization. Our results reveal, for the first time, the amino acid residues involved in its self-oligomerization.

These six applications of mass spectrometry-based approaches show their potential in the characterization of different protein biophysical properties. The investigation of a more complex protein system can then be pursued.

Acknowledgements

In the summer of 2007, I stepped in WashU campus cheerfully but was full of uncertainty. After five years, I step out the campus in the same scene but am full of enthusiasm for science.

I thank my advisor, Prof. Michael L. Gross, for his full support and guidance during my five years of thesis research. He provided an outstanding research environment, the opportunities to collaborate with distinguished scientists, and most importantly, he allowed me to choose my own research topics, which strengthens my independency and amplifies my interest in science. He is the father of my research career.

I thank the entire staff scientists in our facility, especially Don L. Rempel and Henry W. Rohrs for their assistance in data modeling and instrument troubleshooting. I enjoy the time discussing my results and thoughts with Don in the "late" evenings.

I would like to thank the members, both current and past, in our Mass Spectrometry Resource (Danforth campus): Joyce Neff, Ilan Vidavsky, Daryl Giblin, Justin Sperry, Bich Vu, Micah Wilcox, Adam Brustkern, Sandy Kerfoot, Manohari Silva, Dian Su, Hao Zhang, Brian Gau, Tingting Tu, Jiawei Chen, Qiang Zhang, Cui Weidong, Jun Zhang, Lisa Jones, Manolo Plasencia, Sergio Castro, Yining Huang, Ying Zhang,

Yuetian Yan, Daniel Weisz, Jing Li, Hanliu Wang, and Ben Niu; (Med school campus): Prof. Reid Townsend, Petra Gilmore, and Alan Davis.

I thank my collaborators, Prof. Carl Frieden, Kanchan Garai from Departments of Biochemsitry and Molecular Biophysics, Washington University; Prof. Kathryn Yamada, James Laing, and Evelyn Kanter from Cardiovascular Division, Washington University School of Medicine; Prof. Robert Blankenship, Jianzhong Wen, Xinliu Gao, Prof. Himadri Pakrasi, Haijun Liu from Department of Chemistry and Biology, Washington University; Brady Summers from University of Missouri-Kansas City, for providing such interesting research projects.

I thank my Dissertation Advisory and Examination Committee members, Prof. Robert Blankenship, Prof. Liviu Mirica, Prof. Carl Frieden, Prof. Kathryn Yamada, and Prof. Gary Patti, for their guidance in my thesis research.

This thesis research is supported by the National Institutes of Health and National Center for Research Resources (Grant No. 2P41RR000945) and Washington University Dean's Dissertation Fellowship (Spring, 2012).

Finally, I thank my mother, Tsai-Yun Chang, for her support, and my brother, Yu-Tin Huang, for being the model of my research career.

Table of Contents

Chapter 3

HD Exchange and PLIMSTEX Determine the Affinities and Order of Binding of Ca^{2+} with Troponin C

Chapter 5

Hydrogen/Deuterium Exchange and Electron-Transfer Dissociation Mass Spectrometry Determine the Interface and Dynamics of Apolipoprotein E Oligomerization

Chapter 6

Hydrogen/Deuterium Exchange Mass Spectrometry Probes the Apolipoprotein E-amyloid-β (Aβ 40) Interactions

Chapter 7

Hydrogen-deuterium exchange mass spectrometry reveals the interaction of Fenna-Matthews-Olson protein and chlorosome CsmA protein

List of Figures

Chapter 1

Chapter 2

Chapter 3

Chapter 4

Chapter 5

Chapter 6

Chapter 7

List of Tables

Chapter 2

Chapter 3

Chapter 4

Chapter 5

Chapter 7

Chapter 1

Introduction:

Protein-ligand Interaction, Protein Post-translational Modification, Hydrogen/Deuterium Exchange, and Mass Spectrometry

1.1 ABSTRACT

One of the essential steps in proteomics is the identification and location of post-translational modifications. Furthermore, an additional need is the characterization of protein-ligand interactions. Both are essential in understanding various biological processes including signal transduction, chemical catalysis, and cellular communication. The recent evolution and improvement of mass spectrometry (MS) makes it a powerful technique for the study of protein chemistry. Given that the measurement is fast, and the sample-size requirement is small, its application has expanded from academic institutes into biopharmaceutical companies. Mass spectrometry coupled with HPLC separation and product-ion sequencing (MS/MS) can not only confirm the protein sequence but also localize chemical modification sites. Moreover, the implementation of MS-based protein footprinting strategies, including hydrogen/deuterium exchange, enable us to study the biophysical properties of proteins (e.g. their dynamics, binding affinities, binding interfaces). The principles and instrumentation of protein/peptides mass spectrometry and hydrogen/deuterium exchange are introduced in this chapter.

1.2 PROTEIN-LIGAND INTERACTION

Protein-ligand interactions occur both inside and outside the cell and are the basis of complex, coordinated, dynamic network systems that coordinate various biological processes and modulate, for example, cell growth and cell cycles (*1*). The ligands that bind proteins include other proteins, peptides, DNA, small organic molecules, and metal ions. These complex interactions alter protein function and further influence downstream signal cascades. Malfunctioning of these systems can result in disease (*2*). Drugs, as a category of ligands, are designed to interact with proteins and adjust their functions and prevent unwanted downstream responses (*2*).

Troponin C, for example, which is one subject of study in this thesis, presents in both skeletal and cardiac muscle, interacts with Ca^{2+}, and further interacts with other subunits (troponin I and T). These interactions are the basis of muscle contraction (*3*). Any factor that changes the interactions between the various troponins may be involved in cardiac-related diseases, and some drugs are, therefore, designed to maintain the multiple functions of troponins (*4*).

Given that understanding the properties of protein-ligand interaction is the foundation of drug design, we propose that any method that expedites the study of protein-ligand interactions will facilitate drug development. Moreover, these methods can

help us understand the mechanisms of the complex biological networks and further improve our knowledge of biological therapies for diseases.

1.3 PROTEIN POST-TRANSLATIONAL MODIFICATION

Protein post-translational modification (PTM), a late step in protein biosynthesis that places a chemical modification on a side chain, is another important element in biological processes. It regulates protein function, signaling transduction, and cell behavior. Protein methylation or acetylation, for example, can be the basis for protein recognition by chromodomains (*5*). Protein nitration may be involved in cardiovascular diseases (*6, 7*). Protein glycosylation, a common PTM, has been recognized as a key element in protein folding, internalization, binding, and is also crucial to immune response (*8, 9*). Protein phosphorylation is involved in protein functional activity, occurs principally at the hydroxyamino acids, tyrosine, serine, and threonine, and converts a neutral side chain to a negative charge, thereby mediating cell-signaling transduction (*5*).

Protein PTMs, especially phosphorylation, normally require kinase activation, which is another category of protein-protein interaction. It occurs differently under different biological conditions. Connexin 43 (Cx43), for example, which is also studied as part of this thesis, is a channel protein that modulates normal electrical and contractile activity. Cx43 can be phosphorylated by several different kinases, under both normal and

disease conditions. The modification regulates the gap-junction-channel assembly, function, and turnover. The locations of the phosphorylation sites on Cx43 with the activation of calmodulin protein kinase II (CAMKII), however, were unknown prior to our study. Therefore, understanding protein PTMs either qualitatively or quantitatively, and especially under different biological environments, is essential for understanding global protein function in specific biological processes.

1.4 RESOLUTION OF PROTEIN-LIGAND INTERACTIONS

The ability to locate protein-ligand interaction and protein PTMs has been acknowledged as one of the challenging issues in biomedicine and biophysics owing to the complex architecture and the lack of a complete suite of approaches.

The qualitative analysis of protein PTMs is often achieved by gel-based analyses (SDS page staining and western blot), which provide only positive/negative information. Most of the strategies that are used to predict or characterize protein-ligand interaction, such as circular dichroism (CD) (*10*), fluorescence (*11*), small angle X-ray scattering (SAXS) (*12*), size-exclusion chromatography (*13*), and native gel (*14*), give global information on protein structure or size as modified owing to ligand binding. These techniques provide fast measurements but at low resolution (little if any site specificity). X-ray crystallography (*15*) and NMR (*16*), on the other hand, provide high resolution (~

2 Å) measurements of protein structures. The protein concentration and sample amount, however, need to be high (mM or high μM range for NMR, and mg of sample for x-ray). Furthermore, the protein cannot be large for NMR, and protein dynamics (e.g., flexibility) are difficult to measure by X-ray crystallography.

MS, on the other hand, can provide fast measurement for small amounts of sample (μg). Our goal is to continue to develop MS tool to study protein-ligand interactions and to utilize MS in the identification and localization of protein PTMs

1.5 MASS SPECTROMETRY; REVIEW OF BASIC PRINCIPLES

The basic functions of MS are to generate ions from either inorganic or organic compounds, to separate these ions by their mass-to-charge ratios (*m/z*) and to detect them according to their respective *m/z* values. A mass spectrometer is composed of an ion source, a mass analyzer, and a detector. The majority of application before 1980's were the analysis of small molecules. It was not until the late 1980's, when John Fenn invented electrospray ionization (ESI) (*17*), Franz Hillenkamp and Michael Karas developed matrix-assisted laser desorption ionization (MALDI) (*18*), and numerous researchers improved mass analyzers, that the analysis of large bioorganic molecules including proteins, peptides, carbohydrates, and pieces of DNA and RNA became possible.

One property of ESI is that it multiply charges the analyte. Under denaturing conditions, the protein is highly charged and shows a broad distribution. MALDI, on the other hand, usually gives a dominant singly charged species and minimal multiple charging. ESI is the dominant ionization method used in the research reported in this thesis.

Nowadays, the large variety of ionization techniques and mass analyzers makes the analysis of proteins and peptides feasible and powerful. Moreover, the combination of different mass analyzers (hybrid mass spectrometers) provides protein measurement and sequencing in a high-resolution manner.

In conducting this thesis research, two hybrid mass spectrometers were mainly used (ESI-quadrupole/time-of-flight and ESI-linear ion trap/orbitrap). These are described in the following sections.

1.5.1 Quadrupole/time-of-flight

A quadrupole mass analyzer consists of four hyperbolically or cylindrically shaped rod electrodes. The pairs of opposite rods are held at the same polarity, which is composed of a DC and an AC component. If the applied voltage is composed of a DC voltage U and a radio frequency (RF) voltage V with the frequency ω, the total potential Φ is given by equation 1.

$$\Phi = U + V\cos\omega t \qquad \text{Eq. 1}$$

The equations of ion motion are given as equation 2 in which the distance between two rods is $2r_0$. These differential equations can be expressed as the Mathieu equation, for which a solution can be found.

$$\frac{d^2x}{dt^2} + \frac{e}{m_i r_0^2}(U + V\cos\omega t)x = 0$$

$$\frac{d^2y}{dt^2} - \frac{e}{m_i r_0^2}(U + V\cos\omega t)y = 0 \qquad \text{Eq. 2}$$

The dimensionless form of equation 2 can be written as:

$$\frac{d^2u}{d\xi^2} + (a_u + 2q_u\cos 2\xi)u = 0 \qquad \text{Eq. 3}$$

where u represents the coordinate axes x and y, ξ is defined as $\omega t/2$, and a_u and q_u are defined as:

$$a_u = \frac{4eU}{m_i r_0^2 \omega}$$

$$q_u = \frac{2eV}{m_i r_0^2 \omega} \qquad \text{Eq. 4 and 5}$$

By plotting the parameter a vs. q when the ion trajectory is stable, one obtains the stability diagram of the two-dimensional quadrupole field. Any ion that stays within the stability region can be transmitted through the quadrupole analyzer and be detected. When operating near the tip of the stability diagram, other ions, even those of nearby *m/z*, will have unstable trajectories. This property enables a quadrupole to function as a mass selector in which only ion with specific *m/z* range can be transmitted to and fragmented

in the collision cell (usually an octupole). The product ions can then be analyzed by a sequel mass analyzer. This concatenation is known as mass spectrometry/mass spectrometry (MS/MS).

In the MS-only mode, the quadrupole is operated under RF only condition ($a_u = 0$) in which all ions can be transmitted and analyzed by the following mass analyzer.

The principle of time-of-flight (TOF), which is the second mass analyzer in the quadrupole-TOF (Q-TOF) instrument, is that ions of different *m/z* are dispersed in time during their flight through a field-free drift path of known length. Provided all the ions are given the same kinetic energy, lighter ions will arrive earlier at the detector than the heavier ions. Given that an ion with electric charge q and mass m at high electrical potential U is accelerated, converting its potential energy into kinetic energy (E_k), we can equate two types of energy as:

$$E = qU = \frac{1}{2}mv^2 = E_k \qquad \text{Eq. 6}$$

The velocity (v) of the ion in the flight tube, therefore, can be obtained.

$$v = \sqrt{\frac{2qU}{m}} \qquad \text{Eq. 7}$$

This characteristic of ion movement in the flight tube, however, demands that ions emerge from a pulsed ion source, such as MALDI, in which all the ions start their journey at the same time or at least within a sufficiently short time interval. This arrangement is

not suitable for continuous ion sources such as ESI because the ions will overlap. Incompatibility between continuous ion sources and pulsed ToF instruments was resolved in early 1990's. The solution is an orthogonal TOF in which ions are introduced into the TOF mass analyzer along an axis perpendicular to their initial direction of motion. By taking advantage of this orthogonal design, quadupole and ToF mass analyzers can be combined to form the basis of a powerful tandem mass spectrometer. To complete the MS/MS design, we need only to incorporate some means of causing ions selected by the Q to be activated and undergo fragmentation.

If the TOF is coupled with a reflectron, the dispersion of kinetic energy of ions having the same mass is minimized, and the mass resolving power is improved significantly. A modern Q-TOF instrument can have mass resolving power as high as 40,000 over a wide mass range or even higher; such high resolving power is an asset in protein analysis.

1.5.2 Linear ion trap/Orbitrap

A linear ion trap, or linear quadrupole ion trap (LIT or LTQ), functions similarly as a quadrupole mass analyzer but uses a trapping potential well formed by placing electrodes of slightly higher potential adjacent to the front and rear ends of the multipole. This property enables the LTQ to trap ions with high capacity, accumulate ions until a

population suitable for the sequel analyzer is reached, select ions of interest, and fragment ions with relatively higher efficiency as compared to the quadrupole.

The orbitrap, also known as the Kingdon trap (*19*), is a type of Fourier transform (FT) mass analyzer. It incorporates a straight electrode along the axis of a surrounding cylindrical electrode (**Figure 1-1**). Ions tangentially approaching the central electrode that is set to an attractive electric potential do not hit the electrode but become captured in a rotational motion around it, owing to a balance of an outward centrifugal forces and an inward electrical force. Their trajectory is defined by an equilibrium of the centrifugal force and the electrostatic force generated by applying a voltage between central electrode and enclosing cylinder. The oscillation of ions, thus, creates an image current as detected by a differential amplifier connected to the halves of the outer electrode; the image current is then transformed to frequency-based signal. The correlation between the frequency of harmonic axial oscillation ω_z with field curvature k and ion with mass m_i and charge q can be defined as:

$$\omega_z = \sqrt{k\left(\frac{q}{m_i}\right)} \qquad \text{Eq. 8}$$

The combination of an LTQ and an orbitrap provides extremely high resolving power (100,000 at *m/z* 400, accurate mass measurement (0.5 - 5 ppm), and efficient MS/MS capability that increases the confidence in protein and peptide identification, for

example. For this reason, we conducted much of the research reported in this thesis with the LTQ-Orbitrap.

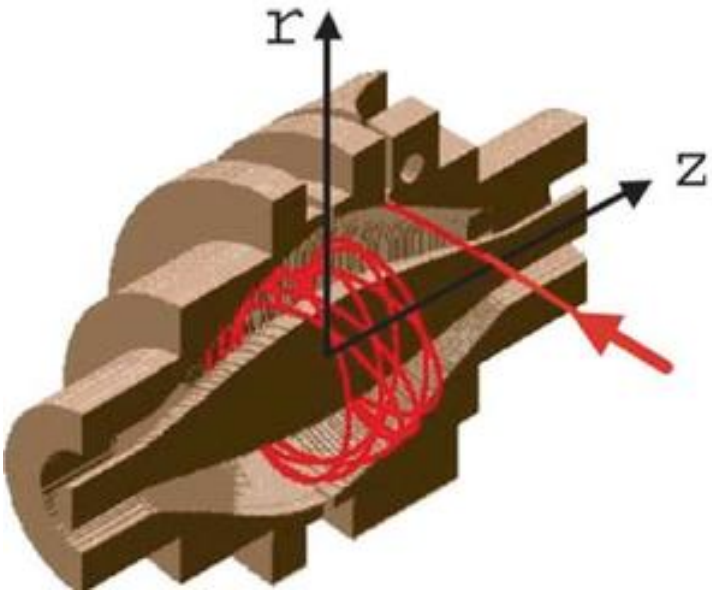

Figure 1-1. Cutaway view of the Orbitrap mass analyzer. Ions are injected into the Orbitrap at the point indicated by the red arrow. Taken from Perry et al. 2008. Mass Spectrometry Reviews.

1.6 GAS-PHASE FRAGMENTATION

The ability to induce ion fragmentation in tandem mass spectrometry (MS/MS) is important to identify peptides and proteins with high confidence, especially when dealing with complex protein mixtures. Moreover, it allows one to localize protein modification sites such as phosphorylation, which will be important in chapter two of the thesis. Peptide ions that are fragmented in the gas phase produce a series of product ions indicated by a, b, or c if the charge is retained on the N-terminus and by x, y or z if the

charge is maintained on the C-terminus (**Figure 1-2**). Obtaining these sequential ions is essential to reconstruct peptide sequences.

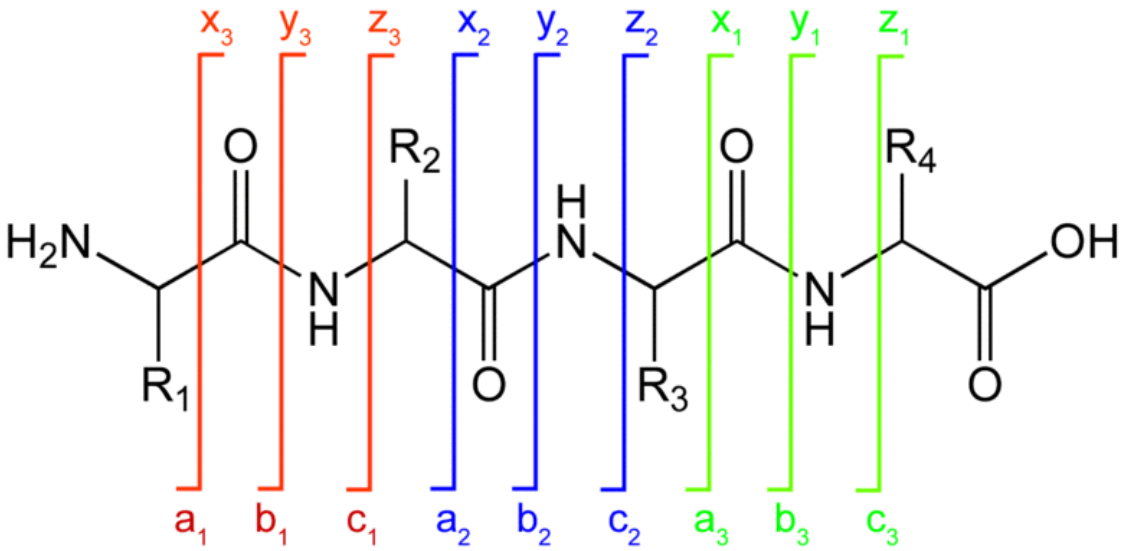

Figure 1-2. The fragmentation sites of peptide during gase-phase fragmentation.

There are two types of fragmentation strategies, collision-induced dissociation, or collisionally activated dissociation (CID/CAD), and electron transfer or electron capture dissociation (ETD/ECD). They are now widely used in general proteomics approaches (*20, 21*).

1.6.1 Collision-induced dissociation

Collision-induced dissociation (CID) occurs when an ion beam passes through a collision cell where an inert collision gas (e.g., He, N_2, Ar) is set to a pressure approximately 1000 times above that of the surrounding high vacuum. Ions with initial internal energy will take up energy by making collisions with the inert gas atoms or

molecules and dissociate along any fragmentation pathway available at this specific level of internal energy.

CID typically yields fragment ions whereby a peptide bond is cleaved to produce y and b-type ions (**Figure 1-3**) (*22*). Given that a basic requirement for the CID process is the collision gas, which is used in most of the tandem mass spectrometers, CID has become a standard and routine fragmentation strategy in the proteomics work flow (*20*). The propensity to lose labile functional groups during CID, however, has been recognized as an obstacle in localizing protein post-translational modifications. Phosphorylated peptides, for example, can easily lose their phosphate group (as H_3PO_4) during CID (**Figure 1-4**) (*22*). This phenomenon makes an unambiguous identification of multiple phosphorylation sites on a single peptide difficult, especially when unphosphorylated peptides that undergo water loss are present in the same ion cluster. It was later found that a unique electron-based fragmentation strategy, electron transfer dissociation (ETD) or electron-capture dissociation (ECD), can prevent this phenomenon.

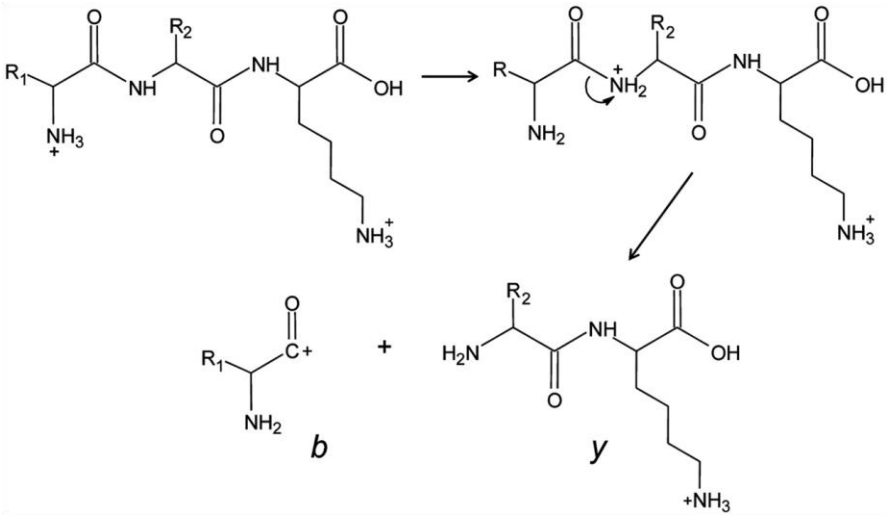

Figure 1-3. The mechanism of CID fragmentation pathway, which yields y and b-type ions. Taken from Syka et al. 2004. PNAS.

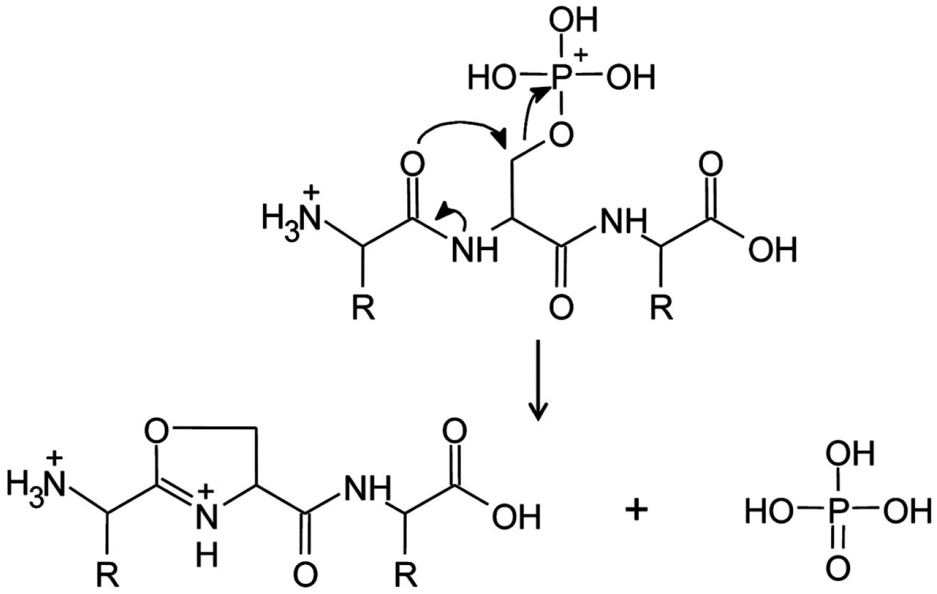

Figure 1-4. The neutral loss of phosphate group (H_3PO_4) of a phosphorylated peptide during CID. Taken from Syka et al. 2004. PNAS.

1.6.2 Electron transfer dissociation

Electron transfer dissociation (ETD) was invented in early 2000's by Hunt, Syka, and Coon (*23*). ETD employs a radical anion in the gas phase to transfer an electron to a

peptide ion of interest, leading to a unique fragmentation pathway that produces z and c-type ions (**Figure 1-5**). The Thermo LTQ-Orbitrap XL (ETD) instrument, for example, which was used to conduct much of the research in this thesis, utilizes fluoranthene as the reagent and produces fluoranthene radical anions via a chemical ionization (CI) process (called electron capture). The electron-transfer process then takes place in the linear ion trap whereby the radical anion transfers an electron to the positively charged peptide or protein in a process that is promoted by the opposite charges of the two species.

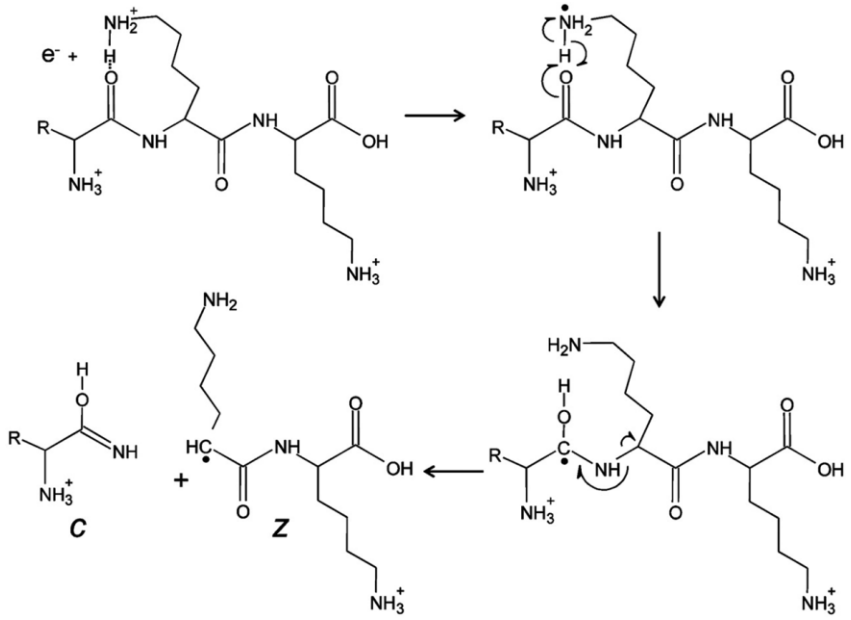

Figure 1-5. A proposed mechanism of ETD fragmentation, which yields z and c-type ions. Taken from Syka et al. 2004. PNAS.

ETD cleaves randomly along the peptide backbone while side chains and modifications such as phosphorylation remain intact. The technique only works well for

higher charge state ions (z > 2). Relative to CID, ETD is advantageous, however, for the fragmentation of longer peptides or even entire proteins. This makes the technique important for top-down proteomics.

Although a number of workers have investigated ETD, its mechanism is still under debate (*24, 25*). The advantage of ETD in the identification of protein post-translational modifications, especially phosphorylation, is unquestioned (*22, 26*). An example of the combination of CID and ETD in the identification of phosphorylation sites on Cx43 under the activation of CaMKII is described in this thesis.

1.7 MASS SPECTROMETRY-BASED PROTEIN FOOTPRINTING

Mass spectrometry-based protein footprinting (*27-29*) is a modern strategy that utilizes the advantages of MS and chemical modification (hydrogen/deuterium exchange, hydroxyl-radical oxidative modification, chemical crosslinking, etc.) to generate a mass shift that is readily seen by MS. Footprinting can capture minor changes in protein solvent accessibilities that are induced by interactions or by the presence of PTMs. These approaches can probe protein conformational changes associated with protein-ligand (ligand: protein, DNA, peptide, drug etc.) interactions and protein dynamics. Hydrogen/deuterium exchange is considered here to be a footprinting strategy because

like other strategies, it introduces new covalent bonds in a protein. The modifications, however, are reversible.

1.8 HYDROGEN/DEUTERIUM EXCHANGE

Kaj Ulrik Linderstrøm-Lang in late 1940's first developed hydrogen/deuterium exchange (H/DX) by measuring the small molecular mass increments that occur following uptake of D. Given that hydrogen and deuterium nuclei are grossly different in their magnetic properties, nuclear magnetic resonance (NMR) soon became the main means to measure the extent of deuterium uptake (*30*). In the 1990's, mass spectrometry began to evolve as another powerful tool in protein analysis and H/DX. The utilization of hydrogen/deuterium exchange MS (H/DX-MS) for the study of protein-ligand interactions, protein dynamics, and protein folding is now an accepted approach (*28, 31-33*).

Proteins have three types of hydrogens with different deuterium exchange rates (**Figure 1-6**). The first class includes amide hydrogens that exchange with deuterium at middle rates (half lives of seconds to hours). A second class are hydrogens attached to the functional groups of side chain, and they exchange with deuterium at very fast rates (half lives of μs), and they are easily back-exchanged to hydrogen by returning the protein to a protic solvent. The third class includes hydrogens covalently bonded to carbon. These are

essentially not exchangeable with deuterium in D_2O. These characteristics of H/DX enable us to measure the extent of deuterium uptake of the amide residues (amino acids) on a reasonable time frame, thereby revealing a wide range of protein dynamics.

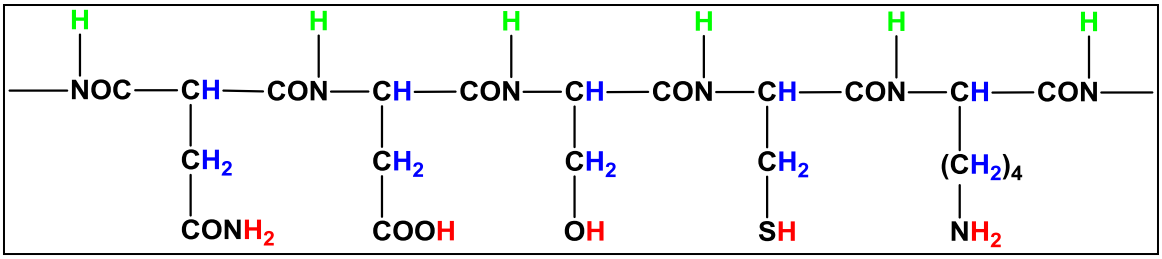

Hydrogen	Exchange Rate
OH, SH, NH_2, CO_2H, $CONH_2$	Fast
Main chain NH	Medium
Aliphatic CH Aromatic CH	Extremely slow (Non-exchangeable)

Figure 1-6. Proteins have three types of exchangeable hydrogens: (1) amide hydrogens, green; (2) carbon hydrogens, blue; (3) side-chain hydrogens, red.

1.8.1 Rates of H/DX are pH and temperature dependent

H/DX is an acid and base-catalyzed reaction. The intrinsic rate of exchange is expressed as equation 9:

$$k_{ex} = k_{acid}[H_3O^+] + k_{base}[OH^-] + k_{water} \qquad \text{Eq. 9}$$

Given that the rate of water catalysis is six orders of magnitude smaller than that of acid catalysis and 13 orders of magnitude smaller than that of base catalysis, this term is

usually ignored. Although the amide hydrogens of different amino acids have different intrinsic exchange rates, the overall exchange rate reaches its lowest value near pH 2.5 and 0 ºC (**Figure 1-7**) (*34*). Therefore, H/DX can be quenched by adding sufficient acid to bring the pH to 2.5 and by cooling in ice water prior to MS analysis.

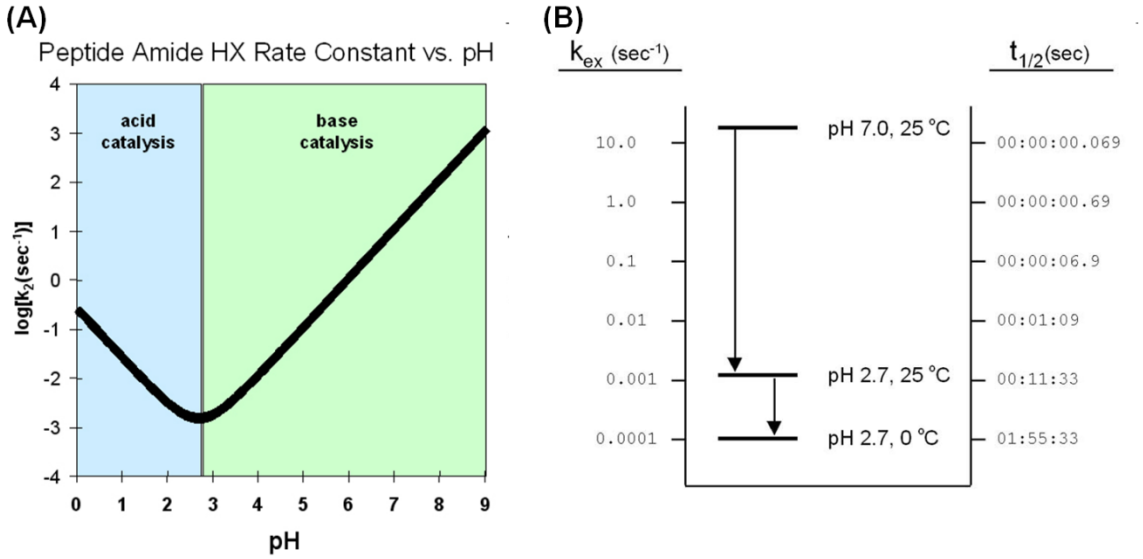

Figure 1-7. The rates of H/DX depend on pH (A) and temperature (B). Taken from HXMS website: http://www.hxms.neu.edu/research/tutorial_theory.htm.

The overall half life of H/DX, however, is relatively short as compared to other covalent labeling strategies even under the quenching condition (overall half life ~ 40 min) (*31*). Thus, it is essential to keep the analyzing time short, within 10 min, to obtain sufficient information of deuterium uptake. One can correct the extent of back exchange by incorporating a 100% deuterated sample under the same analysis process and follow equation 10:

$$D = \frac{m - m_{0\%}}{m_{100\%} - m_{0\%}} N \qquad \text{Eq. 10}$$

where D is the adjusted deuterium level, N is the total number of exchangeable amide hydrogens, m is the experimentally measured mass, $m_{0\%}$ is the mass of the undeuterated protein/peptide, and $m_{100\%}$ is the mass of the fully deuterated protein/peptide (*31*).

1.8.2 Exchange kinetics (EX1 vs. EX2)

In the H/DX experiment, the concentration of D_2O present at the equilibrium is much greater than that of water. Therefore, H/DX follows pseudo-first order kinetics in which the correlation between the number of deuteriums taken up and the exchange rate can be illustrated as:

$$D = N - \sum_{i=1}^{N} e^{-k_i t} \qquad \text{Eq. 11}$$

where D is the deuterium level, N is the total number of exchangeable amide hydrogens, k is the exchange rate, and t is the exchange time. One can calculate the number of amide hydrogens at different exchange rates by fixing the rate constants and using kinetic curve fitting processes, or calculate the exchange rates corresponding to different groups of amide hydrogens that are defined prior to the fitting process (*31*).

H/DX kinetics, sometimes, becomes more complex according to different characteristics of protein folding. The most popular model for hydrogen exchange of native proteins dissolved in D_2O is:

$$NH_{cl} \underset{k_{cl}}{\overset{k_{op}}{\leftrightarrow}} NH_{op} \xrightarrow{k_{rc}} ND \quad \text{Eq. 12}$$

in which the opening motion of protein proceeds with the rate constant k_{op} and the closing motion with the rate constant k_{cl}. In the open form, deuterium exchange can occur with the rate constant k_{rc}. Therefore, the observed exchange rate k_{ex} can be described as (*35*):

$$k_{ex} = \frac{k_{op}k_{rc}}{k_{cl}+k_{rc}} \quad \text{Eq. 13}$$

When $k_{rc} << k_{cl}$, equation 13 simplifies to $k_{ex} = k_{rc}(k_{op}/k_{cl})$. Proteins having this behavior, called EX2 kinetics, give one major group of deuterium uptake distribution in H/DX experiments, and one can obtain the overall information of H/DX kinetics of the protein. The apparent free energy of opening or exchange, ΔG_{HX}, is expressed as $-RT\ln K_{op}$ and can be calculated with data from EX2 exchange. Thus, hydrogen exchange in the EX2 model provides thermodynamic data. Most proteins, including those discussed in this thesis, follow EX2 behavior.

When $k_{cl} << k_{rc}$, then $k_{ex} = k_{op}$. Proteins having this behavior, called EX1, give mutiple groups of deuterium uptake distribution in H/DX experiments, making the data interpretation difficult. The information of protein folding/unfolding, however, can be obtained under this condition. The shortest H/DX time in solution that has been captured by MS, thus far, is in the range of μs (*36*).

1.8.3 H/DX at the Global-level

The extent of deuterium uptake of a protein can be measured globally by investigating the average differences between the masses of the deuterated protein and the undeuterated protein. H/DX is initiated by diluting the proteins in D_2O buffer at physiological pH (or any suitable pH) and held for various times at 25 °C (or other suitable temperatures) before quenching the exchange by adding acid to decrease the pH to 2.5 and by lowering the temperature to 0 °C. The deuterated samples are loaded onto a C_8 or C_{18} trap column, allowing labile side-chain sites to back exchange and salts and ionic buffers to be removed. After elution from the column, the protein may be purified further via a cooled HPLC system and analyzed by mass spectrometry. This strategy enables us to monitor the global changes of hydrogen bonding and solvent accessibility of the protein of interest owing to various perturbations including ligand binding.

1.8.4 H/DX at the Peptide-level

Protein conformational changes sometimes occur only at small regions of a large protein, and in that case, differences reported by H/DX are very often "washed out" by investigating the whole protein. To reveal these minor changes, we need higher spatial resolution provided by H/DX-MS. H/DX coupled with enzymatic digestion prior to mass spectrometry analysis, as mentioned above, affords spatial resolution at the "peptide-level" (i.e., to regions of the protein that are 6-10 amino-acid residues in length (*37*)) (**Figure 1-**

8). The uptake extent of deuterium is measured as the mass-to-charge differences between the centroid of the isotopic distribution of the deuterated peptide and the undeuterated peptide. The enzymes used to achieve peptide resolution in H/DX are mainly acidic proteases, such as pepsin or protease XIII, which are active under the quenching conditions (pH ~ 2.5).

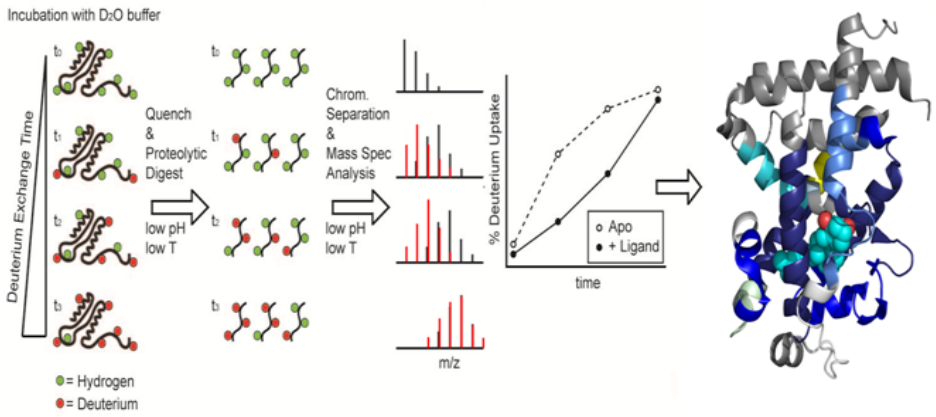

Figure 1-8. H/DX workflow that provides "peptide-level" information. Taken from Chalmers et al. 2011. Expert Review Proteomics.

1.8.5 H/DX at the Residue-level

To refine the spatial resolution to the "residue (amide) level", one can incorporate multiple enzymatic digestions and analyze overlapping peptides (*38*), or apply appropriate gas-phase fragmentation of the deuterated peptides released upon pepsin digestion.

Gas-phase hydrogen scrambling, however, is an obstacle to achieving this goal, especially when using collision-induced dissociation (CID) or collisionally activated dissociation (CAD) to fragment the peptide (*39-44*). Scrambling of H and D in the gas phase, however, can be largely prevented by fragmenting the peptides with electron-transfer dissociation (ETD) or electron-capture dissociation (ECD) (*45, 46*).

To provide assurance that the conditions are accompanied by minimal scrambling, Jørgensen (*44-46*) established a set of standard peptides that can be evaluated as test cases for scrambling. Several other methods were also established for the same purpose (*47, 48*). Two approaches, top-down (*49-53*) and bottom-up H/DX (*54, 55*), allow single-residue resolution to be achieved. The former strategy does not require an enzymatic digestion step, thereby shortening the time of the experimental protocol and lowering the extent of back exchange, but it does require that the protein be pure and fragmentation be complete and the coverage be good. Both are difficult to achieve as protein size becomes larger. The latter strategy, on the other hand, utilizing enzymatic digestion, LC/MS analysis, and tandem mass spectrometry (ETD or ECD), provides information with fewer restrictions and more confidence that the results are not compromised by scrambling. An example of utilizing bottom-up H/DX for the study of ApoE oligomerization is included in this thesis.

1.9 STUDY THE BIOPHYSICAL PROPERTIES OF PROTEINS BY H/DX

1.9.1 Protein dynamics

Protein conformational changes affect many biological functions, including enzymatic catalysis and selective interactions of macromolecules. Proteins consisting of multiple domains joined by flexible linkers can undergo large movements that result in the repacking of adjacent domains. The slow dynamics of protein conformational changes usually involve breaking and making relatively strong hydrogen bonds, and they are associated with low-solvent accessibility at short times of exchange. Therefore, H/DX kinetics has the potential to identify, with reasonable resolution, domain-packing interactions that correspond to different protein conformational states in large proteins.

1.9.2 Affinity of protein-ligand interaction

Measuring the affinity of protein-ligand interactions is important in many areas of biophysics and in the design of future drugs. Several methods can be used to measure binding affinities including FRET (fluorescence resonance energy transfer) (*56*), NMR (*57*), CD (circular dichroism) (*58*), calorimetry (*59*), SPR (surface plasmon resonance) (*60, 61*), and ESI mass spectrometry (*62*).

There are two approaches that utilize H/DX to measure the thermodynamic properties of protein-ligand interactions: SUPREX (Stability of Unpurified Proteins from

Rates of H/D Exchange) (*63, 64*), and PLIMSTEX (Protein-Ligand Interactions by Mass Spectrometry, Titration, and H/D Exchange) (*65-67*). One may ask why MS methods could play a role in this well-developed area. The answer is MS can provide site specificity.

SUPREX incorporates different amounts of denaturants (urea or guanidinium chloride) in the solution of a protein. A SUPREX curve can be obtained by plotting the deuterium uptake of protein (at constant exchange time) as a function of increasing amounts of denaturant. Because proteins unfold in the presence of denaturants, increasing deuterium uptake occurs with the unfolding. Once a binding ligand is present in solution, the protein stability usually increases compared to the protein in the apo state, causing the SUPREX curve to shift to higher denaturant concentrations. By measuring the differences of $C^{1/2}_{\mathrm{SUPREX}}$, which is the midpoint of the transition between the native state and unfolded state, and by following equation 14 and 15, one can obtain the dissociation constant of the protein-ligand complex.

$$-\Delta G^{0}_{\mathrm{f}} = mC^{\frac{1}{2}}_{\mathrm{SUPREX}} + RT \ln \frac{\left(\frac{k_{\mathrm{int}}t}{0.693}\right)-1}{\frac{n^{n}}{2^{n-1}}[P]^{n-1}} \qquad \text{Eq. 14}$$

$$\Delta\Delta G^{0}_{\mathrm{f}} = -nRT \ln\left[1 + \left(\frac{[L]}{k_{\mathrm{d}}}\right)\right] \qquad \text{Eq. 15}$$

One disadvantage of SUPREX is that the presence of denaturant may influence the protein-ligand interactions; after all, proteins in vivo do not bind ligands in solutions containing denaturants.

PLIMSTEX, developed in the M. Gross group, utilizes deuterium uptake differences between apo (absence of ligand) and holo states (ligand bound). A PLIMSTEX curve can be obtained by titrating a protein solution with increasing amounts of ligand followed by subjecting the protein to H/DX for a given, constant time, a time for which H/DX is relatively constant and for which small errors in sampling time would have minimal impact on the titration.

The fitting process of the PLIMSTEX curve involves three parameters (D_0, ΔD_i, and β_i) in which D_0 is the deuterium uptake of the apo state, ΔD_i is the decrease of deuterium uptake due to each ligand binding, and β_i (i = 1 to n) is the overall binding constant. To fit the data, a model must build a relationship between the overall deuterium shift and the total ligand concentration as shown in equation 16.

$$\Delta D(\beta_1, \dots, \beta_n, D_0, \Delta D_1, \dots, \Delta D_n, [Lig_T]) = D_0 - \sum_{i=1}^{n} \Delta D_i \left(\frac{[Prot\text{-}Lig_i]}{[Prot_T]}\right) \qquad \text{Eq. 16}$$

ΔD_i is weighted by its binding fraction $[Prot\text{-}Lig_t]/[Prot_T]$, which is a function of total ligand concentration $[Lig_T]$ and the overall binding constant β_i. β_i is the product of all the stepwise equilibrium constants as shown in equation 17.

$$\beta_i = K_1 K_2 \cdots K_i \qquad \text{Eg. 17}$$

The binding fraction in equation 16 for each protein-ligand species can then be expressed as:

$$\frac{[Prot\text{-}Lig_i]}{[Prot_T]} = \frac{\beta_i [Lig]^i}{1+\sum_{i=1}^{n} \beta_i [Lig]^i} \qquad \text{Eg. 18}$$

The calculation of the binding fractions requires the free-ligand concentration, [*Lig*], which can be inferred from the total ligand concentration and the extent of complexation. The analytical derivative of [*Lig*] with respect to [Lig_T], which is a function of [*Lig*], [$Prot_T$], and β_i, can be written as:

$$\frac{d[Lig]}{d[Lig_T]}(\beta_1, \ldots, \beta_n, [Prot_T], [Lig_T]) =$$

$$\frac{\sum_{i=0}^{n} \beta_i [Lig]^i}{\sum_{i=0}^{n} (i+1)\beta_i [Lig]^i + Prot_T(\sum_{i=1}^{n} i^2 \beta_i [Lig]^{i-1}) - Lig_T(\sum_{i=1}^{n} i\beta_i [Lig]^{i-1})} \qquad \text{Eg. 19}$$

We applied the concept of PLIMSTEX to troponin C, a Ca^{2+} binding protein, and to the troponin C-troponin I interactions, and described the outcomes in this thesis.

1.10 SCOPE AND SIGNIFICANCE OF THE THESIS

Mass spectrometry, introduced in this chapter, is now a powerful tool in the characterization of both protein post-translational modifications and protein-ligand interactions. Mass spectrometry-based proteomics and protein footprinting are two strategies with significant growth rates, and they are now widely used to address various biochemical/biophysical issues including protein dynamics, folding and unfolding, and

protein interactions. We are interested in utilizing and expanding these two approaches to gain a better understanding of three disease-related proteins, connexin 43, troponin, and apolipoprotein E, and another protein (Fenna-Matthews-Olson protein) that is important in the photosynthetic system of green sulfur bacteria.

Thus, we first describe in the thesis a mass spectrometry-based proteomics strategy to identify the phosphoylation sites of connexin 43 in vitro, under the activation of CaMKII, and in vivo. The neutral loss of the phosphate group from phosphorylated peptide ions under CID gas-phase fragmentation, however, presented an obstacle to the unambiguous identification of multiple phosphorylation sites on a single peptide. We show that the combination of CID and ETD offers complementary identification of the phosphorylation sites on this heavily phosphorylated protein. This strategy, therefore, is becoming a standard platform for future studies of protein phosphorylation.

We then utilized hydrogen/deuterium exchange (H/DX), one of the mass spectrometry-based protein footprinting strategies, to study the biophysical properties (binding interfaces, binding affinities, and protein dynamics) of five protein-ligand interaction systems. These systems are: (1) troponin C and its interaction with four Ca^{2+} ions, (2) troponin C dynamics within the troponin complex and the interactions of the three subunits (TnC, TnI, and TnT) with each other, (3) the oligomerization of human

apolipoprotein E as compared to a mutant-forced monomer, (4) the apolipoprotein E-Aβ40 interactions, and (5) the interactions between Fenna-Matthews-Olson protein (FMO) and CsmA baseplate protein. We also applied ETD, a newly explored fragmentation method that can provide H/DX information at the residue-level, in the study of ApoE oligomerization.

Our results show that H/DX is, indeed, a powerful strategy that can provide the investigation of protein-ligand interaction in a high-resolution manner and provide solutions to important biochemical problems.

1.11 REFERENCES

1. Alberghina, L., Mavelli, G., Drovandi, G., Palumbo, P., Pessina, S., Tripodi, F., Coccetti, P., and Vanoni, M. (2012) Cell growth and cell cycle in Saccharomyces cerevisiae: Basic regulatory design and protein–protein interaction network, *Biotechnology Advances 30*, 52-72.

2. Metz, J. T., and Hajduk, P. J. (2010) Rational approaches to targeted polypharmacology: creating and navigating protein–ligand interaction networks, *Current Opinion in Chemical Biology 14*, 498-504.

3. Soman, J., Tao, T., and Phillips, G. N. (1999) Conformational variation of calcium-bound troponin C, *Proteins: Structure, Function, and Bioinformatics 37*, 510-511.

4. Li, M. X., Robertson, I. M., and Sykes, B. D. (2008) Interaction of cardiac troponin with cardiotonic drugs: A structural perspective, *Biochemical and Biophysical Research Communications 369*, 88-99.

5. Seet, B. T., Dikic, I., Zhou, M.-M., and Pawson, T. (2006) Reading protein modifications with interaction domains, *Nat Rev Mol Cell Biol 7*, 473-483.

6. Aulak, K. S., Koeck, T., Crabb, J. W., and Stuehr, D. J. (2004) Dynamics of protein nitration in cells and mitochondria, *American Journal of Physiology - Heart and Circulatory Physiology 286*, H30-H38.

7. Bhattacharjee, A., Majumdar, U., Maity, D., Sarkar, T. S., Goswami, A. M., Sahoo, R., and Ghosh, S. (2009) In vivo protein tyrosine nitration in S. cerevisiae: Identification of tyrosine-nitrated proteins in mitochondria, *Biochemical and Biophysical Research Communications 388*, 612-617.

8. Muthana, S. M., Campbell, C. T., and Gildersleeve, J. C. (2011) Modifications of Glycans: Biological Significance and Therapeutic Opportunities, *ACS Chemical Biology*.

9. Wong, C.-H. (2005) Protein Glycosylation: New Challenges and Opportunities, *The Journal of Organic Chemistry 70*, 4219-4225.

10. Gopal, V., and Guruprasad, K. (2010) Structure prediction and validation of an affibody engineered for cell-specific nucleic acid targeting, *Systems and Synthetic Biology 4*, 293-297.

11. Bains, G., Patel, A. B., and Narayanaswami, V. (2011) Pyrene: A Probe to Study Protein Conformation and Conformational Changes, *Molecules 16*, 7909-7935.

12. Zheng, W., and Tekpinar, M. (2011) Accurate Flexible Fitting of High-Resolution Protein Structures to Small-Angle X-Ray Scattering Data Using a Coarse-Grained Model with Implicit Hydration Shell, *Biophysical journal 101*, 2981-2991.

13. NISHIKATA, M., KASAI, K.-i., and ISHII, S.-i. (1977) Affinity Chromatography of Trypsin and Related Enzymes, *Journal of Biochemistry 82*, 1475-1484.

14. Hu, G. F., and Vallee, B. L. (1994) A Gel Retardation Assay for the Interaction of Proteins and Carbohydrates by Fluorophore-Assisted Carbohydrate Electrophoresis, *Analytical Biochemistry 218*, 185-191.

15. Vinogradova, M. V., Stone, D. B., Malanina, G. G., Karatzaferi, C., Cooke, R., Mendelson, R. A., and Fletterick, R. J. (2005) Ca2+-regulated structural changes in troponin, *Proceedings of the National Academy of Sciences of the United States of America 102*, 5038-5043.

16. Shaw, G. S., Golden, L. F., Hodges, R. S., and Sykes, B. D. (1991) Interactions between paired calcium-binding sites in proteins: NMR determination of the stoichiometry of calcium binding to a synthetic troponin-C peptide, *Journal of the American Chemical Society 113*, 5557-5563.

17. Fenn, J., Mann, M., Meng, C., Wong, S., and Whitehouse, C. (1989) Electrospray ionization for mass spectrometry of large biomolecules, *Science 246*, 64-71.

18. Strupat, K., Karas, M., and Hillenkamp, F. (1991) 2,5-Dihydroxybenzoic acid: a new matrix for laser desorption—ionization mass spectrometry, *International Journal of Mass Spectrometry and Ion Processes 111*, 89-102.

19. Makarov, A. (2000) Electrostatic Axially Harmonic Orbital Trapping: A High-Performance Technique of Mass Analysis, *Analytical Chemistry 72*, 1156-1162.

20. Nesvizhskii, A. I., Vitek, O., and Aebersold, R. (2007) Analysis and validation of proteomic data generated by tandem mass spectrometry, *Nat Meth 4*, 787-797.

21. Sobott, F., Watt, S. J., Smith, J., Edelmann, M. J., Kramer, H. B., and Kessler, B. M. (2009) Comparison of CID Versus ETD Based MS/MS Fragmentation for the Analysis of Protein Ubiquitination, *Journal of The American Society for Mass Spectrometry 20*, 1652-1659.

22. Boersema, P. J., Mohammed, S., and Heck, A. J. R. (2009) Phosphopeptide fragmentation and analysis by mass spectrometry, *Journal of Mass Spectrometry 44*, 861-878.

23. Syka, J. E. P., Coon, J. J., Schroeder, M. J., Shabanowitz, J., and Hunt, D. F. (2004) Peptide and protein sequence analysis by electron transfer dissociation

mass spectrometry, *Proceedings of the National Academy of Sciences of the United States of America 101*, 9528-9533.

24. Sohn, C. H., Chung, C. K., Yin, S., Ramachandran, P., Loo, J. A., and Beauchamp, J. L. (2009) Probing the Mechanism of Electron Capture and Electron Transfer Dissociation Using Tags with Variable Electron Affinity, *Journal of the American Chemical Society 131*, 5444-5459.

25. Moore, B. N., Ly, T., and Julian, R. R. (2011) Radical Conversion and Migration in Electron Capture Dissociation, *Journal of the American Chemical Society 133*, 6997-7006.

26. Huzarska, M., Ugalde, I., Kaplan, D. A., Hartmer, R., Easterling, M. L., and Polfer, N. C. (2010) Negative Electron Transfer Dissociation of Deprotonated Phosphopeptide Anions: Choice of Radical Cation Reagent and Competition between Electron and Proton Transfer, *Analytical Chemistry 82*, 2873-2878.

27. Xu, G., and Chance, M. R. (2007) Hydroxyl Radical-Mediated Modification of Proteins as Probes for Structural Proteomics, *Chemical Reviews 107*, 3514-3543.

28. Engen, J. R. (2009) Analysis of Protein Conformation and Dynamics by Hydrogen/Deuterium Exchange MS, *Anal. Chem. 81*, 7870-7875.

29. Gau, B., Garai, K., Frieden, C., and Gross, M. L. (2011) Mass Spectrometry-based Protein Footprinting Characterizes the Structures of Oligomeric Apolipoprotein E2, E3, and E4 *Biochemistry 50*, 8117-8126.

30. Wedin, R. E., Delepierre, M., Dobson, C. M., and Poulsen, F. M. (1982) Mechanisms of hydrogen exchange in proteins from NMR studies of individual tryptophan indole amine hydrogens in lysozyme, *Biochemistry 21*, 1098-1103.

31. Zhang, Z., and Smith, D. L. (1993) Determination of amide hydrogen exchange by mass spectrometry: A new tool for protein structure elucidation, *Protein Science 2*, 522-531.

32. Konermann, L., Pan, J., and Liu, Y.-H. (2011) Hydrogen exchange mass spectrometry for studying protein structure and dynamics, *Chemical Society Reviews 40*, 1224-1234.

33. Chalmers, M. J., Busby, S. A., Pascal, B. D., West, G. M., and Griffin, P. R. (2011) Differential hydrogen/deuterium exchange mass spectrometry analysis of protein-ligand interactions, *Expert Review of Proteomics 8*, 43-59.

34. Bai, Y., Milne, J. S., Mayne, L., and Englander, S. W. (1993) Primary structure effects on peptide group hydrogen exchange, *Proteins: Structure, Function, and Bioinformatics 17*, 75-86.

35. Ferraro, D. M., Lazo, N. D., and Robertson, A. D. (2003) EX1 Hydrogen Exchange and Protein Folding†, *Biochemistry 43*, 587-594.

36. Pan, J., Han, J., Borchers, C. H., and Konermann, L. (2010) Characterizing Short-Lived Protein Folding Intermediates by Top-Down Hydrogen Exchange Mass Spectrometry, *Anal. Chem. 82*, 8591-8597.

37. Rand, K. D., Zehl, M., Jensen, O. N., and Jorgensen, T. J. D. (2009) Protein Hydrogen Exchange Measured at Single-Residue Resolution by Electron Transfer Dissociation Mass Spectrometry, *Anal. Chem. 81*, 5577-5584.

38. Mayne, L., Kan, Z.-Y., Sevugan Chetty, P., Ricciuti, A., Walters, B., and Englander, S. (2011) Many Overlapping Peptides for Protein Hydrogen Exchange Experiments by the Fragment Separation-Mass Spectrometry Method, *Journal of The American Society for Mass Spectrometry 22*, 1898-1905.

39. Jorgensen, T. J. D., Gardsvoll, H., Ploug, M., and Roepstorff, P. (2005) Intramolecular Migration of Amide Hydrogens in Protonated Peptides upon Collisional Activation, *Journal of the American Chemical Society 127*, 2785-2793.

40. Demmers, J. A. A., Rijkers, D. T. S., Haverkamp, J., Killian, J. A., and Heck, A. J. R. (2002) Factors Affecting Gas-Phase Deuterium Scrambling in Peptide Ions and

Their Implications for Protein Structure Determination, *Journal of the American Chemical Society 124*, 11191-11198.

41. Hoerner, J. K., Xiao, H., Dobo, A., and Kaltashov, I. A. (2004) Is There Hydrogen Scrambling in the Gas Phase? Energetic and Structural Determinants of Proton Mobility within Protein Ions, *Journal of the American Chemical Society 126*, 7709-7717.

42. Ferguson, P. L., Pan, J., Wilson, D. J., Dempsey, B., Lajoie, G., Shilton, B., and Konermann, L. (2006) Hydrogen/Deuterium Scrambling during Quadrupole Time-of-Flight MS/MS Analysis of a Zinc-Binding Protein Domain, *Analytical Chemistry 79*, 153-160.

43. Jorgensen, T. J. D., Bache, N., Roepstorff, P., Gardsvoll, H., and Ploug, M. (2005) Collisional Activation by MALDI Tandem Time-of-flight Mass Spectrometry Induces Intramolecular Migration of Amide Hydrogens in Protonated Peptides, *Molecular & Cellular Proteomics 4*, 1910-1919.

44. Rand, K. D., and Jorgensen, T. J. D. (2007) Development of a Peptide Probe for the Occurrence of Hydrogen (1H/2H) Scrambling upon Gas-Phase Fragmentation, *Analytical Chemistry 79*, 8686-8693.

45. Zehl, M., Rand, K. D., Jensen, O. N., and Jorgensen, T. J. D. (2008) Electron Transfer Dissociation Facilitates the Measurement of Deuterium Incorporation into Selectively Labeled Peptides with Single Residue Resolution, *Journal of the American Chemical Society 130*, 17453-17459.

46. Rand, K. D., Adams, C. M., Zubarev, R. A., and Jorgensen, T. J. D. (2008) Electron Capture Dissociation Proceeds with a Low Degree of Intramolecular Migration of Peptide Amide Hydrogens, *Journal of the American Chemical Society 130*, 1341-1349.

47. Rand, K. D., Zehl, M., Jensen, O. N., and Jorgensen, T. J. D. (2010) Loss of Ammonia during Electron-Transfer Dissociation of Deuterated Peptides as an Inherent Gauge of Gas-Phase Hydrogen Scrambling, *Analytical Chemistry 82*, 9755-9762.

48. Hamuro, Y., Tomasso, J. C., and Coales, S. J. (2008) A Simple Test To Detect Hydrogen/Deuterium Scrambling during Gas-Phase Peptide Fragmentation, *Analytical Chemistry 80*, 6785-6790.

49. Sterling, H. J., and Williams, E. R. (2010) Real-Time Hydrogen/Deuterium Exchange Kinetics via Supercharged Electrospray Ionization Tandem Mass Spectrometry, *Analytical Chemistry 82*, 9050-9057.

50. Kaltashov, I. A., Bobst, C. E., and Abzalimov, R. R. (2009) H/D Exchange and Mass Spectrometry in the Studies of Protein Conformation and Dynamics: Is There a Need for a Top-Down Approach?, *Analytical Chemistry 81*, 7892-7899.

51. Pan, J., Han, J., Borchers, C. H., and Konermann, L. (2009) Hydrogen/Deuterium Exchange Mass Spectrometry with Top-Down Electron Capture Dissociation for Characterizing Structural Transitions of a 17 kDa Protein, *Journal of the American Chemical Society 131*, 12801-12808.

52. Pan, J., Han, J., Borchers, C. H., and Konermann, L. (2010) Characterizing Short-Lived Protein Folding Intermediates by Top-Down Hydrogen Exchange Mass Spectrometry, *Analytical Chemistry 82*, 8591-8597.

53. Pan, J., Han, J., Borchers, C. H., and Konermann, L. (2011) Conformer-Specific Hydrogen Exchange Analysis of Aβ(1-42) Oligomers by Top-Down Electron Capture Dissociation Mass Spectrometry, *Anal. Chem. 83*, 5386-5393.

54. Rand, K. D., Zehl, M., Jensen, O. N., and Jorgensen, T. J. D. (2009) Protein Hydrogen Exchange Measured at Single-Residue Resolution by Electron Transfer Dissociation Mass Spectrometry, *Analytical Chemistry 81*, 5577-5584.

55. Landgraf, R., Chalmers, M., and Griffin, P. (2012) Automated Hydrogen/Deuterium Exchange Electron Transfer Dissociation High Resolution

Mass Spectrometry Measured at Single-Amide Resolution, *Journal of The American Society for Mass Spectrometry 23*, 301-309.

56. Khamir, M., Adam, D. H., Raghunandan, K., Peter, J. W., and Jennifer, J. L. (2009) A computational approach to inferring cellular protein-binding affinities from quantitative fluorescence resonance energy transfer imaging, *PROTEOMICS 9*, 5371-5383.

57. Lee, F., Samantha, R., and Dan, F. (2005) Determination of protein-ligand binding affinity by NMR: observations from serum albumin model systems, *Magnetic Resonance in Chemistry 43*, 463-470.

58. Mayhood, T. W., and Windsor, W. T. (2005) Ligand binding affinity determined by temperature-dependent circular dichroism: Cyclin-dependent kinase 2 inhibitors, *Analytical Biochemistry 345*, 187-197.

59. Bains, G., and Freire, E. (1991) Calorimetric determination of cooperative interactions in high affinity binding processes, *Analytical Biochemistry 192*, 203-206.

60. Monfregola, L., Vitale, R. M., Amodeo, P., and Luca, S. D. (2009) A SPR strategy for high-throughput ligand screenings based on synthetic peptides

mimicking a selected subdomain of the target protein: A proof of concept on HER2 receptor, *Bioorganic & Medicinal Chemistry 17*, 7015-7020.

61. Blow, N. (2009) Proteins and proteomics: life on the surface, *Nat Meth 6*, 389-393.

62. Kitova, E., El-Hawiet, A., Schnier, P., and Klassen, J. (2012) Reliable Determinations of Protein–Ligand Interactions by Direct ESI-MS Measurements. Are We There Yet?, *Journal of The American Society for Mass Spectrometry 23*, 431-441.

63. Hopper, E., Roulhac, P., Campa, M., Patz, E., and Fitzgerald, M. (2008) Throughput and efficiency of a mass spectrometry-based screening assay for protein—Ligand binding detection, *Journal of The American Society for Mass Spectrometry 19*, 1303-1311.

64. Powell, K. D., Ghaemmaghami, S., Wang, M. Z., Ma, L., Oas, T. G., and Fitzgerald, M. C. (2002) A General Mass Spectrometry-Based Assay for the Quantitation of Protein−Ligand Binding Interactions in Solution, *Journal of the American Chemical Society 124*, 10256-10257.

65. Zhu, M. M., Rempel, D. L., Du, Z., and Gross, M. L. (2003) Quantification of Protein-Ligand Interactions by Mass Spectrometry, Titration, and H/D Exchange: PLIMSTEX, *J. Am. Chem. Soc. 125*, 5252-5253.

66. Zhu, M. M., Rempel, D. L., and Gross, M. L. (2004) Modeling data from titration, amide H/D exchange, and mass spectrometry to obtain protein-ligand binding constants, *J. Am. Soc. Mass Spectrom. 15*, 388-397.

67. Zhu, M. M., Chitta, R., and Gross, M. L. (2005) PLIMSTEX: a novel mass spectrometric method for the quantification of protein-ligand interactions in solution, *Int. J. Mass Spectrom. 240*, 213-220.

Chapter 2*

Identification of CaMKII Phosphorylation Sites in Connexin43 by High-Resolution Mass Spectrometry

* This chapter is based on recent publication: Huang, R. Y. C., Laing, J. G., Kanter, E. M., Berthoud, V. M., Rohrs, H. W., Townsend, R. R., Bao, M., and Yamada, K. A. Identification of CaMKII Phosphorylation Sites in Connexin43 by High-Resolution Mass Spectrometry. *Journal of Proteome Research*, **2011**, 10, 1098-1109. Copyright 2011 American Chemical Society (Huang, R. Y. C., and Laing, J. G. contributed equally to this work.)

2.1 ABSTRACT

Connexin43 (Cx43), a major cardiac gap junction channel protein, plays an important role in normal electrical and contractile activity. Phosphorylation of Cx43, under both normal and disease conditions, regulates the gap junction channel assembly, function and turnover. The C-terminal domain of Cx43 contains numerous amino acid residues that are phosphorylated by protein kinases. Our knowledge of the specific residues and kinases involved, however, is incomplete. The objective of this study is to identify amino acid residues in the Cx43-CT that are targets of the multi-functional protein kinase, Ca^{2+}/calmodulin protein kinase II (CaMKII), an enzyme known to play critical roles in Ca^{2+} homeostasis, transcription, apoptosis and ischemic heart disease. We subjected fusion protein containing the Cx43-CT to phosphorylation by CaMKII in vitro, digestion with Lys-C and trypsin followed by enrichment of phosphorylated peptides using TiO2, and analysis with a combination of two fragmentation strategies (collision-induced dissociation (CID) and electron transfer dissociation (ETD)) in an LTQ Orbitrap. We deduced the sites of modification by interpreting tandem spectra from these "orthogonal" methods of gas phase peptide fragmentation. We have identified 15 serine residues, including one novel site, in the Cx43-CT that are phosphorylated by

CaMKII, the activity of which may be important in regulating Cx43 in normal and diseased hearts.

2.2 INTRODUCTION

Cardiovascular gap junctions, formed by 2 docking hemichannels, each composed of 6 connexin subunits, are large specialized aggregates of intercellular channels and are important in cell-to-cell communication (1). There are five different connexins expressed in cardiac muscle and vasculature (1-3). Connexin43 (Cx43) is the predominant connexin expressed in working myocardium (2). Cx43 is not only responsible for electrical propagation throughout the chamber walls, and thus for normal electrical activation and subsequent ventricular contraction, but it is also a critical determinant of abnormal propagation, contractile dysfunction and arrhythmia secondary to pathophysiological remodeling during disease states (4, 5).

The expression, trafficking, distribution, turnover, permeability and gating of Cx43 are regulated primarily by phosphorylation (6, 7). There are eighteen serine residues in the carboxyl terminal tail of Cx43 that have been reported as sites of protein phosphorylation (6, 8-10), the majority of which have been identified as targets of a variety of kinases including mitogen-activated protein kinase (MAPK), protein kinase C (PKC), cyclin-dependent kinase $p34^{cdc2}$, casein kinase (CK) and protein kinase A (PKA) (6). Interestingly, four serine residues in the carboxyl terminus of Cx43 show a complex time-dependent pattern of both phosphorylation and dephosphorylation during

myocardial ischemia. Specifically, S306 is dephosphorylated and S330 is phosphorylated early after ischemia; subsequently, S297 and S368 are dephosphorylated during the critical time when gap junction uncoupling occurs (8). Finally, S330 is also dephosphorylated during the later stages of ischemia (8). Correspondingly, Lampe et al. have observed an 8-fold reduction in phosphorylated (p)S325/S328/S330 in ischemic tissue (11).

Details pertaining to the phosphorylation and dephosphorylation of the eighteen serine residues in the carboxyl terminus of Cx43 are incomplete and, at times, contradictory. Phosphorylation of S368, for example, the most widely studied phosphorylated residue, has been associated with reduced gap junction intercellular communication via a PKC-dependent mechanism in epithelial cells and fibroblasts (12). Changes in gap junctional conductance in response to PKC activation, however, depend on cell type and the state of phosphorylation of Cx43. Furthermore, the exact role of phosphorylation of S368 in ischemia and ischemic preconditioning is not clear because conflicting results have been reported (8, 13-16). The availability, affinity and specificity of commercial antibodies directed toward phosphorylated residues in Cx43 may, in part, limit the studies on alterations in the phosphorylation state of different amino acid residues.

With the recent evolution and improvement of mass spectrometry, it now appears to be a powerful technique that can be used as a tool to identify the modified amino acid residues in phosphorylated peptides. Collision-induced dissociation (CID), a fragmentation strategy utilized in the general proteomics workflow, will cause the neutral loss of the phosphate group from phosphorylated peptide, thus making an unambiguous determination of muti-phosphorylated sites difficult. Electron transfer dissociation (ETD) and electron capture dissociation (ECD), as introduced in chapter 1, leave post-translational modifications intact during fragmentation and prevent this phenomenon (17).

We report here the use of high-resolution tandem mass spectrometry with the combination of CID and ETD to identify targets of the multifunctional protein kinase, Ca^{2+}/calmodulin-dependent protein kinase II (CaMKII) (18), on the carboxyl terminus of Cx43. CaMKII plays a central role in regulating a variety of cellular functions in the heart such as Ca^{2+} homeostasis, transcription and apoptosis (18, 19). In addition, increased expression and/or activation of CaMKII have been shown to occur in cardiac disease states such as hypertrophy, heart failure, myocardial ischemia and infarction, and are thought to promote disease pathogenesis (20-24). Recently, we have found that CaMKII co-localizes with Cx43 at intercellular junctions in the infarct border zone (25). Cx43,

however, has never, to our knowledge, been shown to be a target of CaMKII. De Pina-Benabou et al. (26) hypothesized that CaMKII phosphorylation of the carboxyl terminus of Cx43 was the mechanism by which K^+ produced an increase in coupling between spinal cord astrocytes, and they predicted four serine residues that could be potential phosphorylation targets for CaMKII based on the consensus sequence RXXSX. Although Cx43 has not been shown to be a substrate for CaMKII, this enzyme has been shown to phosphorylate Cx32 in hepatocytes and Cx36 in neurons (27, 28). The specific CaMKII phosphorylation sites, however, have not been identified in Cx32, and the phosphorylation sites identified in Cx36 do not share homology with Cx43.

The current study, therefore, was performed to test the hypothesis that the carboxyl terminus of Cx43 is subject to phosphorylation by CaMKII. We found that CaMKII phosphorylates a variety of reported residues, and one novel serine residue, in the carboxyl terminus of Cx43 in vitro. These results suggest that Cx43 may be a substrate for CaMKII in vivo. The data will be discussed in the context of remodeling of Cx43 during the pathogenesis of chronic ischemic heart disease.

2.3 MATERIALS AND METHODS

2.3.1 Cx43 Fusion Protein

A DNA construct coding for a fusion protein containing amino acids 237-382 of the carboxyl terminus (CT) of rat Cx43 (GI:6978896) subcloned in frame with GST in pGEX-2T (GST-Cx43-CT, MW 42,122 g/mol) was grown in BL21-CodonPlus competent cells (Stratagene/Agilent Technologies, Santa Clara, CA). The fusion protein was purified using a B-PER GST Fusion Protein Purification Kit (Pierce/Thermo Scientific, Rockford, IL) and subsequently dialyzed against Tris-buffered saline for 48 hr. The sequence of the fusion protein was confirmed at the Washington University Protein and Nucleic Acid Chemistry Laboratories. The amino acid sequence of the Cx43-CT present in the fusion protein is shown in bold in **Figure 2-1**.

```
  1 MGDWSALGKL LDKVQAYSTA GGKVWLSVLF IFRILLLGTA VESAWGDEQS AFRCNTQQPG
 61 CENVCYDKSF PISHVRFWVL QIIFVSVPTL LYLAHVFYVM RKEEKLNKKE EELKVAQTDG
121 VNVEMHLKQI EIKKFKYGIE EHGKVKMRGG LLRTYIISIL FKSVFEVAFL LIQWYIYGFS
181 LSAVYTCKRD PCPHQVDCFL SRPTEKTIFI IFMLVVSLVS LALNIIELFY VFFKGVKDRV
241 KGRSDPYHAT TGPLSPSKDC GSPKYAYFNG CSSPTAPLSP MSPPGYKLVT GDRNNSSCRN
301 YNKQASEQNW ANYSAEQNRM GQAGSTISNS HAQPFDFPDD NQNAKKVAAG HELQPLAIVD
361 QRPSSRASSR ASSRPRPDDL EI
```

Figure 2-1. Tandem mass spectrometric coverage of Cx43-CT. The N-terminal, transmembrane, extracellular loop and intracellular loop domains of the protein are indicated in grey. The amino acids of the Cx43-CT present in the fusion protein used in this study are indicated in bold black or red (98% coverage). Amino acids in red were positively identified by tandem mass spectrometry. The 15 serine residues underscored and highlighted in yellow were phosphorylated by CaMKII in vitro.

2.3.2 In vitro Phosphorylation of GST-Cx43-CT by CaMKII

GST-Cx43-CT fusion protein was subjected to in vitro phosphorylation using CaMKII (New England Biolabs, Ipswich, MA) per the manufacturer's instructions. Briefly, GST-Cx43-CT fusion protein (1 – 8 μg) was incubated with 1.2 μmol/L calmodulin, 2 mmol/L $CaCl_2$, 210 μmol/L ATP and 1,500 U CaMKII in a final volume of 10.5 μL at 30ºC for 24 h, after which the reaction was stopped on ice and phosphatase inhibitors were added to a final concentration of 1 mmol/L NaF and 2 mmol/L Na_3VO_4. Control reactions contained fusion protein, calmodulin, $CaCl_2$, ATP and buffer, but no CaMKII. In one experiment we used CK1 (New England Biolabs, 1,500 U, 24 h) per the manufacturer's instructions to test a protein kinase known to phosphorylate the Cx43-CT (11).

2.3.3 Immunoprecipitation

Mouse ventricles flash-frozen in liquid N_2 were pulverized and homogenized in lysis buffer containing 1.5% NP-40 (Surfact-Amps NP-40, Pierce) in phosphate-buffered saline (PBS, Diamedix), rotating for 30 min at 4ºC.

Monoclonal anti-Cx43 (50 μg, Millipore/Chemicon) or mouse IgG (50 μg, Santa Cruz, negative control) antibody was crosslinked to 200 μL of protein G-bound magnetic Dynabeads (Invitrogen) using dimethyl pimelimidate (DMP, Pierce) and triethanolamine

(Sigma) in silanized (10% dimethyldichlorosilyl, P.J. Cobert) tubes. The crosslinked beads were washed in PBS, citrate buffer (pH 5.0), sodium phosphate buffer (pH 8.1), sodium deoxycholate (0.5%) and Tween-20 (0.1%). Each set of antibody-crosslinked beads was incubated with protein from the right and left ventricles of one mouse heart, NaF (1 mM), Na_3VO_3 (2 mM) and protease inhibitor cocktail (1:100, Sigma) for 2 h at 4ºC, rotating. Immunoprecipitated protein was eluted with Rapigest (1.7%, Waters) and 8 M urea in 100 mM Tris buffer (pH 8.5) at 60ºC for 5 min; the elution was repeated and the two volumes were combined. The eluent was dialyzed (Slide-A-Lyzer, Thermo) against 1 L of water for 2 h at 4ºC followed by dialysis against 1 L of water overnight at 4ºC.

2.3.4 Phosphopeptide Clean-up and Enrichment

In vitro phosphorylated GST-Cx43-CT fusion protein or immunoprecipitated full-length native Cx43 was precipitated by using a 2-D Clean-Up Kit (GE Healthcare Waukesha, WI) and resolubilized in 20 μL of 8 M urea in 100 mM Tris, pH 8.5. Proteins were then reduced with 10 mM Tris(2-carboxyethyl)phosphine (TCEP, Thermo Fisher, Rockford, IL) at 25ºC for 30 min followed by alkylation with 20 mM iodoacetamide (Sigma-Aldrich, St. Louis, MO) at 25ºC for 30 min in the dark and quenched with 10 mM dithiothreitol (DTT, Thermo Fisher) at 25ºC for 15 min. The proteins were digested with

1 μg endoproteinase Lys-C (Roche, Mannheim, Germany) at 37ºC overnight, diluted 1:4 with 100 mM Tris pH 8.5, and further digested with 1 μg trypsin (Sigma-Aldrich) in 1 mM triethylammonium bicarbonate, pH 8.5 (TEAB, Sigma-Aldrich) at 37ºC overnight. The peptide solutions were acidified with 2% trifluoroacetic acid (TFA) (Sigma-Aldrich). Phosphopeptide samples were enriched using TiO_2 tips (Glygen, Columbia, MD) that were equilibrated in 0.1% TFA before drawing each sample onto the media. Tips were washed with 100 mM glutamic acid at pH 2.0 and the bound peptides eluted with 1.5% ammonium hydroxide. The eluates were desalted using carbon NuTips (Glygen), lyophilized, and resuspended in 20 mL of 1% formic acid and 1% acetonitrile.

To verify the activity of CaMKII in vitro, 1.5 μg of autocamtide (KKALHRQETVDAL, Calbiochem/EMD Chemicals, Gibbstown, NJ) was incubated with CaMKII for 24 h as described above to produce phospho-autocamtide (KKALHRQEpTVDAL). Commercially available phospho-autocamtide (AnaSpec, Fremont, CA) was run as a positive control.

2.3.5 Mass spectrometry

Autocamtide phosphorylation was verified by using matrix-assisted laser desorption ionization (MALDI). Peptide solution was mixed 1:1 with α-cyano-4-hydroxycinnamic acid (CHCA, Sigma-Aldrich). For MALDI analyses using an ABI 4700

Proteomics Analyzer (Applied Biosystems, Framingham, MA) equipped with an Nd:YAG laser (355 nm, 3 to 7 ns pulses), the instrument was operated in reflector, positive-ion mode with an acceleration voltage of 20 kV. Spectra were averaged from 1000 laser shots at 200 Hz for each spot.

For analysis with a Thermo LTQ Orbitrap XL with electron transfer dissociation (ETD) and/or collision-induced dissociation (CID) (Thermo Fisher, San Jose, CA), samples were loaded and eluted using an autosampler and an Ultra 1D+ UPLC (Eksigent, Dublin, CA). The 75 μm diameter columns were pulled (Sutter Instruments, Novato, CA) and a 12-cm length was packed with Magic C18AQ reverse phase media (Michrom Bioresources, Auburn, CA) (29). Columns were mounted in a PicoView nanospray source (New Objective, Woburn, MA) and eluted with a 60 min gradient from 2% - 60% acetonitrile with 0.1% formic acid. Fluoranthene anion was used for ETD (30). One full mass spectrometry acquisition was used to trigger 3 alternating scans each of CID and ETD. The Orbitrap parameters were: spray voltage, 2.0 kV; capillary temperature, 200ºC; tandem mass spectrometry (MS2) selection threshold, 1000 counts; activation *q*, 0.25; activation time, 30 ms for CID and 100 ms for ETD. For ETD, isolation width was 3.0 *m/z* and reaction time was set as charge-state dependent. Supplemental activation was enabled. MS2 data were centroided during acquisition.

For analysis with an LTQ-FT Ultra (Thermo Fisher, San Jose, CA), samples were loaded onto a C18 75 μm diameter column using a NanoLC-1D (Eksigent). They were eluted with a 180 min analytical gradient from 2% - 50% acetonitrile containing 0.1% formic acid at 260 nL/min. The solution was sprayed into the mass spectrometer by using a PicoView nanospray source (New Objective). One full MS acquisition was used to trigger 8 CID scans. The FT parameters were: spray voltage, 2.0 kV; capillary temperature, 200ºC; MS2 selection threshold, 500 counts; activation *q*, 0.25; activation time, 30 ms. MS2 data were centroided during acquisition.

Alpha and beta casein (Sigma-Aldrich) and/or bovine serum albumin (BSA, Michrom Bioresources) were analyzed as controls in each experiment. In addition, casein was used to determine the optimal amount of protein to be used for detection of phosphopeptides.

Tryptic peptides from immunoprecipitated full-length native Cx43 were analyzed as above with the following exceptions. A 180 min gradient from 2% - 60% acetonitrile with 0.1% formic acid was used for separation. Both data dependent (discovery) and data-directed (inclusion list) methods were used to acquire mass spectra on the Thermo LTQ Orbitrap XL with ETD and CID (31). Parent mass lists for the latter experiment

were created from all doubly, triply and quadruply charged phosphopeptide ions identified in the in vitro experiments.

2.3.6 Mascot database search and determination of phosphorylation sites

Thermo RAW files were processed by using extract_msn (2007 version 4.0, Thermo Fisher, San Jose, CA) with a grouping tolerance of 0.8 Da, an intermediate scan setting of 1, and a minimum of 1 scan per group. The NCBI nonredundant database (version 20090105, restricted to mammals) was searched using MASCOT 2.2.06 (Matrix Science, Oxford, U.K.) with the following settings: enzyme, trypsin; MS tolerance, 10 ppm; MS/MS tolerance, 0.6 Da; maximum number of missed cleavages, 3; peptide charge of 1+, 2+ and 3+; variable modifications were carbamidomethylation of C, oxidation of M, phosphorylation of Y, T, and S, and deamidation of N-terminal Q to E. All identifications of phosphopetides were manually analyzed as described below.

Tryptic peptides containing S, T, or Y, including those with up to 3 missed cleavages, were predicted by in silico digestion (Protein Prospector MS-Digest, prospector.ucsf.edu). Theoretical MS2 spectra were generated (Protein Prospector MS-Product, prospector.ucsf.edu) for phosphopeptides that were identified in the Mascot search. When there were multiple possibilities for phosphorylation (e.g., more than one S, T, or Y in a singly-phosphorylated peptide, or more than two S, T, or Y in a doubly-

phosphorylated peptide) a table of ions was made for each possible phosphopeptide. The product ion spectrum was manually compared to each table and the best match was identified. In cases where the elution profiles of phosphopeptides overlapped, they were separated using extracted ion chromatograms for diagnostic product ions.

2.4 RESULTS AND DISCUSSION

The amino acid sequence of carboxyl terminal domains varies widely across connexins and is thought to confer specific properties to the channels composed of different connexin subtypes (32). The carboxyl terminal domain of Cx43 is structurally disordered, this intrinsically flexible property is important in both cell signaling and regulatory activity (33, 34). It has been shown that this region is involved in intra- and intermolecular interactions (35, 36). Phosphorylation of this region regulates the protein structure, subcellular distribution and function (6-8, 11-16). Seventeen serine and two tyrosine residues in the Cx43-CT have been shown to be targets of various protein kinases under control, stimulated and pathological conditions. Phosphorylation of the Cx43-CT by CaMKII, however, has not been reported.

2.4.1 The phosphorylation activity of CaMKII

To identify sites of CaMKII phosphorylation in the Cx43-CT under controlled conditions in vitro, we first optimized the amount of fusion protein required for recovery

of phosphopeptides and identification of phosphorylated amino acid residues using casein, a known phosphoprotein, at 3 different concentrations: 0.3 μg/20 μL, 1 μg/20 μL and 3 μg/20 μL. We identified 10 phosphorylation sites in casein (**Figure 2-2**), and determined that 3 μg casein in 20 μL reaction volume yielded the best results.

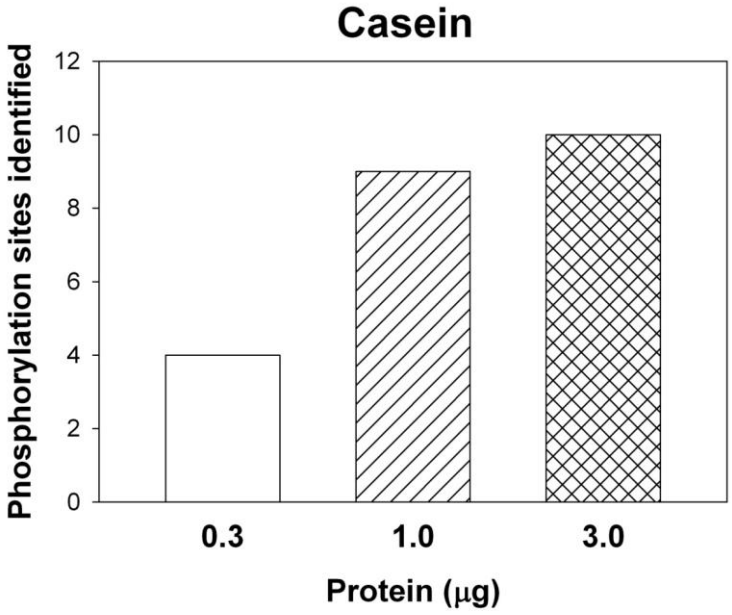

Figure 2-2. The numbers of phosphorylation sites identified on alpha-casein (total 11 phosphorylation sites) with respect to different protein amounts as starting material (0.3, 1.0, 3.0 ug).

To validate the in vitro conditions used for the CaMKII reactions, we incubated a peptide containing the threonine autophosphorylation site of CaMKII, nonphosphorylated autocamtide (KKALHRQETVDAL), with CaMKII in the presence of ATP, Ca^{2+} and calmodulin as described in Materials and Methods. We used nonphosphorylated autocamtide in the absence of CaMKII as a negative control, and phospho-autocamtide

(KKALHRQEpTVDAL) as a positive control. The MALDI spectrum obtained from autocamtide subjected to in vitro phosphorylation demonstrated a phosphopeptide that was identical to that observed from phospho-autocamtide obtained from AnaSpec (**Figure 2-3**). No phosphopeptide was detected in the reaction performed in the absence of CaMKII.

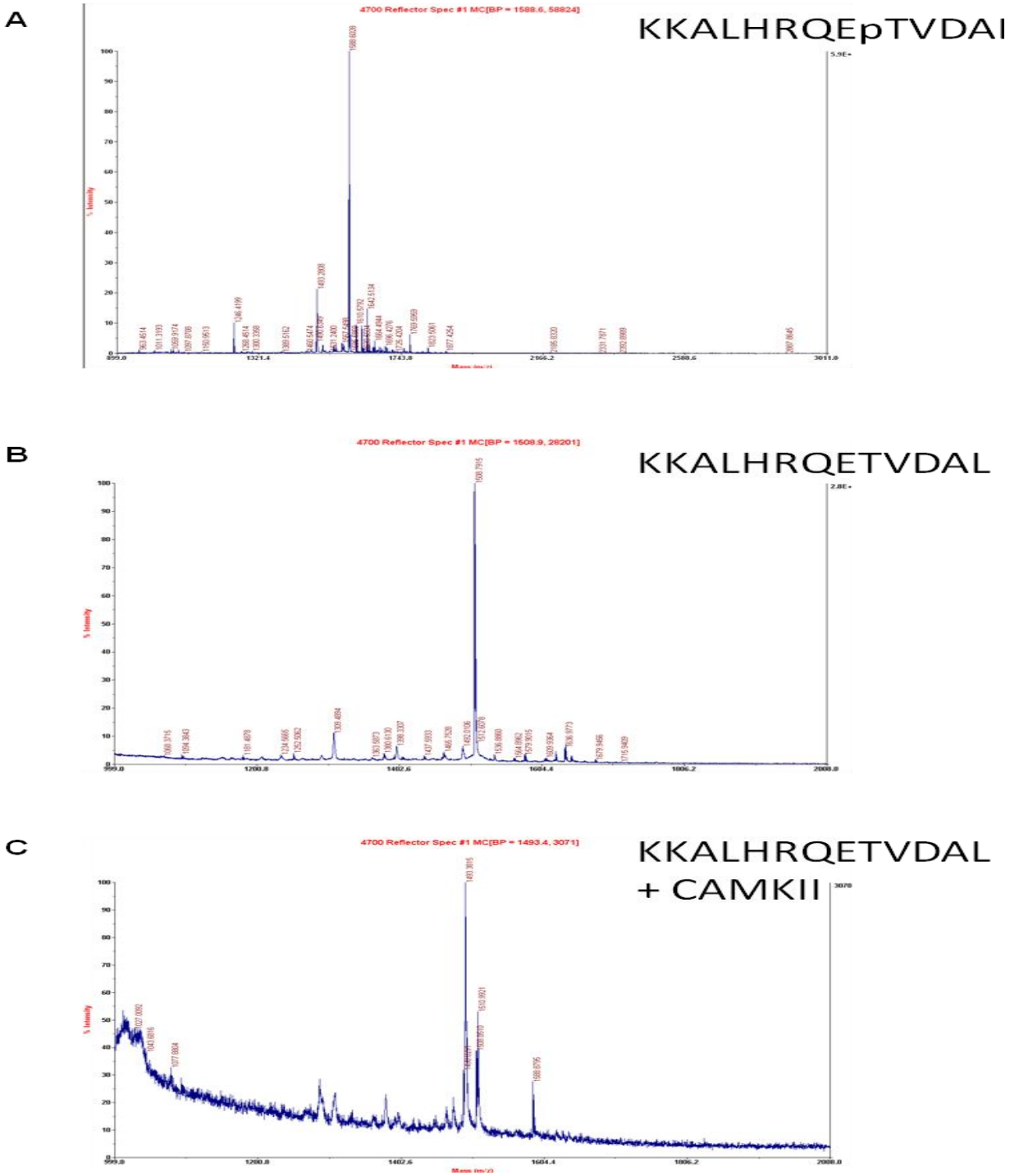

Figure 2-3. MALDI spectra of Autocamtide. (A) Positive control shows the phosphorylated peptide (KKALHRQEpTVDAL) of *m/z* 1588.6028. (B) Negative control shows the non-phosphorylated peptide (KKALHRQETVDAL) of *m/z* 1508.7915. (C) In vitro phsohphorylation shows the phosphorylated peptide (KKALHRQEpTVDAL) of *m/z* 1588.8795.

2.4.2 Phosphorylation of Cx43-CT by CaMKII

We next incubated GST-Cx43-CT fusion protein with CaMKII and subjected the reaction products to enzymatic digestion with Lys-C followed by trypsin and mass spectrometric analysis to identify the amino acid residues that are phosphorylated by CaMKII. Tandem mass spectrometry yielded 98% coverage of the Cx43-CT (**Figure 2-1**). Coverage was comparable for results obtained by using CID and ETD; however, two phosphorylation sites were identified by ETD alone (see below). This is not surprising because ETD-derived alternative fragmentation patterns that complement CID-derived data have been reported previously (37). The sequence corresponding to amino acid residues 259-293, a non-phosphorylated region, was only identified in one experiment, possibly because we used TiO_2 to enrich for phosphopeptides (38). The lack of phosphorylated residues observed in this sequence agrees with previous reports that S262, S279 and S282 are targets of protein kinases other than CaMKII (39, 40).

Four independent phosphorylation experiments were performed followed by digestion and tandem mass spectrometry. No serine residues were phosphorylated in the negative control samples that were incubated in the presence of Ca^{2+}, calmodulin and ATP, but in the absence of CaMKII. Amino acid residues in Cx43-CT that were identified as being phosphorylated by CaMKII are reported in **Table 2-1**, and the

diagnostic ions for these identifications are listed in **Table 2-2**. Several interesting observations can be made from these data.

phosphosite (# of expts)	published or novel	previous kinase association	role
S244 (3)	Novel, unreported site	–	?
S255 (3)	[a,b,c,d]	MAPK[a]; cyclin B/p34^{cdc2} [b,c]	↓ P_o[e]
S257 (3)	[d]	?	?
S296 (3)	[d]	?	?
S297 (2)	[d]	?	?
S306 (4)	[d,f]	?	Maintained coupling[f]
S314 (2)	[g,h]	–	?
S325 (3)/S328 (2)/S330 (2)	[d,i]	CK1[i]	Gap junction formation; P2 form[i]
S364 (3)	[j,k]	PKA[j,k]	cAMP-enhanced GJ assembly[k]
S365 (1)	[l,m]	PKA?[l,m]	Protection from ↓ g_j; P1 form[m]
S369 (2)	[d,l]	PKA?[l]	No effect on GJIC[l]
S372 (3)	[d,n]	PKC[n]	Maintained electrical coupling[n]
S373 (3)	[d,l,o]	PKA?[l]; Akt[o]	No effect on GJIC[l]; Cx43 binding to 14-3-3[o]

[a] Warn-Cramer et al.[40] (1996). [b] Kanemitsu et al.[39] (1998). [c] Lampe et al.[51] (1998). [d] Axelsen et al.[8] (2006). [e] Cottrell et al.[52] (2003). [f] Procida et al.[41] (2009). [g] Munton et al.[9] (2007). [h] Brill et al.[10] (2009). [i] Cooper and Lampe[42] (2002). [j] Shah et al.[53] (2002). [k] TenBroek et al.[54] (2001). [l] Yogo et al.[55] (2002). [m] Solan et al.[56] (2007). [n] Sáez et al.[57] (1997). [o] Park et al.[58] (2007); P_o = gap junction channel open probability

Table 2-1. Serine residues in Cx43-CT phosphorylated by CaMKII with previously published kinase information where available.

Table 2. Phosphoserine-containing Peptides From Cx 43-CT in vitro Phosphorylation

Sequence	Start-end	Charge	Theoretical mass	Observed mass	Phosphorylation site localized	M&SCOT score (CID)	M&SCOT score (ETD)	Diagnostic ions (CID)	Diagnostic ions (ETD)
GRSDPYHATTGPLSPSK	242-258	3	1849.836	1849.841	S244	43	37	b_2, b_3	c_2, c_3; z'_{14}, z'_{15}
GRSDPYHATTGPLSPSK	242-258	3	1849.836	1849.821	S255	23	42	b^*_{14}, y_3, y_4	c_{13}, c_{15}
GRSDPYHATTGPLSPSK	242-258	3	1849.836	1849.840	S257	37	46	b^{-a}_{15}, b^{-a}_{16}	c_{15}, c_{16}; z_2
NNSSC(Carbamidomethyl)RNYNK	294-303	2	1335.503	1335.500	S296	39	N/A	y_7, y_8, y^{-a}_7, y^{-a}_8	N/A
LVTGDRNNSSC(Carbamidomethyl)R	288-299	3	1457.608	1457.613	S296	N/A	61	N/A	c_8, c_9; z_3, z_4
LVTGDRNNSSC(Carbamidomethyl)RNYNK	288-303	3	1976.847	1976.852	S297	36	N/A	b^{-a}_8, y^{-a}_7, [@]	N/A
LVTGDRNN(Deamidated)SSC(Carbamidomethyl)R	288-299	2	1468.592	1468.597	S297	N/A	30	N/A	c_9, c_{11}
QASEQNWANYSAEQNR	304-319	2	1974.786	1974.782	S306	30	N/A	y_{13}, Y_{14}	N/A
QASEQNWANYSAEQNR	304-319	3	1974.786	1974.783	S306	N/A	33	N/A	c_2, c_3; z_{13}, z_{14}
QASEQNWANYSAEQNR	304-319	3	1974.786	1974.782	S314	46	65	b_{10}, y_5, y_6	c_{10}, c_{11}
MGQAGSTISNSHAQPFDFPDDNQNAK	320-345	3	2856.181	2856.191	S328	N/A	59	N/A	c_8, c_9; z_{17}, z^{-a}_{18}
MGQAGSTISNSHAQPFDFPDDNQNAK	320-345	3	2856.181	2856.194	S325	39	55	b_{40}, y^{-a}_{20}, y^{-a}_{21}	c_8, c_9
MGQAGSTISN(Deamidated)SHAQ(Deamidated)PFDFPDDNQNAK	320-345	3	2858.166	2858.149	S330	33	N/A	y_{15}, Y_{16}	N/A
MGQAGSTISNSHAQPFDFPDDN(Deamidated)QNAK	320-345	3	2857.165	2857.188	S330	N/A	N/A	N/A	c_{10}, c_{11}; z_{15}, z_{16}
VAAGHELQPLAIVDQRPSSR	347-366	3	2223.116	2223.102	S364	24	35	y_2, Y_4	c^{+1}_{17}, c^{+1}_{18}; z^{+1}_2, z^{+1}_3
VAAGHELQPLAIVDQRPSSR	347-366	3	2223.116	2223.107	S365	22	N/A	y_2	N/A
ASSRRPRDDLEI	371-382	2	1434.660	1434.641	S372	25	N/A	y^{-a}_{10}, y^{-a}_{11}	N/A
ASSRASSRRPRDDLEI	367-382	3	1835.857	1835.857	S372	N/A	38	N/A	c_5, c_6; z_{10}, z_{11}
ASSRRPRDDLEI	371-382	2	1434.660	1434.641	S373	25	N/A	y_9, y_{10}	N/A
ASSRASSRRPRDDLEI	367-382	3	1916.819	1916.826	S369, S373	N/A	30	N/A	c_6, c_7; z^{+1}_{15}, z^{+1}_{16}; z^{+1}_{13}, z^{+1}_{14}

[@] Loss of H_3PO_4

Table 2-2. Phosphoserine-containing peptides from Cx43-CT in vitro phosphorylation by CaMKII.

One previously identified phosphorylation site, S306, was identified in each of the four experiments (**Figure 2-4**). This serine is dephosphorylated in response to global ischemia in Langendorff perfused rat hearts (8). Dephosphorylation of S306 has recently been shown to contribute to reduce coupling (41). CaMKII and other protein kinases were tested by Axelsen et al. (8) in the in vitro phosphorylation assays using synthetic peptides containing this site; however, they could not identify the kinase(s) responsible for this phosphorylation. The discrepancy between their results and ours is likely due to their use of a short peptide containing amino acid residues 291-313 (with cysteine 298 substituted with an alanine (8)) instead of a protein containing the full length of the carboxyl terminus of Cx43 as substrate for the CaMKII in vitro phosphorylation reaction. We can only speculate that the presence of C298 or a more extensive surrounding sequence may allow the protein to adopt a conformation required for phosphorylation of S306 by CaMKII.

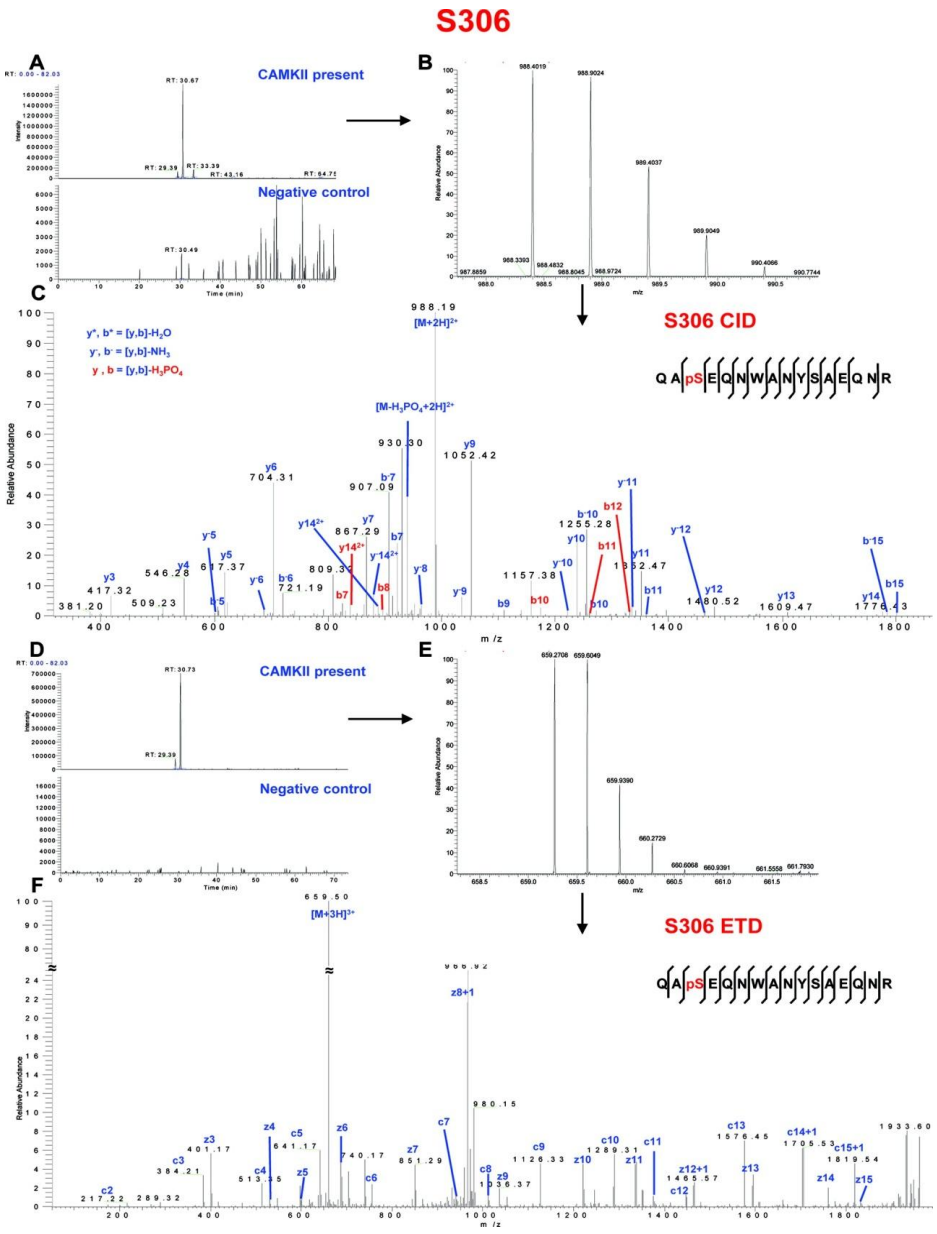

Figure 2-4. CaMKII phosphorylation of Cx43-CT at S306. (A) Extracted chromatogram of *m/z* 988.3930-988.3990. (B) MS spectrum of *m/z* 988.4019 represents doubly charged peptide QASEQNWANYSAEQNR (one phosphorylation site). (C) CID MS2 spectrum indicates phosphorylation on S306. (D) Extracted chromatogram of *m/z* 659.2617-659.2717. (E) MS spectrum of *m/z* 659.2708 represents triply charged peptide QASEQNWANYSAEQNR (one phosphorylation site). (F) ETD MS2 spectrum indicates phosphorylation on S306.

Another substrate for CaMKII was the previously identified serine residue at position 330 (**Figure 2-5**). S330 is one of three serine residues (S325/S328/S330) that has been shown by Lampe et al. (11) to be phosphorylated on Cx43 localized at intercalated disks, and that are involved in the electrophoretic mobility shift of Cx43 to the slowest migrating phosphorylated form (P2) in immunoblots (7). S330 is phosphorylated after 7 min of global ischemia, and subsequently dephosphorylated between 30 and 45 min of ischemia (8). Cooper and Lampe found that S325/S328/S330 are phosphorylated by CK1 (42). Interestingly, we observed phosphorylation of S325/S328/S330 by CaMKII (**Figure 2-5**), but not by CK1. Although we could not detect phosphorylation of S325/S328/S330 by CK1, we found that this kinase phosphorylated S306 and S296. Additional studies will be required to determine whether CaMKII and CK1 compete for target sites on Cx43 in vivo. One example in which these two kinases share target sites is in the Alzheimer's disease protein, tau (43-46).

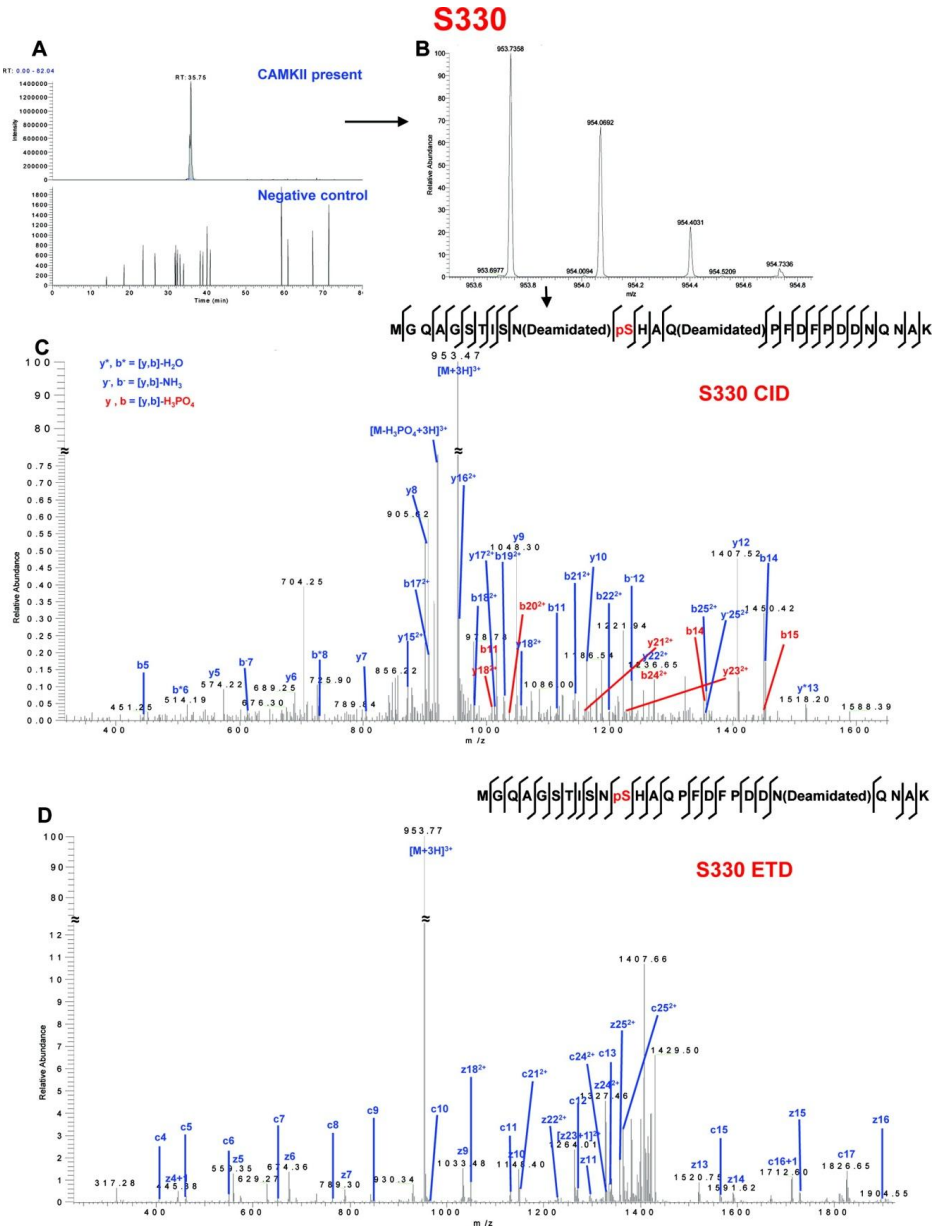

Figure 2-5. CaMKII phosphorylation of Cx43-CT at S330. (A) Extracted chromatogram of *m/z* 953.7332-953.7428. (B) MS spectrum of *m/z* 953.7358 represents triply charged peptide MGQAGSTISNSHAQPFDFPDDNQNAK (one phosphorylation site, two deamidated sites). (C) CID MS2 spectrum indicates phosphorylation on S330. (D) ETD MS2 spectrum indicates phosphorylation on S330.

Importantly, we found one novel serine phosphorylation site that has not been reported previously, S244, and a second site, S314, that has recently been described in the mouse brain synaptosomal preparations (9) and human embryonic stem cells (10) (**Table 2-1**). The spectra identifying these residues are shown in **Figures 2-6 and 2-7**, respectively. We also identified S257, S296 and S297, which have not been linked previously to a specific kinase, as phosphorylation sites for CaMKII. Moreover, phosphorylation of S255, S364, S365, S369, S372 and S373, which have been reported previously to be directly or indirectly associated with other protein kinases was also identified in the GST-Cx43-CT fusion protein after in vitro phosphorylation by CaMKII.

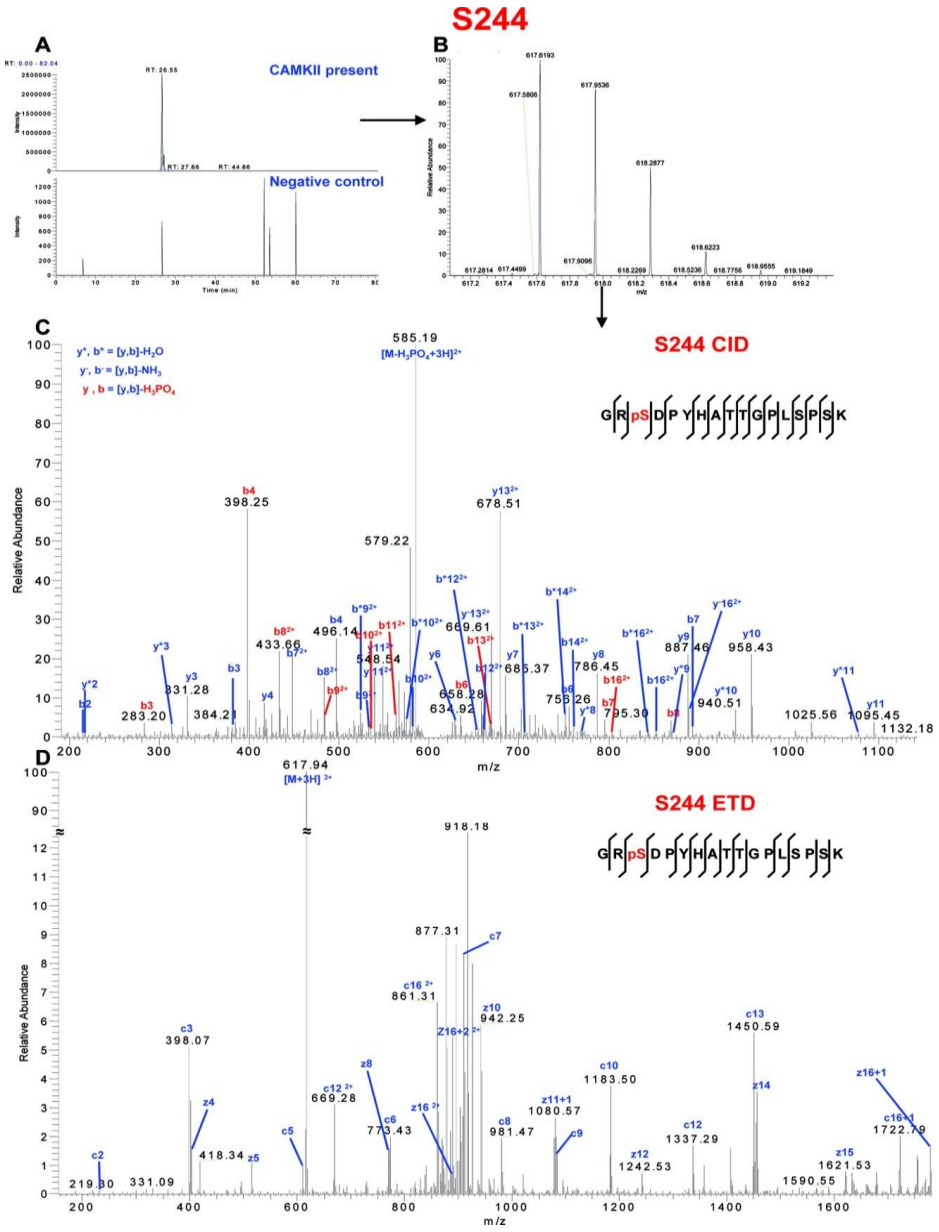

Figure 2-6. CaMKII phosphorylation of Cx43-CT at a novel site, S244. (A) Extracted chromatogram of *m/z* 617.6179-617.6203. (B) MS spectrum of *m/z* 617.6193 represents triply charged peptide GRSDPYHATTGPLSPSK (one phosphorylation site). (C) CID MS2 spectrum indicates phosphorylation on S244. (D) ETD MS2 spectrum indicates phosphorylation on S244.

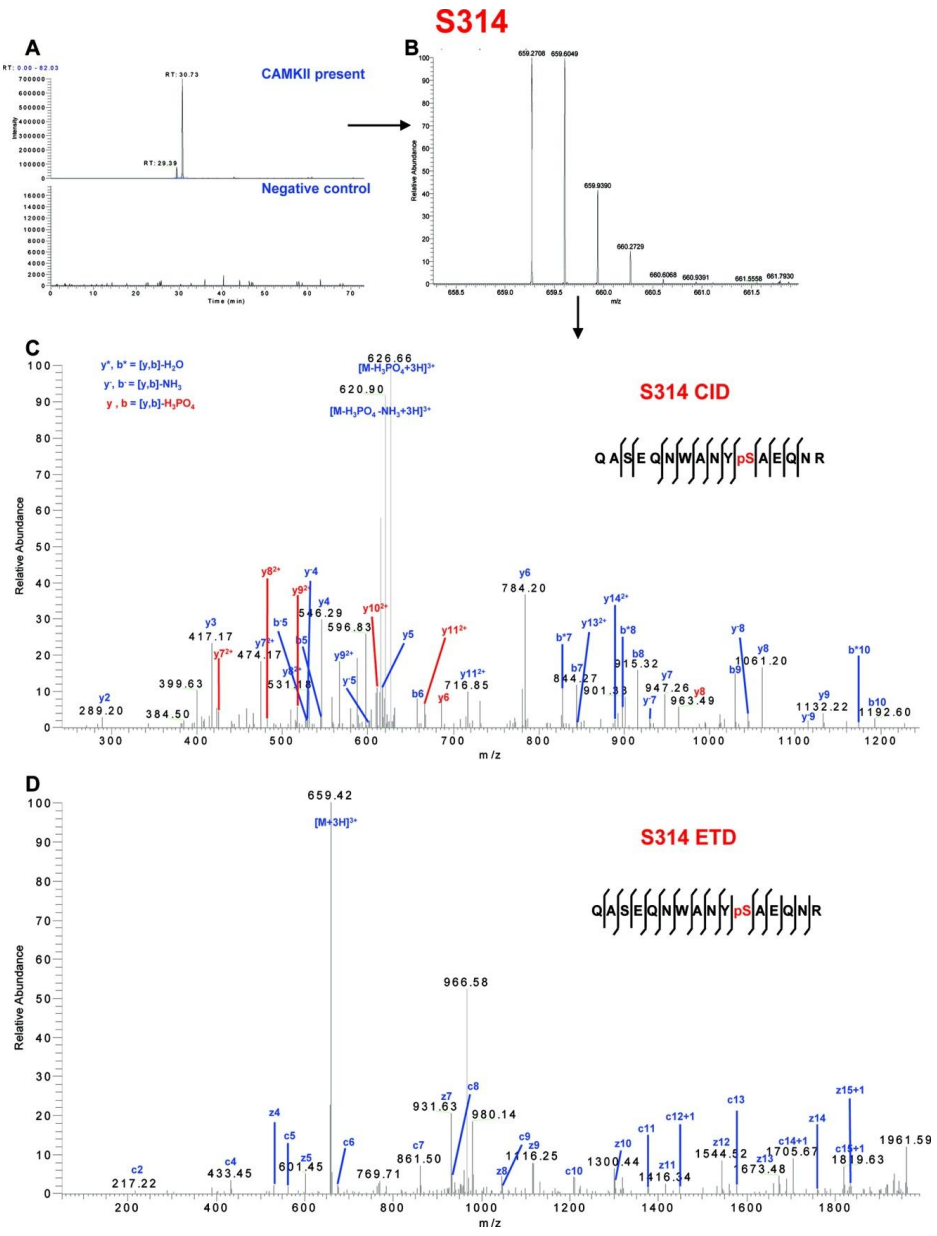

Figure 2-7. CaMKII phosphorylation of Cx43-CT at S314. (A) Extracted chromatogram of *m/z* 659.2613-659.2717. (B) MS spectrum of *m/z* 659.2708 represents triply charged peptide QASEQNWANYSAEQNR (one phosphorylation site). (C) CID MS2 spectrum indicates phosphorylation on S314. (D) ETD MS2 spectrum indicates phosphorylation on S314.

In summary, we identified a total of 15 putative serine phosphorylation sites for CaMKII in the carboxyl terminus of Cx43, bringing the total number of reported phosphorylation sites in the carboxyl terminus of Cx43 to 21 (19 Ser and 2 Tyr). Interestingly, two of these sites, S328 and S369, were identified by ETD alone. In each case, the phosphorylated serine is part of a multiply phosphorylated peptide fragment, therefore hampers the unambiguous identification under CID fragmentation. This is an example in which combined use of CID and ETD as complementary fragmentation techniques provides enhanced identification of post-translationally modified amino acid residues. Because no phosphopeptides were identified in the control, CaMKII-free reactions, it is unlikely that phosphorylation of these residues was non-enzymatic or nonspecific.

In one experiment, we identified phosphorylation of S306, S372 and S373 in full-length native Cx43 immunoprecipitated from murine ventricular myocardium. Additional studies will be required to determine whether the serine residues in Cx43-CT identified in the present study, both in vitro and in vivo, are phosphorylated by CaMKII in vivo. Our data suggest that some residues may be targets for multiple protein kinases, implying that modulation of gap junction assembly and/or intercellular communication may depend on the combined levels of activity of the different protein kinases under

different pathophysiological conditions. It also remains to be determined not only which protein kinase pathways are activated in the initial phases of ischemic injury that result in phosphorylation of Cx43, but also which pathways are activated subsequently that lead to dephosphorylation of Cx43 during ischemia and subsequent rephosphorylation in post-ischemic tissue.

2.5 CONCLUSIONS AND LIMITATIONS

Mass spectrometry is a powerful technique that has allowed for identification of several phosphorylation sites, including a novel site at S244, that are targets of an important, biologically relevant protein kinase, CaMKII. In the present study, we identified four putative CaMKII serine phosphorylation sites (S296, S365, S369 and S373) that had been postulated by Payne et al. (47) and confirmed by Pearson et al. (48) as CaMKII phosphorylation sites based on an RXXS consensus sequence. Two CaMKII sites identified in our study (S244 and S306) conform to a KXXS sequence, which is also a consensus sequence for PKC (49). Utilization of ETD can potentially enhance the ability in phosphorylation site localization, particularly when multiple potential phosphorylation sites are present in a given peptide. It should be noted that conditions used in the present study were to drive the phosphorylation reaction to completion, and that steady state phosphorylation of Cx43 by CaMKII was not meant to represent

transient signaling activity of CaMKII. Thus, residues observed to be phosphorylated in the present study exist in different structural environments and may not be phosphorylated by CaMKII in vivo under the same physiological or pathophysiological condition or time frame. Finally, because CaMKII activity levels exhibit dynamic changes during acute and chronic ischemia, the mass spectrometric analyses performed in our study should be applied to full-length protein isolated from native cardiac tissue subjected to various pathophysiological conditions to elucidate whether and to what extent CaMKII regulates the phosphorylation state of Cx43 in diseased myocardium. For example, analysis of Cx43 extracted from CaMKII transgenic mice subjected to myocardial infarction (50) would reveal how activation and inhibition of CaMKII influence phosphorylation of Cx43 associated with cardiac dysfunction or arrhythmogenesis during myocardial ischemia in vivo.

2.6 ACKNOWLEDGEMENTS

The authors would like to thank Ms. Petra Gilmore in the Proteomics Core Facilities for expert sample preparation and TiO_2 protocol development and Mr. Hao Zhang for assistance and guidance with the set-up and maintenance of the LTQ-Orbitrap. This work was supported by National Centers for Research Resources NIH Grant 2P41RR000954, UL1 RR024992, and NIH/NHLBI Grant HL066350 (to K.A.Y.).

2.7 REFERENCES

1. Söhl, G.; Willecke, K. Gap junctions and the connexin protein family. *Cardiovasc. Res.* **2004**, *62*, 228-232.

2. van Veen, T. A. B.; van Rijen, H. V. M.; Opthof, T. Cardiac gap junction channels: modulation of expression and channel properties. *Cardiovasc. Res* **2001**, *51*: 217-229.

3. Kreuzberg, M. M.; Willecke, K.; Bukauskas, F. F. Connexin-mediated cardiac impulse propagation: connexin 30.2 slows atrioventricular conduction in mouse heart. *Trends Cardiovasc. Med.* **2006**, *16*, 266-272.

4. Saffitz, J. E.; Schuessler, R. B.; Yamada, K. A. Mechanisms of remodeling of gap junction distributions and the development of anatomic substrates of arrhythmias. *Cardiovasc. Res.* **1999**, *42*, 309-317.

5. Severs, N. J.; Bruce, A. F.; Dupont, E.; Rothery, S. Remodelling of gap junctions and connexin expression in diseased myocardium. *Cardiovasc. Res.* **2008**, *80*, 9-19.

6. Lampe, P. D.; Lau, A. F. The effects of connexin phosphorylation on gap junctional communication. *Int. J. Biochem. Cell Biol.* **2004**, *36*, 1171–1186.

7. Solan, J. L.; Lampe, P. D. Connexin43 phosphorylation: structural changes and biological effects. *Biochem. J.* **2009**, *419*, 261-272.

8. Axelsen, L. N.; Stahlhut, M.; Mohammed, S.; Larsen, B. D.; Nielsen, M. S.; Holstein-Rathlou, N.-H.; Andersen, S.; Jensen, O. N.; Hennan, J. K.; Kjølbye, A. L. Identification of ischemia-regulated phosphorylation sites in connexin43: a possible target for the antiarrhythmic peptide analogue rotigaptide (ZP123). *J. Mol. Cell Cardiol.* **2006**, *40*, 790-798.

9. Munton, R.P.; Tweedie-Cullen, R.; Livingstone-Zatchej, M.; Weinandy, F.; Waidelich, M.; Longo, D.; Gehrig, P.; Potthast, F.; Rutishauser, D.; Gerrits, B.;

Panse, C.; Schlapbach, R.; Mansuy, I.M. Qualitative and quantitative analyses of protein phosphorylation in naive and stimulated mouse synaptosomal preparations. *Mol Cell Proteomics* **2007**, *6*, 283-293.

10. Brill, L.M.; Xiong, W.; Lee, K.-B.; Ficarro, S.B.; Crain, A.; Xu, Y.; Terskikh, A.; Snyder, E.Y.; Ding, S. Phosphoproteomic analysis of human embryonic stem cells. *Cell Stem Cell* **2009**, *5*, 204-213.

11. Lampe, P. D.; Cooper, C. D.; King, T. J.; Burt, J. M. Analysis of connexin43 phosphorylated at S325, S328 and S330 in normoxic and ischemic heart. *J. Cell Sci.* **2006**, *119*, 3435-3442.

12. Lampe, P. D.; TenBroek, E. M.; Burt, J. M.; Kurata, W. E.; Johnson, R. G.; Lau, A. F. Phosphorylation of connexin43 on serine368 by protein kinase C regulates gap junctional communication. *J. Cell Biol.* **2000**, *149*, 1503–1512.

13. Ek-Vitorin, J. F.; King, T. J.; Heyman, N. S.; Lampe, P. D.; Burt, J. M. Selectivity of connexin 43 channels is regulated through protein kinase C-dependent phosphorylation. *Circ. Res.* **2006**, *98*, 1498 –1505.

14. Matsushita, S.; Kurihara, H.; Watanabe, M.; Okada, T.; Sakai, T.; Amano, A. Alterations of phosphorylation state of connexin 43 during hypoxia and reoxygenation are associated with cardiac function. *J. Histochem. Cytochem.* **2006**, *54*, 343-353.

15. Hund, T. J.; Lerner, D. L.; Yamada, K. A.; Schuessler, R. B.; Saffitz, J. E. Protein kinase Cε mediates salutary effects on electrical coupling induced by ischemic preconditioning. *Heart Rhythm* **2007**, *4*, 1183-1193.

16. Naitoh, K.; Yano, T.; Miura, T.; Itoh, T.; Miki, T.; Tanno, M.; Sato, T.; Hotta, H.; Terashima, Y.; Shimamoto, K. Roles of Cx43-associated protein kinases in suppression of gap junction-mediated chemical coupling by ischemic preconditioning. *Am. J. Physiol. Heart Circ. Physiol.* **2009**, *296*, H396-H403.

17. Boersema, P. J.; Mohammed, S.; Heck, A. J. R. Phosphopeptide fragmentation and analysis by mass spectrometry. *J. Mass Spectrom.* **2009**, *44*, 861-878.

18. Braun, A. P.; Schulman, H. The multifunctional calcium/calmodulin-dependent protein kinase: from form to function. *Annu. Rev. Physiol.* **1995**, *57*, 417-445.

19. Zhu, W.-Z.; Wang, S.-Q.; Chakir, K.; Yang, D.; Zhang, T.; Heller Brown, J.; Devic, E.; Kobilka, B. K.; Cheng, H.; Xiao, R.-P. Linkage of β_1-adrenergic stimulation to apoptotic heart cell death through protein kinase A-independent activation of Ca^{2+}/calmodulin kinase II. *J. Clin. Invest.* **2003**, *111*, 617-625.

20. Hagemann, D.; Bohlender, J.; Hoch, B.; Krause, E.-G.; Karczewski, P. Expression of Ca^{2+}/calmodulin-dependent protein kinase II δ-subunit isoforms in rats with hypertensive cardiac hypertrophy. *Mol. Cell. Biochem.* **2001**, *220*, 69-76.

21. Backs, J.; Backs, T.; Neef, S.; Kreusser M. M.; Lehmann, L. H.; Patrick, D. M.; Grueter, C. E.; Qi, X.; Richardson, J. A.; Hill, J. A.; Katus, H. A.; Bassel-Duby, R.; Maier L. S.; Olson, E. N. The δ isoform of CaM kinase II is required for pathological cardiac hypertrophy and remodeling after pressure overload. *Proc. Natl. Acad. Sci.* **2009**, *106*, 2342-2347.

22. Hoch, B.; Meyer, R.; Hetzer, R.; Krause E.-G.; Karczewski, P. Identification and expression of δ-isoforms of the multifunctional Ca^{2+}/calmodulin-dependent protein kinase in failing and nonfailing human myocardium. *Circ. Res.* **1999**, *84*, 713-721.

23. Vila-Petroff, M.; Salas, M. A.; Said, M.; Valverde, C. A.; Sapia, L.; Portiansky, E.; Hajjar, R. J.; Kranias, E. G.; Mundiña-Weilenmann, C.; Mattiazzi, A. CaMKII inhibition protects against necrosis and apoptosis in irreversible ischemia-reperfusion injury. *Cardiovasc. Res.* **2007**, *73*, 689-698.

24. Yoo, B.; Lemaire A.; Mangmool, S.; Wolf, M. J.; Curcio, A.; Mao, L.; Rockman, H. A. β_1-Adrenergic receptors stimulate cardiac contractility and CaMKII activation in vivo and enhance cardiac dysfunction following myocardial infarction. *Am. J. Physiol. Heart Circ. Physiol.* **2009**, *297*, H1377-H1386.

25. Hund, T. J.; Decker, K. F.; Kanter, E.; Mohler, P. J.; Boyden, P. A.; Schuessler, R. B.; Yamada, K. A.; Rudy, Y. Role of activated CaMKII in abnormal calcium homeostasis and I_{Na} remodeling after myocardial infarction: insights from mathematical modeling. *J. Mol. Cell. Cardiol.* **2008**, *45*, 420-428.

26. De Pina-Benabou, M.H.; Srinivas, M,; Spray, D.C.; Scemes, E. Calmodulin kinase pathway mediates the K+-induced increase in gap junctional communication between mouse spinal cord astrocytes. *J. Neurosci.* **2001**, *21*, 6635-6643.

27. Saez, J. C.; Nairn, A. C.; Czernik, A. J.; Spray, D. C.; Hertzberg, E. L.; Greengard, P.; Bennett, M. V. L. Phosphorylation of connexin 32, a hepatocyte gap-junction protein, by cAMP-dependent protein kinase, protein kinase C and Ca^{2+}/calmodulin-dependent protein kinase II. *Eur. J. Biochem.* **1990**, *192*, 263-273.

28. Alev, C.; Urschel, S.; Sonntag, S.; Zoidl, G.; Fort, A. G.; Höher, T.; Matsubara, M.; Willecke, K.; Spray, D. C.; Dermietzel, R. The neuronal connexin36 interacts with and is phosphorylated by CaMKII in a way similar to CaMKII interaction with glutamate receptors. *Proc. Natl. Acad. Sci.* **2008**, *105*, 20964-20969.

29. Schieltz, D.M.; Washburn, M.P.; Hays, L.G. *Analysis of Complex Protein Mixtures Using Nano-LC Coupled to MS/MS*, Cold Spring Harbor Laboratory Press, Proteins and proteomics. **2003,** Chapter 8.

30. Syka, J.E.P.; Coon, J.J.; Schroeder, M.J.; Shabanowitz, J.; Hunt, D.F. Peptide and protein sequence analysis by electron transfer dissociation mass spectrometry. *Proc. Natl. Acad. Sci.* **2004,** *101*, 9528-9533.

31. Domon, B.; Aebersold, R. Options and considerations when selecting a quantitative proteomics strategy. *Nat. Biotech*. **2010**, *28*, 710-721.

32. Yeager, M. Structure of cardiac gap junction intercellular channels. *J. Struct. Biol.* **1998**, *121*, 231-245.

33. Dunker, AK,; Obradovic, Z. The protein trinity—linking function and disorder. *Nat. Biotechnol.* **2001**, *19*, 805-806.

34. Bouvier, D; Spagnol, G; Chenavas, S; Kieken, F; Vitrac, H; Brownell, S; Kellezi, A; Forge, V; Sorgen, PL. Characterization of the structure and intermolecular interactions between the connexin40 and connexin43 carboxyl terminal and cytoplasmic loop domains. *J. Biol. Chem.* **2009,** *284*, 34257-24271.

35. Delmar, M; Coombs, W; Sorgen, P; Duffy, HS; Taffet, SM. Structural bases for the chemical regulation of connexin43 channels. *Cardiovasc. Res.* **2004**, *62*, 268-275.

36. Hervé, J-C; Bourmeyster, N; Sarrouilhe, D; Duffy, HS. Gap junctional complexes: from partners to functions. *Prog. Biophys. Mol. Biol.* **2007**, *94*, 29-65.

37. Sobott, F.; Watt, S. J.; Smith, J.; Edelmann, M. J.; Kramer, H. B.; Kessler, B. M. Comparison of CID versus ETD based MS/MS fragmentation for the analysis of protein ubiquitination. *J. Am. Soc. Mass Spectrom.* **2009**, *20*, 1652-1659.

38. Jensen, S. S.; Larsen, M. R. Evaluation of the impact of some experimental procedures on different phosphopeptide enrichment techniques. *Rapid Commun. Mass Spectrom.* **2007**, *21*, 3635-3645.

39. Kanemitsu, M. Y.; Jiang, W.; Eckhart, W. Cdc2-mediated phosphorylation of the gap junction protein, connexin43, during mitosis. *Cell Growth Diff.* **1998**, *9*, 13-21.

40. Warn-Cramer, B. J.; Lampe, P. D.; Kurata, W. E.; Kanemitsu, M. Y.; Loo, L. W. M.; Eckhart, W.; Lau, A. F. Characterization of the mitogen-activated protein kinase phosphorylation sites on the connexin-43 gap junction protein. *J. Biol. Chem.* **1996**, *271*, 3779–3786.

41. Procida, K.; Jørgensen, L.; Schmitt, N.; Delmar, M.; Taffet, S. M.; Holstein-Rathlou, N.-H.; Nielsen, M. S.; Braunstein, T. H. Phosphorylation of connexin43 on serine 306 regulates electrical coupling. *Heart Rhythm* **2009**, *6*, 1632-1638.

42. Cooper, C. D.; Lampe, P. D. Casein kinase 1 regulates connexin43 gap junction assembly. *J. Biol. Chem.* **2002**, *277*, 44962-44968.

43. Singh, T. J.; Wang, J.-Z.; Novak, M.; Kontzekova, E.; Grundke-Iqbal, I.; Iqbal, K. Calcium/calmodulin-dependent protein kinase II phosphorylates tau at Ser-262 but only partially inhibits its binding to microtubules. *FEBS Lett.* **1996**, *387*, 145-148.

44. Gupta, R. P.; Abou-Donia, M. B. Tau phosphorylation by diisopropyl phosphorofluoridate (DFP)-treated hen brain supernatant inhibits its binding with microtubules: role of Ca^{2+}/calmodulin-dependent protein kinase II in tau phosphorylation. *Arch. Biochem. Biophys.* **1999**, *365*, 268-278.

45. Bennecib, M.; Gong, C.-X.; Grundke-Iqbal, I.; Iqbal, K. Inhibition of PP-2A upregulates CaMKII in rat forebrain and induces hyperphosphorylation of tau at Ser 262/356. *FEBS Lett.* **2001**, *490*, 15-22.

46. Hanger, D. P.; Byers, H. L.; Wray, S.; Leung, K.-Y.; Saxton, M. J.; Seereeram, A.; Reynolds, C. H.; Ward, M. A.; Anderton, B. H. Novel phosphorylation sites in tau from Alzheimer brain support a role for casein kinase 1 in disease pathogenesis. *J. Biol. Chem.* **2007**, *282*, 23645-23654.

47. Payne, M. E.; Schworer, C. M.; Soderling, T. R. Purification and characterization of rabbit liver calmodulin-dependent glycogen synthase kinase. *J. Biol. Chem.* **1983**, *258*, 2376-2382.

48. Pearson, R. B.; Woodgett, J. R.; Cohen, P.; Kemp, B. E. Substrate specificity of a multifunctional calmodulin-dependent protein kinase. *J. Biol. Chem.* **1985**, *260*, 14471-14476.

49. Kennelly, P. J.; Krebs, E. G. Consensus sequences as substrate specificity determinants for protein kinases and protein phosphatases. *J. Biol. Chem.* **1991**, *266*, 15555-15558.

50. Zhang, R.; Khoo, M. S. C.; Wu, Y.; Yang, Y.; Grueter, C. E.; Ni, G.; Price, E. E. Jr.; Thiel, W.; Guatimosim S.; Song, L.-S.; Madu, E. C.; Shah, A. N.; Vishnivetskaya, T. A.; Atkinson, J. B.; Gurevich, V. V.; Salama, G.; Lederer, W. J.; Colbran, R. J.; Anderson, M. E. Calmodulin kinase II inhibition protects against structural heart disease. *Nat. Med.* **2005**, *11*, 409-417.

51. Lampe, P. D.; Kurata, W. E.; Warn-Cramer, B.; Lau, A. F. Formation of a distinct connexin43 phosphoisoform in mitotic cells is dependent upon $p34^{cdc2}$ kinase. *J. Cell Sci.* **1998**, *111*, 833-841.

52. Cottrell, G.T.; Lin, R.; Warn-Cramer, B. J.; Lau, A. F.; Burt, J. M. Mechanism of v-Src- and mitogen-activated protein kinase-induced reduction of gap junction communication. *Am. J. Physiol. Cell. Physiol.* **2003**, *284*, C511-C520.

53. Shah, M. M.; Martinez, A.-M.; Fletcher, W. H. The connexin43 gap junction protein is phosphorylated by protein kinase A and protein kinase C: in vivo and in vitro studies. *Mol. Cell. Biochem.* **2002**, *238*, 57-68.

54. TenBroek, E. M.; Lampe, P. D.; Solan, J. L.; Reynhout, J. K.; Johnson, R. G. Ser364 of connexin43 and the upregulation of gap junction assembly by cAMP. *J. Cell Biol.* **2001**, *155*, 1307-1318.

55. Yogo, K.; Ogawa, T.; Akiyama, M.; Ishida, N.; Takeya, T. Identification and functional analysis of novel phosphorylation sites in Cx43 in rat primary granulose cells. *FEBS Lett.* **2002**, *531*, 132-136.

56. Solan, J. L.; Marquez-Rosado, L.; Sorgen, P. L.; Thornton, P. J.; Gafken, P. R.; Lampe, P. D. Phosphorylation at S365 is a gatekeeper event that changes the structure of Cx43 and prevents down-regulation by PKC. *J. Cell Biol.* **2007**, *179*, 1301-1309.

57. Sáez, J. C.; Nairn, A. C.; Czernik, A. J.; Fishman, G. I.; Spray, D. C.; Hertzberg, E. L. Phosphorylation of connexin43 and the regulation of neonatal rat cardiac myocyte gap junctions. *J. Mol. Cell. Cardiol.* **1997**, *29*, 2131–2145.

58. Park, D. J.; Wallick, C. J.; Martyn, K. D.; Lau, A. F.; Jin, C. Warn-Cramer, B. J. Akt phosphorylates connexin43 on ser373, a "mode-1" binding site for 14-3-3. *Cell Commun. Adhes.* **2007**, *14*, 211-226.

Chapter 3*

HD Exchange and PLIMSTEX Determine the Affinities and Order of Binding of Ca^{2+} with Troponin C

* This chapter is based on recent publication: Reproduced with permission from Huang, R. Y. C., Rempel, D. L., and Gross, M. L. HD Exchange and PLIMSTEX Determine the Affinities and Order of Binding of Ca^{2+} with Troponin C. *Biochemistry*, **2011**, 50, 5426-5435. Copyright 2011 American Chemical Society

3.1 ABSTRACT

Troponin C (TnC), present in all striated muscle, is the Ca^{2+}-activated trigger that initiates myocyte contraction. The binding of Ca^{2+} to TnC initiates a cascade of conformational changes involving the constituent proteins of the thin filament. The functional properties of TnC and its ability to bind Ca^{2+} have significant regulatory influence on the contractile reaction of muscle. Changes in TnC may also correlate with cardiac and various other muscle-related diseases. We report here the implementation of the PLIMSTEX strategy (Protein Ligand Interaction by Mass Spectrometry, Titration and H/D Exchange) to elucidate the binding affinity of TnC with Ca^{2+} and, more importantly, to determine the order of Ca^{2+} binding of the four EF hands of the protein. The four equilibrium constants, $K_1 = (5 \pm 5) \times 10^7\ M^{-1}$, $K_2 = (1.8 \pm 0.8) \times 10^7\ M^{-1}$, $K_3 = (4.2 \pm 0.9) \times 10^6\ M^{-1}$, and $K_4 = (1.6 \pm 0.6) \times 10^6\ M^{-1}$, agree well with determinations by other methods and serve to increase our confidence in the PLIMSTEX approach. We determined the order of binding to the four EF hands to be III, IV, II, and I by extracting from the H/DX results the deuterium patterns for each EF hand for each state of the protein (apo through fully Ca^{2+} bound). This approach, demonstrated for the first time, may be general for determining binding orders of metal ions and other ligands to proteins.

3.2 INTRODUCTION

The basis of muscle contraction has been well studied over four decades. There are primarily two types of proteins involved in this process: troponin and tropomyosin (*1-11*). Muscle contraction is initiated by an increase in intracellular free Ca^{2+} concentration and is controlled by the binding of Ca^{2+} to troponin (*1-3, 8-10, 12-17*). Troponin, which is present in skeletal and cardiac muscle of various species of mammals, birds, and some invertebrates, has three subunits: troponin C (TnC), troponin T (TnT), and troponin I (*6*). Each subunit plays a special rule in modulating the movement of muscle filament.

Troponin C, which is the subject of this study, is an 18 kDa protein that is structurally homologous in skeletal and cardiac muscle (*1, 3*) but has different Ca^{2+} stoichiometry in these two tissues. Skeletal troponin C has four helix-loop-helix motifs (EF hands) that bind to Ca^{2+}. The EF-hand motif, which is a conserved structure first identified in parvalbumins (*18*), allows Ca^{2+} to interact with carboxyl and hydroxyl groups of amino-acid sidechains located at positions 1, 3, 5, 7, 9, and 12 of a 12-membered loop (*1, 19*). One of the EF hands (EF-I) in cardiac troponin C is defunct so the protein binds only three Ca^{2+} (*1, 2, 7, 20-23*). In skeletal troponin C, two of four EF hands are located in the C-terminal (EF-III and EF-IV) and have higher affinities for Ca^{2+} ($K_a \sim 10^7\ M^{-1}$) than the other two EF hands; they are usually saturated with Ca^{2+} or Mg^{2+}

in tissue. The binding of Ca^{2+} at these two sites helps maintain the interaction between the C-terminus of troponin C, the N-terminus of troponin I, and the C-terminus of troponin T (*1, 24-27*). The latter subunit binds to tropomyosin on the muscle thin filament, serving as a key in complex formation. When the two N-terminal EF hands (EF-I and EF-II), which have lower affinities for Ca^{2+} ($K_a \sim 10^5$-10^6 M^{-1}), bind to Ca^{2+}, troponin C undergoes a conformational change to form a hydrophobic core (*15, 23, 26, 28-30*). The inhibitor region on the C-terminus of troponin I then interacts with this core and releases tropomyosin and actin. The free actins are able to interact with the myosin heads on the thick filament and produce muscle contraction (*1-3*).

The Ca^{2+} binding to troponin C and its relation to muscle-contraction disorders have implications in cardiac-related diseases. The amino-acid sequence of troponin C and the phosphorylation of troponin I induced by over-activation of protein kinase A and C (*31, 32*) affect the binding of Ca^{2+} to troponin C. Newly designed drugs interact with troponin C and adjust its affinities to Ca^{2+} (*33, 34*).

The Ca^{2+}-binding and protein-target binding properties of troponin C have been the subjects of numerous studies using NMR (*21, 25, 35-37*), calorimetry (*38*) and fluorescence (*26*). Hydrogen/deuterium exchange (H/DX) coupled with mass spectrometry is another powerful method to study protein conformation, protein-protein

or protein-ligand interactions (*39-46*). With H/DX, one can measure the relative rates of exchange of backbone amide hydrogen with deuterium and thereby follow changes in H-bonding, which often is parallel to relative solvent accessibilities. Recently, H/DX was applied to study the regulatory function of human cardiac troponin complex and the conformational changes of troponin complex induced by Ca^2 binding (*47, 48*).

We describe here the use of PLIMSTEX (Protein–ligand interactions by mass spectrometry, titration, and H/D exchange) (*49-51*) to determine again the affinities of Ca^{2+} to rabbit skeletal troponin C. The purpose of the determination is to test the ability of PLIMSTEX to extract these values in a complex 4:1 interaction. From the determined affinities (equilibrium constants), we calculated the fractional species for the variousTnC-Ca^2 states as a function of [Ca^{2+}]. The deuterium exchange patterns of four peptic peptides representing the four EF hands of rabbit skeletal troponin C (EF-I peptide 28-44: DADGGGDISVKELGTVM; EF-II peptide 63-73: EVDEDGSGTID; EF-III peptide 100-109: FRIFDRNADG; EF-IV peptide 136-149: MKDGDKNNDGRIDF) were then measured. Guided by the fractional species calculation, the deuterium patterns for each EF-hand were measured as a function of the various Ca^{2+} binding states (i.e., 0, 1, 2, 3, and 4) to determine how D distributions change as a function of the binding states. Previous efforts to elucidate the binding properties of Ca^{2+} to troponin C used NMR,

fluorescence measurement, Ca^{2+} ion-selective electrode measurements, and mutagenesis (*36, 37, 52, 53*). Although some insights were achieved, a full understanding on the Ca^{2+} binding order is still lacking. Our strategy provided data that, for the first time, gives the binding order of Ca^{2+} to full length troponin C in a single and relatively simple experiment. Our ultimate goal is to extend the approach to study the effect of troponin I and troponin T on the affinities and orders of binding of Ca^{2+} to troponin C.

3.3 EXPERIMENTAL PROCEDURE

3.3.1 Materials

Rabbit skeletal Troponin C (TnC) was purchased from Ocean Biologics Inc (Seattle, WA). Potassium chloride, calcium chloride, EGTA tetra sodium salt [ethylene-bis(oxyethylenenitrilo)tetraacetic acid tetrasodium], and HEPES hemisodium salt [*N*-(2-hydroxyethyl)piperazine-*N*′-(2-ethanesulfonic acid) hemisodium salt] were purchased from Sigma-Aldrich (St.Louis, MO). Deuterium oxide was purchased from Cambridge Isotope Laboratories Inc (Andover, MA). Immobilized pepsin on agarose was purchased from Pierce (Rockford, IL).

3.3.2 Apo TnC preparation

TnC was dialyzed against EGTA to obtain apo-TnC. A 1 mL protein solution containing 180 μg of TnC was prepared in 10 mM HEPES and 150 mM KCl. The

solution was dialyzed by using Slide-A-Lyzer Dialysis Cassettes 7000 MWCO (Pierce, CA). The dialysis membrane was first boiled two times in 10 mM EGTA for 10 min to remove heavy metals from the membrane and then soaked in deionized H_2O for 10 min. The protein solution was then injected into the cassette and dialyzed against 10 mM HEPES, 150 mM KCl and 1 mM EGTA for 2 h. The buffer was exchanged for fresh buffer, and the solution was dialyzed overnight at 4 °C. The protein solution was then dialyzed against 10 mM HEPES, 150 mM KCl for 3 h, fresh buffer was added, and the protein was dialyzed again for 3 h at 4 °C. The concentration of the final protein solution was measured by using a UV spectrophotometer at 280 nm absorption ($a = 0.2\ (mg/mL)^{-1}\ cm^{-1}$). The protein solution was stored at -80 °C.

3.3.3 H/D exchange (H/DX) protocol

H/DX was initiated by diluting the protein solution 1:40 into D_2O buffer (10 mM HEPES, 150 mM KCl) at 25 °C. At various times, H/DX was quenched by adding sufficient 1 M HCl at 0 °C to give a final pH of 2.5.

For Global protein H/DX experiments, a quenched protein solution was loaded onto a C8 guard column (1 mm x 15 mm, Optimize Technologies, Oregon, City, OR). The column was pre-equilibrated with 200 µL 0.2% formic acid in water (0 °C). After loading the protein solution, the column was washed with 250 µL 0.2% formic acid in ice

cold normal water (0 °C) to back-exchange the labile sites on side chains. The protein was eluted by using a gradient from 5% to 40% solvent B in 3 min, 40% to 100% solvent B in 3 min and back to 5% solvent B in 2 min. (Waters CapLC, Manchester, U.K; solvent A, water containing 0.1% formic acid; solvent B, acetonitrile containing 0.1% formic acid).

For peptide-level H/DX experiments, 5 μL of immobilized pepsin on agarose was added to the solution. Protein digestion took place at 0 °C for 3 min. The final solution was centrifuged for 2-3 s to bring down the agarose beads. The peptide-containing supernatant was then loaded onto a C18 guard column (1 mm x 15 mm, Optimize Technologies, Oregon, City, OR). The column was pre-equilibrated with 200 μL of 0.2% formic acid in water (0 °C). After loading, the column was washed with 250 μL of aqueous 0.2% formic acid (H_2O) to back-exchange the labile sites. The protein was eluted by using a gradient from 5% to 35% solvent B in 3 min, 35% to 80% solvent B in 4 min, 80% to 100% solvent B in 1 min and back to 5% solvent B in 2 min. All LC connection lines were immersed in a water-ice (0 °C) bath. (Waters nanoACQUITY UPLC, Manchester, U.K; solvent A, water containing 0.1% formic acid; solvent B, acetonitrile containing 0.1% formic acid).

3.3.4 LC-ESI/MS analysis with a Q-TOF mass spectrometer

Global protein H/DX results were acquired on a Waters (Micromass) (Manchester, U.K.) Q-TOF Ultima spectrometer equipped with a Z-spray ESI source. The instrument settings were: capillary voltage, 3.0 kV; cone voltage, 80 V; source and desolvation temperatures, 80 °C and 180 °C, respectively. The cone and desolvation gas flow rates were 40 and 400 L/h, respectively. The MS profile used for quadrupole transmission was: scan from *m*/*z* 500, dwell for 5% of the scan time, ramp to *m*/*z* 1000 for 45% of the scan time, and then dwell at *m*/*z* 1000 for 50% of the scan time.

Peptide-level H/DX results were acquired on a Maxis (Bruker) (Bremen, Germany) Q-TOF spectrometer. The instrument settings were: capillary voltage, 3.8 kV; nebulizer gas, 0.4 Bar; drying gas flow rate and temperature, 4.0 L/min and 180 °C; funnel RF, 400 V(pp).

3.3.5 LC-ESI/MS/MS analysis of protein digests

To establish the peptide profile from the pepsin digestion of TnC, 100 pmol TnC was digested with pepsin for 3 min, and the peptides were identified by accurate mass and sequencing by product-ion analysis on a Thermo LTQ XL Orbitrap (Thermo Fisher, San Jose, CA). Samples were loaded and eluted by using an Ultra 1D+ UPLC and autosampler (Eksigent, Dublin, CA). A 75 μm diameter column was pulled with a laser-based column puller (Sutter Instruments, Novato, CA) and packed with 12 cm of Magic

C18AQ reverse-phase media (Michrom Bioresources, Auburn, CA). The column was interfaced via a nanospray source (New Objective, Woburn, MA) and eluted with a 60 min gradient from 2-98% solvent B (acetonitrile with 0.1% formic acid). The spray voltage was 2.0 kV, and the capillary temperature was 200 °C. One full mass spectral acquisition triggered six scans of MS/MS whereby the most abundant precursor ions were activated for sequencing. The product-ion spectra (MS/MS) data were centroided during the acquisition.

3.3.6 Mascot database search

Thermo RAW files were processed using extract_msn (2007 version 4.0, Thermo Fisher, San Jose, CA) with a grouping tolerance of 0.8 Da, an intermediate scan setting of 1, and a minimum of 1 scan per group. The NCBI nonredundant database (version 20080718, restricted to mammals) was searched by using MASCOT 2.2.06 (Matrix Science, Oxford, U.K.) with the following settings: enzyme, none; MS tolerance, 10 ppm; MS/MS tolerance, 0.8 Da; maximum number of missed cleavages, 3; peptide charge of 1+, 2+ and 3+; oxidation of methionine was set as variable modification.

3.3.7 Data analysis

The uptake of deuterium by the global protein was the average mass differences between the masses of the deuterated protein and the undeuterated protein. The back-

exchange rate was measured to be one deuterium loss per minute (*45*). No correction for back exchange was applied because the time between sample quench and the measurement with the mass spectrometer was less than 3 min, and all data were treated consistently. For global protein analysis, deconvoluted spectra were generated by using the MaxEnt1 algorithm (MassLynX version 4.0). The parameter settings were: resolution, 1.00 Da/channel; uniform Gaussian width at half height, 1.00 Da; minimum intensity ratios, 33% for left peaks and right peaks.

3.3.8 Kinetic modeling

The global protein kinetic data were fit with a fixed-rate-constant binning model by MathCAD (Math-Soft. Inc. Cambridge, MA) in which the root mean square (RMS) was minimized (*50, 51*). All exchangeable H's were separated into four fixed rate-constant bins (k = 10, 1, 0.1, 0.01 min^{-1}). These rate constants were selected because the rates of exchange change measurably in the time frame 0.17 min to 540 min, and the H/DX became relatively constant after 60 min; hence the brackets of 10 min^{-1} (fast exchangers, half-life ~0.07 min) and 0.01 min^{-1} (slow exchangers, half-life ~69 min) were chosen. Although the largest rate constant for H/DX is >100 min^{-1} for unstructured peptides (*54*), we are yet unable to obtain data at the short times that correspond to this rate constant. Three trials were fit separately, and the results were averaged and reported

with standard deviations.

3.3.9 Titration and species fraction calculation

The method for fitting the titration curve was described previously (*51*). Briefly, there are nine parameters involved in the 1:4 protein-ligand binding systems: K_{a1}, K_{a2}, K_{a3}, K_{a4}, D_0, $\Delta D_1, \Delta D_2, \Delta D_3, \Delta D_4$; K_a is the binding constant; D_0 is the deuterium uptake of protein in the absence of ligands (Apo form); ΔD_x is the difference between the average of deuterium uptake of the complex in the presence of x ligands and that of the apo form. The non-linear least squares fitting utilized the "Minimize" function of MathCAD (Math-Soft. Inc. Cambridge, MA) to minimize the root mean square (RMS) of all inputs by optimizing the parameters being searched. To obtain the nine parameters in single fitting cycle with acceptable precision, a significant number of titration points would be needed (>500) by applying a resampling statistical method (*51*). Because it was difficult to fit the titration curve by varying all nine parameters in one fitting cycle, a repeat fitting cycle strategy was used to obtain the K's and ΔD's values reported here.

The fitting process was started by making a guess of the D's (D_0, $\Delta D_1, \Delta D_2, \Delta D_3, \Delta D_4$) values. The initial values for D_0 was set as experimental data, and the values for $\Delta D_1, \Delta D_2, \Delta D_3, \Delta D_4$ were obtained through a PLIMSTEX experiment at high-protein concentration (100 times the $1/K_a$ or K_d as reported previously) (**Figure 3-3**). We fixed

these D's values and searched for *K*'s in the initial fitting process. After the four *K'*s (K_{a1}, K_{a2}, K_{a3}, K_{a4}) were obtained, the repeat-fitting processes were then started. In the first half cycle, we fixed the *K*'s obtained in the initial process and searched for the *D*'s. We then fixed the $\Delta D_1, \Delta D_2, \Delta D_3$, and searched for K_{a1}, K_{a2}, K_{a3}, K_{a4}, D_0, and ΔD_4 to finish the cycle. This fitting cycle was repeated until the relative differences between *K*'s values before and after each cycle of fitting were less than 10%. Three trials of experiments were applied with this strategy separately, and the results were averaged and reported with standard deviations.

Once the binding affinities of Ca^{2+} were determined, the information for fractionally bound TnC species as a function of Ca^{2+} was obtained and presented as a deuterium pattern (d_0, d_1, . . .) in which other isotopes (e.g.,^{13}C, ^{15}N, ^{18}O) had been removed by using an isotopic pattern calculation. To obtain these patterns, each mass list from three experimental trials was extracted from their individual spectra as an x,y file (x: mass-to-charge ratio; y: intensity). A program in MathCAD was applied to find the isotopic peak envelope among the list by providing the chemical formula and charge state of the target peptide. The peak area in each envelope was applied for fractional species calculation, and the isotopes (^{13}C, ^{15}N, ^{18}O) were removed from the output by using the

information provided via the Isotope Simulation function in Qual Browser 2.0.7 (Xcalibur, Thermo Fisher, San Jose, CA).

3.4 RESULTS

3.4.1 H/DX kinetics of apo- and holo-TnC

Binding of four Ca^{2+} induces a conformational change in troponin C. Previous studies showed that the structure of the holo (Ca^{2+} saturated) state of skeletal troponin C is more structurally open than the semi-apo state (two Ca^{2+} bound). The center partial-loop structure between the N and C-terminal EF hands forms a less flexible helix whereas the Ca^{2+} is bound to the two EF hands near the N-terminus (EF-I and EF-II) (*1, 4, 12, 55*). A detailed structure of apo-troponin C has eluded determination owing to the unstructured C-terminus in the absence of Ca^{2+} (*37, 56*).

We began our study by measuring the kinetics of H/DX of rabbit skeletal troponin C in the Ca^{2+} saturated (holo) and Ca^{2+} absent (apo) states (**Figure 3-1**); the output is a plot of deuterium uptake as a function of exchange times (10 s to 9 h). To generate the holo state of troponin C, we made the protein stock solution (40 μM) containing 10 mM HEPES, 150 mM KCl, and 1 mM $CaCl_2$, pH 7.4. Using KCl mimics physiological conditions, and excess Ca^{2+} (the ratio of Ca^{2+} concentration to protein concentration was 25) insures that the four EF hands of troponin C are saturated with Ca^{2+}. To generate the

apo state of troponin C, we replaced $CaCl_2$ with 3 mM EGTA to insure that no Ca^{2+} was present in the protein.

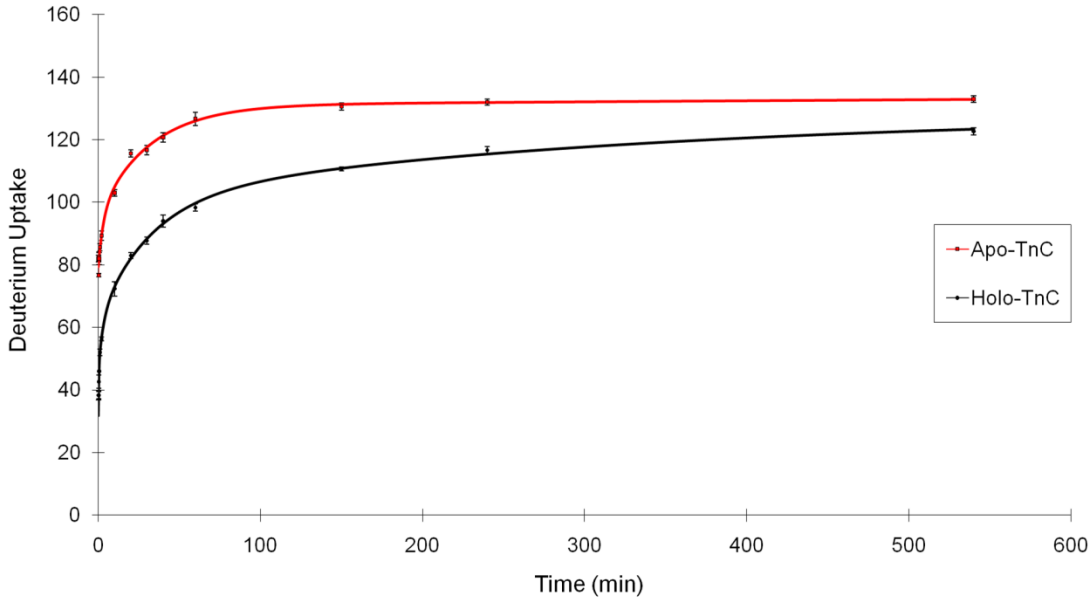

Figure 3-1. Kinetics of H/D exchange for rabbit skeletal troponin C. Apo-troponin C in 3 mM EGTA (squares, red) shows more extensive D uptake than holo troponin C in 1 mM $CaCl_2$ (diamonds, black). The fitted curves are shown as solid lines.

Rabbit skeletal troponin C has 158 exchangeable amide protons (excluding one proline). Because the percentage of D_2O in the experiment was 97%, the maximum number of observable exchange events is 153. After 20 min of H/DX, the mass of apo troponin C shifted by 116 ± 1 Da, indicating that ~75% of the amide sites are exchangeable at this time. This high level of exchange is in accord with the general view that troponin C in solution is highly flexible, dynamic, and solvent-exposed in the absence of Ca^{2+}. In the presence of Ca^{2+}, the number of amides undergoing H/DX

decreased to 83 ± 1 Da after 20 min of exchange, indicating that ~32 amide sites no longer exchange as a consequence of Ca^{2+} binding. A more stabilized secondary structure, an increase in hydrogen bonding, a decrease in solvent accessibility of some amide sites, and/or a combination of these factors decreased the H/DX rates.

To understand quantitatively how Ca^{2+} binding affects the exchange rate, we fit the kinetic curve with four exchange rate bins (k = 10, 1, 0.1, 0.01 min^{-1}) (**Table 3-1**). The results show that the apo state has 79 ± 1 sites with an exchange rate constant of 10 min^{-1}, whereas the holo state has only 26 ± 2 sites with the same rate constant, indicating that ~53 fast-exchanging sites are affected by Ca^{2+} binding. In the holo state, these sites shift to the lower exchange rates including those with an exchange rate constant of 1 min^{-1} where the apo state has 1 ± 1 sites whereas the holo state has 24 ± 2 sites. There are also significant differences for those amides undergoing exchange with a rate constant of 0.01 min^{-1}; whereas the holo state has 61 ± 3 sites, 37 ± 4 amides in the apo state exchange at this corresponding low rate. The overall shift to states having low exchange rate constants is consistent with troponin C possessing a more rigid secondary structure upon Ca^{2+} binding.

Kinetic Fit	# of H's per fixed-rate bin			
k (min^{-1})	10	1	0.1	0.01
Apo	79 ± 1	1 ± 1	16 ± 3	37 ± 4
Holo	26 ± 2	24 ± 2	3 ± 2	61 ± 3

Table 3-1. Numbers of amide hydrogen undergoing exchange for D for apo and holo troponin C. The kinetic modeling used four fixed exchange rate constants and "binned" the number of amides with respect to the rate constants.

3.4.2 Affinities for Ca^{2+} binding of troponin C

Several methods can be used to measure the binding affinities for protein-protein interactions and protein-small molecule interactions; these methods include FRET (fluorescence resonance energy transfer) (*57*), NMR (*58*), CD (circular dichorism) (*59*), calorimetry (*60*) and SPR (surface plasmon resonance) (*61, 62*). Because there is a significant difference in deuterium uptake between apo-TnC and holo-TnC, we can apply PLIMSTEX (Protein–ligand interactions by mass spectrometry, titration, and H/DX) to measure the equilibrium constants for Ca^{2+} binding to TnC (*45, 49-51, 63*) in a relatively simple experiment.

Our titration format varies the relative concentration of Ca^{2+} and monitors by MS the extent of H/DX as a function of time. Because EF-III and EF-IV are known from previous studies to be high-affinity sites, they are often saturated with Ca^{2+}. To insure the protein was in the full apo state (no bound Ca^{2+}), we carried out a two-step dialysis

procedure (see Experimental). The deuterium uptake of the dialyzed TnC was comparable to that of TnC in the presence of EGTA (data not shown), indicating the dialysis was successful in removing Ca^{2+} from the protein. This purified protein sample was used as the starting material for the titration (**Figure 3-2**); the troponin C concentration for the titration was 0.3 μM, which falls into the range of K_d's determined previously (*64*). The time for H/DX (97% D_2O buffer, 10 mM HEPES, 150 mM KCl, pH 7.4) was necessarily constant at 1 h, a time for which H/DX had become relatively constant, and for which small errors in sampling time would have minimal impact on the titration. We also performed the titration at high-protein concentration, 15 μM, which is ~100 times the K_d values (**Figure 3-3**). A titration at this protein concentration will usually give a "sharp break" curve that reveals the stoichiometry of the ligand binding (*49*); in this case, rabbit skeletal troponin C binds four Ca^{2+}, in agreement with previous findings. The other purpose for conducting this "sharp break" titration is to obtain an estimate of the *ΔD'*s values to aid the PLIMSTEX curve fitting process (see Experimental). At high-protein concentration, the equilibrium shifts toward the protein-ligand complex, and the resulting *ΔD'*s values will be similar to the actual *ΔD'*s, which report the change in the protein secondary structure owing to each ligand binding.

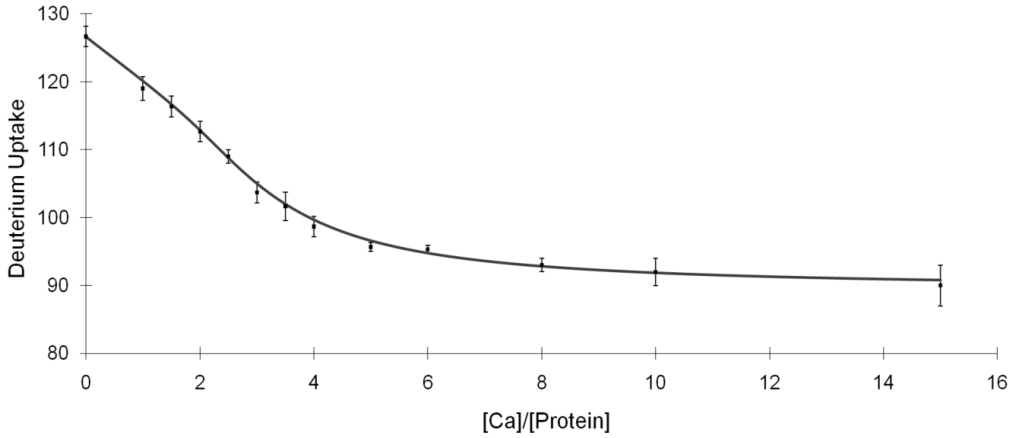

Figure 3-2. PLIMSTEX curve of Troponin C titrated with Ca^{2+} and followed by MS-based H/DX. The concentration of the protein for the titration was 0.3 μM.

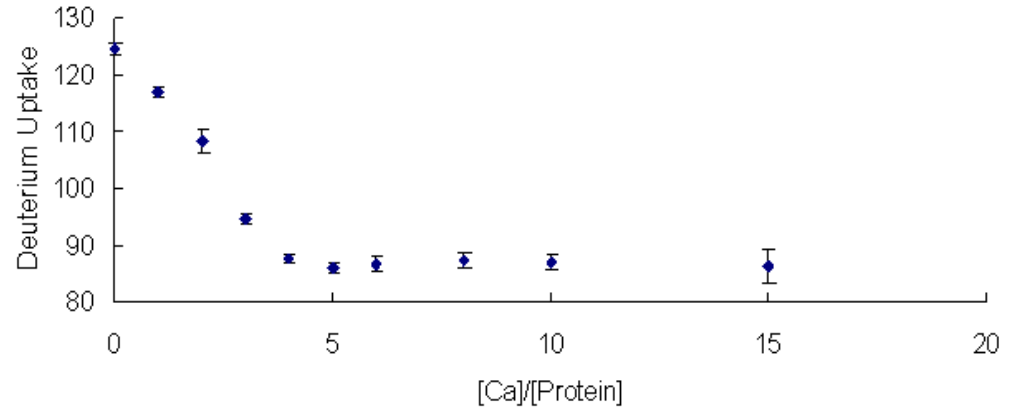

Figure 3-3. "Sharp-break" PLIMSTEX titration curve; protein concentration = 15 μM. The junction of the two arms of the curves indicates the stoichiometry of Ca^{2+} binding is 4:1.

In this manner, we obtained ΔD_1, ΔD_2, ΔD_3, *and* ΔD_4 as 6, 15, 31, and 37, respectively. These values serve as the initial guesses for the repeat-fitting cycle described in the experimental section. The relative variations of K_2, K_3 and K_4 all decreased to ~10% after we performed three cycles of the fitting (**Figure 3-4**). Although the relative variation of K_1 was not constrained over each fitting cycle, probably because the number of experimental points is insufficient, its value still is in a reasonable range. Given that the affinities are known and that the main purpose of the study is to investigate the order of binding, we did not pursue the titration further because additional improvements would not affect significantly the determination of the binding order.

Previous studies show that skeletal troponin C has two Ca^{2+} binding sites, EF-III and EF-IV, located near the C-terminus; their binding affinities are comparable at (2.1 ± 0.7) x 10^7 M^{-1} (*64*). Two additional sites are located near the N-terminus of skeletal troponin C, EF-I and EF-II, and their binding affinities for Ca^{2+} are in the range of 3 x 10^5 to 5 x 10^6 M^{-1} (*20, 64*). Although the equilibrium constants show variability from study to study (possibly because the affinities are relatively small), the consensus is that the equilibrium constants for the N-terminal EF hands are in the range of 10^5-10^6 M^{-1} and smaller than those for the C terminus (*37*).

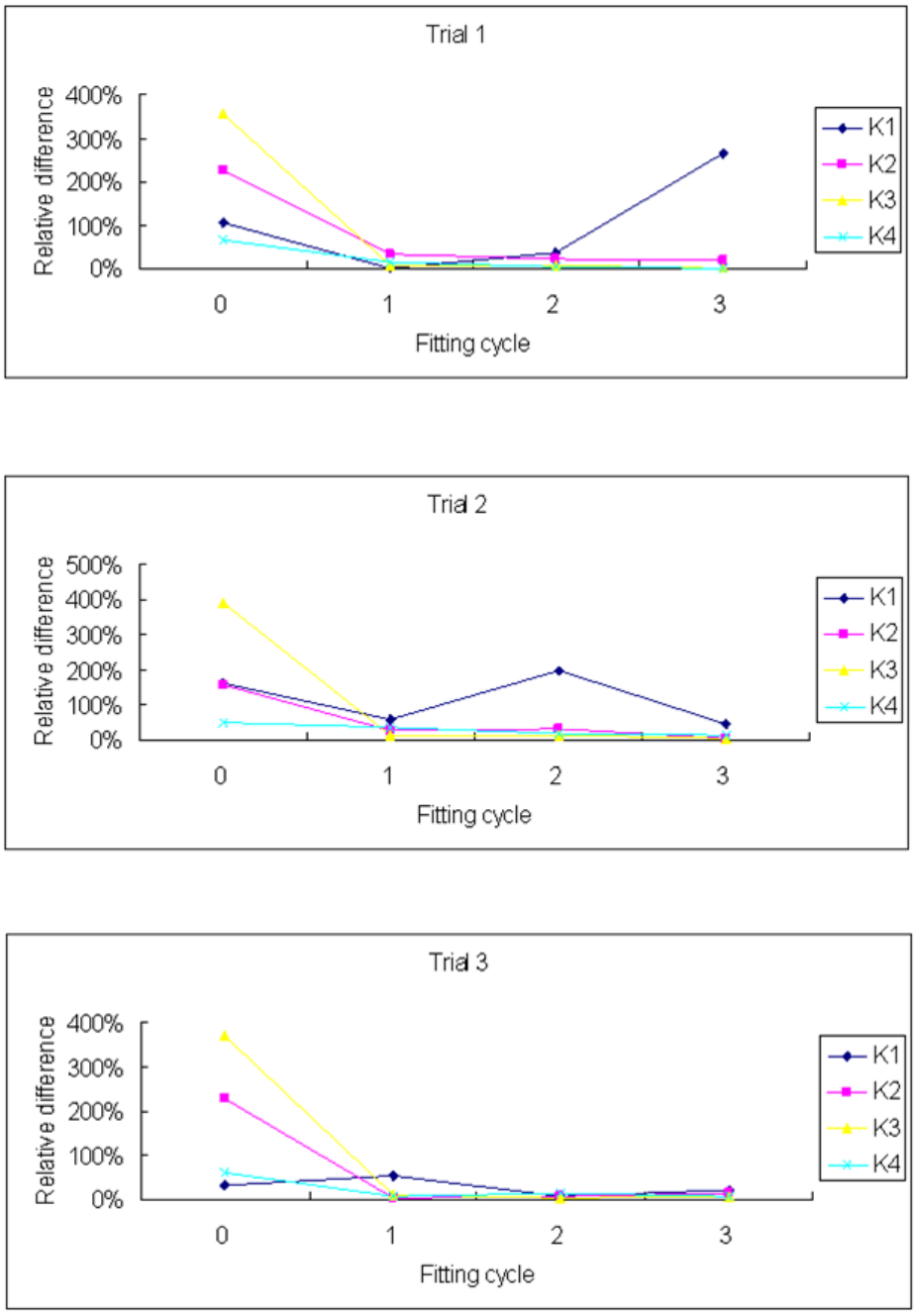

Figure 3-4. Relative differences between K's values before and after each cycle of fitting as a function of the number of fitting cycles.

We fit the titration curve to a non-linear least squares model that was previously described (*51*). The output of the fitting produced four K_a's (**Table 3-2**), two with high values of (5 ± 5) x 10^7 M^{-1} and (1.8 ± 0.8) x 10^7 M^{-1}, which are within a factor of 3 of previous results. The other two K_a's have smaller values of (4.2 ± 0.9) x 10^6 M^{-1} and (1.6 ± 0.6) x 10^6 M^{-1}, which are also within the range of values from previous studies. The fitting parameter D_0 (127 ± 1), which represents the deuterium uptake in the apo state is in agreement with the experimental results (127 ± 2).

K	**Experimental Value**	**Literature Values**
K_1	(5 ± 5) x 10^7 M^{-1}	2 x 10^7 M^{-1} (1);(2.1 ± 0.7) x 10^7 M^{-1}(64)
K_2	(1.8 ± 0.8) x 10^7 M^{-1}	2 x 10^7 M^{-1} (1);(2.1 ± 0.7) x 10^7 M^{-1}(64)
K_3	(4.2 ± 0.9) x 10^6 M^{-1}	5 x 10^6 M^{-1} (20);(3.2 ± 1.3) x 10^5 M^{-1}(64)
K_4	(1.6 ± 0.6) x 10^6 M^{-1}	5 x 10^6 M^{-1} (20) ;(3.2 ±1.3) x 10^5 M^{-1}(64);
ΔD_4	38 ± 1	N/A
D_0	127 ± 1	N/A
RMS	0.62	

Figure 3-2. Four Ca^{2+} binding constants of troponin C obtained by fitting PLIMSTEX titration curves.

3.4.3 Fractional species and binding order

The titration study provides us the four equilibrium constants (K_a) for Ca^{2+} binding to troponin C. These values are not new, and they can be determined by other approaches. Remarkable, however, is that three of the four values (K_2, K_3 and K_4) can be extracted with reasonable precision from a single titration, probably because each addition of Ca^{2+} to the protein induces a change in conformation that responds to H/DX.

Because the binding affinities are different, it is likely that Ca^{2+} binding is cooperative and occurs, at least in part, in a stepwise manner.

The next level of information is the order of binding, which we sought to determine by following the H/DX extent at the EF-hand level. One prospect is to examine the deuterium distribution for the various EF hands as a function of Ca^{2+} concentration. These EF-hand regions may be removed from the protein following H/DX as peptides by pepsin digestion and submitted to LC-MS analysis. When an EF hand binds Ca^{2+}, we expect the extent of H/DX will decrease. By identifying the state of Ca^{2+} binding (e.g., 0, 1, 2, 3, 45 for which the change occurs, we should be able to determine in a straightforward way the order for Ca^{2+} binding. The interaction between Ca^{2+} and troponin C at any titration point, however, results in a mixture of Ca^{2+}-binding states, and the deuterium distribution of any given EF hand at each titration point is of a mixture of different Ca^{2+} bound states. The challenge is to extract from this mixture of states the deuterium distribution of an EF hand for a single state (**Figure 3-5**).

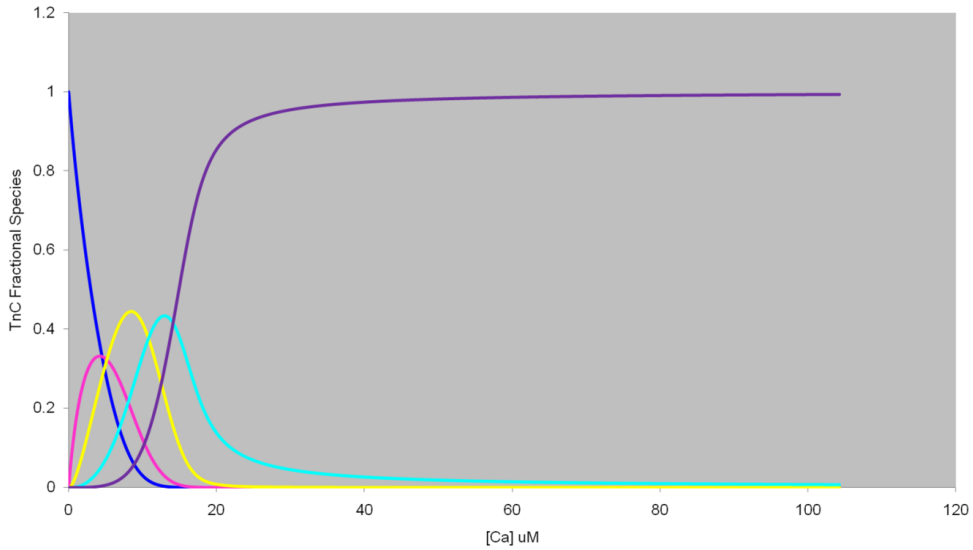

Figure 3-5. Fractional species curves showing the distribution of each TnC:xCa^{2+} as a function of Ca^{2+} concentration (μM). (Blue: zero Ca^{2+}-bound; Pink: 1 Ca^{2+}-bound;, Yellow: 2 Ca^{2+}-bound; Light blue: 3 Ca^{2+}-bound; Purple: 4 Ca^{2+}- bound).

The four equilibrium constants, determined by PLIMSTEX or any other method, are a source of fractional species information that allow the determination of the population of the various Ca^{2+} states as a function of [Ca^{2+}]. We hypothesized that knowing these fractional species will lead us to the required deuterium distributions. To test this hypothesis, we used the previously reported and likely more reliable K_1 value (2.1 x 10^{7} M^{-1}) and the K_2, K_3, and K_4 values (1.8 x 10^{7} M^{-1}, 4.2 x 10^{6} M^{-1}, 1.6 x 10^{6} M^{-1}, respectively) determined by PLIMSTEX to calculate the fractional species as a function of total [Ca^{2+}] and determine the population of the five troponin C species, TnC:xCa^{2+} (x = 0-4) when the protein concentration was 4.2 μM (**Figure 3-5**). The reason for choosing a literature K_1 is the precision for our K_1 value is not high because the titration is

underdetermined, and we don't want that to affect the precision for the fractional-species determination. We chose seven Ca^{2+} concentrations from the fractional-species plot, including [Ca^{2+}] = 0 (100% apo TnC) and Ca^{2+} = 2 mM (100% holo TnC) (**Table 3-3**) for our search for the required deuterium distributions. To obtain the needed experimental data, we conducted H/DX for 1 h in 90% D_2O buffer (10 mM HEPES, 150 mM KCl, pH 7.4), quenched the exchanging solution, digested the protein with pepsin for 3 min on ice-water, and analyzed the peptide mixture by LC/MS.

[Ca] µM	**TnC-0Ca**	**TnC-1Ca**	**TnC-2Ca**	**TnC-3Ca**	**TnC-4Ca**
0	100.0%	0.0%	0.0%	0.0%	0.0%
8.4	7.4%	19.7%	44.5%	23.7%	4.7%
10.4	2.3%	10.4%	39.8%	35.6%	11.9%
12.1	0.0%	4.9%	29.7%	42.6%	22.8%
13.8	0.0%	0.0%	18.2%	43.1%	38.7%
16.7	0.0%	0.0%	0.0%	29.1%	70.9%
2000	0.0%	0.0%	0.0%	0.0%	100.0%

Table 3-3. Various solution concentrations chosen for H/DX to determine the order of binding of Ca^{2+} with troponin C. The values are calculated fractional species of each Ca^{2+}-bound TnC species and are taken from the fractional species curves in Figure 3.

MS analysis directly gave us the complete isotopic distribution for specific deuterated peptides, but this distribution represents various states of the protein, not the single state we sought. Nevertheless, from these distributions, we can calculate the representative isotopic distribution for each Ca^{2+}-bound troponin C species (see **Figure 3-6** for an example of this idea). The upper left spectrum shows the deuterium-containing isotopic distribution when $[Ca^{2+}]$ = 16.7 μM for the triply charged peptic peptide FRIFDRNADG, which is from the EF-III region. From Table 3-3, we know that there is 30% TnC-3Ca^{2+} species and 70% of TnC-4Ca^{2+} species in the solution when the total $[Ca^{2+}]$ is 16.7 μM. Because we know the deuterium distribution of this peptide when $[Ca^{2+}]$ = 2 mM (representing 100% TnC-4Ca^{2+} species, lower left in **Figure 3-6**), we can remove that pattern from the experimental distribution to give the deuterium distribution for the peptide representing this region of the protein when it exists as TnC-3Ca^{2+} (right pattern in **Figure 3-6**).

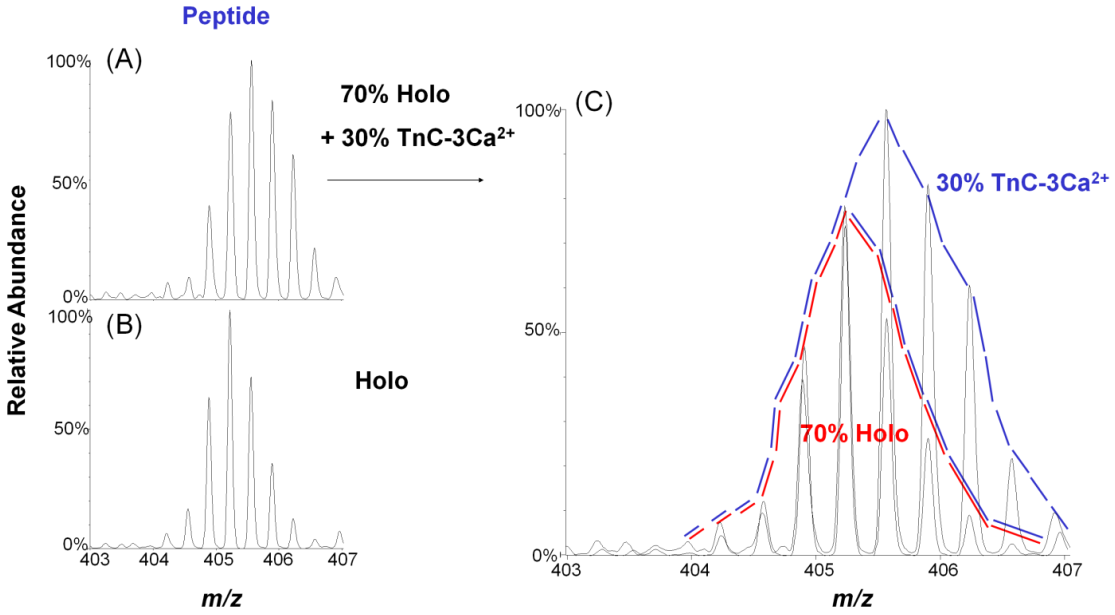

Figure 3-6. (A) Deuterium-containing isotopic distribution of the triply charged peptic peptide 100-109 (FRIFDRNADG). The distribution can be represented as a mixture of 70% holo (TnC-4Ca^{2+}, red area in C) and 30% TnC-3Ca^{2+} states as shown in (C), which is an enlarged view of A. (B) Deuterium-containing isotopic distribution of triply charged peptic peptide 100-109 (FRIFDRNADG). The distribution represents 100% Holo state (TnC-4Ca^{2+}) in 1 mM $CaCl_2$. (C) Enlarged view of (A). Although the triply charged peptide is for demonstration, the doubly charged peptide was used for analysis.

To sort out the required isotopic distributions, we implemented an algorithm with Mathcad 2001 Professional (Math-Soft, Inc., Cambridge, MA). We extracted mass lists containing all peptide information from each spectrum and input them into MathCAD as x,y files for peak-finding and fractional-species calculation. The basis for this algorithm is in matrix algebra as given in equation 1.

$$\underset{\text{Matrix A}}{\begin{bmatrix} I_{00} & I_{01} \ldots . I_{0m} \\ I_{10} & I_{11} \ldots . I_{1m} \\ \vdots & \vdots \\ I_{n0} & I_{n1} \ldots . I_{nm} \end{bmatrix}} = \underset{\text{Matrix B}}{\begin{bmatrix} IS_{00} & IS_{01} \ldots . IS_{0x} \\ IS_{10} & IS_{11} \ldots . IS_{1x} \\ \vdots & \vdots \\ IS_{n0} & IS_{n1} \ldots . IS_{nx} \end{bmatrix}} X \underset{\text{Matrix C}}{\begin{bmatrix} PS_{00} & PS_{01} \ldots . PS_{0m} \\ PS_{10} & PS_{11} \ldots . PS_{1m} \\ \vdots & \vdots \\ PS_{x0} & PS_{x1} \ldots . PS_{xm} \end{bmatrix}} \quad (1)$$

In this equation, matrix A is the input of the experimental results; that is, the isotopic abundances for a single peptide, I, from peak 0 to peak n as a function of the various ligand concentrations. Matrix C provides the fractional species information; that is, the population of each species, PS, from species 0 to x as a function of the ligand concentrations. For troponin C, binding to Ca^{2+}, x = 4, and there exist five species: TnC-$0Ca^{2+}$, TnC-$1Ca^{2+}$, TnC-$2Ca^{2+}$, TnC-$3Ca^{2+}$, and TnC-$4Ca^{2+}$. Matrix B is the output of isotopic abundances of species, IS, from peak 0 to peak n as a function of various Ca^{2+} binding states.

In the implementation, we normalized each row of each matrix so that their sum is equal to 1, and we required that the values in matrix B be positive. We fit the output in matrix B to the best values; this procedure requires minimizing the differences between matrix A and the product of matrix B and C. The intensity input can be the intensity of the peak centroid or its area in a peak-profile mode; the latter was used in this work so that each part in the isotopic distribution pattern was considered, in principle increasing

the accuracy of the calculation. By comparing the distribution of the peaks and their area, we obtained a deuterium isotopic pattern of each peptic peptide as a function of the Ca^{2+} binding state. Changes in H-bonding or solvent accessibility for various regions of the protein induced by Ca^{2+} binding can be determined by simply analyzing the shift of the isotopic distribution.

3.4.4 Order of Ca^{2+} binding

Our hypothesis was that changes in the deuterium distributions for peptides from regions involved in Ca^{2+} binding as a function of the states of the protein (TnC-0Ca^{2+} to TnC-4Ca^{2+}) will report the order of Ca^{2+} binding. To test this hypothesis, we needed four abundant peptic peptides each representing one of the four EF hands to follow as a function of the fractional species calculation, and we were able to obtain these reporter peptides by pepsin digestion. The four peptides are doubly charged DADGGGDISVKELGTVM (28-44) containing EF-I; doubly charged, EVDEDGSGTID (63-73) containing EF-II; doubly charged FRIFDRNADG (100-109) containing EF-III; and triply charged, MKDGDKNNDGRIDF (136-149) containing EF-IV. The outcome of the matrix-algebra calculation gave us the deuterium distributions convolved with the native distribution of C-13, N-15 and O-18 of each EF hand for the five states of Ca^{2+} binding to troponin C. We then removed all isotope components except D for these four

unique peptic peptides by using the theoretical isotope ratio provided via the Isotope Simulation function in Qual Browser 2.0.7 (Xcalibur, Thermo Fisher, San Jose, CA). The isotope deconvolution process is illustrated in **Figure 3-7**. Briefly, each deuterium-containing isotopic pattern is a mixture of various numbers of deuterium-containing species (d_0, d_1, d_2…) with their isotopic species. By knowing the chemical formula for a particular peptide, we can calculate the isotope distribution (except that of D from H/DX) and remove it from the distribution, leaving a pure deuterium distribution (**Figure 3-8**). We submit that any slight change of the deuterium uptake can be readily revealed by this strategy.

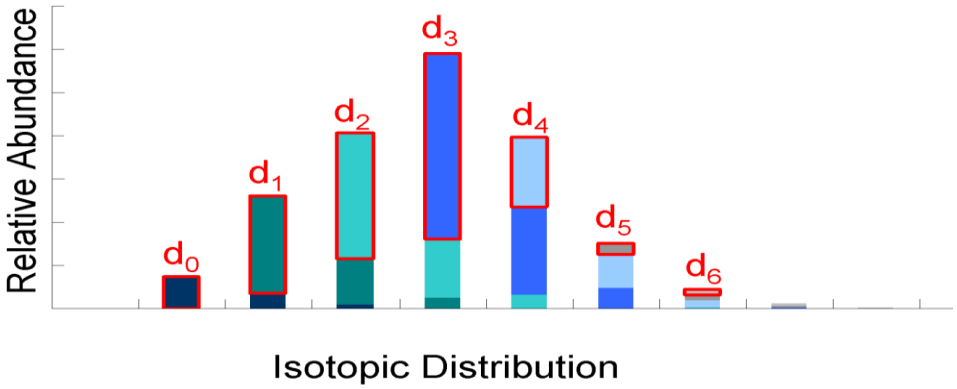

Figure 3-7. Deuterium distribution convolved with the native isotopic distribution of doubly charged peptide 63-73. Bars represent the different numbers of deuteriums (d_0, d_1, d_2…) comprising each peak, and their heights include other isotopic contributions (C-13, N-15, O-18) (dark blue to light blue). Removing the native isotopic distribution leaves the deuterium distribution (bars outlined with red frames).

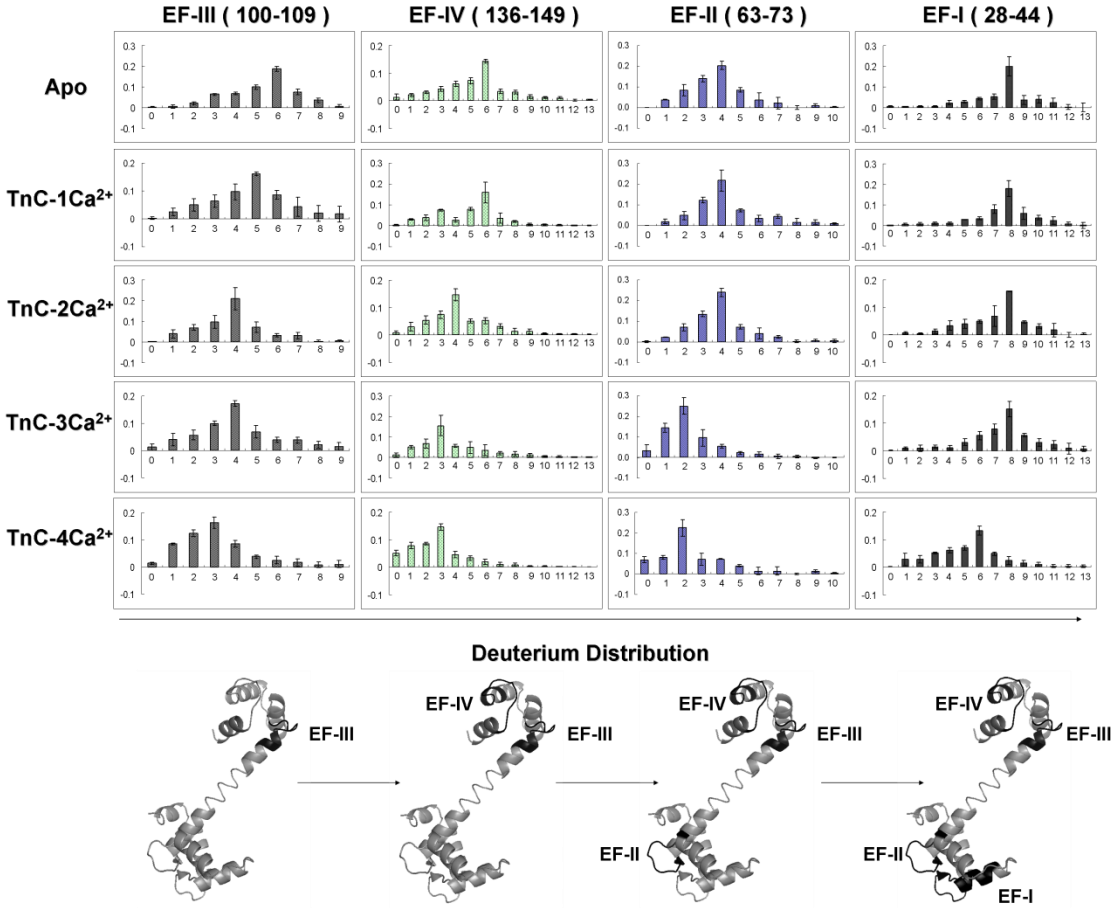

Figure 3-8. Top: Each column represents the deuterium distributions of the peptic peptide of EF hands: III, IV, II, I (left to right). Each row represents the various Ca^{2+} bound TnC states: Apo (Absent Ca^{2+}) to 4 Ca^{2+} bound TnC (top to bottom). Bottom: X-ray crystal structure of rabbit skeletal troponin C (PDB: 1TCF) in gray, and the four EF hands are in black.

Comparing the variation of the deuterium-distribution centroid for the four peptic peptides as a function of different Ca^{2+} bound troponin C states (**Figure 3-8**), we see that the first shift from higher to lower deuterium content (indicating onset of protection) occurs for peptic peptide 100-109 containing EF-III for the transition of TnC-0Ca^{2+} to TnC-1Ca^{2+} whereas the deuterium distributions of the peptides representing the other

three EF hands remain largely unaffected. This indicates that EF-III in skeletal troponin C is first to bind Ca^{2+}, although the binding may not be complete as the D distribution continues to shift to more protection as more calcium binds. Peptic peptide 136-149 from EF-IV showed a similar but more conclusive shift from a centroid of six to four deuteriums for TnC-2Ca^{2+}, indicating that EF-IV is the second Ca^{2+} binding site. Similar to EF-III, the D distribution shows additional minor shifts as the protein continues to take up calcium. Although the shifts for EF-III and IV do not occur sharply as various states of Ca^{2+} binding are achieved, the results clearly show the higher propensity for binding Ca^{2+} by EF-III and EF-IV (~10^7 M^{-1}) than by EF-II and EF-I. Sykes and coworkers (*53*) studied the binding of Ca^{2+} to synthetic EF-III and EF-IV peptides of troponin C by 1H-NMR. Their results show that Ca^{2+} binds to synthetic EF-III peptide; the resulting Ca^{2+}-EF-III then associates with the apo-EF-IV peptide to form a heterodimer Ca^{2+}-EF-III/EF-IV. The heterodimer then binds the second calcium to give 2Ca^{2+}-EFIII/EFIV. Our results on the intact protein agree with this general picture of stepwise binding.

Because the N-terminal EF-I and EF-II have lower binding affinities to Ca^{2+} (~10^6 M^{-1}), they should bind after EF-III and IV. Indeed, the deuterium content (most abundant ion) of the peptic peptide containing EF-II shifts from four to two deuteriums at the transition to TnC-3Ca^{2+}, whereas the peptic peptide representing EF-I shifts from eight to

six deuteriums at the transition to TnC-4Ca^{2+}. Thus, the third Ca^{2+} binds at EF-II followed by the last Ca^{2+} binding at EF-I. Sykes and coworkers (*37*) also studied Ca^{2+} binding to EF hands in N-terminus of chicken skeletal troponin C by using NMR. Although the overall binding picture for full length TnC remained unclear, they could conclude that EF-II is the first site in the N-terminus of troponin C that binds to Ca^{2+} and EF-I is the last Ca^{2+} binding site, a conclusion that is consistent with the results of H/DX presented here.

To illustrate more clearly the order of Ca^{2+} binding, we normalized the deuterium-uptake values for the four peptides to their most probable deuterium (highest intensity peak) uptake. This allows us to view the relative deuterium uptake as a function of different TnC-Ca^{2+} states (**Figure 3-9**). The outcome clearly shows that the order of Ca^{2+} binding to the four Ca^{2+} binding sites in intact skeletal troponin C is EF-III > EF-IV > EF-II >EF-I, although there is likely to be some simultaneous binding of Ca^{2+} by EF-III and IV.

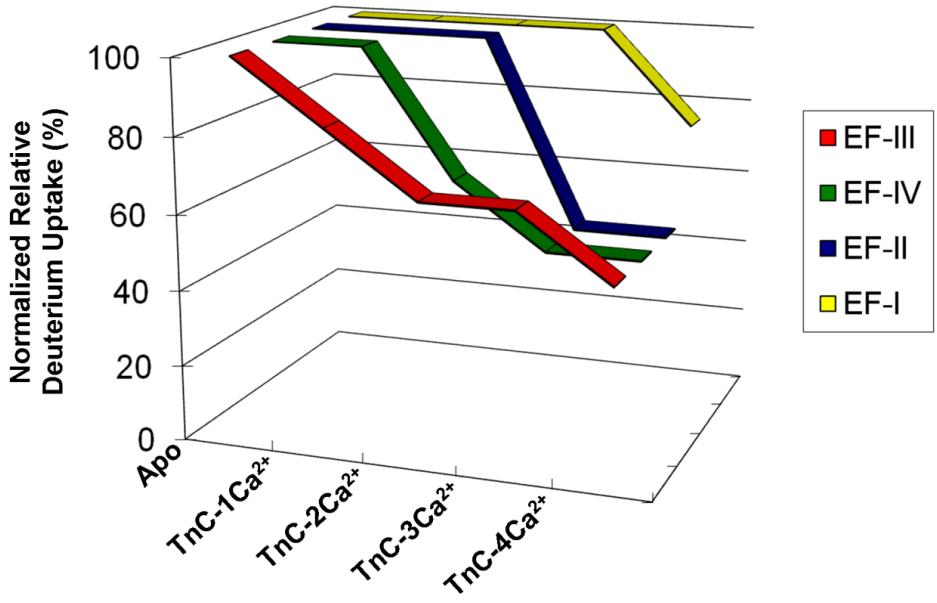

Figure 3-9. A plot of the normalized relative deuterium uptake based on the centroids of the deuterium distributions for four peptic peptides containing the four EF hands as a function of various Ca^{2+}-bound TnC states.

3.5 DISCUSSION

The advantage of H/DX coupled with MS is that changes in the extent of H/DX, whether caused by increased H bonding or decreased solvent accessibility or both, can be used to compare two or more states. The conclusions do not depend highly on the abundances of the various isotopomers but principally on their *m/z*. The PLIMSTEX strategy further extends the advantage of H/DX by affording, via ligand titrations at a fixed concentration of protein, the protein-ligand binding affinities. The equilibrium

constants are essential for the design of an experimental approach to extract deuterium distributions for regions of a protein as a function of its binding state.

We illustrate the approach to determine the binding order of Ca^{2+} to troponin C. Although troponin C is a well-studied protein, establishing the order of Ca^{2+} binding has proven difficult. The kinetics of HDX at the protein or global level demonstrates that the protein is considerably stabilized as a consequence of Ca^{2+} binding. The differences in the apo and holo states allow the binding affinities of troponin C with Ca^{2+} to be measured in a single-titration format. The values of the equilibrium constants allow calculation of fractional species for troponin C. From H/DX experiments at known fractional species, we can extract the deuterium distribution of four regions of the protein that bind Ca^{2+}. Those distributions shift to lower mass when Ca^{2+} binds at the site, providing a basis for determining the binding order of the four Ca^{2+} ions.

Previous studies on Ca^{2+} binding to troponin C by Ca^{2+} titration (*36, 37, 52, 53, 64*) indicated the binding is cooperative and affected by pH. Those studies, however, did not give a clear outcome of the binding order of Ca^{2+} to troponin C probably because the similar binding affinities of Ca^{2+} in each terminal region of troponin C cause the states to coexist at various Ca^{2+} concentrations. Nevertheless, our results indicate the Ca^{2+} binding to skeletal troponin C occurs in the order EF-III > EF-IV > EF-II > EF-I. This

determination is attributed to the high sensitivity of MS in the H/DX platform and the ability to extract from the data specific D distributions for the five binding states of the protein.

The reasons for this trend of binding are not completely understood. Preferential binding at the C terminus is well-established. Binding details may be an outcome of the various charge states of the protein in different pH environments or the difference of the secondary and tertiary structure of the Ca^{2+} binding sites with respect to individual Ca^{2+} binding (*52*). Nevertheless, our results can help understanding the detailed mechanism of the muscle contraction. It will be of interest to see whether this approach can be applied to determine binding orders of other proteins and ligands.

3.6 ACKNOWLEDGEMENT

We thank Dr. Henry Rohrs for assistance with the LTQ-Orbitrap analysis and database searching. This research was supported by the NCRR of the NIH (Grant No. 21 2P41RR000954) to MLG.

3.7 REFERENCES

1. Filatov , A. G. K., T. V. Bulargina, N. B. Gusev. (1999) Troponin: Structure, Properties, and Mechanism of Functioning, *Biochemistry (Moscow) 64*, 1155-1164.

2. Grabarek, Z., Tao, T., and Gergely, J. (1992) Molecular mechanism of troponin-C function, *Journal of Muscle Research and Cell Motility 13*, 383-393.

3. Zot, A. S., and Potter, J. D. (1987) Structural Aspects of Troponin-Tropomyosin Regulation of Skeletal Muscle Contraction, *Annual Review of Biophysics and Biophysical Chemistry 16*, 535-559.

4. Herzberg, O., and James, M. N. G. (1988) Refined crystal structure of troponin C from turkey skeletal muscle at 2.0 A resolution, *Journal of Molecular Biology 203*, 761-779.

5. Gulati, J., Babu, A., Su, H., and Zhang, Y. F. (1993) Identification of the regions conferring calmodulin-like properties to troponin C, *Journal of Biological Chemistry 268*, 11685-11690.

6. Li, Y., Mui, S., Brown, J. H., Strand, J., Reshetnikova, L., Tobacman, L. S., and Cohen, C. (2002) The crystal structure of the C-terminal fragment of striated-

muscle α-tropomyosin reveals a key troponin T recognition site, *Proceedings of the National Academy of Sciences of the United States of America 99*, 7378-7383.

7. Kobayashi, T., and Solaro, R. J. (2005) CALCIUM, THIN FILAMENTS, AND THE INTEGRATIVE BIOLOGY OF CARDIAC CONTRACTILITY, *Annual Review of Physiology 67*, 39-67.

8. Takeda, S. (2005) Crystal structure of troponin and the molecular mechanism of muscle regulation, *J Electron Microsc (Tokyo) 54*, i35-41.

9. Davis, J. P., and Tikunova, S. B. (2008) Ca2+ exchange with troponin C and cardiac muscle dynamics, *Cardiovasc Res 77*, 619-626.

10. Sun, Y.-B., Lou, F., and Irving, M. (2009) Calcium- and myosin-dependent changes in troponin structure during activation of heart muscle, *J Physiol 587*, 155-163.

11. Paul, D. M., Morris, E. P., Kensler, R. W., and Squire, J. M. (2009) Structure and Orientation of Troponin in the Thin Filament, *J. Biol. Chem. 284*, 15007-15015.

12. Satyshur, K. A., Rao, S. T., Pyzalska, D., Drendel, W., Greaser, M., and Sundaralingam, M. (1988) Refined structure of chicken skeletal muscle troponin C in the two- calcium state at 2.0A resolution, *J. Biol. Chem. 263*, 1628-1647.

13. Jayashree, S., Terence, T., and George, N. P., Jr. (1999) Conformational variation of calcium-bound troponin C, *Proteins: Structure, Function, and Genetics 37*, 510-511.

14. Sykes, B. D. (2003) Pulling the calcium trigger, *Nat Struct Mol Biol 10*, 588-589.

15. Vinogradova, M. V., Stone, D. B., Malanina, G. G., Karatzaferi, C., Cooke, R., Mendelson, R. A., and Fletterick, R. J. (2005) Ca2+-regulated structural changes in troponin, *Proceedings of the National Academy of Sciences of the United States of America 102*, 5038-5043.

16. Sun, Y.-B., Brandmeier, B., and Irving, M. (2006) Structural changes in troponin in response to Ca2+ and myosin binding to thin filaments during activation of skeletal muscle, *Proceedings of the National Academy of Sciences 103*, 17771-17776.

17. Reece, K. L., and Moss, R. L. (2008) Intramolecular Interactions in the N-Domain of Cardiac Troponin C Are Important Determinants of Calcium Sensitivity of Force Development, *Biochemistry 47*, 5139-5146.

18. Kawasaki H, K. R. (1994) Calcium-binding proteins 1: EF-hands, *Protein Profile 4*, 297-490.

19. Gillis, T. E., Marshall, C. R., and Tibbits, G. F. (2007) Functional and evolutionary relationships of troponin C, *Physiol. Genomics 32*, 16-27.

20. Calvert, M. J., Ward, D. G., Trayer, H. R., and Trayer, I. P. (2000) The Importance of the Carboxyl-terminal Domain of Cardiac Troponin C in Ca2+-sensitive Muscle Regulation, *J. Biol. Chem. 275*, 32508-32515.

21. Li, M., Saude, E., Wang, X., Pearlstone, J., Smillie, L., and Sykes, B. (2002) Kinetic studies of calcium and cardiac troponin I peptide binding to human cardiac troponin C using NMR spectroscopy, *European Biophysics Journal 31*, 245-256.

22. Takeda, S., Yamashita, A., Maeda, K., and Maeda, Y. (2003) Structure of the core domain of human cardiac troponin in the Ca2+-saturated form, *Nature 424*, 35-41.

23. Li, M., Wang, X., and Sykes, B. (2004) Structural based insights into the role of troponin in cardiac muscle pathophysiology, *Journal of Muscle Research and Cell Motility 25*, 559-579.

24. Li, Z., Gergely, J., and Tao, T. (2001) Proximity Relationships between Residue 117 of Rabbit Skeletal Troponin-I and Residues in Troponin-C and Actin, *Biophys. J. 81*, 321-333.

25. Li, M. X., and Sykes, B. D. (2000) Role of the Structural Domain of Troponin C in Muscle Regulation: NMR Studies of Ca2+ Binding and Subsequent Interactions with Regions 1-40 and 96-115 of Troponin I, *Biochemistry 39*, 2902-2911.

26. Ferguson, R. E., Irving, M., Corrie, J. E. T., Trentham, D. R., and Sykes, B. D. (2003) NMR Structure of a Bifunctional Rhodamine Labeled N-Domain of Troponin C Complexed with the Regulatory "witch" Peptide from Troponin I: Implications for in Situ Fluorescence Studies in Muscle Fibers, *Biochemistry 42*, 4333-4348.

27. Blumenschein, T. M. A., Stone, D. B., Fletterick, R. J., Mendelson, R. A., and Sykes, B. D. (2006) Dynamics of the C-Terminal Region of TnI in the Troponin Complex in Solution, *Biophys. J. 90*, 2436-2444.

28. Wang, Z. Y., Sarkar, S., Gergely, J., and Tao, T. (1990) Ca2(+)-dependent interactions between the C-helix of troponin-C and troponin-I. Photocross-linking and fluorescence studies using a recombinant troponin-C, *J. Biol. Chem. 265*, 4953-4957.

29. Wang, Z., Gergely, J., and Tao, T. (1992) Characterization of the Ca(2+)-triggered conformational transition in troponin C, *Proceedings of the National Academy of Sciences of the United States of America 89*, 11814-11817.

30. Foguel, D., Suarez, M. C., Barbosa, C., Rodrigues, J. J., Sorenson, M. M., Smillie, L. B., and Silva, J. L. (1996) Mimicry of the calcium-induced conformational state of troponin C by low temperature under pressure, *Proceedings of the National Academy of Sciences of the United States of America 93*, 10642-10646.

31. Chandra, M., Dong, W.-J., Pan, B.-S., Cheung, H. C., and Solaro, R. J. (1997) Effects of Protein Kinase A Phosphorylation on Signaling between Cardiac Troponin I and the N-Terminal Domain of Cardiac Troponin C, *Biochemistry 36*, 13305-13311.

32. Finley, N. L., and Rosevear, P. R. (2004) Introduction of Negative Charge Mimicking Protein Kinase C Phosphorylation of Cardiac Troponin I: EFFECTS ON CARDIAC TROPONIN C, *J. Biol. Chem. 279*, 54833-54840.

33. Baryshnikova, O. K., Li, M. X., and Sykes, B. D. (2008) Defining the Binding Site of Levosimendan and Its Analogues in a Regulatory Cardiac Troponin C-Troponin I Complex, *Biochemistry 47*, 7485-7495.

34. Li, M. X., Robertson, I. M., and Sykes, B. D. (2008) Interaction of cardiac troponin with cardiotonic drugs: A structural perspective, *Biochemical and Biophysical Research Communications 369*, 88-99.

35. Spyracopoulos, L., and Sykes, B. D. (2001) Structure, Dynamics, and Thermodynamics of the Structural Domain of Troponin C in Complex with the Regulatory Peptide 1-40 of Troponin I, *Biochemistry 40*, 10063-10077.

36. Olle, T., Torbjorn, D., Sture, F., and Eva, T. (1983) Calcium and Cadmium Binding to Troponin C, *European Journal of Biochemistry 134*, 453-457.

37. Li, M. X., Gagne, S. M., Tsuda, S., Kay, C. M., Smillie, L. B., and Sykes, B. D. (1995) Calcium Binding to the Regulatory N-Domain of Skeletal Muscle Troponin C Occurs in a Stepwise Manner, *Biochemistry 34*, 8330-8340.

38. Yamada, K. (1999) Thermodynamic analyses of calcium binding to troponin C, calmodulin and parvalbumins by using microcalorimetry, *Molecular and Cellular Biochemistry 190*, 39-45.

39. Bobst, C. E., Abzalimov, R. R., Houde, D., Kloczewiak, M., Mhatre, R., Berkowitz, S. A., and Kaltashov, I. A. (2008) Detection and Characterization of Altered Conformations of Protein Pharmaceuticals Using Complementary Mass Spectrometry-Based Approaches, *Analytical Chemistry 80*, 7473-7481.

40. Englander, S. (2006) Hydrogen exchange and mass spectrometry: A historical perspective, *J. Am. Soc. Mass Spectrom. 17*, 1481-1489.

41. Konermann, L., Pan, J., and Liu, Y.-H. (2011) Hydrogen exchange mass spectrometry for studying protein structure and dynamics, *Chemical Society Reviews 40*, 1224-1234.

42. Bou-Assaf, G. M., Chamoun, J. E., Emmett, M. R., Fajer, P. G., and Marshall, A. G. (2010) Advantages of Isotopic Depletion of Proteins for Hydrogen/Deuterium Exchange Experiments Monitored by Mass Spectrometry, *Anal. Chem. 82*, 3293-3299.

43. Chalmers, M. J., Busby, S. A., Pascal, B. D., West, G. M., and Griffin, P. R. (2011) Differential hydrogen/deuterium exchange mass spectrometry analysis of protein-ligand interactions, *Expert Review of Proteomics 8*, 43-59.

44. Engen, J. R. (2009) Analysis of Protein Conformation and Dynamics by Hydrogen/Deuterium Exchange MS, *Anal. Chem. 81*, 7870-7875.

45. Sperry, J. B., Shi, X., Rempel, D. L., Nishimura, Y., Akashi, S., and Gross, M. L. (2008) A Mass Spectrometric Approach to the Study of DNA-Binding Proteins: Interaction of Human TRF2 with Telomeric DNA, *Biochemistry 47*, 1797-1807.

46. Hopper, E. D., Roulhac, P. L., Campa, M. J., Patz Jr, E. F., and Fitzgerald, M. C. (2008) Throughput and Efficiency of a Mass Spectrometry-Based Screening Assay for Protein-Ligand Binding Detection, *J. Am. Soc. Mass Spectrom. 19*, 1303-1311.

47. Kowlessur, D., and Tobacman, L. S. (2010) Troponin Regulatory Function and Dynamics Revealed by H/D Exchange-Mass Spectrometry, *Journal of Biological Chemistry 285*, 2686-2694.

48. Bou-Assaf, G. M., Chamoun, J. E., Emmett, M. R., Fajer, P. G., and Marshall, A. G. (2011) Complexation and calcium-induced conformational changes in the cardiac troponin complex monitored by hydrogen/deuterium exchange and FT-ICR mass spectrometry, *International Journal of Mass Spectrometry 302*, 116-124.

49. Zhu, M. M., Rempel, D. L., Du, Z., and Gross, M. L. (2003) Quantification of Protein-Ligand Interactions by Mass Spectrometry, Titration, and H/D Exchange: PLIMSTEX, *Journal of the American Chemical Society 125*, 5252-5253.

50. Zhu, M. M., Chitta, R., and Gross, M. L. (2005) PLIMSTEX: a novel mass spectrometric method for the quantification of protein-ligand interactions in solution, *International Journal of Mass Spectrometry 240*, 213-220.

51. Zhu, M. M., Rempel, D. L., and Gross, M. L. (2004) Modeling data from titration, amide H/D exchange, and mass spectrometry to obtain protein-ligand binding constants, *Journal of the American Society for Mass Spectrometry 15*, 388-397.

52. Iida, S. (1988) Calcium Binding to Troponin C. II. A Ca2+ Ion Titration Study with a Ca2+ Ion Sensitive Electrode, *J Biochem 103*, 482-486.

53. Gary, S. S., Robert, S. H., and Brian, D. S. (1992) Stoichiometry of calcium binding to a synthetic heterodimeric troponin-C domain, *Biopolymers 32*, 391-397.

54. Bai, Y., Milne, J. S., Mayne, L., and Englander, S. W. (1993) Primary structure effects on peptide group hydrogen exchange, *PROTEINS: Structure, Function, and Genetics 17*, 75-86.

55. Houdusse, A., Love, M. L., Dominguez, R., Grabarek, Z., and Cohen, C. (1997) Structures of four Ca2+-bound troponin C at 2.0 A resolution: further insights into the Ca2+-switch in the calmodulin superfamily, *Structure 5*, 1695-1711.

56. Shaw, G. S., Golden, L. F., Hodges, R. S., and Sykes, B. D. (1991) Interactions between paired calcium-binding sites in proteins: NMR determination of the stoichiometry of calcium binding to a synthetic troponin-C peptide, *Journal of the American Chemical Society 113*, 5557-5563.

57. Khamir, M., Adam, D. H., Raghunandan, K., Peter, J. W., and Jennifer, J. L. (2009) A computational approach to inferring cellular protein-binding affinities from quantitative fluorescence resonance energy transfer imaging, *PROTEOMICS 9*, 5371-5383.

58. Lee, F., Samantha, R., and Dan, F. (2005) Determination of protein-ligand binding affinity by NMR: observations from serum albumin model systems, *Magnetic Resonance in Chemistry 43*, 463-470.

59. Mayhood, T. W., and Windsor, W. T. (2005) Ligand binding affinity determined by temperature-dependent circular dichroism: Cyclin-dependent kinase 2 inhibitors, *Analytical Biochemistry 345*, 187-197.

60. Bains, G., and Freire, E. (1991) Calorimetric determination of cooperative interactions in high affinity binding processes, *Analytical Biochemistry 192*, 203-206.

61. Monfregola, L., Vitale, R. M., Amodeo, P., and Luca, S. D. (2009) A SPR strategy for high-throughput ligand screenings based on synthetic peptides mimicking a selected subdomain of the target protein: A proof of concept on HER2 receptor, *Bioorganic & Medicinal Chemistry 17*, 7015-7020.

62. Blow, N. (2009) Proteins and proteomics: life on the surface, *Nat Meth 6*, 389-393.

63. Rempel, D. L., Zhao, J., Giblin, D. E., and Gross, M. L. (2003) Probing Ca2+-Induced Conformational Changes in Porcine Calmodulin by H/D Exchange and ESI-MS: Effect of Cations and Ionic Strength, *Biochemistry 42*, 15388-15397.

64. Potter, J. D., and Gergely, J. (1975) The calcium and magnesium binding sites on troponin and their role in the regulation of myofibrillar adenosine triphosphatase, *J. Biol. Chem. 250*, 4628-4633.

Chapter 4*

Hydrogen-Deuterium Exchange Mass-Spectrometry Reveals Troponin C Dynamics and Binding within the Troponin Complex

* This work was contributed equally by Richard Y.-C. Huang and Brady J. Summers. Brady at the time was an undergraduate student at the University of Missouri-Kansas City, Kansas City, was trained in our group during the summer of 2011. His project and stipend was sponsored by the Amgen Scholars Program.

4.1 ABSTRACT

The troponin protein complex exists in the thin filament of striated muscle myocytes (along with tropomyosin and actin) and plays a regulatory role in muscle contraction by binding calcium ions released by nerve impulses. The complex is composed of three subunits; troponin C (TnC), the calcium binder; troponin I (TnI), the inhibitor; and troponin T (TnT), the anchor and structural support. The interactions within the troponin complex to produce muscle contraction and the role of the complex plays in cardiac-related diseases motivate its study. We used solution phase hydrogen/deuterium exchange (H/DX) monitored by mass spectrometry at both the global and peptide level to understand better the structural dynamics within the rabbit skeletal troponin complex. We determined that the major effector of structure in calcium-activated TnC is TnI, and that TnT plays a minor role in the interactions of TnC. We also compared the binding affinity between TnC and TnI in the absence or presence of TnT by using PLIMSTEX (protein-ligand interaction by mass spectrometry, titration, and H/D exchange). Our titration curves, when fit with 1:1 binding model, provided binding constants, $(1.9 \pm 0.4) \times 10^6$ M^{-1}; $(2.4 \pm 0.2) \times 10^6$ M^{-1} in the absence or presence of TnT. The outcomes further confirm

that TnT has little effect on the binding between TnC and TnI and is a demonstration of the utility of H/DX in studying the properties of one protein in a complex.

4.2 INTRODUCTION

Troponin, a 72 kDa protein complex in skeletal and cardiac muscle of mammals, is composed of three subunits: troponin C (TnC), troponin I (TnI) (*1*), and troponin T (TnT) (*2, 3*). Each subunit has its own unique function, and all are essential for muscle contraction (*4*). TnT binds to tropomyosin on the thin filament, serving as a key in complex formation (*5, 6*). TnI blocks the actin from interacting with the myosin head by anchoring its C-terminal region (Inhibitor region) (*2*). TnC, a calcium sensor, usually has four Ca^{2+} binding sites (only three for cardiac TnC). Two sites located at the C-terminal domain have high Ca^{2+} binding affinities (~10^7 M^{-1}), are saturated with Ca^{2+} under normal physiological conditions so as to maintain the stability of the complex (*3, 7, 8*). When the intracellular free Ca^{2+} concentration increases, Ca^{2+} binds to the N-terminal domain of TnC, changing the conformation of TnC and forming a hydrophobic pocket in the N-terminal region (*4, 9, 10*). This region then interacts with the "inhibitor region" of TnI and releases actin, whereby muscle contraction is initiated through the interaction of actin and the myosin head. Any factor that affects the TnC-TnI interaction will influence the efficiency of muscle movement and may have implications in cardiac disease. For example, phosphorylation of TnI may be induced by over-activation of protein kinase A and C to affect both the binding of Ca^{2+} to TnC and the interaction between TnC and TnI

(*11-14*). To overcome this, some drugs are designed to interact with TnC and adjust its affinities to Ca^{2+} (*15*, *16*).

The binding of TnC, TnI and TnT in the complex have been studied by numerous approaches including NMR (*17*, *18*), calorimetry (*6*), and fluorescence (*19*, *20*). An X-ray crystallography study on the chicken-skeletal troponin complex (*2*) shows that complex formation utilizes an interaction between the C-terminal region of TnC and the N-terminal region of TnI such that the C-terminal regions of TnI can bind to TnT through a coiled-coil helical interaction (**Figure 4-1**). The detailed conformation changes of each subunit upon the addition of each neighboring subunit, however, are not well understood.

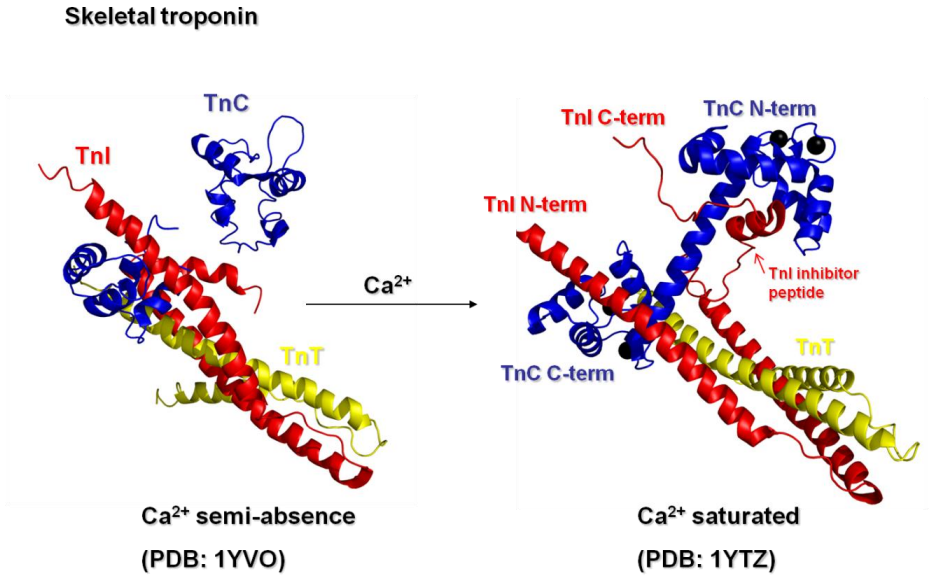

Figure 4-1. X-ray crystal structure of chicken skeletal troponin complex. Blue: troponin C (TnC); Red: troponin I (*1*); Yellow: troponin T (TnT 103-248). The complex with $2Ca^{2+}$ loaded onto TnC is shown on the left (PDB: 1YVO), and the complex with $4Ca^{2+}$ loaded onto TnC is on the right (PDB: 1YTZ)

We recently studied the binding of Ca^{2+} to rabbit skeletal TnC, as shown in the previous chapter, and determined the binding affinities and binding order by using hydrogen/deuterium exchange (H/DX) coupled with mass spectrometry (*21*). This approach is now widely used to study protein conformation, protein-protein, or protein-ligand interactions (*22-25*). With H/DX, one monitors the changes in H-bonding caused by changes in folding and interactions with ligands and other proteins. Recently, H/DX was applied to study the regulatory function of human cardiac troponin complex and the conformational changes of troponin complex induced by Ca^{2+} binding (*26, 27*).

To understand more completely the role played by individual subunits in the troponin complex formation, we extended our study on the physical properties of rabbit skeletal TnC from that of the protein itself to that of the protein within the troponin complex. By monitoring the changes of the extent of deuterium uptake of TnC with the addition of TnI and TnT, we probed changes in H-bonding caused by changes in solvent accessibility of TnC in the complex. We then examined the binding affinities between TnC and TnI in the absence or presence of TnT by PLIMSTEX (protein-ligand interaction by mass spectrometry, titration, and H/D exchange) (*28, 29*) to determine whether TnT influences the TnC-TnI interaction. Finally, by conducting enzymatic digestion and comparing the deuterium uptake of peptide regions from each subunit with

the addition of neighboring subunits, we verified the interface locations for each interaction site to assess whether H/DX can determine whether the troponin complex is stabilized by binding to TnT.

This H/DX study of the skeletal troponin complex is also motivated by our general goal to develop and implement mass-spectrometry-based methods to determine biophysical properties of proteins alone and in more complex settings such as in protein complexes.

4.3 EXPERIMENTAL

4.3.1 Materials

Rabbit skeletal Troponin C (TnC), troponin I (*1*), troponin T (TnT) were purchased from Ocean Biologics Inc (Seattle, WA). Porcine pepsin, citric acid, sodium citrate, sodium chloride, ethanolamine, potassium chloride, calcium chloride, EGTA tetrasodium salt [ethylene-bis(oxyethylenenitrilo)tetraacetic acid tetrasodium], and HEPES hemisodium salt [*N*-(2-hydroxyethyl)piperazine-*N*′-(2-ethanesulfonic acid) hemisodium salt] were purchased from Sigma-Aldrich (St.Louis, MO). Deuterium oxide was purchased from Cambridge Isotope Laboratories Inc (Andover, MA). The synthetic TnI inhibitor peptide RGKFKRPPLRR was purchased from Genscript (Piscataway, NJ).

4.3.2 Troponin complex preparation

TnC, TnI, and TnT were dialyzed against HEPES buffer (10 mM HEPES, 150 mM KCl, pH 7.4) for 2 h at 4 °C using Slide-A-Lyzer Dialysis Cassettes 7000 MWCO (Pierce, CA) followed by exchange with fresh buffer and overnight dialysis. The concentration of the final protein solution was measured by the BCA protein assay following the manufacturer's protocol (Thermo Fisher, Rockford, IL). The protein solution was aliquoted and stored at -80 °C.

The TnC alone was prepared in the presence of 1 mM $CaCl_2$ or 3 mM EGTA in HEPES buffer (10 mM HEPES, 150 mM KCl, pH 7.4) to generate Ca^{2+} absent or saturated form of TnC. To generate troponin complexes with different compositions of subunits, TnC, TnI, or TnT was mixed separately in 1:1 ratio in the presence of 1 mM $CaCl_2$ in HEPES buffer and equilibrated at 25 °C for at least 1 h. All samples were prepared in 20 μM protein concentration.

4.3.3 H/D exchange (H/DX) protocol

For global protein HDX measurement, 40 pmol of protein sample was diluted tenfold in D_2O buffer (10 mM HEPES, 150 mM KCl) at 25 °C. At various times, the exchange was quenched by adding sufficient 1 M HCl at 0 °C to give a final pH of 2.5. The quenched protein solution was then loaded onto a C8 guard column (1 mm x 15 mm, Optimize Technologies, Oregon, City, OR) via an Agilent 1100 HPLC (Santa Clara, CA)

operated at 50 μM/min flow rate with 0.1% TFA for 3 min. The protein was eluted by using a gradient from 5% to 50% solvent B in 0.3 min, 50% to 100% solvent B in 5.2 min and isocratic flow at 100% solvent B for 0.5 min, then back to 5% solvent B in 0.1 min at 50 μM/min flow rate. All LC connection lines were immersed in a water-ice (0 °C) bath. (Waters nanoAcquity UPLC, Manchester, U.K; solvent A, water containing 0.1% formic acid; solvent B, acetonitrile containing 0.1% formic acid).

For peptide-level H/DX measurement, 80 pmole of protein sample was diluted tenfold in D_2O buffer (10 mM HEPES, 150 mM KCl) at 25 °C for 30 min and quenched by adding 1 M HCl. The quenched sample was injected into an on-line pepsin-digestion device, immersed in a water-ice (0 °C) bath, containing immobilized pepsin in a 1 mm × 2 cm guard column (Upchurch Scientific, WA) (*30*) via an Agilent 1100 HPLC (Santa Clara, CA) operated at 50 μM/min flow rate with 0.1% TFA for 3 min. The digested protein solution was trapped on a C18 guard column (1 mm x 1.5 cm, Optimize Technologies, Oregon City, OR) and separated by a C18 analytical column (1 mm x 5 cm, Dionex, Bannockburn, IL) via an Agilent 1200 HPLC (Santa Clara, CA) with a gradient operated under 50 μM/min flow rate. The gradient settings were: 5% to 15% solvent B in 0.3 min, 15% to 50% solvent B in 5.2 min, 50% to 100% solvent B in 0.5 min, and isocratic flow at 100% solvent B for 1.5 min, then back to 5% solvent B in 0.1 min.

Solvent A was water containing 0.1% formic acid, and solvent B was 80% acetonitrile in water containing 0.1% formic acid.

4.3.4 LC-ESI/MS analysis with a Q-TOF mass spectrometer

Global protein H/DX results were acquired on a Waters (Micromass) (Manchester, U.K.) Q-TOF Ultima spectrometer equipped with a Z-spray ESI source. The instrument settings were: capillary voltage, 3.2 kV; cone voltage, 80 V; source and desolvation temperatures, 80 °C and 180 °C; the cone and desolvation gas flow rates were 40 and 400 L/h. The MS profile used for quadrupole transmission was to scan from *m*/*z* 300, dwell for 5% of the scan time, ramp to *m*/*z* 1000 for 45% of the scan time, and then dwell at *m*/*z* 1000 for 50% of the scan time.

Peptide-level H/DX results were acquired on a MaXis (Bruker) (Bremen, Germany) Q-TOF spectrometer. The instrument settings were: capillary voltage, 3.8 kV; nebulizer gas, 0.8 Bar; drying gas flow rate and temperature, 5.0 L/min and 200 °C.

4.3.5 LC-ESI/MS/MS analysis of protein digests

To confirm the peptide sequences for peptic peptides of TnC, TnI and TnT, three protein solutions were subjected to on-line pepsin-digestion separately as described previously (*31*) and analyzed on a Thermo LTQ XL ETD Orbitrap (Thermo Fisher, San Jose, CA). The instrument settings were: spray voltage, 3.5 kV; sheath gas flow rate, 8

(arbitrary units); capillary temperature, 275 °C; capillary voltage, 35 V; and tube lens, 110 V. One full mass spectral acquisition triggered six MS/MS scans (precursor ion activation with CID). The peaks in the product-ion spectra (MS/MS) were centroided for each peptide during the acquisition.

4.3.6 Mascot database search

Thermo RAW files were processed by using extract_msn (2007 version 4.0, Thermo Fisher, San Jose, CA) with a grouping tolerance of 0.8 Da, an intermediate scan setting of 1, and a minimum of 1 scan per group. The NCBI non-redundant database (version 20110722, restricted to mammals) was searched by using MASCOT 2.2.06 (Matrix Science, Oxford, U.K.) with the following settings: enzyme, none; MS tolerance, 10 ppm; MS/MS tolerance, 0.8 Da; maximum number of missed cleavages, 3; peptide charge of 1+, 2+ and 3+; variable oxidation of methionine.

4.3.7 Data analysis

The uptake of deuterium was determined by the mass-to-charge differences between the centroid of the isotopic distribution of the deuterated peptide and the undeuterated peptide, or the average mass differences between the masses of the deuterated protein and the undeuterated protein. No correction for back exchange was applied because the time between sample quench and the measurement with the mass

spectrometer was less than 6 min, and all data were treated consistently. For global protein analysis, MaxEnt1 algorithm (MassLynX version 4.0) was used to generate decharged spectra. The parameter settings were: resolution, 1.00 Da/channel; uniform Gaussian width at half height, 1.00 Da; minimum intensity ratios, 33% for left peaks and right peaks. For peptide analysis, the centroid of the peptide isotopic distribution was analyzed using HDExaminer 1.0 (Sierra Analytics, Modesto, CA).

4.3.8 Kinetic modeling

The global protein kinetic data were fitted with a fixed-rate-constant binning model by using MathCAD (Math-Soft. Inc. Cambridge, MA) as described previously (*29, 32*). Briefly, all exchangeable H's were separated into four fixed rate-constant bins (k = 10, 1, 0.1, 0.01 min^{-1}), and the root-mean-square (RMS) was minimized during the fitting process. Three trials were fit separately, and the results were averaged and reported with standard deviations.

4.3.9 PLIMSTEX titration

To obtain the binding affinity between TnC and TnI and to examine whether TnT could affect the interaction between them, the TnC alone and TnC-TnT (1:1) complex were first incubated at 20 μM protein concentration in HEPES buffer (10 mM HEPES, 150 mM KCl) in the presence of 1 mM $CaCl_2$ for 1 h at 25 °C. The two complex samples

were than incubated with various TnI concentrations (from 8 μM to 300 μM) for 1 h at 25 °C in the same buffer system. The H/DX experiment was then started, as described in previous section. The H/DX time was 30 min, chosen because the extent of H/DX had become relatively constant at that time, and small errors in sampling time would have minimal impact on the titration accuracy. The method for fitting the titration curve was described previously (*29, 32*). A 1:1 protein-ligand binding system was used invoking three fit parameters: K_{a1}, D_0, ΔD_1; where K_{a1} is the binding constant; D_0 is the deuterium uptake of protein in the absence of ligands (apo form); and ΔD_1 is the difference between the average of deuterium uptake of the complex in the presence of ligand and that of the apo form. The parameters were optimized in the searching process to minimize the root mean square (RMS) of all inputs. MathCAD (Math-Soft. Inc. Cambridge, MA) was used in this fitting process. Three trials of experiments were fitted separately, and the results were averaged and reported with standard deviations.

4.4 RESULTS AND DISCUSSION

4.4.1 H/DX kinetics of TnC within the Tn complex

Troponin C (TnC) acts as a calcium sensor in the troponin complex. Two Ca^{2+} binding sites (EFIII and EFIV) with high binding affinities (~$10^7 M^{-1}$), located at the C-terminal domain, are often saturated with Ca^{2+} and stabilize the three-part complex. The

other two binding sites, located at the N-terminal domain, have lower Ca^{2+}binding affinities (~10^6 M^{-1}) (*3, 21*). Once the four sites are saturated with Ca^{2+}, a "hydrophobic pocket" forms near the N-terminal region of TnC, providing the location for interaction with the "inhibitor region" of TnI to initiate muscle contraction.

The solvent accessibility and the hydrogen bonding of TnC are affected significantly by interacting with Ca^{2+} as revealed by our earlier H/DX study (*21*). Most of the changes occur at the four Ca^{2+} binding regions (EF-hands). The additional presence of TnI and TnT are likely to have significant influence on the physical properties of TnC and its dynamics in solution. Marshall and coworkers (*27*) studied the conformational changes of cardiac TnC (cTnC), cTnI and cTnT in the binary (cTnC-cTnI) and ternary complexes (cTnC-cTnI-cTnT) in the presence and absence of Ca^{2+} by using H/DX FTICR MS. They concluded that the amide exchange rates of C-terminal regions of cTnC are largely affected by the interaction with cTnI and cTnT and that the N-terminal regions of cTnC are mainly affected by cTnI. Although skeletal troponin is structurally similar to cardiac troponin, the binding properties between each subunit might be different.

To address how TnI and TnT affect the dynamics and conformation of TnC, we designed a different H/DX kinetics experiment to study global TnC in the presence or absence of TnI and TnT (**Figure 4-2**). We added excess amounts of Ca^{2+} in the solution

(1 mM) to stabilize the binary (TnC-TnI; TnC-TnT) and the ternary (TnC-TnI-TnT) complexes. The ratio for each subunit in solution was 1:1 and the complexes were equilibrated for 1 h at 25 °C before initiating the H/DX.

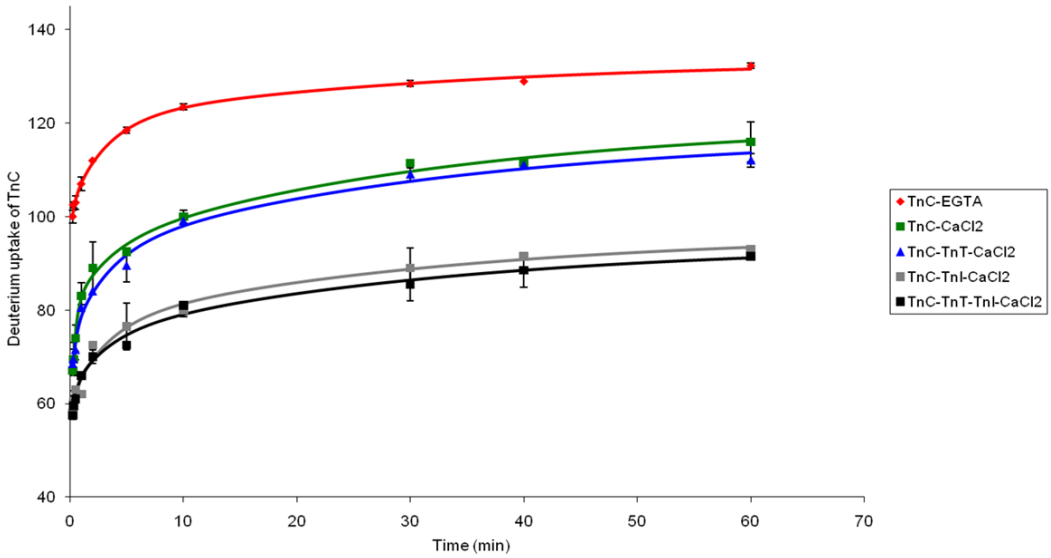

Figure 4-2. Kinetics of H/D exchange for rabbit skeletal TnC. Apo-TnC in 3 mM EGTA (diamonds, red) shows the most extensive D uptake. Ca^{2+} loaded TnC (squares, green) and Ca^{2+} loaded TnC-TnT complexs (squares, blue) show similar D uptake. Ca^{2+} loaded TnC-TnI complex (squares, gray) and Ca^{2+} loaded TnC-TnI-TnT complex (squares, black) show further decrease of D uptake. The fitted curves are shown as solid lines.

It is obvious that the presence of Ca^{2+} (green line) affects the conformation of TnC significantly, as is well known and consistent with the H/DX results reported in the previous chapter (*21*). Interestingly, the addition of TnT to TnC has minor impact on the hydrogen bonding of TnC (blue line); only approximately five amide hydrogens on TnC

are affected when TnT binds. Thus, the binding of TnT affects in a minor way the solvent accessibility of TnC, indicating that the interaction between these two subunits is either weak or highly localized. The addition of TnI to TnC further increases H-bonding, decreasing the solvent accessibility of TnC (gray line; ~20 D lower than the D uptake of TnC alone). The decrease shows that the N-terminal regions of TnC can interact with the inhibitor region of TnI in the presence of Ca^{2+}. Again underscoring the minor effects of TnT, we find its addition to the TnC-TnI binary complex (black line) produces only minor effects on TnC.

To probe more deeply how TnI and TnT binding in the complex affects the exchange kinetics, we fit the kinetic curve with four exchange rate-constant bins (k = 10, 1, 0.1, 0.01 min^{-1}) (**Table 4-1**). The results are consistent with those reported previously (*21*). Ca^{2+} binding affects 48 fast-exchanging amides of TnC; TnC in the absence of Ca^{2+} exchanges 96 ± 1 amides with a rate constant of 10 min^{-1}, whereas when loaded with Ca^{2+}, 48 ± 2 amides exchange with the same rate constant. Although the overall kinetics is affected by the addition of TnI and TnT, there is no significant effect on the number of fast-exchanging amides. There are slower exchanging amides (k = 1 min^{-1}) that are affected upon TnT binding. Ca^{2+}-loaded TnC has 32 amides whereas TnC in the Ca^{2+}-loaded TnC-TnT complex has 24 amides that exchange with

this rate constant. The addition of TnI further affects the number of amides that exchange with this rate constant: 8 TnC amides in the Ca^{2+}-loaded TnC-TnI complex exchange with a rate constant of 1 min^{-1}, whereas 12 TnC amides in the ternary complex (TnC-TnI-TnT) that exchange with this rate constant. The effect of TnI binding on TnC is principally to slow down the exchange of amides in the k = 1 min^{-1} rate constant regime, whereas there is little effect on exchange for TnT binding.

pKinetic Fit	**# of H's per fixed-rate bin**				**Total**
***k* (min^{-1})**	**10**	**1**	**0.1**	**0.01**	
TnC-EGTA	**96 ± 1**	**7 ± 1**	**19 ± 1**	**13 ± 1**	**135**
TnC-$CaCl_2$	**48 ± 2**	**32 ± 6**	**14 ± 2**	**28 ± 4**	**122**
TnC-TnT-$CaCl_2$	**49 ± 1**	**24 ± 1**	**18 ± 2**	**26 ± 4**	**117**
TnC-TnI-$CaCl_2$	**54 ± 1**	**8 ± 1**	**16 ± 1**	**20 ± 3**	**98**
TnC-TnT-TnI-$CaCl_2$	**50 ± 4**	**12 ± 6**	**13 ± 2**	**20 ± 2**	**95**

Table 4-1. The numbers of exchangeable amide hydrogens of five TnC complexes with respect to four fixed exchange rate constants.

Binding with TnI, on the other hand, reduces further the number of amides exchanging at k = 1 min^{-1}, producing more hydrogen bonds and presumably reducing solvent accessibility for a portion of TnC. There are no significant differences for amides

of TnC that exchange with smaller rate constants (k = 0.1 and 0.01 min^{-1}) as a function of binding to TnI or TnT. Thus, TnC binding to Ca^{2+} reduces significantly the number of fast exchanging amides, and TnI binding reduces further the number of amides exchanging with k = 1 min^{-1}. The affected amides apparently shift to a very slow exchange regime where k < 0.01 min^{-1}. We find little effect for the binding of TnT.

4.4.2 PLIMSTEX study of TnI binding of TnC and TnC-TnT complex

TnC-TnI interaction is known to be the key factor in muscle contraction (*2, 3, 33*). Swenson and coworkers (*19, 20*) studied the affinities between skeletal TnC and TnI in the presence of different metal cations (Ca^{2+} and Mg^{2+}) by inserting specific fluoros-probes and measured the changes of fluorescence. Given that our global H/DX measurement on TnC shows significant decrease of deuterium uptake in the presence of TnI, it is of interest to investigate the TnC-TnI interactions by applying PLIMSTEX (*28, 29*).

To do this, we titrated TnC, at a concentration of 20 μM, with TnI at concentration ranging from 8 to 300 μM (**Figure 4-3, blue curve**) in the presence of 1 mM $CaCl_2$. H/DX was initiated by twenty-fold dilution of the mixtures into D_2O buffer as described in the experimental section. We further examined the influence of TnT on

the TnC-TnI interaction by first making the TnC-TnT complex in 1:1 ratio, as described in the experimental section, and titrated with TnI (**Figure 4-3, pink curve**).

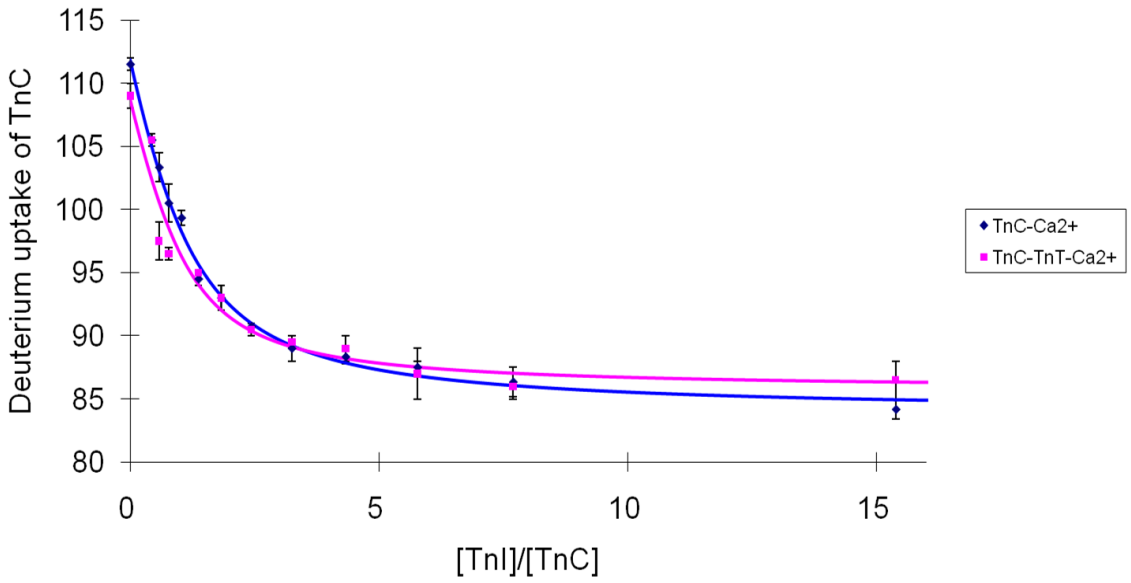

Figure 4-3. PLIMSTEX curve of Ca^{2+}-loaded TnC (blue) and Ca^{2+}-loaded TnC-TnT complex (*34*) titrated with TnI. The concentration of the protein for the titration was 1 μM.

Ka Values	(TnC+Ca^{2+})-TnI	(TnC+Ca^{2+})-TnI inhibitor peptide	(TnC+TnT+Ca^{2+})-TnI
Ka_1	(1.9 ± 0.4) x 10^6 M^{-1}	N/A (no D-uptake differences)	(2.4 ± 0.2) x 10^6 M^{-1}
Literature Ka	1.1 x 10^9 M^{-1}	(5.3 ± 1.1) x 10^5 M^{-1}	N/A
ΔD_1	28 ± 1	N/A	23 ± 1
D_0	112 ± 1	N/A	109 ± 1
RMS	0.945	N/A	0.956

Table 4-2. TnC-TnI affinities obtained by PLIMSTEX strategy. The fitting process utilizes 1:1 binding model and three search parameters (K_{a1}, D_0, ΔD_1).

Given that the two curves are similar, we conclude that the presence of TnT has minor impact on the TnC-TnI interaction. To have a quantitative understanding on the

strength of the interactions, we fitted the curves to obtain affinities by using 1:1 binding model in MathCAD, in which three variants were optimized in the searching process (K_{a1}, D_0, ΔD_1) (**Table 4-2**). The fitted results of ΔD_1 are 28 for the TnC-TnI interaction and 23 for (TnC + TnT)-TnI interaction, which are in good agreement to the experimental results of 27 and 23, respectively. The values of D_0, which are 112 for TnC-TnI interaction and 109 for (TnC+TnT)-TnI interaction also agree with the experimental results of 111 and 110, respectively. Fitting the titration curves also afford the affinities (K_{a1}). They are (1.9 ± 0.4) x 10^6 M^{-1} for the interaction of Ca^{2+}-loaded TnC interacting with TnI, and (2.4 ± 0.2) x 10^6 M^{-1} for Ca^{2+}-loaded TnC-TnT complex interacting with TnI. When compared to the Swenson fluorescence results (*19, 20*) for the affinity of Ca^{2+}-loaded TnC interacting with 5-(iodoacetamido)-eosin (IAE) labeled TnI (1.7 x 10^9 M^{-1}), our affinity values are three magnitudes smaller. Given that they titrated TnI with TnC at 25 nM TnI concentration under similar buffer condition (10 mM Pipes, 0.3 M KCl, 0.01% NaN_3, 1 mM $CaCl_2$, pH 7.0) to ours but having the presence of 0.5 mM dithiothreitol (DTT) or 2-mercaptoethanol (β-ME) and at lower temperature (0 ºC), these differences may change the stability of the TnC-TnI complex and cause the discrepancy between our results. The use of reducing agents (DTT and β-ME), for example, reduces three cysteine residues (Cys-48, 64, and 133) of TnI and one cysteine of TnC (Cys-98),

making them feasible for fluoros-probes labeling. This cysteine reduction, however, may affect the physical properties of TnC-TnI complex from stability and conformational point of views.

Swenson also measured the affinity of Ca^{2+}-loaded TnC interacting, with a TnI inhibitor peptide (residues 104-115, RGKFKRPPLRR) in addition to full-length TnI, and they obtained a value of $(6 \pm 1) \times 10^5\ M^{-1}$. Our H/DX results on the TnC-TnI inhibitor peptide at a TnC concentration of 20 μM, and peptide-to-TnC ratio of 5:1, however, show no uptake differences between apo TnC and holo TnC (TnI inhibitor peptide loaded) (**Figure 4-4**). This suggests that the interaction between TnC and TnI inhibitor peptide 104-115 is weak and that the presence of full length TnI is essential for the interaction. In any event, our PLIMSTEX results show that TnT has no significant impact on the TnC-TnI interaction, in agreement with our H/DX kinetics measurements.

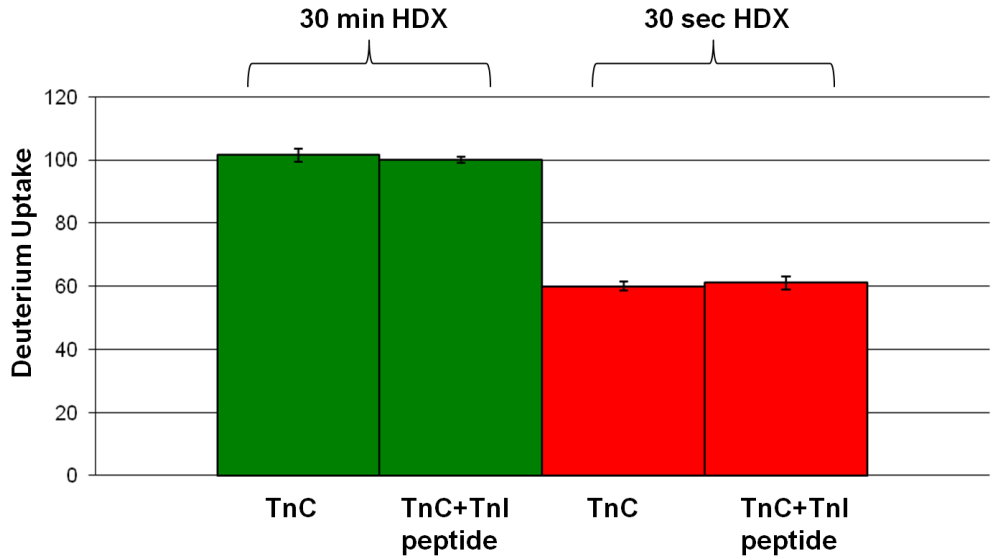

Figure 4-4. D uptake of TnC with or without the presence of TnI inhibitor peptide (residues 104-115, RGKFKRPPLRR). The ratio of peptide to TnC is 5:1. The extent of D uptake at 30 s exchange time (*19*) and 30 min exchange time (green) show no detectable differences between the apo and holo states.

4.4.3 H/DX reveals structural changes of TnC, TnI and TnT within the complex

To expand the global studies of TnC-TnI, TnC-TnT, and TnC-TnI-TnT interactions, we followed the conformational changes of each subunit in the presence of additional subunits with site specificity by conducting pepsin digestion and examining the H/DX of the released peptides. Eight different protein mixtures were prepared: TnC-EGTA; Ca^{2+} loaded TnC; TnI alone; TnT alone; TnI-TnT; Ca^{2+} loaded TnC-TnI; Ca^{2+} loaded TnC-TnT; and Ca^{2+} loaded TnC-TnI-TnT. Each subunit was mixed with 1:1 ratio at 20 μM protein concentration and equilibrated for 1 h at 25 °C before conducting the

H/DX for 30 min and then digesting with pepsin. The extent of D uptake on each subunit was analyzed separately and plotted as a function of peptide regions from N to C-terminal domain (**Figure 4-5**).

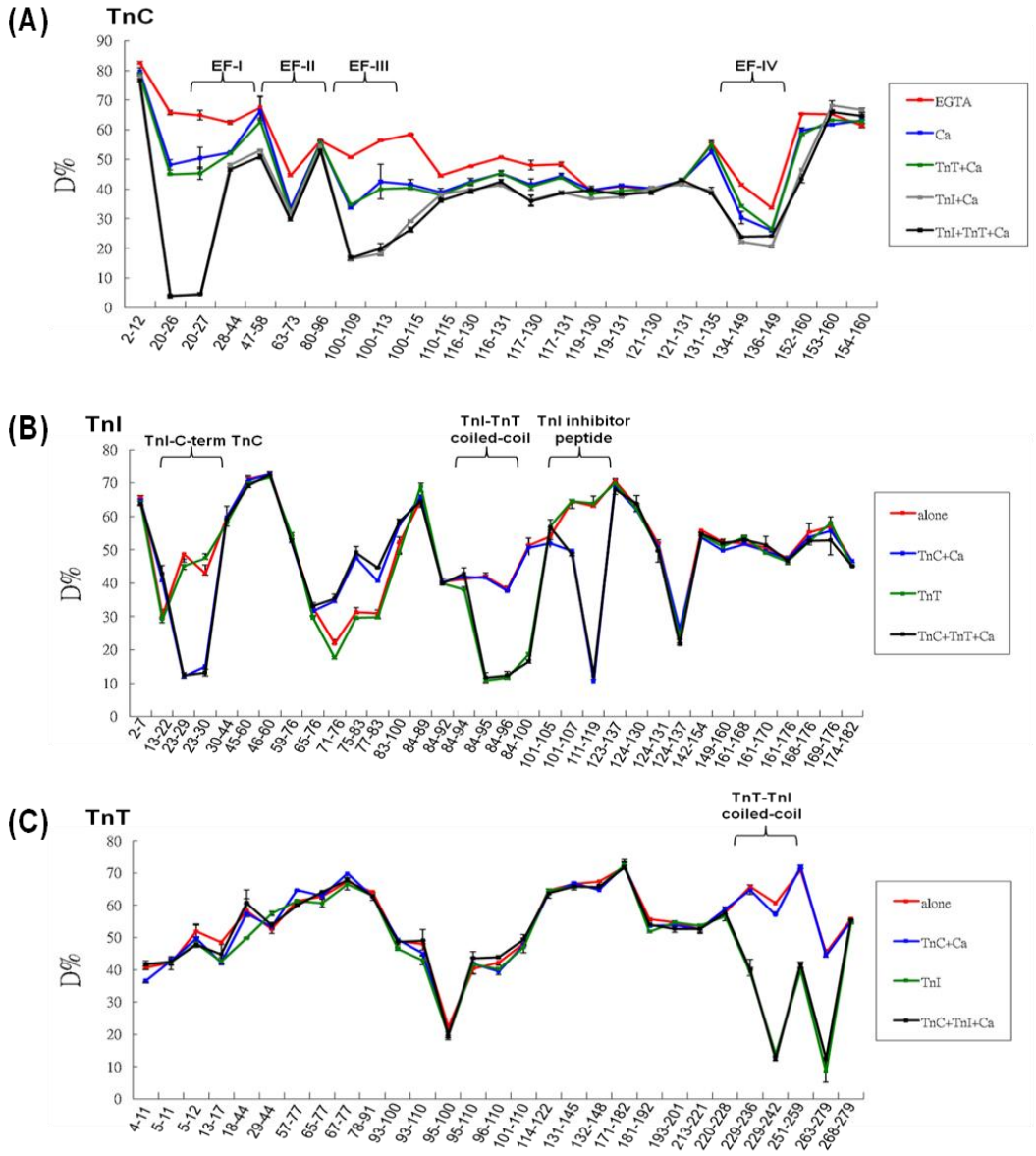

Figure 4-5. Peptide level D uptake diagrams. Each diagram shows the relative D uptake (%) with respect to peptide sequence from N-terminal to C-terminal (Left to right). (A) Peptide level D uptake of TnC, (B) peptide level D uptake of TnI, (C) peptide level D uptake of TnT. The deuterium exchange time was 30 min.

For TnC, it is obvious that the addition of Ca^{2+} alters the H-bonding and solvent accessibility of the four EF hands (**Figure 4-5A, blue curve**). In the presence of TnI, regions comprising EFI and EFIII show significant increases in protection (**Figure 4-5A, gray and black curves**). These D uptake differences indicate that the interface between TnC and TnI involves these EF hands. Swenson and coworkers (*19*) also studied the interactions of TnI to TnC fragments, and they concluded that TnI interacts to both N and C-terminal domain of TnC. Our results provide a more detailed picture of their interaction. The addition of TnT to make a three-part complex, however, doesn't have structural impact on the TnC exchange, which agrees well with our global measurement (**Figure 4-5A, green curve**).

For TnI, the binding with TnC imparts major protection to two regions of TnI, the N-terminal region (23-30) and the C-terminal region (101-119). The latter is known to be the inhibitor region (**Figure 4-5B, blue and black curves**). Interestingly, two regions, the N-terminal region (13-22) and the middle regions of TnI (71-83), show more D uptake or more solvent exposure in the presence of TnC. This structural protrusion of TnI could be an outcome of the TnC-TnI interactions located at the N and C-terminal domains. The presence of TnT only imparts protection on residues 84-100 of TnI (**Figure 4-5B, green**

and black curves). These results are consistent with the view that this region is the TnI-TnT coiled-coil interface (*2*).

For TnT, the presence of TnC has only minor effects in the extent of H/DX, further confirming that there are no significant interactions between TnC and TnT. The addition of TnI to TnC and TnT, however, shows a significant decrease of in H/DX extent in the region 229-268 of TnT (**Figure 4-5C, green and black curves**). This region is also known to be the TnI-TnT coiled-coil interface.

To afford a structural view of the conformational changes of each subunit in the various complexes, we mapped our peptide level H/DX results onto the X-ray crystal structure of chicken skeletal troponin (PDB: 1YTZ) (*2*) (**Figure 4-6**). Given that the sequence homology of skeletal troponin between rabbit and chicken is high (>82%), we mapped our H/DX results in regions where there is amino-acid sequence identity. The interfaces between each subunit, as determined by H/DX, agree well with the crystal structure (**Figure 4-6, regions shown in gray or black**). Moreover, our studies show that regions 13-22 and 71-83 of TnI protrude more when bound to TnC.

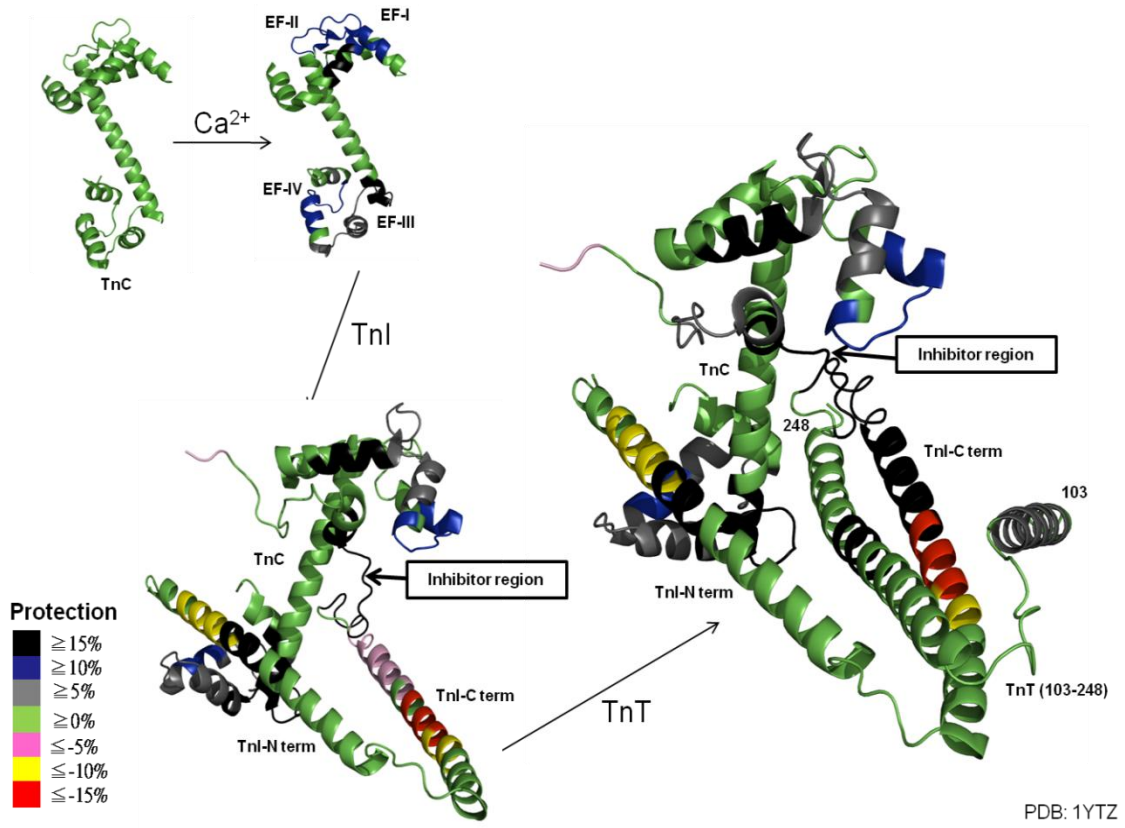

Figure 4-6. A map of the peptide-level H/DX onto X-ray crystal structure of chicken skeletal troponin complex (PDB: 1YTZ). Different colors represent different extents of H/DX or protection—see figure legend. "Protection" was defined as the relative D uptake differences (%) between two states. A decrease of relative D uptake was defined as positive protection.

4.5 CONCLUSIONS

Improving our knowledge of TnC-TnI-TnT interactions is important in understanding the detailed mechanism of muscle contraction. We began our study, as shown in the previous chapter, of the skeletal TnC-Ca^{2+} interactions and the binding orders of Ca^{2+} to TnC by conducting H/DX-MS and PLIMSTEX (*21*). We then extended our H/DX study to the dynamics of skeletal TnC within the whole complex and their interactions for two reasons: to improve our understanding of the TnC-TnI-TnT interactions and to test further the ability of H/DX and PLIMSTEX to provide insight into protein complexes. Although H/DX is now established as a structural tool for protein dynamics, protein-ligand, protein-protein interactions (*24*), its applications to complexes are limited. Here is an area where NMR and X-ray crystallography may not succeed. Unlike other covalent labeling strategies, H/DX can "mark" all amide hydrogens except proline and reveal changes of H-bonding at the peptide level, many of which are related to solvent accessibility-associated, even for proteins in complexes. The potential of H/DX has been successfully applied to study the biophysical properties of the whole cardiac troponin complex (*26*) and that of the individual subunit in the skeletal troponin complex, as shown here.

By utilizing H/DX on the rabbit skeletal troponin complex, we conclude that TnC is largely affected by TnI but not by TnT within the complex. We further examined the TnC-TnI binding affinities with or without the presence of TnT. Our results show that the affinities are in the range of 10^6 M^{-1}, which, when compared to previous fluorescence measurements (*19, 20*), show a discrepancy of three orders of magnitude. This difference may be an outcome of the different stability of protein complex in different environments. The minor influence of TnT on the TnC-TnI interaction, however, agrees with our global H/DX measurements and with previous X-ray crystallography.

By the addition of enzymatic digestion in the H/DX work flow, we can refine the spatial resolution to the peptide level and reveal the interfaces between each subunit. This provides more detailed information on the conformational changes of each subunit within the complex in a systematic way. This high-resolution information is difficult to achieve by X-ray crystallography.

4.6 ACKNOWLEDGMENTS

This project was supported by grants from the National Center for Research Resources (5P41RR000954-35) and the National Institute of General Medical Sciences (8 P41 GM103422-35) from the National Institutes of Health to MLG. Brady Summers was supported by the Amgen Scholars Summer Program at Washington University.

4.7 REFERENCES

1. Li, Y., Mui, S., Brown, J. H., Strand, J., Reshetnikova, L., Tobacman, L. S., and Cohen, C. (2002) The crystal structure of the C-terminal fragment of striated-muscle α-tropomyosin reveals a key troponin T recognition site, *Proceedings of the National Academy of Sciences of the United States of America 99*, 7378-7383.

2. Vinogradova, M. V., Stone, D. B., Malanina, G. G., Karatzaferi, C., Cooke, R., Mendelson, R. A., and Fletterick, R. J. (2005) Ca2+-regulated structural changes in troponin, *Proceedings of the National Academy of Sciences of the United States of America 102*, 5038-5043.

3. Filatov , A. G. K., T. V. Bulargina, N. B. Gusev. (1999) Troponin: Structure, Properties, and Mechanism of Functioning, *Biochemistry (Moscow) 64*, 1155-1164.

4. Sun, Y.-B., Brandmeier, B., and Irving, M. (2006) Structural changes in troponin in response to Ca2+ and myosin binding to thin filaments during activation of skeletal muscle, *Proceedings of the National Academy of Sciences 103*, 17771-17776.

5. Zot, A. S., and Potter, J. D. (1987) Structural Aspects of Troponin-Tropomyosin Regulation of Skeletal Muscle Contraction, *Annual Review of Biophysics and Biophysical Chemistry 16*, 535-559.

6. Mukhopadhyay, S., Langsetmo, K., Stafford, W. F., Henry, G. D., Baleja, J. D., and Sarkar, S. (2005) Identification of a Region of Fast Skeletal Troponin T Required for Stabilization of the Coiled-coil Formation with Troponin I, *Journal of Biological Chemistry 280*, 538-547.

7. Potter, J. D., and Gergely, J. (1975) The calcium and magnesium binding sites on troponin and their role in the regulation of myofibrillar adenosine triphosphatase, *J. Biol. Chem. 250*, 4628-4633.

8. Davis, J. P., and Tikunova, S. B. (2008) Ca2+ exchange with troponin C and cardiac muscle dynamics, *Cardiovasc Res 77*, 619-626.

9. Calvert, M. J., Ward, D. G., Trayer, H. R., and Trayer, I. P. (2000) The Importance of the Carboxyl-terminal Domain of Cardiac Troponin C in Ca2+-sensitive Muscle Regulation, *J. Biol. Chem. 275*, 32508-32515.

10. Wang, Z., Gergely, J., and Tao, T. (1992) Characterization of the Ca(2+)-triggered conformational transition in troponin C, *Proceedings of the National Academy of Sciences of the United States of America 89*, 11814-11817.

11. Chandra, M., Dong, W.-J., Pan, B.-S., Cheung, H. C., and Solaro, R. J. (1997) Effects of Protein Kinase A Phosphorylation on Signaling between Cardiac Troponin I and the N-Terminal Domain of Cardiac Troponin C, *Biochemistry 36*, 13305-13311.

12. Finley, N. L., and Rosevear, P. R. (2004) Introduction of Negative Charge Mimicking Protein Kinase C Phosphorylation of Cardiac Troponin I: EFFECTS ON CARDIAC TROPONIN C, *J. Biol. Chem. 279*, 54833-54840.

13. Li, M. X., Wang, X., Lindhout, D. A., Buscemi, N., Van Eyk, J. E., and Sykes, B. D. (2003) Phosphorylation and Mutation of Human Cardiac Troponin I Deferentially Destabilize the Interaction of the Functional Regions of Troponin I with Troponin C, *Biochemistry 42*, 14460-14468.

14. McDonough, J. L., and Van Eyk, J. E. (2004) Developing the next generation of cardiac markers: Disease-induced modifications of troponin I, *Progress in Cardiovascular Diseases 47*, 207-216.

15. Baryshnikova, O. K., Li, M. X., and Sykes, B. D. (2008) Defining the Binding Site of Levosimendan and Its Analogues in a Regulatory Cardiac Troponin C-Troponin I Complex, *Biochemistry 47*, 7485-7495.

16. Li, M. X., Robertson, I. M., and Sykes, B. D. (2008) Interaction of cardiac troponin with cardiotonic drugs: A structural perspective, *Biochemical and Biophysical Research Communications 369*, 88-99.

17. Li, M. X., and Sykes, B. D. (2000) Role of the Structural Domain of Troponin C in Muscle Regulation: NMR Studies of Ca2+ Binding and Subsequent Interactions with Regions 1-40 and 96-115 of Troponin I, *Biochemistry 39*, 2902-2911.

18. Spyracopoulos, L., and Sykes, B. D. (2001) Structure, Dynamics, and Thermodynamics of the Structural Domain of Troponin C in Complex with the Regulatory Peptide 1-40 of Troponin I, *Biochemistry 40*, 10063-10077.

19. Swenson, C. A., and Fredricksen, R. S. (1992) Interaction of troponin C and troponin C fragments with troponin I and the troponin I inhibitory peptide, *Biochemistry 31*, 3420-3429.

20. Ingraham, R. H., and Swenson, C. A. (1984) Binary interactions of troponin subunits, *Journal of Biological Chemistry 259*, 9544-9548.

21. Huang, R. Y. C., Rempel, D. L., and Gross, M. L. (2011) HD Exchange and PLIMSTEX Determine the Affinities and Order of Binding of Ca2+ with Troponin C, *Biochemistry 50*, 5426-5435.

22. Zhang, Z., and Smith, D. L. (1993) Determination of amide hydrogen exchange by mass spectrometry: A new tool for protein structure elucidation, *Protein Science 2*, 522-531.

23. Englander, S. (2006) Hydrogen exchange and mass spectrometry: A historical perspective, *J. Am. Soc. Mass Spectrom. 17*, 1481-1489.

24. Engen, J. R. (2009) Analysis of Protein Conformation and Dynamics by Hydrogen/Deuterium Exchange MS, *Anal. Chem. 81*, 7870-7875.

25. Chalmers, M. J., Busby, S. A., Pascal, B. D., West, G. M., and Griffin, P. R. (2011) Differential hydrogen/deuterium exchange mass spectrometry analysis of protein-ligand interactions, *Expert Review of Proteomics 8*, 43-59.

26. Kowlessur, D., and Tobacman, L. S. (2010) Troponin Regulatory Function and Dynamics Revealed by H/D Exchange-Mass Spectrometry, *Journal of Biological Chemistry 285*, 2686-2694.

27. Bou-Assaf, G. M., Chamoun, J. E., Emmett, M. R., Fajer, P. G., and Marshall, A. G. (2011) Complexation and calcium-induced conformational changes in the cardiac troponin complex monitored by hydrogen/deuterium exchange and FT-ICR mass spectrometry, *International Journal of Mass Spectrometry 302*, 116-124.

28. Zhu, M. M., Rempel, D. L., Du, Z., and Gross, M. L. (2003) Quantification of Protein-Ligand Interactions by Mass Spectrometry, Titration, and H/D Exchange: PLIMSTEX, *J. Am. Chem. Soc. 125*, 5252-5253.

29. Zhu, M. M., Chitta, R., and Gross, M. L. (2005) PLIMSTEX: a novel mass spectrometric method for the quantification of protein-ligand interactions in solution, *Int. J. Mass Spectrom. 240*, 213-220.

30. Busby, S. A., Chalmers, M. J., and Griffin, P. R. (2007) Improving digestion efficiency under H/D exchange conditions with activated pepsinogen coupled columns, *International Journal of Mass Spectrometry 259*, 130-139.

31. Huang, R. Y. C., Garai, K., Frieden, C., and Gross, M. L. (2011) Hydrogen/Deuterium Exchange and Electron-Transfer Dissociation Mass Spectrometry Determine the Interface and Dynamics of Apolipoprotein E Oligomerization, *Biochemistry 50*, 9273-9282.

32. Zhu, M. M., Rempel, D. L., and Gross, M. L. (2004) Modeling data from titration, amide H/D exchange, and mass spectrometry to obtain protein-ligand binding constants, *J. Am. Soc. Mass Spectrom. 15*, 388-397.

33. Sykes, B. D. (2003) Pulling the calcium trigger, *Nat Struct Mol Biol 10*, 588-589.

34. Koshman, Y. E., Waters, S. B., Walker, L. A., Los, T., Tombe, P. d., Goldspink, P. H., and Russell, B. (2008) Delivery and visualization of proteins conjugated to quantum dots in cardiac myocytes, *Journal of Molecular and Cellular Cardiology 45*, 853-856.

Chapter 5*

Hydrogen/Deuterium Exchange and Electron-Transfer Dissociation Mass Spectrometry Determine the Interface and Dynamics of Apolipoprotein E Oligomerization

* This chapter is based on recent publication: Reproduced with permission from Huang, R. Y. C., Garai, K., Frieden C., and Gross, M. L. Hydrogen/Deuterium Exchange and Electron-Transfer Dissociation Mass Spectrometry Determine the Interface and Dynamics of Apolipoprotein E Oligomerization. *Biochemistry*, **2011**, 50, 9273-9282.

5.1 ABSTRACT

Apolipoprotein E, a 34 kDa protein, plays a key role in triglyceride and cholesterol metabolism. Of the three common isoforms (ApoE2, 3 and 4), only ApoE4 is a risk factor for Alzheimer's Disease. All three isoforms of wild-type ApoE self-associate to form oligomers, a process that may have functional consequences. Although the C-terminal domain, residues 216-299, of ApoE is believed to mediate self-association, the specific residues involved in this process are not known. Here we report the use of hydrogen/deuterium exchange (H/DX) coupled with enzymatic digestion to identify those regions in the sequence of full-length apoE involved in oligomerization. For this determination, we compared the results of H/DX of the wild-type proteins and those of monomeric forms obtained by modifying four residues in the C-terminal domain. The three wild type and mutant isoforms show similar structures based on their similar H/DX kinetics and extents of exchange. Regions of the C-terminus (residues 230-270) of the ApoE isoforms show significant differences of deuterium uptake between oligomeric and monomeric forms, confirming that oligomerization occurs at these regions. To achieve single amino acid resolution, we examined the extents of H/DX by using electron transfer dissociation (ETD) fragmentation of peptides representing selected regions of both the

monomeric and the oligomeric forms of ApoE4. From these experiments, we could identify the specific residues involved in ApoE oligomerization. In addition, our results verify that ApoE4 is composed of a compact structure at its N-terminal domain. Regions of C-terminal domain, however, appear to lack defined structure.

5.2 INTRODUCTION

Apolipoprotein E (ApoE), a 299-residue, 34 kDa protein, a major lipid transporter in plasma and the central nervous system (*1-3*), is intimately involved in triglyceride and cholesterol metabolism (*2*). There are three major isoforms, ApoE2, ApoE3 and ApoE4, that differ only by single amino acid changes (*3*). ApoE3 has a cysteine at position 112 and an arginine at 158, whereas ApoE2 has cysteines, and ApoE4 has arginines at these two positions. These single amino acid differences cause significant differences in their biochemical and functional properties (*2, 3*). For example, ApoE4 is a major risk factor for Alzheimer's disease and cardiovascular diseases, whereas ApoE2 serves a protective role (*4*).

Lipid-free ApoE consists of a 22 kDa N-terminal domain (1-191), which harbors the LDL receptor binding site, and a 10 kDa C-terminal domain (216-299), which has high affinity for lipids (*5-7*), linked by a protease-sensitive hinge region (*3, 8*). Structures of full length, wild-type ApoE are unknown, although x-ray crystallography of the N-terminal domain shows it is a monomer comprised of a four-helix bundle (*9*). The lack of structure of the wild-type proteins is probably due to a high tendency for them to aggregate at the high concentrations needed for crystallization (*8, 10*) and the likely presence of amphipathic helices in the full length protein (*11, 12*). Recently, however, an

NMR structure of a monomeric mutant of ApoE3 was determined (*13*). Lipid-free ApoE exists predominantly as a tetramer at μM concentrations and dissociates to dimers and monomers at nM concentrations (*1, 2, 10, 14-17*). A form of ApoE3 that remains monomeric at 600 μM can be obtained by making four or five substitutions in the C-terminal region without apparently affecting the overall secondary structure or function (*18*). This monomeric form is a reference point for our study to analyze the structure and oligomerization properties of ApoE isoforms.

We chose hydrogen/deuterium exchange (H/DX) coupled with mass spectrometry (MS) (*19-22*) as a structural tool to measure the relative rates of exchange of amide hydrogens with deuteriums from D_2O and draw conclusions based on the measured *m/z* and their changes, rather than ion abundances. The experimental outcome allows inferences on the stability of the hydrogen bonding, the extent of which is inverse to relative solvent accessibilities. To achieve a high-resolution comparison of the three isoforms of ApoE and their monomeric mutants, we coupled H/DX with enzymatic digestion and analyzed the exchanged peptides.

H/DX with digestion affords spatial resolution at the "peptide level" (i.e., to regions of the protein that are 6-10 amino-acid residues in length (*23*)) Although one can sometimes incorporate multiple enzymatic digestions to generate overlapping peptide

fragments and improve the resolution to one or a few amide sites, we chose gas-phase fragmentation of the deuterated peptides released upon pepsin digestion because it has greater potential to achieve resolution at the amino-acid level. Fragmentation cannot be collisionally induced dissociation (CID) (collision-activated dissociation (CAD)), as indicated in chapter 1, because it causes scrambling of H and D (*24-29*). To overcome this, we fragmented the peptides with electron-transfer dissociation (ETD) (*30*) under experimental conditions that we determined to be sufficiently "gentle" to avoid scrambling.

To insure minimal scrambling, we followed Jørgensen, who established a set of standard peptides as tests (several other methods were also established for the same purpose (*31, 32*)), using a bottom-up H/DX (*23*) to afford resolution at a single-amide site. The latter allowed us to improve the resolution to the single amide level so that we can identify those residues involved in self-association. This approach also affords an opportunity to continue the development of a structural model for the full-length, wild-type ApoE proteins.

5.3 EXPERIMENTAL PROCEDURES

5.3.1 Protein expression

Apolipoprotein E was expressed in *E. coli* and purified as described previously by

Garai et al. (*33*). Briefly, ApoE proteins were expressed in *Escherichia coli* (Strain BL21, DE3 competent cells, Stratagene), which was grown in LB media to OD_{600} = 0.6. Mutations were introduced into the c-DNA of ApoE using the QuikChange site-directed mutagenesis kit (Stratagene). All sequences were verified by using DNA sequencing. In all cases, the monomeric mutants contained the following four substitutions: F257A/W264R/L279Q and V287E.

5.3.2 Materials

Potassium chloride, HEPES hemisodium salt [*N*-(2-hydroxyethyl)piperazine-*N*′-(2-ethanesulfonic acid) hemisodium salt], *tris*(2-carboxyethyl)phosphine hydrochloride (TCEP), porcine pepsin, citric acid, sodium citrate, sodium chloride, and ethanolamine were purchased from Sigma-Aldrich (St.Louis, MO). The synthetic peptide HHHHHHIIKIIK used to test the extent of H/D scrambling was purchased from Genscript (Piscataway, NJ). D_2O was from Cambridge Isotope Laboratories Inc (Andover, MA), and high purity guanidine hydrochloride was from Pierce (Rockford, IL).

5.3.3 Preparation of ApoE stock solution

ApoE, dissolved in 4 M GdnCl, 0.1% β-mercaptoethanol, was dialyzed against 10 mM HEPES and 150 mM KCl containing 100 μM TCEP disulfide reductant by using

Slide-A-Lyzer Dialysis Cassettes 7000 MWCO (Pierce, CA) for 2 h. The buffer was exchanged for fresh buffer, and the solution was dialyzed overnight at 4 °C. The concentration of the final protein solution was established by absorbance at 280 nm (ε = 44950 $cm^{-1}M^{-1}$) (*34*). The protein solutions were stored at -80 °C as 50 μL aliquots.

5.3.4 H/D Exchange (H/DX) Protocol

The protein stock solution was first diluted in buffer (10 mM HEPES, 150 mM KCl, pH 7.4) to prepare a 4 μM final analytical concentration and equilibrated at 25 °C for 2 h. H/DX was initiated by diluting the protein solution 1:10 into D_2O buffer (10 mM HEPES, 150 mM KCl, pD 7.4) at 25 °C. At varying times, the H/DX was quenched by adding sufficient 1 M HCl at 0 °C to give a final pH of 2.5.

For peptide-level H/DX experiments, the quenched solution was injected into an on-line pepsin-digestion device (**Figure 5-1**) containing immobilized pepsin in a 1 mm diameter × 2 cm length guard column (Upchurch Scientific, Oak Harbor, WA), which was prepared as described previously (*35*). The quenched solution was injected into the pepsin column in 0.1% formic acid via an Agilent 1100 HPLC (Santa Clara, CA) operated at 50 μL/min flow rate for 3 min. The digested protein solution was trapped on a C18 guard column (1 mm diameter x 1.5 cm length, Optimize Technologies, Oregon City, OR). The peptide mixture was then eluted from the trap column and separated with

a C18 analytical column (1 mm diameter x 5 cm length, Dionex, Bannockburn, IL) via an Agilent 1200 HPLC (Santa Clara, CA) with a gradient operated at 50 µL/min flow rate. Solvent A was water containing 0.1% formic acid, and solvent B was 80% acetonitrile, 20% water containing 0.1% formic acid. The gradient settings were: 5% to 15% solvent B in 0.3 min, 15% to 50% solvent B in 5.2 min, 50% to 100% solvent B in 0.5 min, and isocratic flow at 100% solvent B for 1.5 min, then returned to 5% solvent B in 0.1 min. All LC connection lines were immersed in a water-ice (0 °C) bath.

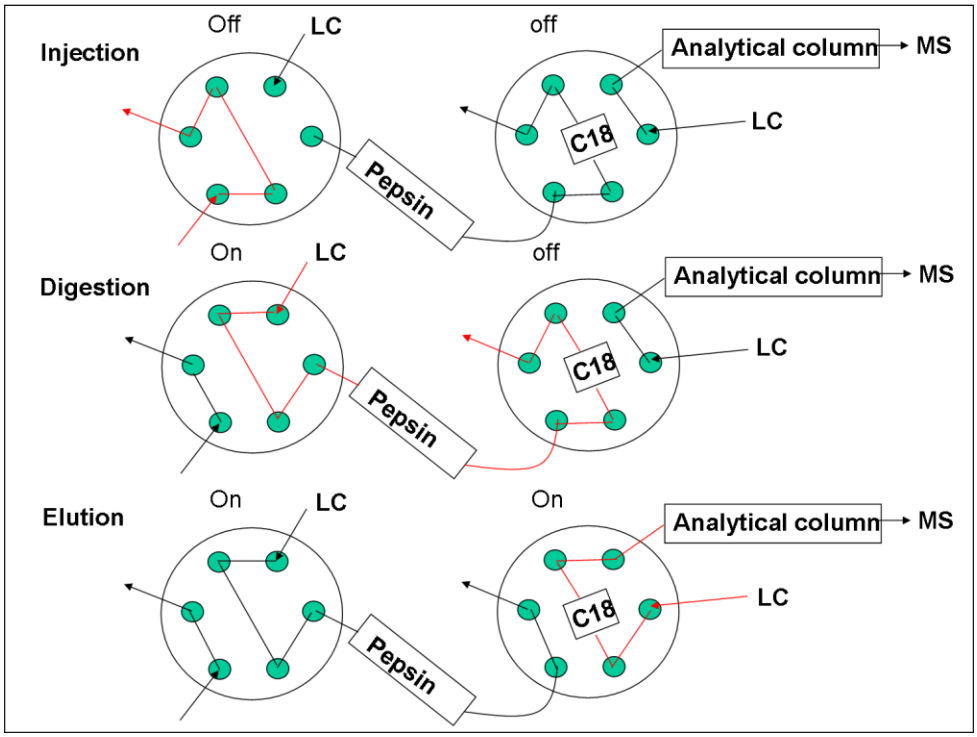

Figure 5-1. Diagram for on-line pepsin digestion device.

5.3.5 LC-ESI/MS Analysis with a Q-TOF Mass Spectrometer

Peptide-level H/DX results were acquired on a Maxis (Bruker, Bremen, Germany) quadrupole time-of-flight (Q-TOF) mass spectrometer. The settings were: capillary voltage, 3.8 kV; nebulizer gas, 0.4 bar; drying gas flow rate and temperature, 4.0 L/min and 180 °C, respectively; funnel RF, 400 V(pp).

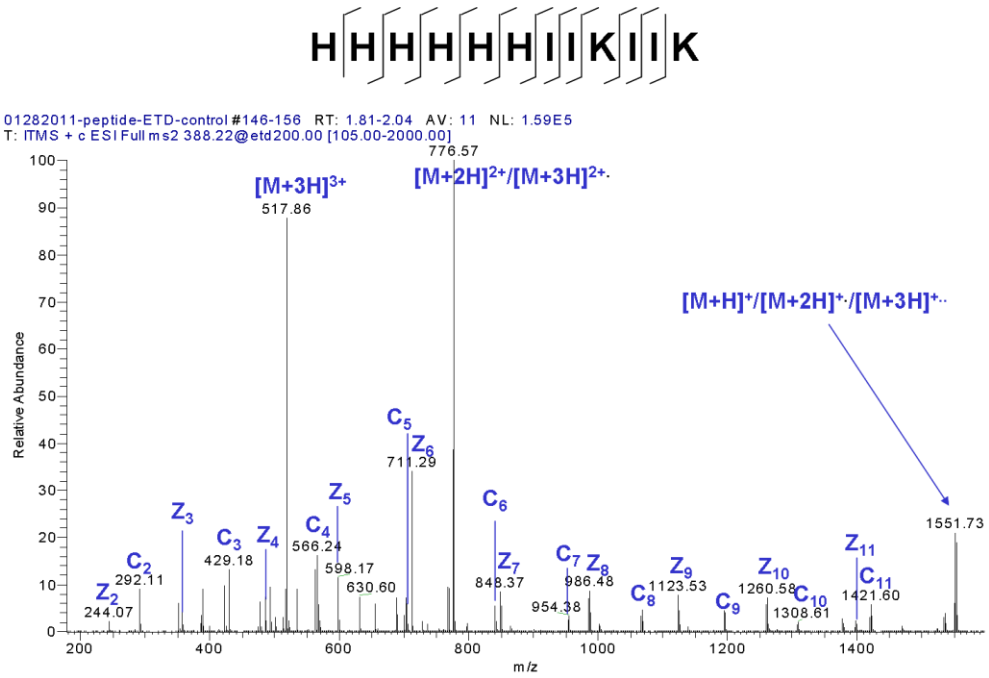

Figure 5-2. ETD product ion spectrum of standard peptide HHHHHHIIKIIK.

5.3.6 Test of hydrogen scrambling

In the test procedure, described previously by Jørgensen and coworkers (*30*), 100 µM of synthetic peptide, HHHHHHIIKIIK **(Figure 5-2)**, was prepared in D_2O and kept at 4 °C overnight to allow complete deuterium exchange. The solution was diluted 50-fold

with cold H_2O buffer (50% MeOH, 0.5 M acetic acid, pH 2.5) and frozen on dry ice to quench the exchange reaction. When needed for analysis, the peptide solution was manually thawed and injected into the ESI source via a pre-cooled 500 μL syringe (Hamilton, Reno, NV) operated at 50 μM/min flow rate.

Three instrumental conditions were chosen: (1) capillary temperature, 50 °C; capillary voltage, 20 V; tube lens, 50 V; (2) capillary temperature, 100 °C; capillary voltage, 50 V; tube lens, 50 V, and (3) capillary temperature, 200 °C; capillary voltage, 100 V; tube lens, 100 V. The active hydrogens of the test peptide were exchanged with deuterium and submitted to back exchange for approximately 1 min. The maximum number of deuteriums remaining in the peptide was approximately 4.5, which agreed with Jørgensen's results under similar conditions (*29*). Upon fragmenting the peptide by ETD, we found the deuterium content for the c_5 ion to be low (~0.6 D) under the first condition, indicating low H/D scrambling. As the capillary temperature and voltage were increased, increasing deuterium content was found in the N-terminal c_5 ion (deuterium uptakes for the c ions are in **Figure 5-3),** indicating that the first set of instrument parameters were optimum. Another advantage for tuning the experiment by using this standard peptide was that the solution flow rate and other instrument parameters were easily optimized to afford good peptide ion signals.

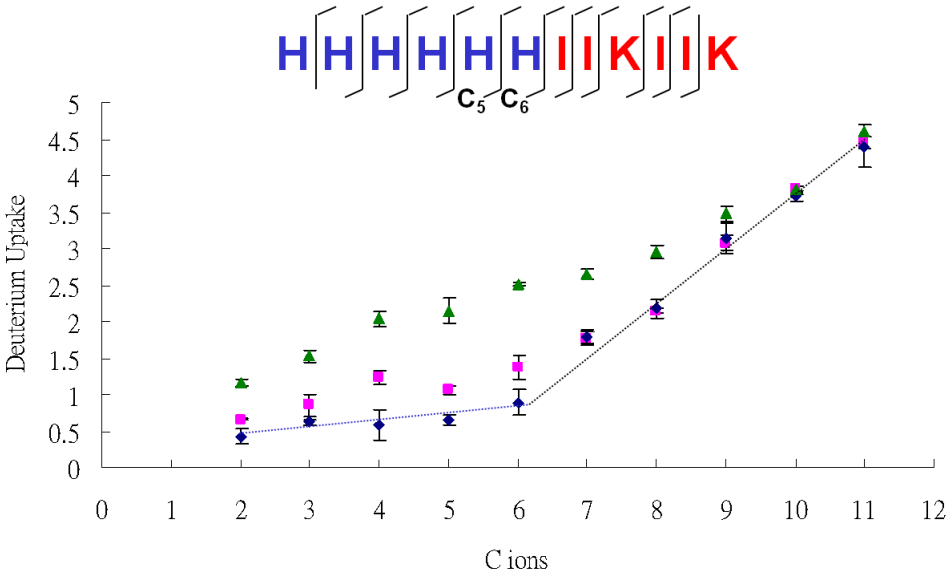

	Capillary Temperature	Capillary Voltage	Tube lens
☆	50 ◦ C	20 V	50 V
	100 ◦ C	50 V	50 V
	200 ◦ C	100 V	100 V

Figure 5-3. The deuterium uptake of C ions of the standard peptide HHHHHHIIKIIK after performing the H/DX-ETD. Three different ESI conditions were marked in different colors (blue, pink, and green).

5.3.7 LC-ESI/MS/MS Analysis with an Orbitrap-ETD Mass Spectrometer

To confirm the sequence for each peptic peptide, the protein was digested as described previously and analyzed on a Thermo LTQ XL Orbitrap (Thermo Fisher, San Jose, CA). The settings were: spray voltage, 3.5 kV; sheath gas flow rate, 8 (arbitrary units); capillary temperature, 275 °C; capillary voltage, 35 V; and tube lens, 110 V. One full mass spectral acquisition triggered three scans of MS/MS (precursor ion activation to give CID) whereby the most abundant precursor ions were activated for sequencing. The

peaks observed in the product-ion spectra (MS/MS) were centroided for each peptide during the acquisition.

H/DX-ETD MS was performed on a Thermo LTQ XL Orbitrap (Thermo Fisher, San Jose, CA), using the fluoranthene radical anion to cause ETD. One full mass-spectrum acquisition was used to trigger three scans of ETD. The parameters were: spray voltage, 3.5 kV; sheath gas flow rate, 8 (arbitrary units); capillary temperature, 50 °C; capillary voltage, 20 V; tube lens, 50 V; tandem MS selection threshold, 1000 counts; activation time, 100 ms for ETD. For ETD, the isolation width was 6.0 *m/z*, and the reaction time was "charge-state" dependent. A precursor mass list was generated based on the deuterated peptides' centroid *m/z*, and MS/MS data were centroided during acquisition.

5.3.8 Mascot database search

Thermo RAW files were processed by using extract_msn (2007 version 4.0, Thermo Fisher, San Jose, CA) with a grouping tolerance of 0.8 Da, an intermediate scan setting of 1, and a minimum of 1 scan per group. The NCBI nonredundant database (version 20101004, restricted to human) was searched by using MASCOT 2.2.06 (Matrix Science, Oxford, U.K.) employing the following settings: enzyme, none; MS tolerance,

10 ppm; MS/MS tolerance, 0.8 Da; maximum number of missed cleavages, 3; peptide charge of 1+, 2+ and 3+; oxidation of methionine was set as variable modification.

5.3.9 Data analysis

For peptide-level H/DX, the uptake of deuterium for each peptide was measured as the average differences between the centroid masses of the deuterated peptide and the undeuterated peptide. The back-exchange was measured to be one deuterium loss per minute. No correction for back exchange was applied because the time between sample quench and the measurement with the mass spectrometer was less than 6 min, and all data were treated consistently. The centroid and width of the deuterium containing isotopic distribution for each peptide was analyzed using HX-Express software (*36*).

For H/DX-ETD, the centroid of the deuterium-containing isotopic distribution for each product ion was obtained through MagTran 1.03 (Amgen, Thousand Oaks, CA). A minimum of 10% relative ion abundance threshold was applied in the data processing. The deuterium uptake for n^{th} amino acid was determined as the difference between the centroid of c_{n-1} and c_{n-2} ions or the difference between the centroid of z_{n+1} and z_n ions. All experiments were performed in at least triplicate.

5.4 RESULTS AND DISCUSSION

5.4.1 Regions involved in ApoE self-association revealed by H/DX kinetics study

Apolipoprotein E isoforms exist predominantly as tetramers at μM concentrations and dissociate into dimers and monomers at nM concentrations (*17*). The C-terminal domain seems to play the major role in this self-association (*10*). At analytical concentrations higher than μM, the protein tends to aggregate (*17, 37*), hindering the elucidation of the full-length structure. Wang and coworkers (*18*) showed that a monomeric form of ApoE3 could be generated by substituting in the C-terminal region four to five bulky hydrophobic residues with either smaller hydrophobic or polar/charged residues. Although these substitutions prevent oligomerization, an understanding of the key residues involved in the self-association process and the differences between the ApoE isoforms remains to be achieved.

In this study, we performed peptide-level H/DX kinetic measurements at seven different exchange times (0.5, 1, 3, 5, 10, 30, 60 min) on all three isoforms of ApoE including the wild-type proteins and their monomeric mutants. Starting with protein solutions for which the analytical concentration was 4 μM (where ApoE exists predominantly as tetramer), the proteins were equilibrated at 25 °C for 2 h followed by introduction of D_2O to initiate exchange and MS analysis to afford the kinetics of exchange at the peptide level for ApoE4 (**Figure 5-4**). Although the extents of H/DX for all regions of the wild-type proteins and the monomeric mutants located in the N-terminal

domain are similar, as revealed by peptic peptides, significant differences between the wild type and monomeric mutant occur in the C-terminal region for peptides 230-243 and 262-270, and small differences for peptide 271-279. These differences are most obvious at early exchange times (0.5-1 min). We suggest that this behavior is a consequence of the time-dependent dissociation of tetramer to monomer as discussed below. Interestingly, two substitution sites used to produce the monomeric mutant are located in two of these regions (W264R and L279Q) (*18*). Information for the peptide containing residue F257A (Peptide 257-261) was missing because the peptide signal intensity was low, and the signal dropped even more caused by further dispersion of signals by uptake of deuterium. Peptide 230-243 showed a dramatic decrease in deuterium uptake for this region of the wild type compared to the monomer. Overall, the regions that are affected by self-association are near the C-terminus, and this is consistent with previous findings that the C-terminal domain contains the residues important for ApoE oligomerization.

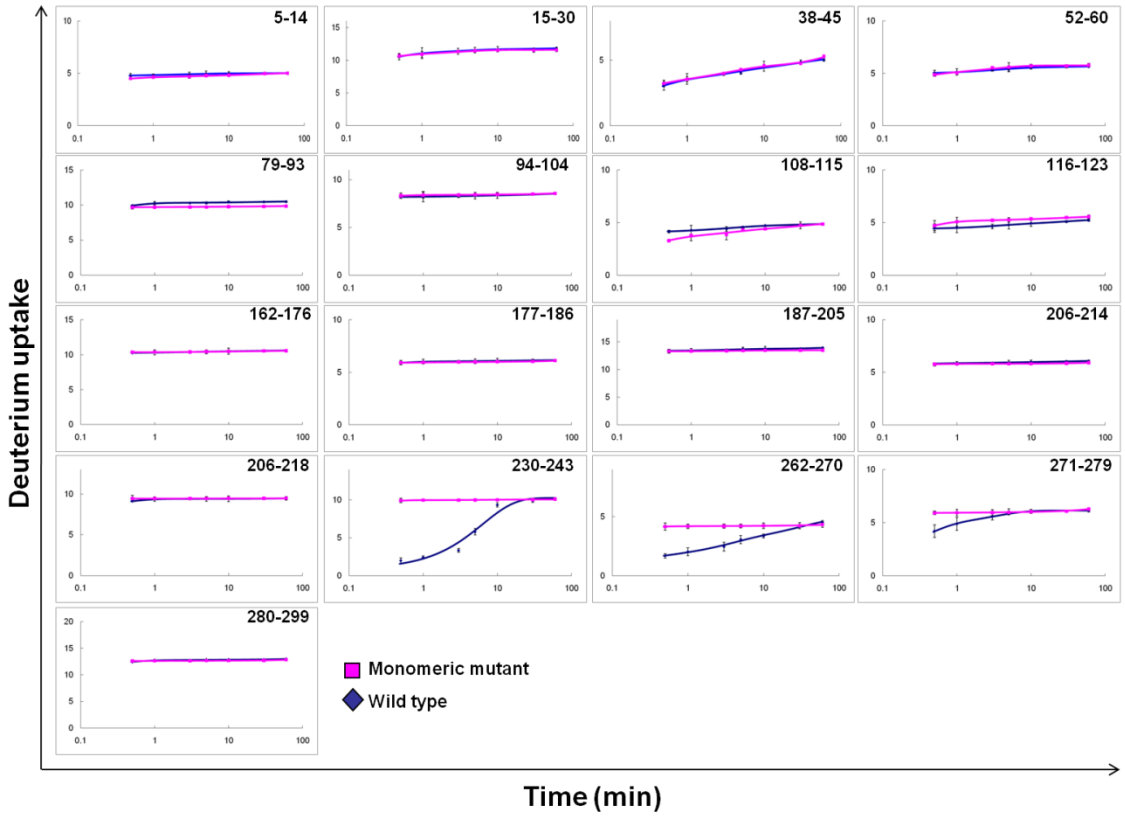

Figure 5-4. Peptide-level H/DX kinetics of ApoE4. A comparison between wild type (blue) and monomeric mutant (pink) shows significant differences in H/DX only for peptides 230-243 and 262-270 and small difference for peptide 271-279.

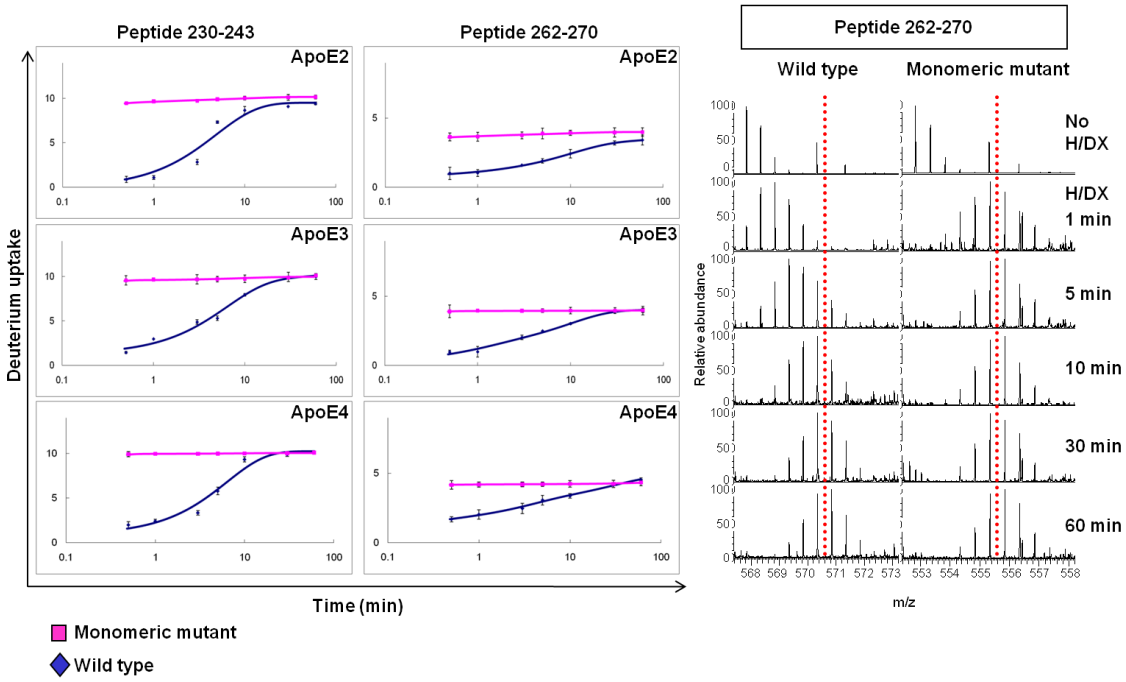

Figure 5-5. Comparison of H/DX kinetics of peptide 230-243 and 262-270 among all three isoforms (ApoE2, ApoE3, and ApoE4). An example of the mass spectra of peptide 262-270 of ApoE4 as a function of H/DX time is shown on the right (the red, dotted line is a reference to guide the eye).

The deuterium uptake of the two regions represented by peptides 230-243 and 262-270 of all the wild-type isoforms are time-dependent as shown in **Figure 5-5**. This slow H/DX of the C-terminal peptide fragments (residues 230-243 and 262-270) of the wild-type ApoE isoforms may be consistent with the slow dissociation of the ApoE oligomers. Garai and Frieden (*17*) showed that association-dissociation of ApoE isoforms fit a monomer-dimer-tetramer model and that the rate for dissociation at neutral pH is slow. The H/DX experiments were carried out by diluting ApoE from 4 µM to 400 nM analytical concentration in the D_2O buffer; the result is dissociation of the tetramers to

monomers. Although wild-type ApoE exists as a mixture of monomers, dimers and tetramers at 400 nM (*17*), deuterium uptake by the wild-type ApoE at this concentration reaches completion owing to the reversibility of the monomer-dimer-tetramer process. The dissociation rate constants for the isoforms, as measured by Garai and Frieden, are approximately 10^{-4} s^{-1} for dimer-monomer and 10^{-3} s^{-1} for tetramer-dimer conversion, the equilibrium constants for both processes are in the range of 10^{7} M^{-1} (*17*). We fit the H/DX kinetic data with a fixed-rate-constant binning model by using MathCAD (Math-Soft. Inc. Cambridge, MA), as previously described (*38, 39*), whereby iterations were continued until the root mean square (RMS) was minimized. We chose three fixed rate-constant bins (k = 10, 1, 0.1 min^{-1}); the latter bin on the basis of the time needed to effect nearly complete exchange (**Table 5-1**). According to the model, nearly all the amide hydrogens in these two regions of the wild-type ApoE exchange in 0.1 min^{-1} (1.6×10^{-3} s^{-1}) rate-constant bin, whereas all amide hydrogens of the monomeric mutants undergo fast exchange rate (k = 10 min^{-1}), indicating that the mutants are flexible in these two regions.

	Kinetic Fit	# of H's per fixed-rate bin		
Peptide 230-243	**k (min^{-1})**	**10**	**1**	**0.1**
WT	**ApoE2**	**0 ± 0**	**2 ± 1**	**8 ± 1**
	ApoE3	**0 ± 0**	**3 ± 1**	**7 ± 1**
	ApoE4	**1 ± 0**	**1 ± 0**	**8 ± 1**
MM	**ApoE2**	**9 ± 1**	**0 ± 0**	**0 ± 0**
	ApoE3	**10 ± 1**	**0 ± 0**	**0 ± 0**
	ApoE4	**10 ± 1**	**0 ± 0**	**0 ± 0**
Peptide 262-270	**k (min^{-1})**	**10**	**1**	**0.1**
WT	**ApoE2**	**1 ± 0**	**0 ± 0**	**2 ± 0**
	ApoE3	**0 ± 0**	**1 ± 0**	**3 ± 1**
	ApoE4	**1 ± 0**	**1 ± 0**	**2 ± 1**
MM	**ApoE2**	**4 ± 1**	**0 ± 0**	**0 ± 0**
	ApoE3	**4 ± 1**	**0 ± 0**	**0 ± 0**
	ApoE4	**4 ± 1**	**0 ± 0**	**0 ± 0**

Table 5-1. Numbers of amide hydrogen undergoing H/D exchange for wild-type (WT) and monomeric-mutant ApoE's isoforms. The kinetic modeling used three fixed exchange rate constants and "binned" the number of amides with respect to the rate constants.

The H/DX kinetics do not reveal the two-step behavior observed by Garai et al. (17) but instead are an integrated view of the various states of the protein. Given that the peptide-level H/DX kinetics for the wild-type ApoE's C-terminal regions (~10^{-3} s^{-1}) agrees well with the average dissociation constant determined for tetramer-dimer-monomer process (*17*), we suggest that the oligomeric proteins must first dissociate to monomers and then undergo H/DX in the two C-terminal regions.

ApoE2 and ApoE3 show similar H/DX behavior (**Figures 5-6 and 5-7**). A comparison of the H/DX kinetics for monomeric mutant of all three isoforms (**Figure 5-8**)

reveals that some regions have minor differences among the three isoforms (peptide 15-30, 116-123, and 271-279) where ApoE4 takes up slightly more deuterium than ApoE2 and ApoE3. Overall, the three isoforms must share similar structures and properties with respect to oligomerization. These properties as revealed by H/DX are also consistent with the differences found in our study using fast photochemical oxidation (FPOP) (*40*).

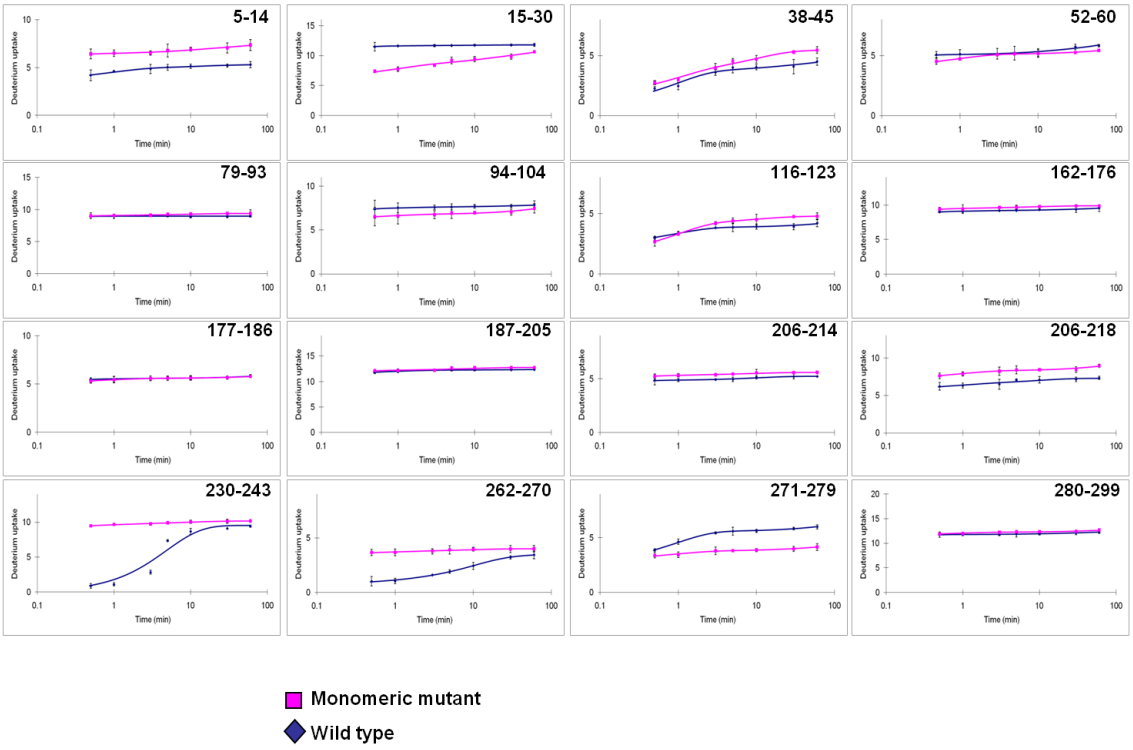

Figure 5-6. Peptide-level H/DX kinetics of ApoE2. The extent of deuterium uptake is plotted as a function of exchange time. Wild type is marked in blue and monomeric mutant is marked in pink.

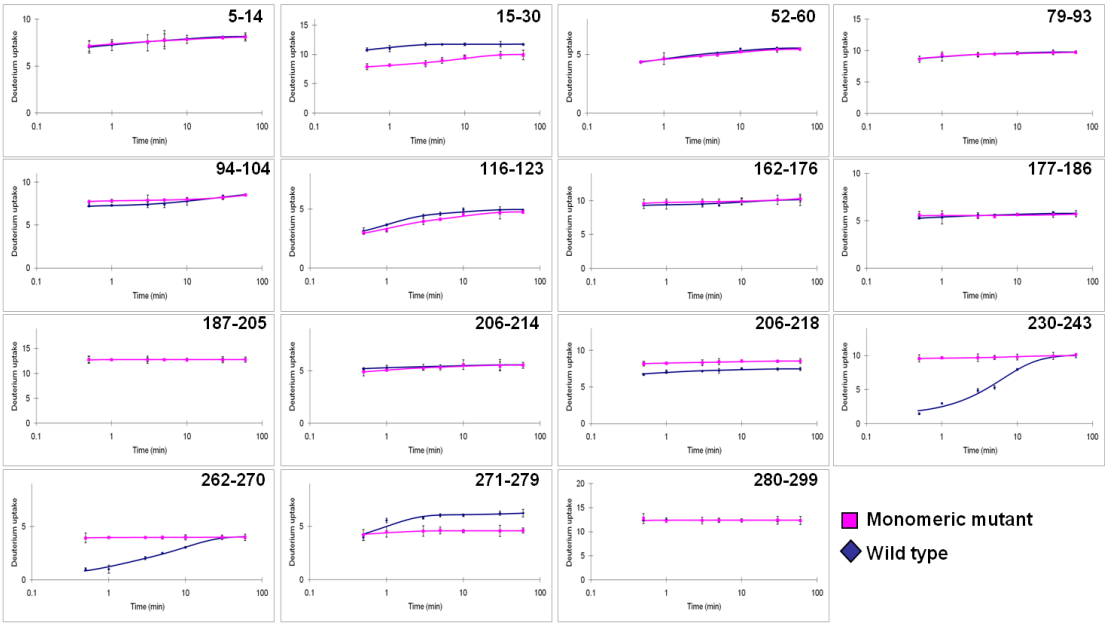

Figure 5-7. Peptide-level H/DX kinetics of ApoE3. The extent of deuterium uptake is plotted as a function of exchange time. Wild type is marked in blue and monomeric mutant is marked in pink.

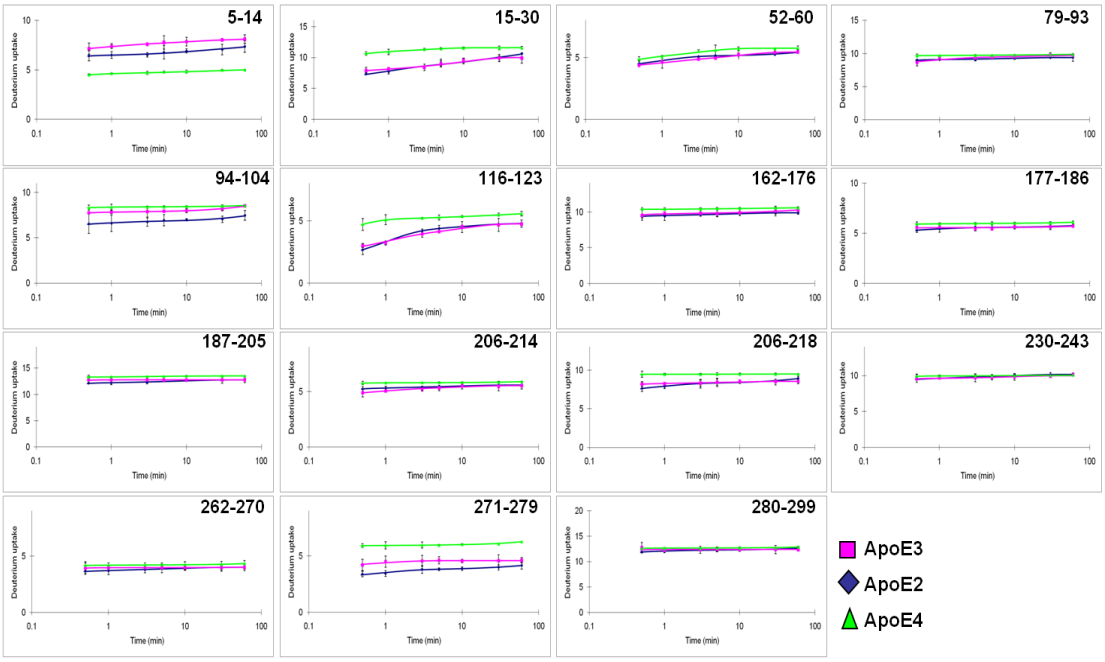

Figure 5-8. Peptide-level H/DX kinetics of ApoE2, ApoE3 and ApoE4 monomeric mutant. The extent of deuterium uptake is plotted as a function of exchange time. ApoE2 is marked in blue, ApoE3 is marked in pink, and ApoE4 is marked in green.

5.4.2 H/DX-ETD reveals residues involved in self-association of ApoE4

Peptide-level H/DX kinetics, as shown in this study, can reveal not only those regions that are involved in protein:protein interactions but also the dynamics of the interactions. To improve the resolution of the H/DX experiments, we chose a bottom-up strategy whereby, following H/DX of the protein and proteolysis, we subjected the peptide to ETD fragmentation (**Figure 5-9**). This approach is more appropriate than a top-down one because our ApoE samples contain several post-translational oxidations that disperse the signal and increase the difficulty of the top-down H/DX experiment. Furthermore, extensive sequence coverage for any 34 kDa protein is difficult to achieve in a top-down experiment.

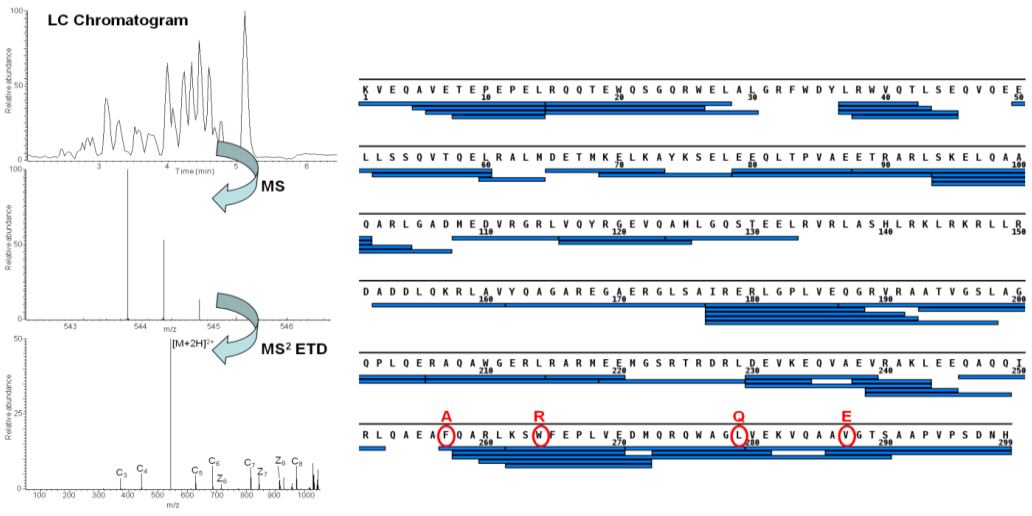

Figure 5-9. A diagram of the H/DX-ETD procedure. A peptide of interest produced from on-line pepsin digestion is subjected to ETD fragmentation. Peptide coverage (~89%) of ApoE4 by applying this strategy is shown in right (four substitution sites to achieve the MM are marked in red).

Bottom-up H/DX-ETD experiments were performed under the same conditions as for peptide-level H/DX experiments in which a 4 μM (analytical concentration) protein solution was equilibrated at 25 °C for 2 h followed by diluting the protein solution 1:10 into D_2O buffer for 1 min, a time at which there is a large difference in H/DX between wild types and the monomeric mutants of ApoE. After quenching the exchange, the protein solution was submitted to on-line pepsin digestion, and the peptides were analyzed by MS and ETD whereby the selection of the precursor ion was directed by a precursor-mass list containing the peptides of interest. This list utilized the centroid *m/z* of the deuterium-containing isotopic distribution of the peptides of interest. ETD usually generates a product-ion spectrum of good signal-to-noise for those peptides that are doubly or more highly charged. Peptides that are +4 or higher, however, will show increased H/D scrambling due to the more energetic collisions they undergo upon acceleration in the ESI declustering field than do lower charged ions (*30*). Therefore, we selected doubly and triply charged peptides that had sufficient ion signal for ETD fragmentation.

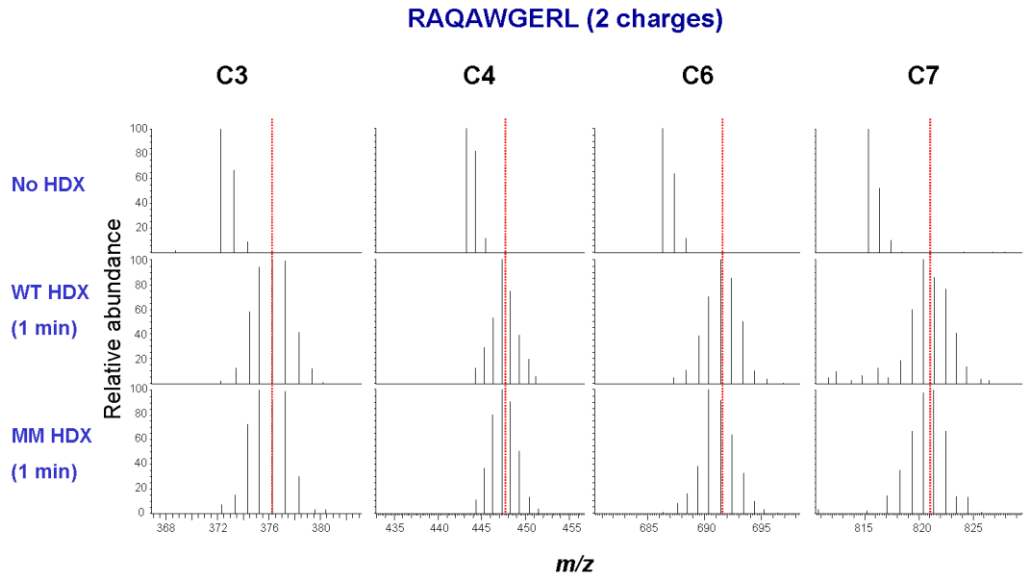

Figure 5-10. ETD product-ion spectra of peptide 206-214 of ApoE4 after H/DX. The centroid of the distribution of C ions from MM is shown as red dotted line, showing there are no significant differences in H/DX between WT and MM.

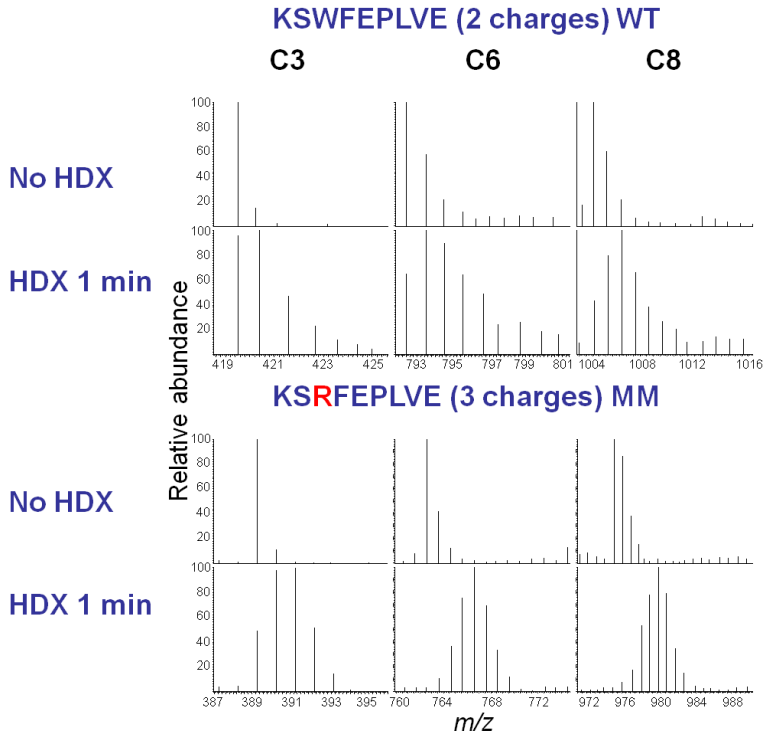

Figure 5-11. ETD product-ion spectra of peptide 262-270 of ApoE4 after H/DX. The centroid of the distribution of c ions from monomeric mutant shows there are significant differences in the extent of H/DX between WT and MM for this region.

Although the c ions of peptides 206-214 show no significant differences in H/DX for wild type ApoE4 and monomeric mutant forms after 1 min (**Figure 5-10**), the region 262-270 (**Figure 5-11**) undergoes significantly different H/DX. We measured the extent of deuteration at each amide site, using the difference of the isotopic-distribution centroid between two adjacent product ions (c or z ions). For example, the extent of deuterium on the n^{th} amino acid is the difference between the centroid of c_{n-1} and c_{n-2} ions or between the centroid of z_{n+1} and z_n ions. The outcome is a deuterium-uptake diagram for each amide of each residue of the ApoE4 wild type and its monomeric mutant. We analyzed 132 out of 274 amides with exchangeable backbone hydrogens (excluding proline and the *N*-terminal amine hydrogens for each peptide), giving a coverage of ~ 50%. The coverage depends highly on the quality of the product-ion spectra; that quality was reduced when working under ESI conditions that minimize scrambling. No correction for back exchange was made because all experiments were treated consistently. Although three of four substitution sites of the ApoE4 monomeric mutant are located on C-terminal peptic peptides, which we selected for ETD fragmentation, these sites are located separately on different peptides; thus, the extents of back exchange should be similar for the same set of peptides from the two protein isoforms and will not affect conclusions about the relative differences of H/DX.

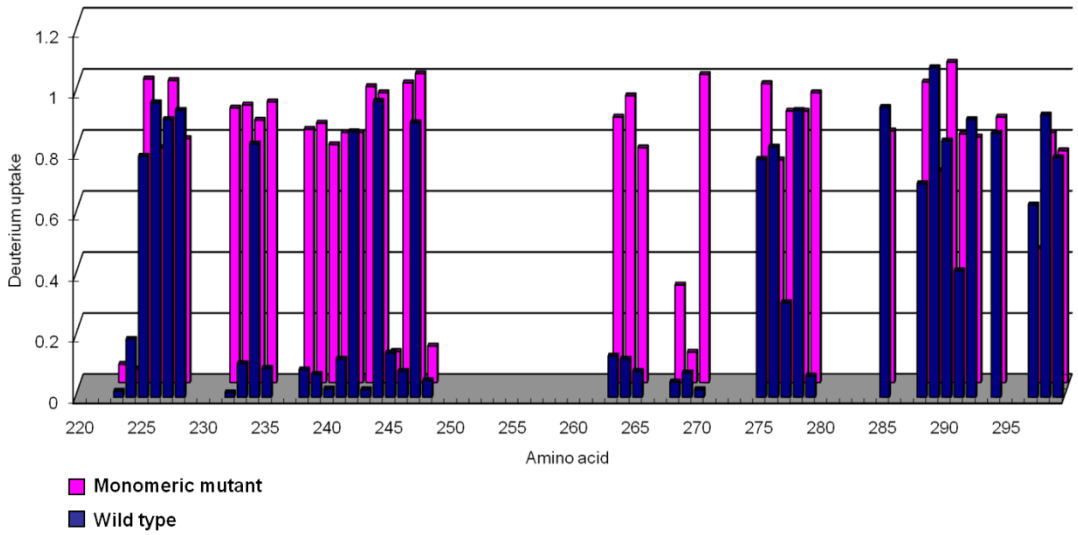

Figure 5-12. The extent of deuterium uptake of various amino-acid residues in the C-terminal domain of ApoE4 (Residue 220-299). Several residues of wild type (blue) have lower level (<0.3D) of deuterium uptake compared to the monomeric mutant (pink). Note: The gaps correspond to missing information.

There are clearly no significant differences for all the amides examined in the N-terminal region of the wild type and the monomeric mutant form of ApoE4 (the complete extents of deuteration are in **Table 5-2**). Not surprisingly, several amides in the C-terminal region underwent relatively low deuterium uptake (< 0.3 D) for the wild type ApoE4 whereas they exchanged more deuterium (> 0.7 D) for the monomeric mutant (**Figure 5-12**). The residues associated with these amides are: Val232, Lys233, Gln235, Glu238, Val239, Arg240, Ala241, Leu243, Gln246, Ser263, Trp264 (Arg in the monomeric mutant form), Phe265, Leu268, Glu270, and Leu279 (Gln in the monomeric mutant form). Interestingly, two of the substitution sites (Trp264Arg and Leu279Gln) are

on the list, indicating the important roles played by the two residues in the self-association process. Several residues (e.g., Glu234 and Lys242) showed no significant differences in deuterium uptake between the wild-type and monomeric-mutant forms, indicating that these two residues are minimally affected by the self association of ApoE4. Weisgraber and coworkers (*10*), who studied the ApoE oligomerization by truncating various sites in the C-terminal region, found that residues within 267-299 are critical for tetramerization. Our study, using the full-length protein, show that three residues within this region are important in the ApoE self asoociation. Moreover, 12 additional residues, which are close to this region, also play a role in self association. A potential spinoff of this work is the use of H/DX results as a basis for designing future mutation studies in ApoE and other proteins.

5.4.3 The structure of ApoE4

Before mapping the H/DX-ETD results onto a structure of ApoE that contains the X-ray crystal structure of the N-terminal domain (PDB: 1GS9) (*41*), we wished to establish that a low extent of deuteration for a specific amide indicated low solvent accessibility and not extensive back exchange. Thus, we prepared a nearly 100% deuterium-exchanged ApoE4 monomeric mutant by diluting the protein solution into D_2O buffer at 25 °C and exchanging for 24 h. After submitting the protein to on-line

pepsin digestion and ETD-MS analysis (*42*), we found that the average percent back exchange was (13 ± 4)%. (Each deuterium uptake for a single amide was normalized to its corresponding $D_{100\%}$ value, and the normalization was treated separately for each trial of experiments—see **table 5-2)**.

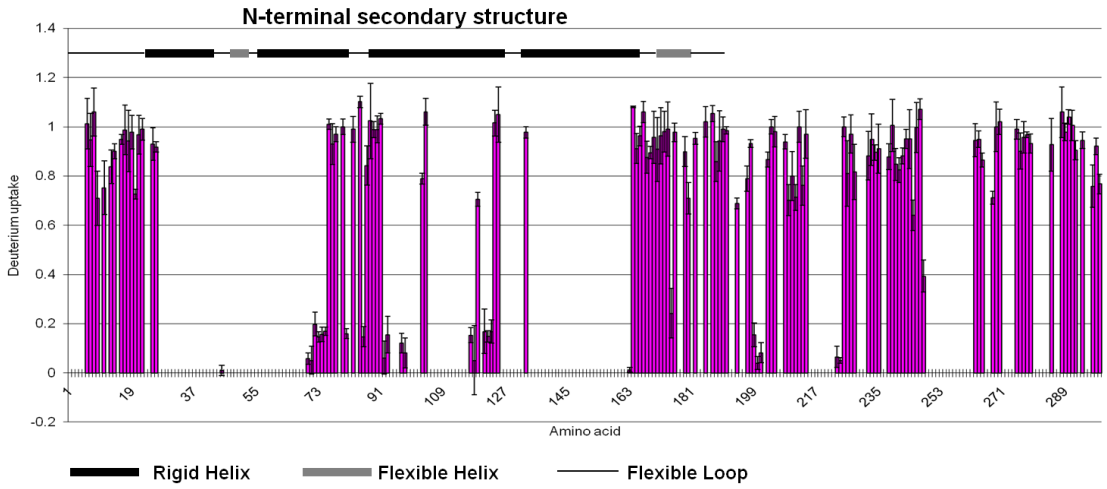

Figure 5-13. The extent of deuterium uptake of each amide of ApoE4 monomeric mutant after correcting for back exchange (pink). Most of the amides in the C-terminus have high extent of deuterium uptake, indicating a flexible structure in this region. The extent of deuterium uptake in N-terminal region are consistent with the known secondary structure (top). (flexible loop, black line; flexible helix, gray box; rigid helix, black box). Note: The gaps correspond to missing information.

The deuterium uptake at a single amide of the ApoE4 monomeric mutant (**Figure 5-13**), show that the ApoE4 structure is primarily compact in the N-terminal region and more flexible in the C-terminal region, as previously assumed (*43*). Previous studies indicated that the C-terminal domain should contain amphipathic helices and several flexible loop regions (*11, 12*). Four possible helices, represented by peptide regions 190-

199, 210-223, 238-266, and 271-276, exist in the C-terminal domain, as determined by Wang and coworkers (*5*). Their recent NMR structure of ApoE3 monomeric mutant shows that these helices are in the middle of long, unstructured regions (*44*). Our amide-level H/DX results, when mapped onto a schematic secondary structure of the C-terminal domain of ApoE (**Figure 5-14**), show that peptide regions 190-199 and 271-276 undergo extensive H/DX, consistent with being flexible helices. Although deuterium uptake information is missing for peptide regions 215-222 and 249-262, those regions adjoin those helices in C-terminal domain that also undergo extensive H/DX and should be flexible.

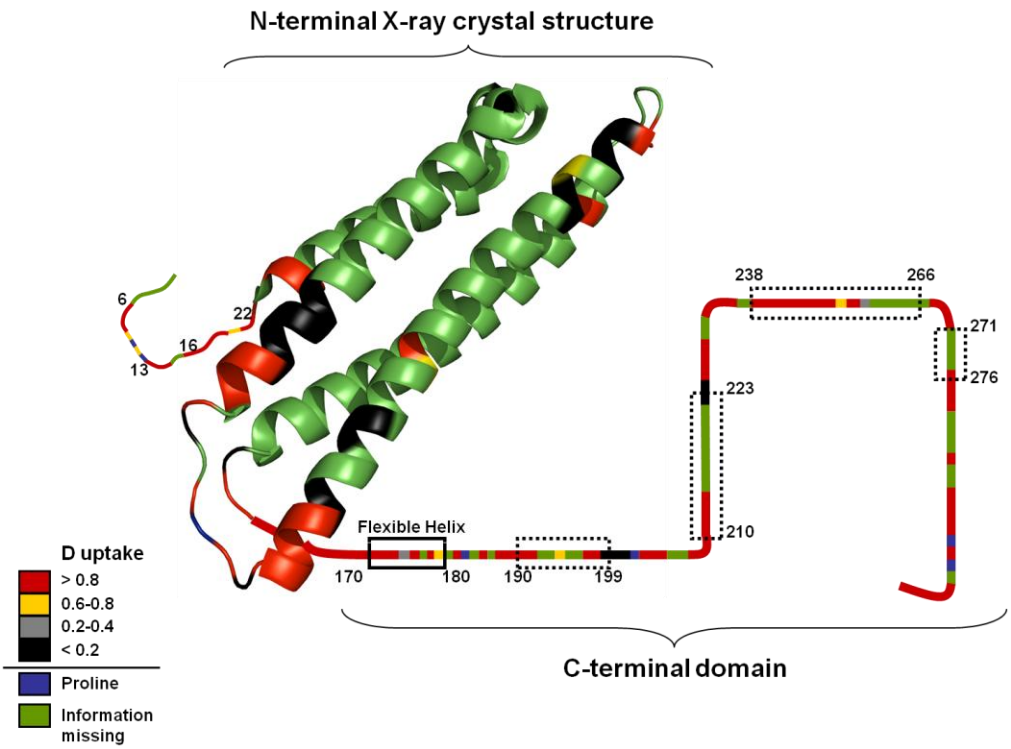

Figure 5-14. Structure of ApoE4 on which residue-level H/DX of ApoE4 monomeric mutant is mapped. Left: X-ray crystal structure of N-terminal region of ApoE4 (PDB: 1GS9). Right: Proposed secondary structure of C-terminal region of ApoE (*5*). Possible helices are shown in dotted boxes. Different colors represent different levels of deuterium uptake for each residue (lower left).

In another peptide-level H/DX experiment, we treated the three ApoE's isoforms with 0.5 M guanidine hydrochloride (GdnCl) (**Figure 5-15**), a concentration at which the protein could lose some tertiary/quaternary structure while maintaining its secondary structure (*43*). The results show that this low concentration of denaturant has more impact on the C-terminal than the N-terminal region of ApoE. This is additional evidence that ApoE is composed of a flexible C-terminal region, making it susceptible to denaturation. Morrow and coworkers (*45*), who studied the denaturation of ApoE at various

concentrations of GdnCl, showed that the regions nearby the C-terminus and in the presence of low concentration of GdnCl, unfold prior to those close to the N-terminal domain. Our results are consistent with their findings.

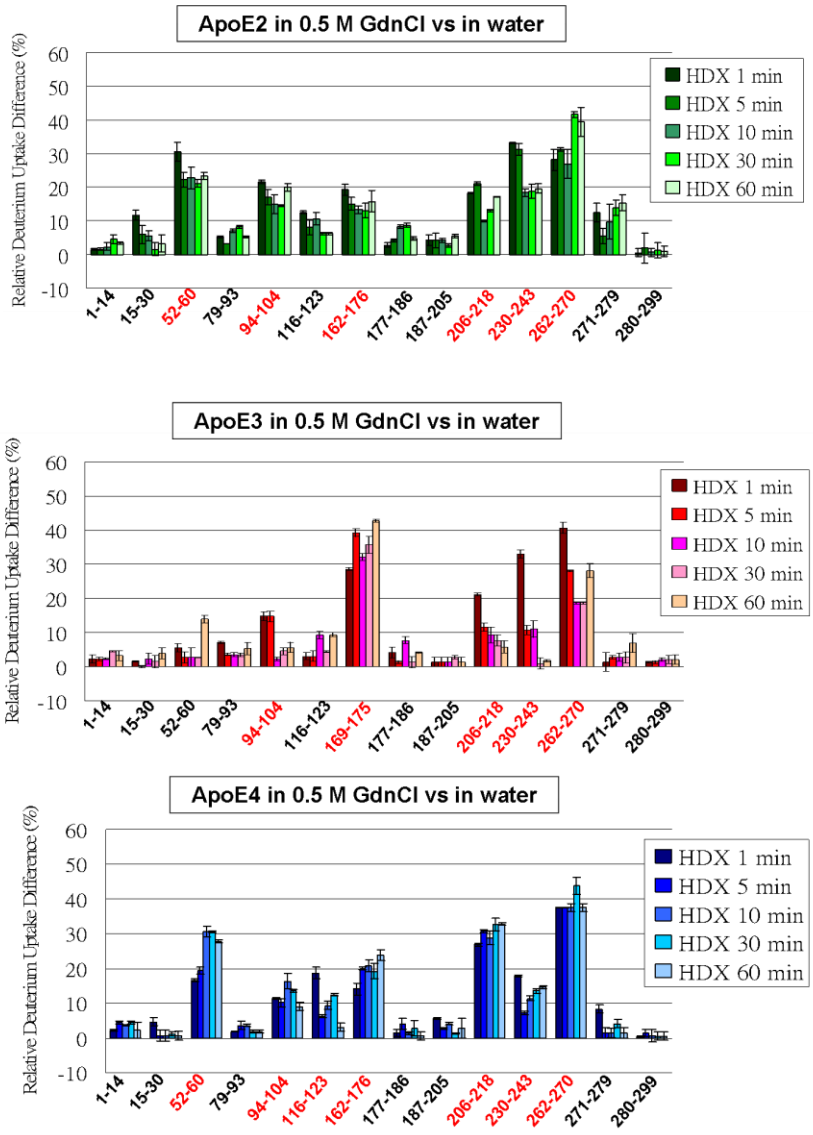

Figure 5-15. Peptide-level H/DX of ApoE2, ApoE3, and ApoE4 with or without the presence of 0.5 M GdnCl. The relative deuterium uptake difference is plotted as different peptide regions. The large difference indicates the regions (red) having less stable H-bonding or more relative solvent accessibilities in the presence of denaturant.

The structure of the N-teminal domain of ApoE was determined by X-ray crystallography and NMR to be a four helix-bundle (*5, 9, 41*). Our results, when compared to the X-ray crystal structure of N-terminal domain (**Figure 5-14**), show that amides in the regions of residues 6-25, 76-91, 124-125, and 165-191 undergo extensive deuterium uptake, consistent with their location at or near the flexible-loop regions and as part of the flexible-helix region (170-180). The amides in regions 70-75 and 92-103, which are located in a rigid helix, undergo low extents of deuteration, in accord with the strong H-bonding in that region of the protein.

Table 5-2. A complete list of deuterium uptake for 132 residues in ApoE4.

Amino acid	WT	STD	MM	STD	D 100%	Normalized MM	STD
V6	0.76	0.11	0.79	0.08	0.78	1.01	0.10
E7	0.78	0.07	0.88	0.10	0.93	0.95	0.11
T8	0.87	0.06	0.87	0.08	0.82	1.06	0.10
E9	0.15	0.14	0.22	0.18	0.31	0.71	0.11
E11	0.98	0.02	0.76	0.11	1.01	0.75	0.11
E13	0.99	0.12	0.82	0.07	0.98	0.84	0.07
L14	0.99	0.02	0.90	0.03	1.00	0.90	0.03
Q16	1.01	0.09	0.94	0.02	0.99	0.95	0.02
Q17	0.84	0.04	0.79	0.08	0.80	0.99	0.10
T18	1.00	0.17	0.83	0.11	0.88	0.94	0.13
E19	0.90	0.05	0.93	0.07	0.95	0.98	0.07
W20	0.20	0.08	0.08	0.03	0.11	0.73	0.02
Q21	0.77	0.03	0.90	0.07	0.93	0.97	0.08
S22	0.83	0.13	0.97	0.04	0.98	0.99	0.04
R25	0.97	0.12	0.93	0.07	1.00	0.93	0.07
W26	0.94	0.05	0.90	0.02	0.98	0.92	0.02
E45	0.09	0.02	0.01	0.02	0.98	0.01	0.02
E70	0.10	0.02	0.06	0.02	0.94	0.06	0.02
L71	0.10	0.04	0.06	0.06	1.08	0.05	0.06
K72	0.17	0.01	0.18	0.04	0.89	0.20	0.05
A73	0.16	0.05	0.15	0.02	1.00	0.15	0.02
Y74	0.13	0.07	0.16	0.03	1.02	0.16	0.03
K75	0.05	0.07	0.17	0.02	1.00	0.17	0.02
S76	0.95	0.02	0.98	0.02	0.97	1.01	0.02
E77	0.88	0.09	0.92	0.08	0.99	0.93	0.08
L78	0.89	0.10	0.95	0.03	0.98	0.97	0.03
E80	0.95	0.05	0.99	0.03	0.99	1.00	0.03
Q81	0.20	0.08	0.16	0.02	1.00	0.16	0.02
T83	0.92	0.04	0.97	0.05	0.98	0.99	0.05
V85	0.86	0.14	1.09	0.02	0.99	1.10	0.02
A86	0.18	0.07	0.15	0.04	1.02	0.15	0.04
E87	0.79	0.04	0.80	0.08	0.95	0.84	0.08
E88	0.92	0.04	0.87	0.13	0.85	1.02	0.15

T89	0.98	0.06	0.94	0.03	0.95	0.99	0.03
R90	0.89	0.14	0.91	0.05	0.92	0.99	0.05
A91	0.95	0.02	0.96	0.02	0.93	1.03	0.02
R92	0.10	0.08	0.06	0.07	1.02	0.06	0.07
L93	0.08	0.04	0.16	0.08	1.03	0.16	0.07
L97	0.17	0.01	0.12	0.04	0.99	0.12	0.04
Q98	0.07	0.11	0.08	0.06	0.98	0.08	0.06
R103	0.72	0.02	0.79	0.02	1.00	0.79	0.02
L104	0.92	0.08	1.05	0.05	0.99	1.06	0.05
Q117	0.18	0.01	0.15	0.03	0.98	0.15	0.03
Y118	0.13	0.08	0.04	0.11	0.78	0.05	0.14
R119	0.76	0.07	0.73	0.03	1.04	0.71	0.03
E121	0.14	0.10	0.15	0.08	0.89	0.17	0.09
V122	0.15	0.04	0.13	0.02	0.88	0.15	0.02
Q123	0.13	0.02	0.11	0.03	0.66	0.17	0.05
A124	1.01	0.07	1.00	0.05	0.99	1.02	0.05
M125	0.75	0.04	0.75	0.08	0.72	1.05	0.11
L133	0.83	0.08	0.87	0.02	0.89	0.98	0.02
Q163	0.02	0.01	0.01	0.01	0.77	0.01	0.01
A164	0.99	0.01	1.07	0.00	0.99	1.08	0.00
G165	0.96	0.10	0.91	0.06	1.00	0.91	0.06
A166	0.77	0.12	0.78	0.03	0.81	0.96	0.04
R167	0.77	0.02	0.74	0.03	0.70	1.06	0.04
E168	0.88	0.01	0.89	0.07	1.01	0.88	0.06
G169	0.89	0.10	0.90	0.03	1.00	0.90	0.03
A170	0.74	0.04	0.71	0.08	0.74	0.96	0.11
E171	0.86	0.02	0.84	0.12	0.93	0.91	0.13
R172	0.91	0.06	0.93	0.11	0.97	0.96	0.11
G173	0.92	0.04	0.97	0.08	0.99	0.98	0.08
L174	0.70	0.08	0.99	0.11	1.00	0.99	0.11
S175	0.07	0.06	0.08	0.03	0.33	0.24	0.10
A176	0.84	0.01	0.86	0.03	0.88	0.98	0.04
E179	0.89	0.02	0.89	0.06	0.99	0.90	0.06
R180	0.23	0.07	0.22	0.02	0.31	0.71	0.06
G182	0.88	0.13	0.80	0.02	0.84	0.95	0.02
V185	0.74	0.08	0.99	0.06	0.97	1.02	0.06
Q187	1.01	0.05	0.98	0.03	0.93	1.05	0.03

G188	0.82	0.07	0.85	0.08	0.99	0.86	0.08
R189	0.76	0.11	0.83	0.11	0.88	0.94	0.12
V190	0.94	0.02	0.97	0.05	0.98	0.99	0.05
R191	0.74	0.10	1.00	0.02	1.02	0.99	0.01
T194	0.28	0.06	0.32	0.01	0.47	0.69	0.02
S197	0.98	0.04	0.77	0.05	0.98	0.79	0.05
L198	0.91	0.03	0.90	0.02	0.96	0.93	0.02
A199	0.08	0.05	0.14	0.04	0.91	0.15	0.05
G200	0.08	0.04	0.03	0.02	0.76	0.04	0.03
Q201	0.16	0.12	0.08	0.04	0.98	0.08	0.04
L203	0.86	0.06	0.88	0.03	1.02	0.87	0.03
Q204	0.41	0.09	0.35	0.01	0.35	1.00	0.03
E205	0.85	0.03	0.99	0.06	1.01	0.98	0.06
Q208	0.33	0.03	0.31	0.01	0.33	0.94	0.03
A209	0.75	0.08	0.66	0.06	0.94	0.70	0.06
W210	0.01	0.02	0.04	0.01	0.05	0.80	0.10
G211	0.97	0.11	0.41	0.03	0.58	0.71	0.05
E212	0.40	0.01	0.32	0.02	0.32	1.00	0.06
R213	0.73	0.04	0.67	0.07	0.88	0.76	0.08
L214	0.99	0.08	0.98	0.10	1.01	0.97	0.10
S223	0.02	0.05	0.06	0.04	0.93	0.06	0.04
R224	0.19	0.05	0.05	0.01	0.89	0.05	0.01
T225	0.79	0.09	1.00	0.04	1.00	1.00	0.04
R226	0.97	0.05	0.77	0.13	0.95	0.81	0.13
D227	0.91	0.03	0.99	0.08	1.02	0.97	0.08
L228	0.94	0.08	0.80	0.11	0.98	0.82	0.11
V232	0.02	0.01	0.90	0.10	1.02	0.88	0.10
K233	0.11	0.02	0.91	0.10	0.96	0.95	0.10
E234	0.83	0.02	0.86	0.03	0.96	0.90	0.03
Q235	0.10	0.04	0.92	0.10	1.01	0.91	0.10
E238	0.09	0.03	0.83	0.05	0.95	0.88	0.05
V239	0.08	0.04	0.85	0.09	0.85	1.01	0.11
R240	0.03	0.01	0.78	0.06	0.92	0.85	0.07
A241	0.13	0.03	0.82	0.05	1.00	0.82	0.05
K242	0.87	0.01	0.82	0.03	0.93	0.88	0.03
L243	0.03	0.01	0.97	0.04	1.02	0.95	0.04
E244	0.97	0.10	0.95	0.12	1.00	0.95	0.12

E245	0.15	0.04	0.10	0.01	0.16	0.64	0.06
Q246	0.09	0.07	0.98	0.10	0.99	1.00	0.10
A247	0.90	0.06	1.01	0.04	0.95	1.07	0.04
Q248	0.06	0.05	0.12	0.02	0.31	0.39	0.07
S263	0.14	0.03	0.87	0.06	0.92	0.95	0.07
W264R	0.13	0.02	0.94	0.03	0.99	0.95	0.03
F265	0.09	0.01	0.77	0.03	0.89	0.87	0.03
L268	0.05	0.01	0.32	0.01	0.45	0.71	0.03
V269	0.08	0.03	0.10	0.01	0.10	1.00	0.10
E270	0.03	0.03	1.01	0.05	0.99	1.02	0.05
Q275	0.78	0.05	0.98	0.04	0.99	0.99	0.04
W276	0.82	0.06	0.73	0.06	0.81	0.90	0.07
A277	0.31	0.08	0.89	0.06	0.93	0.96	0.06
G278	0.94	0.02	0.89	0.01	0.92	0.97	0.01
L279Q	0.07	0.06	0.95	0.04	1.02	0.93	0.04
A285	0.95	0.08	0.83	0.10	0.89	0.93	0.11
G288	0.70	0.02	0.99	0.10	0.93	1.06	0.10
T289	1.08	0.03	0.70	0.03	0.71	0.98	0.04
S290	0.84	0.10	1.05	0.03	1.01	1.04	0.03
A291	0.42	0.07	0.82	0.05	0.81	1.01	0.06
A292	0.91	0.06	0.81	0.04	0.89	0.90	0.04
V294	0.87	0.06	0.87	0.03	0.92	0.95	0.03
D297	0.63	0.10	0.44	0.05	0.58	0.76	0.09
N298	0.93	0.04	0.82	0.03	0.89	0.92	0.03
H299	0.79	0.04	0.76	0.04	0.99	0.77	0.04

5.5 CONCLUSIONS

The observation that ApoE has a high tendency to aggregate has hindered determination of the full-length structures of the three wild-type isoforms. We are approaching structure analysis of the three isoforms and their monomeric mutants by chemical footprinting (*46*) including H/DX coupled with MS. Unlike other covalent protein footprinting methods, H/DX is general, marking all the amino acids except proline and covering nearly the entire protein backbone, provided the proteolysis and LC/MS efficiencies are high.

Our H/DX results not only confirm the role of the C-terminal domain in the oligomerization process but also reveal the dissociation rate of oligomers to give monomers. We found that the three wild-type isoforms largely share oligomerization properties. A bottom-up H/DX-ETD experiment also located deuterium on lipid-free ApoE4 including its wild type and monomeric mutant form and afforded information on approximately 50% of the amides. We obtained clear, single-amide-level H/DX results for ApoE4, identified the residues involved in self-association, and showed they are located in the C-terminal domain (i.e., residues 232-272).

The region of apoE that shows differential H/DX between the wild-type protein and the monomeric mutant includes the residues 244-272, which harbor the lipid-binding

site (*47*) and are involved in Aβ binding, with implications for understanding Alzheimer's Disease (*47*). In addition, residues 241-272 mediate the toxic effects of ApoE4 in neuroblastoma cells (*48*). Thus, the residues 232-272 in the C-terminal domain seem to be involved in the multiple processes that are crucial for biological function and that mediate toxicity. Additional studies along these lines should increase our understanding of ApoE interactions with itself and with various ligands, an understanding that will be difficult to obtain by NMR and X-ray crystallography. Furthermore, H/DX and other footprinting strategies should not only provide information for the design of other ApoE monomeric mutants that contain a minimum number of mutation sites but also be a means for evaluating their equivalency.

5.6 ACKNOWLEDGEMENT

We thank Dr. Jun Zhang for assistance with the H/DX plate form and Berevan Baban for technical assistance. This research was supported by the NCRR of the NIH (Grant No. 21 2P41RR000954) to MLG.

5.7 REFERENCES

1. Yokoyama, S., Kawai, Y., Tajima, S., and Yamamoto, A. (1985) Behavior of human apolipoprotein E in aqueous solutions and at interfaces, *J. Biol. Chem. 260*, 16375-16382.

2. Hatters, D. M., Peters-Libeu, C. A., and Weisgraber, K. H. (2006) Apolipoprotein E structure: insights into function, *Trends in Biochemical Sciences 31*, 445-454.

3. Weisgraber, K. H., C.B. Anfinsen, J. T. E. F. M. R., and David, S. E. (1994) Apolipoprotein E: Structure-Function Relationships, In *Advances in Protein Chemistry*, pp 249-302, Academic Press.

4. Herz, J., and Beffert, U. (2000) Apolipoprotein E receptors: linking brain development and alzheimer's disease, *Nat. Rev. Neurosci. 1*, 51-58.

5. Zhang, Y., Chen, J., and Wang, J. (2008) A complete backbone spectral assignment of lipid-free human apolipoprotein E (apoE), *Biomolecular NMR Assignments 2*, 207-210.

6. Raussens, V., Drury, J., Forte, T. M., Choy, N., Goormaghtigh, E., Ruysschaert, J.-M., and Narayanaswami, V. (2005) Orientation and mode of lipid-binding interaction of human apolipoprotein E C-terminal domain, *Biochem. J. 387*, 747-754.

7. Wetterau, J. R., Aggerbeck, L. P., Rall, S. C., and Weisgraber, K. H. (1988) Human apolipoprotein E3 in aqueous solution. I. Evidence for two structural domains, *J. Biol. Chem. 263*, 6240-6248.

8. Vasudevan, S., Sojitrawala, R., Zhao, W., Cui, C., Xu, C., Fan, D., Newhouse, Y., Balestra, R., Jerome, W. G., Weisgraber, K., Li, Q., and Wang, J. (2007) A Monomeric, Biologically Active, Full-Length Human Apolipoprotein E, *Biochemistry 46*, 10722-10732.

9. Wilson, C., Wardell, M. R., Weisgraber, K. H., Mahley, R. W., and Agard, D. A. (1991) Three-dimensional structure of the LDL receptor-binding domain of human apolipoprotein E, *Science 252*, 1817-1822.

10. Westerlund, J. A., and Weisgraber, K. H. (1993) Discrete carboxyl-terminal segments of apolipoprotein E mediate lipoprotein association and protein oligomerization, *J. Biol. Chem. 268*, 15745-15750.

11. Segrest, J. P., Jones, M. K., De Loof, H., Brouillette, C. G., Venkatachalapathi, Y. V., and Anantharamaiah, G. M. (1992) The amphipathic helix in the exchangeable apolipoproteins: a review of secondary structure and function, *J. Lipid Res. 33*, 141-166.

12. Choy, N., Raussens, V., and Narayanaswami, V. (2003) Inter-molecular Coiled-coil Formation in Human Apolipoprotein E C-terminal Domain, *J. Mol. Biol. 334*, 527-539.

13. Chen, J., Li, Q., and Wang, J. (2011) Topology of human apolipoprotein E3 uniquely regulates its diverse biological functions, *Proc. Natl. Acad. Sci. 108*, 14813-14818.

14. Chou, C.-Y., Lin, Y.-L., Huang, Y.-C., Sheu, S.-Y., Lin, T.-H., Tsay, H.-J., Chang, G.-G., and Shiao, M.-S. (2005) Structural Variation in Human Apolipoprotein E3 and E4: Secondary Structure, Tertiary Structure, and Size Distribution, *Biophys. J. 88*, 455-466.

15. Perugini, M. A., Schuck, P., and Howlett, G. J. (2000) Self-association of Human Apolipoprotein E3 and E4 in the Presence and Absence of Phospholipid, *J. Biol. Chem. 275*, 36758-36765.

16. Aggerbeck, L. P., Wetterau, J. R., Weisgraber, K. H., Wu, C. S., and Lindgren, F. T. (1988) Human apolipoprotein E3 in aqueous solution. II. Properties of the amino- and carboxyl-terminal domains, *J. Biol. Chem. 263*, 6249-6258.

17. Garai, K., and Frieden, C. (2010) The Association Dissociation Behavior of the ApoE Proteins: Kinetic and Equilibrium Studies, *Biochemistry 49*, 9533-9541.

18. Fan, D., Li, Q., Korando, L., Jerome, W. G., and Wang, J. (2004) A Monomeric Human Apolipoprotein E Carboxyl-Terminal Domain, *Biochemistry 43*, 5055-5064.

19. Pan, J., Han, J., Borchers, C. H., and Konermann, L. (2011) Conformer-Specific Hydrogen Exchange Analysis of Ab(1-42) Oligomers by Top-Down Electron Capture Dissociation Mass Spectrometry, *Anal. Chem. 83*, 5386-5393.

20. Chalmers, M. J., Busby, S. A., Pascal, B. D., West, G. M., and Griffin, P. R. (2011) Differential hydrogen/deuterium exchange mass spectrometry analysis of protein-ligand interactions, *Expert Rev. Proteomics 8*, 43-59.

21. Engen, J. R. (2009) Analysis of Protein Conformation and Dynamics by Hydrogen/Deuterium Exchange MS, *Anal. Chem. 81*, 7870-7875.

22. Wang, L., Pan, H., and Smith, D. L. (2002) Hydrogen Exchange-Mass Spectrometry, *Mol. Cell. Proteomics 1*, 132-138.

23. Rand, K. D., Zehl, M., Jensen, O. N., and Jorgensen, T. J. D. (2009) Protein Hydrogen Exchange Measured at Single-Residue Resolution by Electron Transfer Dissociation Mass Spectrometry, *Anal. Chem. 81*, 5577-5584.

24. Jorgensen, T. J. D., Gardsvoll, H., Ploug, M., and Roepstorff, P. (2005) Intramolecular Migration of Amide Hydrogens in Protonated Peptides upon Collisional Activation, *J. Am. Chem. Soc. 127*, 2785-2793.

25. Demmers, J. A. A., Rijkers, D. T. S., Haverkamp, J., Killian, J. A., and Heck, A. J. R. (2002) Factors Affecting Gas-Phase Deuterium Scrambling in Peptide Ions and Their Implications for Protein Structure Determination, *J. Am. Chem. Soc. 124*, 11191-11198.

26. Hoerner, J. K., Xiao, H., Dobo, A., and Kaltashov, I. A. (2004) Is There Hydrogen Scrambling in the Gas Phase? Energetic and Structural Determinants of Proton Mobility within Protein Ions, *J. Am. Chem. Soc. 126*, 7709-7717.

27. Ferguson, P. L., Pan, J., Wilson, D. J., Dempsey, B., Lajoie, G., Shilton, B., and Konermann, L. (2006) Hydrogen/Deuterium Scrambling during Quadrupole Time-of-Flight MS/MS Analysis of a Zinc-Binding Protein Domain, *Anal. Chem. 79*, 153-160.

28. Jorgensen, T. J. D., Bache, N., Roepstorff, P., Gardsvoll, H., and Ploug, M. (2005) Collisional Activation by MALDI Tandem Time-of-flight Mass Spectrometry Induces Intramolecular Migration of Amide Hydrogens in Protonated Peptides, *Mol. Cell. Proteomics 4*, 1910-1919.

29. Rand, K. D., and Jorgensen, T. J. D. (2007) Development of a Peptide Probe for the Occurrence of Hydrogen (1H/2H) Scrambling upon Gas-Phase Fragmentation, *Anal. Chem. 79*, 8686-8693.

30. Zehl, M., Rand, K. D., Jensen, O. N., and Jorgensen, T. J. D. (2008) Electron Transfer Dissociation Facilitates the Measurement of Deuterium Incorporation into Selectively Labeled Peptides with Single Residue Resolution, *J. Am. Chem. Soc. 130*, 17453-17459.

31. Rand, K. D., Zehl, M., Jensen, O. N., and Jorgensen, T. J. D. (2010) Loss of Ammonia during Electron-Transfer Dissociation of Deuterated Peptides as an Inherent Gauge of Gas-Phase Hydrogen Scrambling, *Anal. Chem. 82*, 9755-9762.

32. Hamuro, Y., Tomasso, J. C., and Coales, S. J. (2008) A Simple Test To Detect Hydrogen/Deuterium Scrambling during Gas-Phase Peptide Fragmentation, *Anal. Chem. 80*, 6785-6790.

33. Garai, K., Mustafi, S. M., Baban, B., and Frieden, C. (2010) Structural differences between apolipoprotein E3 and E4 as measured by 19F NMR, *Protein Science 19*, 66-74.

34. Hatters, D. M., Budamagunta, M. S., Voss, J. C., and Weisgraber, K. H. (2005) Modulation of Apolipoprotein E Structure by Domain Interaction, *J. Biol. Chem. 280*, 34288-34295.

35. Busby, S. A., Chalmers, M. J., and Griffin, P. R. (2007) Improving digestion efficiency under H/D exchange conditions with activated pepsinogen coupled columns, *Int. J. Mass Spectrom. 259*, 130-139.

36. Weis, D., Engen, J., and Kass, I. (2006) Semi-automated data processing of hydrogen exchange mass spectra using HX-Express, *J. Am. Soc. Mass Spectrom. 17*, 1700-1703.

37. Garai, K., Baban, B., and Frieden, C. (2011) Self-Association and Stability of the ApoE Isoforms at Low pH: Implications for ApoE-Lipid Interactions, *Biochemistry 50*, 6356-6364.

38. Zhu, M. M., Chitta, R., and Gross, M. L. (2005) PLIMSTEX: a novel mass spectrometric method for the quantification of protein-ligand interactions in solution, *Int. J. Mass Spectrom. 240*, 213-220.

39. Zhu, M. M., Rempel, D. L., and Gross, M. L. (2004) Modeling data from titration, amide H/D exchange, and mass spectrometry to obtain protein-ligand binding constants, *J. Am. Soc. Mass Spectrom. 15*, 388-397.

40. Gau, B., Garai, K., Frieden, C., and Gross, M. L. (2011) Mass Spectrometry-based Protein Footprinting Characterizes the Structures of Oligomeric Apolipoprotein E2, E3, and E4 *Biochemistry 50*, 8117-8126.

41. Peters-Libeu, C. A., Weisgraber, K. H., Segelke, B. W., Rupp, B., Capila, I., Hernáiz, M. J., LeBrun, L. A., and Linhardt, R. J. (2001) Interaction of the N-Terminal Domain of Apolipoprotein E4 with Heparin, *Biochemistry 40*, 2826-2834.

42. Zhang, Z., and Smith, D. L. (1993) Determination of amide hydrogen exchange by mass spectrometry: A new tool for protein structure elucidation, *Protein Science 2*, 522-531.

43. Patel, A. B., Khumsupan, P., and Narayanaswami, V. (2010) Pyrene Fluorescence Analysis Offers New Insights into the Conformation of the Lipoprotein-Binding Domain of Human Apolipoprotein E, *Biochemistry 49*, 1766-1775.

44. Chen, J., Li, Q., and Wang, J. (2011) Topology of human apolipoprotein E3 uniquely regulates its diverse biological functions, *Proc. Nat. Acad. Sci.*, Accepted.

45. Morrow, J. A., Segall, M. L., Lund-Katz, S., Phillips, M. C., Knapp, M., Rupp, B., and Weisgraber, K. H. (2000) Differences in Stability among the Human

Apolipoprotein E Isoforms Determined by the Amino-Terminal Domain, *Biochemistry 39*, 11657-11666.

46. Gau, B., Garai, K., Frieden, C., and Gross, M. L. (2011) Mass Spectrometry-based Protein Footprinting Characterizes the Structures of Oligomeric Apolipoprotein E2, E3, and E4 *Biochemistry*, Accepted.

47. Mahley, R. W., and Rall, S. C. (2000) APOLIPOPROTEIN E: Far More Than a Lipid Transport Protein, *Annual Review of Genomics and Human Genetics 1*, 507-537.

48. Chang, S., Ma, T. r., Miranda, R. D., Balestra, M. E., Mahley, R. W., and Huang, Y. (2005) Lipid- and receptor-binding regions of apolipoprotein E4 fragments act in concert to cause mitochondrial dysfunction and neurotoxicity, *Proc. Natl. Acad. Sci. 102*, 18694-18699.

Chapter 6

Hydrogen/Deuterium Exchange Mass Spectrometry Probes the Apolipoprotein E-Amyloid-β (Aβ 40) Interactions

6.1 ABSTRACT

Apolipoprotein E (ApoE), which may be involved in the clearance of amyloid-β (Aβ) from the brain, is an important factor in various diseases including Alzheimer's Disease (AD). It is a 34 kDa protein consisting of two domains separated by a region of random structure. Each domain has a distinct function and structure. The N-terminal domain, for example, contains receptor-binding and heparin (proteoglycan)-binding regions, whereas the C-terminal domain contains the major lipid-binding site. Although the C-terminal domain (residues 216-299) of ApoE is believed to be the potential region that binds to Aβ, the specific regions involved in this interaction are not yet known. Here we report the use of hydrogen/deuterium exchange (H/DX) coupled with mass spectrometry to identify those regions that are involved in ApoE-Aβ interactions. Given that the C-terminal regions of ApoE contain the interfaces for its oligomerization, the interaction between ApoE and Aβ may be shifted to other sites. Our results suggest, however, that oligomerization of ApoE does compete with the interaction with Aβ. Interestingly, region 52-60 of ApoE, located at the N-terminal domain, show some decrease of deuterium uptake in the presence of Aβ. This finding provides additional

support for the importance of the N-terminal region of ApoE in the ApoE-Aβ complex formation.

6.2 INTRODUCTION

The aggregation and deposition of Aβ as plaques in the brain may be key to understanding the early processes causing Alzheimer's Disease (AD) (*1*). Amyloid-β (Aβ) is formed after sequential cleavage of the amyloid precursor protein (*2*) by α-, β- and γ-secretases. The propensity of Aβ aggregation is different for different sequence lengths of the cleavage products. For example, Aβ(1–42) has higher tendency to form oligomers in solution than Aβ(1–40) (*3*). Recently, an NMR structure of Aβ(1–40) shows it has a helix in the middle region (residue 12-23) whereas the N and C-terminal regions of Aβ40 are unstructured (*4*). Understanding the processes of Aβ aggregation so that one can modulate the population of the various aggregation states of Aβ in the brain may be crucial for the treatment of Alzheimer's Disease.

Apolipoprotein E (ApoE), a major lipid transporter in plasma and the central nervous system (*5-7*), may affect both the deposition and clearance of Aβ from the brain and, hence, play a role in the pathogenesis of Alzheimer's Disease (*1*). There are three major isoforms, ApoE2, ApoE3 and ApoE4, differing in the progression by only single amino-acid substitutions (*7*). These small differences alter significantly their biochemical properties. For example, ApoE4 is a major risk factor for Alzheimer's disease and cardiovascular diseases. In fact, the expression of ApoE4 in humans results in greater Aβ

and amyloid deposition than for expression of ApoE3 (*1*). ApoE2, on the other hand, seems to play a protective role (*8*).

The ApoE proteins consist of a 22 kDa N-terminal domain and a 10 kDa C-terminal domain (*9-11*), linked by a protease-sensitive hinge region. Each domain has a unique function. Whereas the N-terminal domain harbors the LDL receptor binding site, the C-terminal domain binds to lipids with high affinity and forms oligomers through self-interactions in this region (*6, 7, 12*).

ApoE may mediate the level of free Aβ in the brain by forming ApoE-Aβ complexes. Complex formation, however, is different among different isoforms of ApoE and under different conditions (i.e., temperature, pH). Lipidated ApoE4, for example, binds preferentially to an intermediate aggregation form of Aβ with 2-3 fold higher affinity than do ApoE2 and ApoE3 under the same conditions (*13*). Lipid-free ApoE3, on the other hand, forms an ApoE-Aβ complex with apparent higher affinity with respect to ApoE4 (*14*). The C-terminal regions of ApoE (244-272) and the N-terminal regions of Aβ (1-28) are believed to be involved in the ApoE-Aβ interactions (*15, 16*). These same regions of Aβ are likely to be involved also in self-association (*17*). A recent study of the ApoE-Aβ interactions by MD simulation, however, suggests the interactions occur on helix I and IV of the N-terminal domain of ApoE (*18*). Although these studies

led to controversial conclusions on the regions of ApoE that are involved in ApoE-Aβ complex formation, the importance of ApoE in the etiology of Alzheimer's disease is certain. Therefore, understanding the interactions between ApoE and Aβ is essential for the study of this disease.

The oligomerization properties of ApoE were recently studied in our group, as shown in chapter five, by using hydrogen/deuterium exchange (H/DX) and fast photochemical oxidation of proteins (FPOP), both in combination with MS (*19, 20*). The results show that the interfaces for ApoE oligomerization are mainly located at the C-terminal region of ApoE. Given that this region contains potential binding sites with Aβ, as shown in the previous study (*15*), it is our interest to extend the H/DX MS strategy to the study of ApoE-Aβ complex formation.

H/DX coupled with MS (*21-24*) has become a powerful tool that can probe both protein conformational changes associated with protein-ligand interactions (ligand: protein, DNA, peptide, drug etc) and also protein dynamics. Given that ApoE3 appears to form a stable complex with Aβ in a lipid-free environment and that Aβ40 has lower tendency to self-aggregate in solution, we chose these two as our first target in this study. The outcomes may lead to an improved understanding of the ApoE-Aβ complex formation and serve as a useful reference point for future studies of Aβ and ApoE.

6.3 EXPERIMENTAL PROCEDURES

6.3.1 Protein expression

Wild type apolipoprotein E3 (ApoE3WT) was expressed in *E. coli* and purified as described previously by Garai et al. (*25*). Briefly, ApoE proteins were expressed in *Escherichia coli* (Strain BL21, DE3 competent cells, Stratagene), which was grown in LB media to OD_{600} = 0.6.

6.3.2 Materials

HEPES hemisodium salt [*N*-(2-hydroxyethyl)piperazine-*N*′-(2-ethanesulfonic acid) hemisodium salt], Tris(2-carboxyethyl)phosphine hydrochloride (TCEP), porcine pepsin, citric acid, sodium citrate, sodium chloride, potassium chloride, and ethanolamine were purchased from Sigma-Aldrich (St.Louis, MO). Aβ40 was from Keck biotechnology resource laboratory (Yale University, New Haven, CT). D_2O was purchased from Cambridge Isotope Laboratories Inc (Andover, MA).

6.3.3 Preparation of ApoE3-Aβ40 complex

Aβ40 was dissolved in 3 mM NaOH, 150 mM NaCl, 1 mM TCEP, and the monomeric Aβ40 was purified by using size-exclusion chromatography. ApoE3WT-Aβ40 complex was made by mixing ApoE3 and Aβ40 in a ratio of 1:5, a ratio that ensures the interaction was saturated and the ion intensity of ApoE3 was not suppressed

by Aβ40, at 0.5 μM analytical concentration of ApoE3WT in HEPES buffer (10 mM HEPES, 150 mM NaCl, 100 μM TCEP, pH 7.4). The mixture was incubated at 25 °C for various times (30 s, 5 min, 20 min, 1 h, 8 h, 24 h, 52 h) prior to submitting the system to H/DX.

6.3.4 H/D Exchange (H/DX) Protocol

For global H/DX pulse labeling experiments, the ApoE3WT-Aβ40 complex was diluted 1:4 in D_2O buffer (10 mM HEPES, 150 mM NaCl, pD 7.4) at 25 °C for 1 min. The H/DX was quenched by adding sufficient 1 M HCl at 0 °C to give a final pH of 2.5. The quenched protein solution was then loaded onto a C8 guard column (1 mm x 15 mm, Optimize Technologies, Oregon, City, OR) via an Agilent 1100 HPLC (Santa Clara, CA) operated at 50 μM/min flow rate with 0.1% TFA for 3 min. The protein was eluted by using a Waters nanoACQUITY UPLC (Manchester, U.K) with the following gradient settings: 5% to 50% solvent B in 0.3 min, 50% to 100% solvent B in 5.2 min and isocratic flow at 100% solvent B for 0.5 min, then back to 5% solvent B in 0.1 min at 50 μM/min flow rate. All LC connection lines were immersed in a water-ice (0 °C) bath. (solvent A, water containing 0.1% formic acid; solvent B, acetonitrile containing 0.1% formic acid).

For peptide level H/DX experiments, the ApoE3WT-Aβ40 complex was diluted 1:3 in D_2O buffer (10 mM HEPES, 150 mM NaCl, pD 7.4) at 25 °C. At various times (30 s, 3 min, 5 min, 10 min, 30 min, 1 h), the H/DX was quenched as described above. The quenched solution was then injected into an on-line pepsin-digestion device containing immobilized pepsin in a 1 mm diameter × 2 cm length guard column (Upchurch Scientific, Oak Harbor, WA), which was prepared as described previously (*26*). The quenched solution was injected into the pepsin column in 0.1% formic acid via an Agilent 1100 HPLC (Santa Clara, CA) operated at 50 μL/min flow rate for 6 min. The digested protein solution was trapped on a C18 guard column (1 mm diameter x 1.5 cm length, Optimize Technologies, Oregon City, OR). The peptide mixture was then eluted from the trap column and separated with a C18 analytical column (1 mm diameter x 5 cm length, Dionex, Bannockburn, IL) via a Waters nanoACQUITY UPLC (Manchester, U.K) with a gradient operated at 50 μL/min flow rate. Solvent A was water containing 0.1% formic acid, and solvent B was 80% acetonitrile, 20% water containing 0.1% formic acid. The gradient settings were: 5% to 15% solvent B in 0.3 min, 15% to 50% solvent B in 5.2 min, 50% to 100% solvent B in 0.5 min, and isocratic flow at 100% solvent B for 1.5 min, then returned to 5% solvent B in 0.1 min. All LC connection lines were immersed in a water-ice (0 °C) bath.

6.3.5 LC-ESI/MS Analysis with a Q-TOF Mass Spectrometer

All H/DX results were acquired on a MaXis (Bruker, Bremen, Germany) quadrupole time-of-flight (Q-TOF) mass spectrometer. The settings were: capillary voltage, 3.8 kV; nebulizer gas, 0.5 bar; drying gas flow rate and temperature, 8.0 L/min and 200 °C, respectively; funnel RF, 400 V(pp).

6.3.6 LC-ESI/MS/MS Analysis with an Orbitrap Mass Spectrometer

The sequence of each peptic peptide was confirmed by analyzing the digested peptides on a Thermo LTQ XL Orbitrap (Thermo Fisher, San Jose, CA). The settings were: spray voltage, 3.2 kV; sheath-gas flow rate, 8 (arbitrary units); capillary temperature, 275 °C; capillary voltage, 35 V; and tube lens, 110 V. One full mass spectral acquisition triggered three scans of MS/MS (CID fragmentation) whereby the most abundant precursor ions were activated for sequencing. The peaks observed in the product-ion spectra were centroided to provide the mass for each peptide during the acquisition.

6.3.7 Mascot database search

Thermo RAW files were processed by using extract_msn (2007 version 4.0, Thermo Fisher, San Jose, CA) with a grouping tolerance of 0.8 Da, an intermediate scan setting of 1, and a minimum of 1 scan per group. MASCOT 2.2.06 (Matrix Science,

Oxford, U.K.) was used to analyze the results by searching through the NCBI nonredundant database (version 20101004, restricted to human). The MASCOT settings were: enzyme, none; MS tolerance, 10 ppm; MS/MS tolerance, 0.8 Da; maximum number of missed cleavages, 3; peptide charge of 1+, 2+ and 3+; oxidation of methionine was set as variable modification.

6.3.8 Data analysis

The uptake of deuterium for each protein or peptide was measured as the average mass differences between the masses of the deuterated protein and the undeuterated protein, or the average differences between the centroid of all the mass peaks of the deuterated peptide and the undeuterated peptide. Back-exchange was measured to be one deuterium loss per minute. No correction for back exchange was applied because the time between sample quench and the measurement with the mass spectrometer was within 10 min and conclusions were drawn based on comparisons of data taken consistently. The deconvoluted protein mass spectrum was generated with MagTran 1.03 (Amgen, Thousand Oaks, CA). The centroid of the peptide isotopic distribution was analyzed using HDExaminer 1.0 (Sierra Analytics, Modesto, CA). All experiments were performed in at least triplicate.

6.4 RESULTS AND DISCUSSION

6.4.1 Examination of the ApoE3-Aβ40 complex formation by H/DX pulse labeling

Apolipoprotein E isoforms exist predominantly as tetramers at low μM concentrations and dissociate into dimers and monomers at high nM concentrations (*27*). At analytical concentrations higher than μM, the protein starts to aggregate (*27*, *28*). It is known that the C-terminal domain plays a major role in this self-association (*29*). An important question is whether self association competes with the ApoE-Aβ interactions. To monitor the formation of ApoE3WT-Aβ40 complex, we first measured global H/DX kinetics in which the ApoE3WT was mixed with Aβ40 in 1 to 5 ratio at 25 °C for 1 h followed by allowing H/DX for various times (30 s to 24 h) (**Figure 6-1**). The outcome, however, is no significant differences in deuterium uptake of ApoE3WT in the absence or presence of Aβ40. This suggests that these two proteins do not form a stable complex under these conditions.

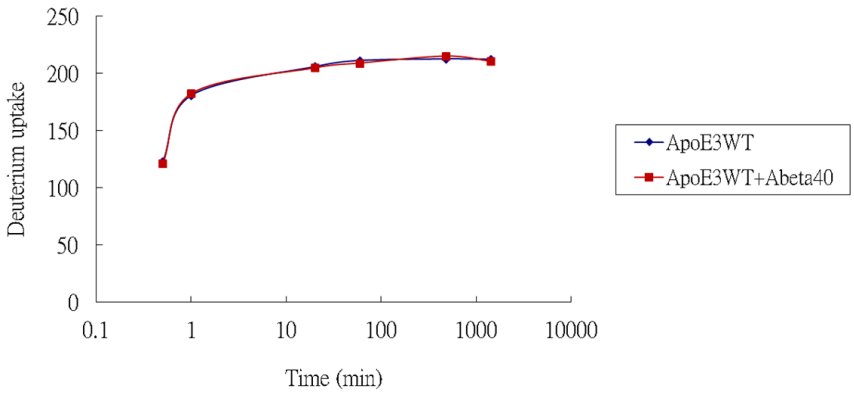

Figure 6-1. Global H/DX kinetics of ApoE3WT. A comparison between apo-ApoE3WT (Aβ40 free, blue) and holo-ApoE3WT (Aβ40 bound, red) shows no differences in H/DX.

One explanation of the above is that the kinetics of complex formation are too slow to allow detection of a complex under those conditions. If so, a more informative way may be to monitor complex formation as a function of the incubation times for these two proteins by using a pulsed H/DX labeling strategy. In this experiment, we mixed ApoE3WT with Aβ40 under same conditions as described above and incubated the resulting solution for various times (30 s to 52 h). The resulting solution was then submitted to pulsed H/DX for 1 min. Pulsing the H/DX allowed it to be a reporter and present a "snapshot" of any slow-forming states of Aβ40 bound to ApoE3WT (**Figure 6-2**).

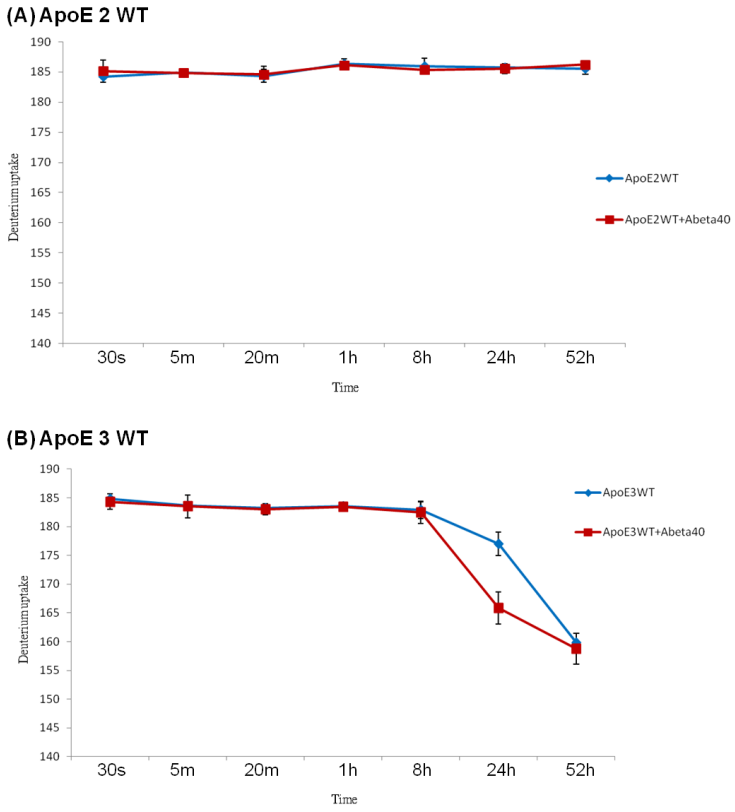

Figure 6-2. Global H/DX pulse labeling of ApoE. (A) A comparison between apo-ApoE2WT (Aβ40 free, blue) and holo-ApoE2WT (Aβ40 bound, red) shows no differences in H/DX. (B) A comparison between apo-ApoE3WT (Aβ40 free, blue) and holo-ApoE3WT (Aβ40 bound, red) shows significant differences in H/DX after 24 h of incubation.

Carter and coworkers (*13*) studied the ApoE-Aβ interactions among the ApoE isoforms by ELISA, and they concluded that the non-lipidated ApoE isoforms interact with Aβ without isoform specificity. To test this interpretation, we incorporated ApoE2WT into our study. Surprisingly, there are no differences in deuterium uptake of ApoE2WT in the presence or absence of Aβ40 (**Figure 6-2A**). ApoE3WT, on the other hand, showed a significant decrease in deuterium uptake for the Aβ40 bound state after

24 h incubation (**Figure 6-2B**). Because our longest incubation time was 52 h, which might not be long enough for ApoE2 to form stable complex with Aβ40, we cannot rule out the possibility of their interactions. Our results, however, indicate that ApoE3WT interacts more strongly with Aβ40 than ApoE2WT.

Interestingly, a significant decrease in deuterium uptake also occurred for apo-ApoE3WT (Aβ40 free) after 24 h of incubation as compared to 8 h, and the D uptake decreased further at longer times (52 h), finally reaching the same level as that for ApoE3WT in the presence of Aβ40 bound. This suggests that ApoE3WT itself forms a more complex structure after long incubation, and its self-interaction interfaces may be shared in any ApoE3WT-Aβ40 complex. Moreover, ApoE3WT may have a higher tendency to form this complex than does ApoE2WT, as the latter does not show this phenomenom. Given that there is a significant difference in deuterium uptake between apo-ApoE3WT and holo-ApoE3WT at 24 h incubation, we chose this condition to conduct H/DX at the peptide-level to provide a more detailed picture of their interactions.

6.4.2 Peptide-level H/DX kinetics reveals the regions of ApoE3WT involved in ApoE3WT-Aβ40 interactions

The higher resolution achievable with bottom-up H/DX may allow localization of some minor changes in the solvent assessibility/H-bonding due to ligand binding.

Peptide-level H/DX kinetics, as shown in our previous study of ApoE (*19*), can not only identify those regions that are involved in protein-protein or protein-ligand interactions but also reveal the dynamics of the interactions. Therefore, we applied this strategy to the ApoE3WT-Aβ40 complex under the conditions determined by the global measurement in which a 0.5 μM (analytical concentration) ApoE3WT solution containing 2.5 μM Aβ40 was equilibrated at 25 °C for 24 h followed by diluting the protein solution 1:3 in D_2O buffer for various times (30 s to 1 h). After quenching the exchange, we submitted the protein to on-line pepsin digestion and analyzed the peptides by LC/MS.

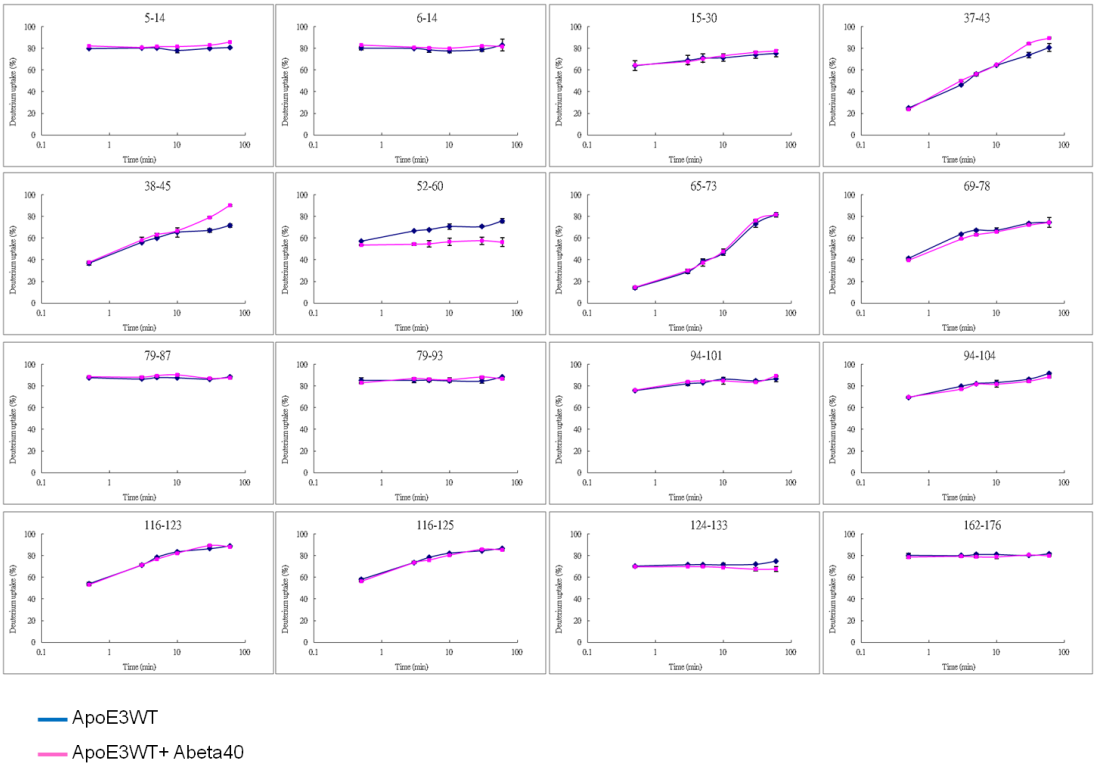

Figure 6-3. Peptide-level H/DX kinetics of the N-terminal regions of ApoE3WT (1-176). A comparison between apo-ApoE3WT (Aβ40 free, blue) and holo-ApoE3WT (Aβ40 bound, red) was plotted for different peptic peptides as a function of H/DX times.

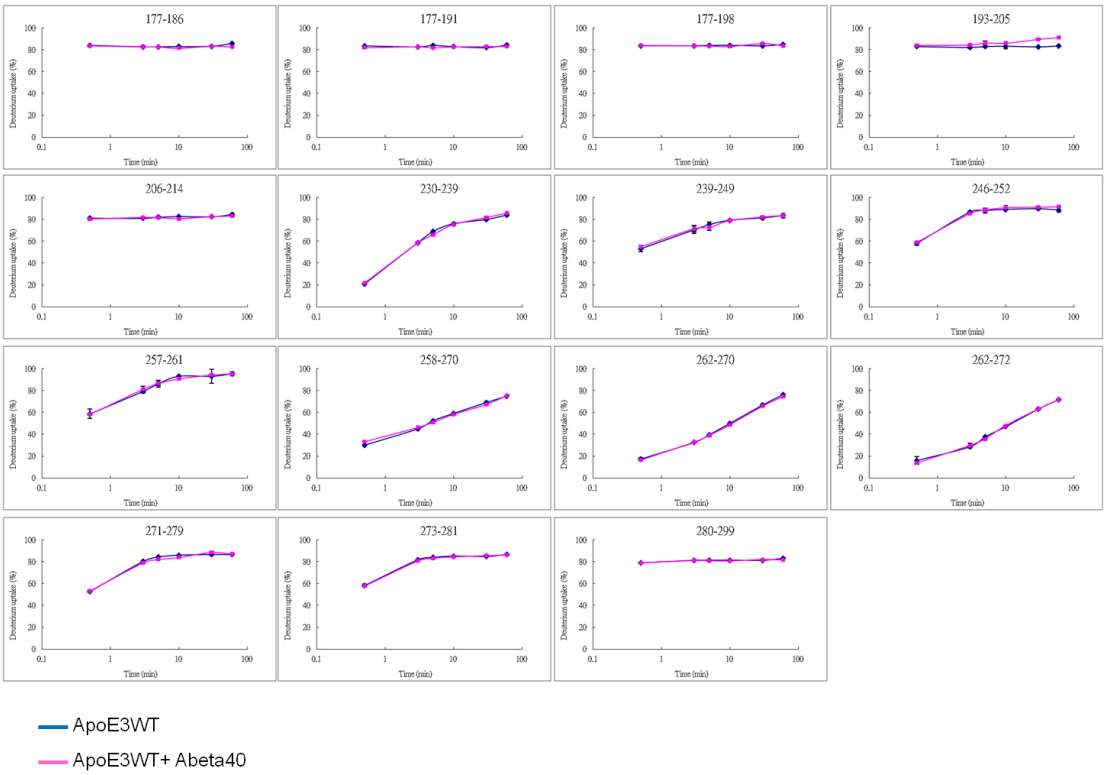

Figure 6-4. Peptide-level H/DX kinetics of the C-terminal regions of ApoE3WT (177-299). A comparison between apo-ApoE3WT (Aβ40 free, blue) and holo-ApoE3WT (Aβ40 bound, red) was plotted for different peptic peptides as a function of H/DX times.

A sequence coverage of ~89% of ApoE3WT ensures a nearly complete picture of the protein. We normalized the value of deuterium uptake of each peptide to the theoretical maximum uptake, as described previously (*30*), and corrected the fraction of deuterium present in the exchanging solution to evaluate the relative deuterium uptake of each peptide (**Figure 6-3 and 6-4**). Figure 6-3 shows peptide-level H/DX kinetics of peptides located at the N-terminal domain of ApoE3WT (residue 1-176). The kinetics plots of apo-ApoE3WT present two categories of deuterium uptake: (1) regions showing

low deuterium uptake at early exchange times and increasing uptake at longer times, (2) regions showing extensive deuterium uptake at the early exchange time and the uptake stays relatively constant at longer times. There are three regions of ApoE3WT represented by peptide 37-45, 65-78, and 116-125 that undergo H/DX characteristic of the first category. These regions, when mapped onto the ApoE3 NMR structure (2L7B) (*31*), are all located, not surprisingly, on rigid helices that should show slow dynamics. Other regions, having the characteristic of the second category, are all located at or near the flexible loop regions. Our results of the N-terminal regions of ApoE3WT agree well with its tertiary structure.

Interestingly, one peptide (residue 52-60) showed a significant decrease (~10%) of deuterium uptake upon the Aβ40 binding. Peptide regions 37-45, on the other hand, showed reverse trends of H/DX, implicating an increase in flexibility upon binding. These results implicate, for the first time, the interfaces of the N-terminal domain of ApoE3WT in the ApoE-Aβ complexes.

The H/DX kinetics of peptide regions located at the C-terminal domain of ApoE3WT, shown in Figure 6-4 (177-299), show there are almost no H/DX differences in this region between apo-ApoE3WT and ApoE3WT in the presence of excess Aβ. Peptides located in region 230-272, however, showed a slow increase in H/DX with time,

indicating a region that exhibits slow protein dynamics. This was observed in our previous study of ApoE oligomerization (*19*) and suggests there may be a slow dissociation of the ApoE oligomers as reported by the slow uptake of D in this region. Given that wild-type ApoE exists as a mixture of monomers, dimers, and tetramers at 500 nM (*27*), and the association constants of ApoE itself and ApoE-Aβ are similar (~10^7 M^{-1}) (*14*, *27*), the reversible association and dissociation processes of monomer-dimer-tetramer may compete with any ApoE3WT-Aβ40 interactions located at the C-terminal regions of ApoE, and hinder investigation of the interfaces of Aβ and apoE by H/DX. Strittmatter and coworkers (*15*) studied the ApoE-Aβ(1−28) interactions by native-gel chromatography and concluded that region 244-272 of ApoE is crucial for binding with Aβ. The ratio of Aβ to ApoE used in their study, however, is 70 times higher than that used in our experiments. We could not use this relatively high amount of Aβ because it will seriously suppress ApoE peptide ions in the H/DX-MS experiment and prevent doing H/DX experiments at this level.

Among all the peptides representing full-length ApoE3WT, only peptide region 52-60 shows protection upon the binding of Aβ40, and only two amide hydrogens in this region are affected by this binding. The global H/DX measurement, however, shows that approximately 10 amide hydrogens of ApoE3WT are affected by binding of Aβ40.

Given that the peptide sequence coverage is not complete (i.e., nearly 90%), the other differences may be located in these 10% missing regions or lost by back exchange during the LC separation. Nevertheless, our results indicate a weak interaction of Aβ40 with ApoE3WT at region 52-60 in the N-terminal domain.

6.4.3 H/DX mapped on a ApoE3 monomeric mutant structure

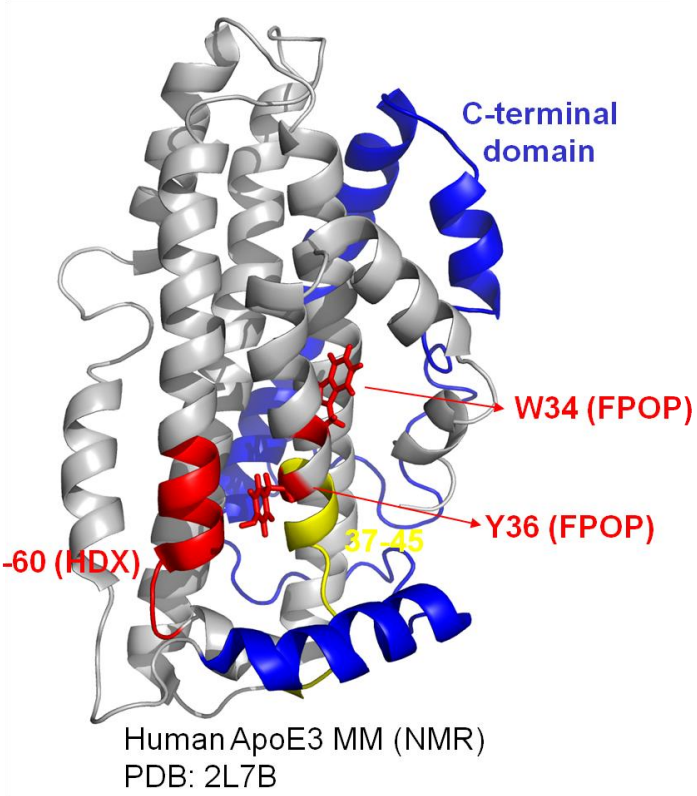

Figure 6-5. H/DX mapping on the ApoE3MM (F257A/W264R/L279Q and V287E) NMR structure (PDB: 2L7B). Region 52-60, having significant decrease of D uptake in the presence of Aβ0 is shown in red. Residue W34 and Y36, having significant decrease of labeling in the presence of Aβ42 by FPOP, are shown in red. Regions 37-45, having allosteric behaviors in the presence of Aβ40 is shown in yellow. The C-terminal domain is shown in blue.

The high propensity of ApoE to oligomerize has hindered determination of the full-length structures of the three wild-type isoforms. Wang and coworkers (*31*), however, recently elucidated the solution NMR structure of a monomeric mutant of ApoE3 (F257A/W264R/L279Q and V287E) (PDB: 2L7B). To provide a clearer picture of the interfaces between ApoE3WT and Aβ40, we mapped our H/DX results onto this structure (**Figure 6-5**).

Interestingly, peptide region 52-60 together with regions 37-45, are proximate to each other in the actual protein structure (**Figure 6-5**). Given that Brian Gau of the Gross lab used fast photochemical oxidation of proteins (FPOP) on ApoE3WT-Aβ42 complexes (*32*) and observed a significant decrease in oxidative modification on the side chains of W34 and Y36 of ApoE3WT when Aβ42 was present. Peptides containing these residues were unfortunately not detected in the H/DX experiments. These two residues, when mapped onto the ApoE3MM NMR structure (**Figure 6-5**) (helix I), are located on adjoining peptide region 52-60 (helix II). Although Aβ42 and Aβ40 have different tendencies to self-associate, they may share the same interfaces in the ApoE-Aβ40 complexes. Our results show that these two helices of ApoE3WT are the potential binding sites to Aβ. Moreover, once they bound to Aβ, the

structures of region 37-45 may be allosterically affected and become more solvent accessible (**Figure 6-5, yellow**).

6.5 CONCLUSIONS

Apolipoprotein E seems to play an important role in the clearance from the brain of Aβ, which is the major risk factor in Alzheimer's disease. The interaction between ApoE and Aβ, however, is complicated by the self-association properties of both of these proteins solution. Lipidation of ApoE alters its oligomerization properties, modulating its interaction with Aβ (*13, 33*). Lipid-free ApoE, on the other hand, may form a stable ApoE-Aβ complex in the presence of excess Aβ (*15*). Wild-type ApoE presents as a mixture of monomer, dimer, and tetramer at low uM concentrations, and the self-association involves C-terminal regions (*19*), which may be the same regions that interact with Aβ. Thus, the populations of different oligomers of ApoE and Aβ in solution may be crucial in determining their interactions.

Our H/DX results are not only consistent with the structure of the N-terminal domain of ApoE3WT but also reveal the regions that are affected in the presence of Aβ40. All of them are located at the N-terminal domain of ApoE3WT. Our results also show that self-association of ApoE3WT occurs at the C-terminal domain and that self-

association may compete with the interaction of Aβ40 and hinder detection of these interactions at the C-terminal domain.

Future studies should be aimed at increasing the population of the ApoE monomer in solution to enhance the interactions of ApoE with Aβ. H/DX and other MS-based footprinting approaches may provide the needed insights that will be difficult to obtain by high-resolution methods of NMR or X-ray crystallography and certainly by the low-resolution methods including CD, absorbance, and fluorescence.

6.6 ACKNOWLEDGEMENT

We thank Berevan Baban for technical assistance. This project was supported by a grant from the National Center for Research Resources (5P41RR000954-35), now the National Institute of General Medical Sciences (8 P41 GM103422-35) of the National Institutes of Health to MLG.

6.7 REFERENCES

1. Kim, J., Jiang, H., Park, S., Eltorai, A. E. M., Stewart, F. R., Yoon, H., Basak, J. M., Finn, M. B., and Holtzman, D. M. (2011) Haploinsufficiency of Human APOE Reduces Amyloid Deposition in a Mouse Model of Amyloid-β Amyloidosis, *The Journal of Neuroscience 31*, 18007-18012.

2. Morrow, J. A., Segall, M. L., Lund-Katz, S., Phillips, M. C., Knapp, M., Rupp, B., and Weisgraber, K. H. (2000) Differences in Stability among the Human Apolipoprotein E Isoforms Determined by the Amino-Terminal Domain, *Biochemistry 39*, 11657-11666.

3. Stine, W. B., Dahlgren, K. N., Krafft, G. A., and LaDu, M. J. (2003) In Vitro Characterization of Conditions for Amyloid-β Peptide Oligomerization and Fibrillogenesis, *Journal of Biological Chemistry 278*, 11612-11622.

4. Vivekanandan, S., Brender, J. R., Lee, S. Y., and Ramamoorthy, A. (2011) A partially folded structure of amyloid-beta(1–40) in an aqueous environment, *Biochemical and Biophysical Research Communications 411*, 312-316.

5. Yokoyama, S., Kawai, Y., Tajima, S., and Yamamoto, A. (1985) Behavior of human apolipoprotein E in aqueous solutions and at interfaces, *J. Biol. Chem. 260*, 16375-16382.

6. Hatters, D. M., Peters-Libeu, C. A., and Weisgraber, K. H. (2006) Apolipoprotein E structure: insights into function, *Trends in Biochemical Sciences 31*, 445-454.

7. Weisgraber, K. H., C.B. Anfinsen, J. T. E. F. M. R., and David, S. E. (1994) Apolipoprotein E: Structure-Function Relationships, In *Advances in Protein Chemistry*, pp 249-302, Academic Press.

8. Herz, J., and Beffert, U. (2000) Apolipoprotein E receptors: linking brain development and alzheimer's disease, *Nat. Rev. Neurosci. 1*, 51-58.

9. Zhang, Y., Chen, J., and Wang, J. (2008) A complete backbone spectral assignment of lipid-free human apolipoprotein E (apoE), *Biomolecular NMR Assignments 2*, 207-210.

10. Raussens, V., Drury, J., Forte, T. M., Choy, N., Goormaghtigh, E., Ruysschaert, J.-M., and Narayanaswami, V. (2005) Orientation and mode of lipid-binding interaction of human apolipoprotein E C-terminal domain, *Biochem. J. 387*, 747-754.

11. Wetterau, J. R., Aggerbeck, L. P., Rall, S. C., and Weisgraber, K. H. (1988) Human apolipoprotein E3 in aqueous solution. I. Evidence for two structural domains, *J. Biol. Chem. 263*, 6240-6248.

12. Vasudevan, S., Sojitrawala, R., Zhao, W., Cui, C., Xu, C., Fan, D., Newhouse, Y., Balestra, R., Jerome, W. G., Weisgraber, K., Li, Q., and Wang, J. (2007) A Monomeric, Biologically Active, Full-Length Human Apolipoprotein E, *Biochemistry 46*, 10722-10732.

13. Stratman, N. C., Castle, C. K., Taylor, B. M., Epps, D. E., Melchior, G. W., and Carter, D. B. (2005) Isoform-specific interactions of human apolipoprotein E to an intermediate conformation of human Alzheimer amyloid-beta peptide, *Chemistry and Physics of Lipids 137*, 52-61.

14. Petrlova, J., Hong, H.-S., Bricarello, D. A., Harishchandra, G., Lorigan, G. A., Jin, L.-W., and Voss, J. C. (2011) A differential association of Apolipoprotein E isoforms with the amyloid-β oligomer in solution, *Proteins: Structure, Function, and Bioinformatics 79*, 402-416.

15. Strittmatter, W. J., Weisgraber, K. H., Huang, D. Y., Dong, L. M., Salvesen, G. S., Pericak-Vance, M., Schmechel, D., Saunders, A. M., Goldgaber, D., and Roses, A. D. (1993) Binding of human apolipoprotein E to synthetic amyloid beta peptide: isoform-specific effects and implications for late-onset Alzheimer disease, *Proceedings of the National Academy of Sciences 90*, 8098-8102.

16. LaDu, M. J., Falduto, M. T., Manelli, A. M., Reardon, C. A., Getz, G. S., and Frail, D. E. (1994) Isoform-specific binding of apolipoprotein E to beta-amyloid, *Journal of Biological Chemistry 269*, 23403-23406.

17. Liu, Q., Wu, W.-h., Fang, C.-l., Li, R.-w., Liu, P., Lei, P., Hu, J., Sun, X., Zheng, Y.-z., Zhao, Y.-f., and Li, Y.-m. (2011) Mapping ApoE/Aβ binding regions to guide inhibitor discovery, *Molecular BioSystems 7*.

18. Luo, J., Maréchal, J.-D., Wärmländer, S., Gräslund, A., and Perálvarez-Marín, A. (2010) In Silico Analysis of the Apolipoprotein E and the Amyloid β Peptide Interaction: Misfolding Induced by Frustration of the Salt Bridge Network, *PLoS Comput Biol 6*, e1000663.

19. Huang, R. Y. C., Garai, K., Frieden, C., and Gross, M. L. (2011) Hydrogen/Deuterium Exchange and Electron-Transfer Dissociation Mass Spectrometry Determine the Interface and Dynamics of Apolipoprotein E Oligomerization, *Biochemistry 50*, 9273-9282.

20. Gau, B., Garai, K., Frieden, C., and Gross, M. L. (2011) Mass Spectrometry-based Protein Footprinting Characterizes the Structures of Oligomeric Apolipoprotein E2, E3, and E4 *Biochemistry 50*, 8117-8126.

21. Pan, J., Han, J., Borchers, C. H., and Konermann, L. (2011) Conformer-Specific Hydrogen Exchange Analysis of Aβ(1-42) Oligomers by Top-Down Electron Capture Dissociation Mass Spectrometry, *Anal. Chem. 83*, 5386-5393.

22. Chalmers, M. J., Busby, S. A., Pascal, B. D., West, G. M., and Griffin, P. R. (2011) Differential hydrogen/deuterium exchange mass spectrometry analysis of protein-ligand interactions, *Expert Rev. Proteomics 8*, 43-59.

23. Engen, J. R. (2009) Analysis of Protein Conformation and Dynamics by Hydrogen/Deuterium Exchange MS, *Anal. Chem. 81*, 7870-7875.

24. Wang, L., Pan, H., and Smith, D. L. (2002) Hydrogen Exchange-Mass Spectrometry, *Mol. Cell. Proteomics 1*, 132-138.

25. Garai, K., Mustafi, S. M., Baban, B., and Frieden, C. (2010) Structural differences between apolipoprotein E3 and E4 as measured by 19F NMR, *Protein Science 19*, 66-74.

26. Busby, S. A., Chalmers, M. J., and Griffin, P. R. (2007) Improving digestion efficiency under H/D exchange conditions with activated pepsinogen coupled columns, *Int. J. Mass Spectrom. 259*, 130-139.

27. Garai, K., and Frieden, C. (2010) The Association Dissociation Behavior of the ApoE Proteins: Kinetic and Equilibrium Studies, *Biochemistry 49*, 9533-9541.

28. Garai, K., Baban, B., and Frieden, C. (2011) Self-Association and Stability of the ApoE Isoforms at Low pH: Implications for ApoE-Lipid Interactions, *Biochemistry 50*, 6356-6364.

29. Westerlund, J. A., and Weisgraber, K. H. (1993) Discrete carboxyl-terminal segments of apolipoprotein E mediate lipoprotein association and protein oligomerization, *J. Biol. Chem. 268*, 15745-15750.

30. Huang, R. Y. C., Wen, J., Blankenship, R. E., and Gross, M. L. (2011) Hydrogen–Deuterium Exchange Mass Spectrometry Reveals the Interaction of Fenna–Matthews–Olson Protein and Chlorosome CsmA Protein, *Biochemistry 51*, 187-193.

31. Chen, J., Li, Q., and Wang, J. (2011) Topology of human apolipoprotein E3 uniquely regulates its diverse biological functions, *Proc. Natl. Acad. Sci. 108*, 14813-14818.

32. Gau, B. (2011) The Advancement of Mass Spectrometry-based Hydroxyl Radical Protein Footprinting: Application of Novel Analysis Methods to Model Proteins and Apolipoprotein E, In *Chemistry*, p 212, Washington University in St. Louis, St. Louis.

33. Garai, K., Baban, B., and Frieden, C. (2011) Dissociation of Apolipoprotein E Oligomers to Monomer Is Required for High-Affinity Binding to Phospholipid Vesicles, *Biochemistry 50*, 2550-2558.

Chapter 7*

Hydrogen-deuterium exchange mass spectrometry reveals the interaction of Fenna-Matthews-Olson protein and chlorosome CsmA protein

* This chapter is based on recent publication: Reproduced with permission from Huang, R. Y. C., Wen, J., Blankenship R. E., and Gross, M. L. Hydrogen-deuterium exchange mass spectrometry reveals the interaction of Fenna-Matthews-Olson protein and chlorosome CsmA protein. *Biochemistry*, **2012**, 51, 187-193. Copyright 2012 American Chemical Society (Huang, R. Y. C., and Wen, J. contributed equally to this work.)

7.1 ABSTRACT

In green-sulfur bacterial photosynthesis, excitation energy absorbed by a peripheral antenna structure known as the chlorosome is sequentially transferred through a baseplate protein to the Fenna-Matthews-Olson (FMO) antenna protein and into the reaction center, which is embedded in the cytoplasmic membrane. The molecular details of the optimized photosystem architecture required for efficient energy transfer are only partially understood. We address here the question of how the baseplate interacts with the FMO protein by applying hydrogen/deuterium exchange coupled with enzymatic digestion and mass spectrometry analysis to reveal the binding interface of the FMO antenna protein and the CsmA baseplate protein. Several regions on the FMO protein, represented by peptides consisting of 123-129, 140-149, 150-162, 191-208 and 224-232, show significant decreases of deuterium uptake after CsmA binding. The results indicate that the CsmA protein interacts with the Bchl *a* #1 side of the FMO protein. A global picture including peptide-level details for the architecture of the photosystem from green sulfur bacteria can now be drawn.

7.2 INTRODUCTION

Billions of years of evolution allowed photosynthetic species to achieve not only an optimized structure for an individual light-harvesting complex but also an appropriate architecture for the overall photosystem to facilitate efficient energy transfer and regulation (*1*). Investigations of the structure and function of the antenna components and their optimized overall architecture are needed to understand their energy-transfer mechanism and to provide a sound basis for the design of artificial and bio-hybrid solar devices. Advances in biochemical and biophysical approaches (e.g., X-ray crystallography, cryo-EM, and ultrafast spectroscopy) have greatly enhanced our understanding of the workings of individual antenna complexes. The exploration of the overall architecture of the photosystem, however, lags behind owing to their complex architecture and the lack of a more complete suite of approaches than is now available to study proteins in complex milieu.

In photosynthetic green-sulfur bacteria, photons are absorbed by the large peripheral chlorosome antenna complex (*2*), which is located on the cytoplasmic side of the membrane. Chlorosomes are attached to the cytoplasmic membrane through a pigment-protein complex known as a baseplate (*3*). The baseplate and the Fenna-Matthews-Olson (FMO) antenna protein (*4*) form a bridge to transfer sequentially the

energy collected by chlorosomes to the reaction center (RC). The baseplate consists of the CsmA protein with Bchl *a* pigments embedded within. The structure of the refolded CsmA protein was determined by NMR, demonstrating that it contains only two small alpha helices connected by a small turn (*3*).

The chlorosome is one of the largest antenna systems known; it contains hundreds of thousands of Bchl *c*, *d* or *e* per chlorosome and is enclosed by a lipid monolayer (*5*). The architecture of chlorosomes has evolved to enable certain organisms to live at extraordinary low-light intensities under which no other phototrophic organism can grow (*6*). Unlike other light-harvesting antennas, efficient energy transfer is achieved by self-assembly of the Bchl *c/d/e* pigments in the chlorosome to yield stable structures without the requirement of a scaffold protein (*6*). Understanding this arrangement is important because it can guide the design of artificial light-harvesting systems. Progress in understanding the chlorosome can occur by taking advantage of recent biochemical and biophysical approaches (*7, 8*).

These recent approaches show that the light energy collected by the Bchl aggregates is funneled to the baseplate protein, which is located at the side of chlorosome closest to the cytoplasmic membrane (*9*). The baseplate protein is a 2D paracrystalline structure that is believed to consist of CsmA (chlorosome protein A) and Bchl *a*.

Chemical crosslinking revealed that CsmA forms oligomers in chlorosomes (*10*). The NMR structure of apo-CsmA (without bound Bchl *a*) from *Chlorobaculum tepidum* (59 amino acids) shows a large extent of alpha helical content. The N-terminal helix (6-36), which has the putative Bchl *a* binding site, is thought to be immersed in the lipid monolayer of the chlorosome, whereas the C-terminal helix (41-49) sticks out of the membrane and may interact with the FMO protein at that point. The existence of the baseplate is predicted to enhance significantly the energy-transfer rate from the chlorosome Bchl aggregates to the RC (*2*) **(Figure 7-1)**.

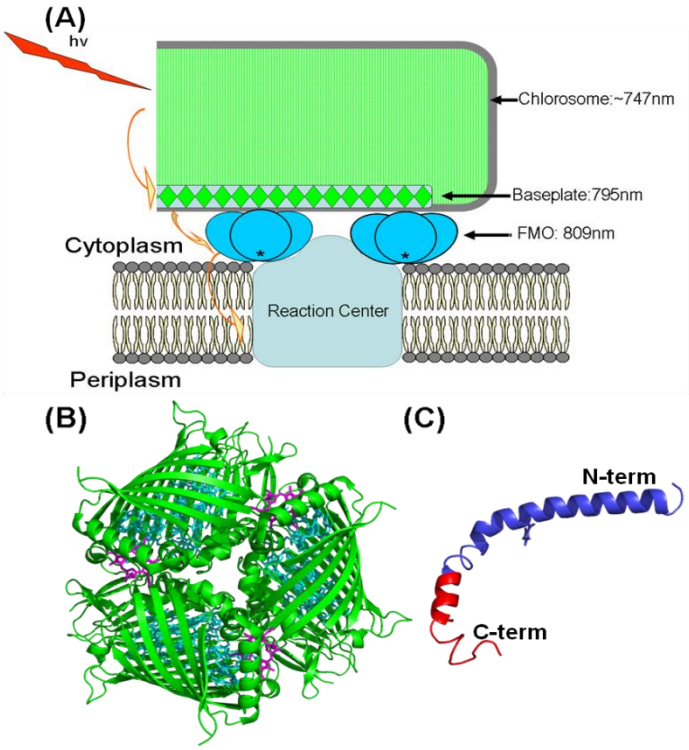

Figure 7-1. Structure model of the photosystem (A), the FMO trimer (B) and the CsmA from baseplate (C). The synthetic peptide of the C-terminal region of CsmA (MRINRNAYGSMGGGSLRGS) used in this study is shown in red.

The FMO protein, which is located between the baseplate and the cytoplasmic membrane (*11*), exists as a trimer, with a three-fold symmetry axis perpendicular to the membrane. This water-soluble protein has been a model system for studies aimed at understanding the structural and functional relationships of pigment-binding photosynthetic antenna complexes (*12-15*). The number of pigments embedded in FMO is important for its function, and recently an 8th Bchl *a* was identified in each monomer (*16, 17*). Several lines of evidence suggest that the side of the protein where this 8th Bchl is located faces the baseplate/chlorosome (*11, 18, 19*).

The connection between the baseplate, the FMO protein, and the RC is likely to be optimized so that excitation energy can be efficiently transferred at high quantum yield. Previous results from SPR studies (*20*) suggest that the C-terminal region of CsmA, especially the conserved INRNAY residues, interact with the FMO protein. The molecular details of their interactions, however, remain unclear. The interaction region between the FMO and the RC is also unknown, although homology modeling with a divergent FMO protein has suggested a possible binding site (*18*).

In this chapter, we describe the use of hydrogen/deuterium exchange (H/DX) coupled with mass spectrometry (MS) (*21-24*) to study the interaction interface and dynamics between FMO and CsmA. With H/DX, we followed the relative rates of

exchange of amide hydrogens, which are measured on the basis of *m/z*, not abundance. Experimental outcomes are a measure of changes in the stability of the hydrogen bonding and the surrounding relative solvent accessibilities of the amides. To achieve resolution at the peptide level of FMO and the complex, we coupled H/DX with enzymatic digestion. The FMO/CsmA binding information obtained through H/DX not only provides novel insights into the interaction interfaces between the proteins but further confirms the orientation of FMO in the photosystem.

7.3 MATERIALS AND METHODS

7.3.1 Materials

The FMO protein from *Chlorobaculum tepidum* was purified following a previously described protocol (*17*). An ESI spectrum of FMO is shown in **Figure 7-2**. The CsmA C-terminal peptide containing 19 amino acids (MRINRNAYGSMGGGSLRGS) was purchased from Biomatik LLC (Wilmington, Delaware).

Potassium chloride, calcium chloride, and HEPES hemisodium salt [*N*-(2-hydroxyethyl)piperazine-*N*′-(2-ethanesulfonic acid) hemisodium salt] were purchased from Sigma-Aldrich (St.Louis, MO). Deuterium oxide was purchased from Cambridge

Isotope Laboratories Inc (Andover, MA). Immobilized pepsin on agarose was purchased from Pierce (Rockford, IL).

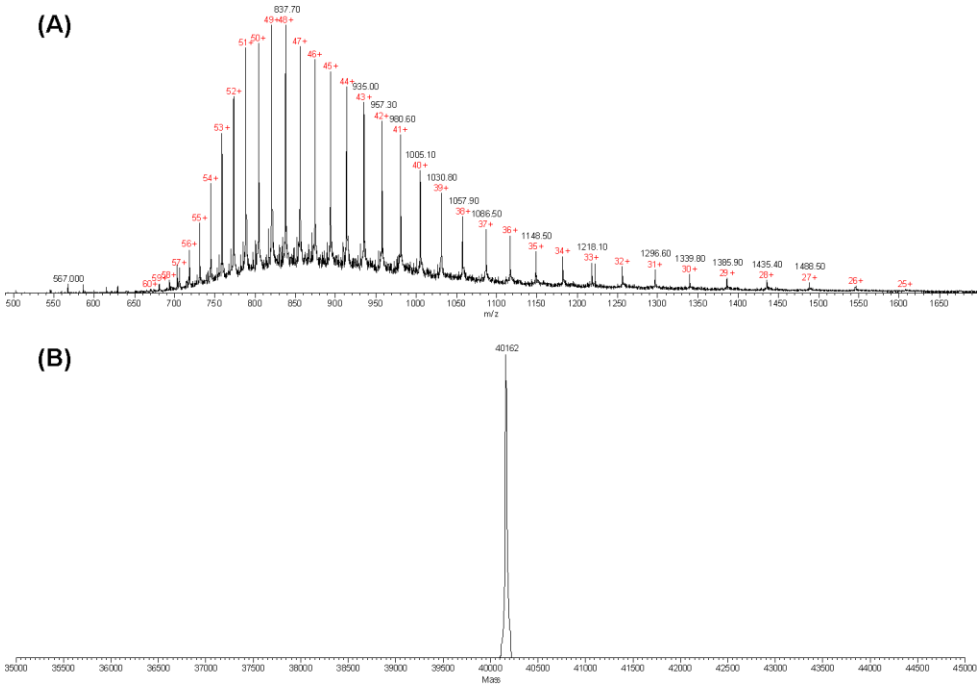

Figure 7-2. ESI mass spectrum of denatured FMO (A) and the deconvoluted spectrum (B).

7.3.2 H/DX Protocol

To achieve good signal-to-noise ratios for the protein signal of FMO, the final concentration of FMO was optimized to 6 μM, and the FMO:CsmA ratio was 1:20 to ensure the interaction was saturated.

For global H/DX measurements, 6 μL of protein was mixed with 74 μL of D_2O buffer (92.5% D_2O) (10 mM HEPES, pD = 7.0, 150 mM KCl) and held for various times at 25 °C before quenching by adding 2 μL of 1 M HCl to lower the pH to 2.5. To

generate the FMO complex with CsmA a modified condition was employed as that used by Miller and coworkers (20); the FMO and the CsmA peptide were incubated 4 h at room temperature in the dark (in 20 mM Tris/HCl, pH = 8.0, with 150 mM KCl) and then kept at 4 °C overnight before conducting the H/DX.

For the peptide-level H/DX, the quenched solution was added with 15 μL of immobilized pepsin on agarose. The digestion was conducted on ice for 3 min. After digestion, the beads were quickly centrifuged (2-3 s) to pellet the pepsin beads, and the supernatant was analyzed by LC/MS.

7.3.3 LC-ESI/MS Analysis with a Q-TOF Mass Spectrometer

The quenched protein solution from global-protein and peptide-level H/DX experiments was loaded onto a C18 guard column (1 mm x 15 mm, Optimize Technologies, Oregon, City, OR), pre-equilibrated with 100 μL of 0.2% formic acid in water (0 °C), and washed with 300 μL of 0.2% formic acid in water (0 °C) to back-exchange the labile side-chain functional groups of the protein and the peptides. The peptides and any remaining protein were eluted with a fast gradient in 8 min starting from 0% solvent B to 90% solvent B at 40 uL/min (Waters nanoACQUITY UPLC, Manchester, U.K; solvent A, 95% water and 5% acetonitrile containing 0.3% formic acid; solvent B, 5% water and 95% acetonitrile containing 0.3% formic acid). To minimize

back exchange, all LC connection lines, injection valve, and sample loop were immersed in water-ice slush (0 °C).

All ESI mass spectra were acquired in the positive-ion mode on a Maxis (Bruker, Billerica, MS) Q-TOF spectrometer equipped with a standard ESI source. The capillary voltage was 3.6 kV, the end-plate offset -500 V, and the dry gas flow rate and temperature at 4L/min and 180 °C, respectively. The MS profiles used for transmission were as follows: funnel RF, 400 V_{pp}; multipole RF, 400 V_{pp}; collision cell voltage, 10 V; collision RF, 3000 V_{pp}; transfer time, 140 us; ion cooler RF, 800 V_{pp}; pre-pulse storage, 25 μs.

7.3.4 LC-ESI-MS/MS Analysis of Protein Digest

Peptides produced by pepsin cleavage of FMO were identified by their accurate masses and product-ion sequencing on a LTQ-FTMS instrument (Thermo, San Jose, CA). The peptide solution from pepsin digestion of 100 pmol FMO was loaded onto a C18 column, 75 μm diameter, which was prepared with a laser-based column puller (Sutter Instruments, Novato, CA) and packed with 12 cm of Magic C18AQ reverse phase media (Michrom Bioresources, Auburn, CA). The peptides were separated over 70 min by using an Eksigent (Dublin, CA) NanoLC-1D column with an LC gradient from 3 to 97% acetonitrile containing 0.1% formic acid at 260 nL/min. The solution was sprayed into

the mass spectrometer by using a PicoView PV-500 nanospray source (New Objective, Woburn, MA) attached to the LTQ-FTMS instrument. One full mass spectral acquisition in the FT mode, operating at a mass resolving power of 100,000 at *m/z* 400, triggered six scans of MS/MS whereby the most abundant precursor ions were activated for sequencing. The MS/MS experiments carried out in the LTQ instrument utilized wide-band activation and dynamic exclusion. The product-ion spectra (MS/MS) data were centroided during the acquisition.

7.3.5 Mascot Database Search

Thermo RAW files were processed by using extract_msn (2007 version 4.0, Thermo Fisher, San Jose, CA) with a grouping tolerance of 0.8 Da, an intermediate scan setting of 1, and a minimum of 1 scan per group. The NCBI non-redundant database (version 20090623, restricted to Other Bacteria) was searched by using MASCOT 2.2.06 (Matrix Science, Oxford, U.K.) with the following settings: enzyme, none; MS tolerance, 10 ppm; MS/MS tolerance, 0.8 Da; maximum number of missed cleavages, 3; peptide charge of 1+, 2+ and 3+; oxidation of methionine was included as a variable modification.

7.3.6 Data Analysis

For global-protein H/DX experiments, the mass spectrum at each H/D exchange time point was deconvoluted by using MagTran 1.03 (Amgen, Thousand Oaks, CA). The

deuterium uptake levels at each time point were taken as the average differences of the centroided masses of the undeuterated protein and the deuterated protein. The protein deuterium uptake was not corrected for back-exchange because the time from quench to observation in the mass spectrometer was less than 6 min, and only relative deuterium levels needed to be compared in all experiments. All of the experiments were conducted in triplicate.

For peptide-level H/DX experiments, each mass list from three experimental trials was extracted from their individual spectra as an x,y file (x: mass-to-charge ratio; y: intensity). The centroid and width of the deuterium-containing isotopic distribution for each peptide was analyzed using HX-Express software (*25*).

7.3.7 Kinetic Modeling

The global protein kinetic data were fit with a fixed-rate-constant binning model by using MathCAD (Math-Soft. Inc. Cambridge, MA) in which the root mean square (RMS) was minimized (*26, 27*). Four rate constants (k = 10, 1, 0.1, 0.01 min^{-1}) were selected because the kinetic data span 0.5-60 min, hence the brackets of 10 min^{-1} (fast exchangers, half-life ~0.07 min) and 0.01 min^{-1} (slow exchangers, half-life ~69 min). Three trials were fit separately, and the results were averaged and reported with standard deviations.

7.4 RESULTS

7.4.1 H/DX kinetics of FMO and FMO/CsmA

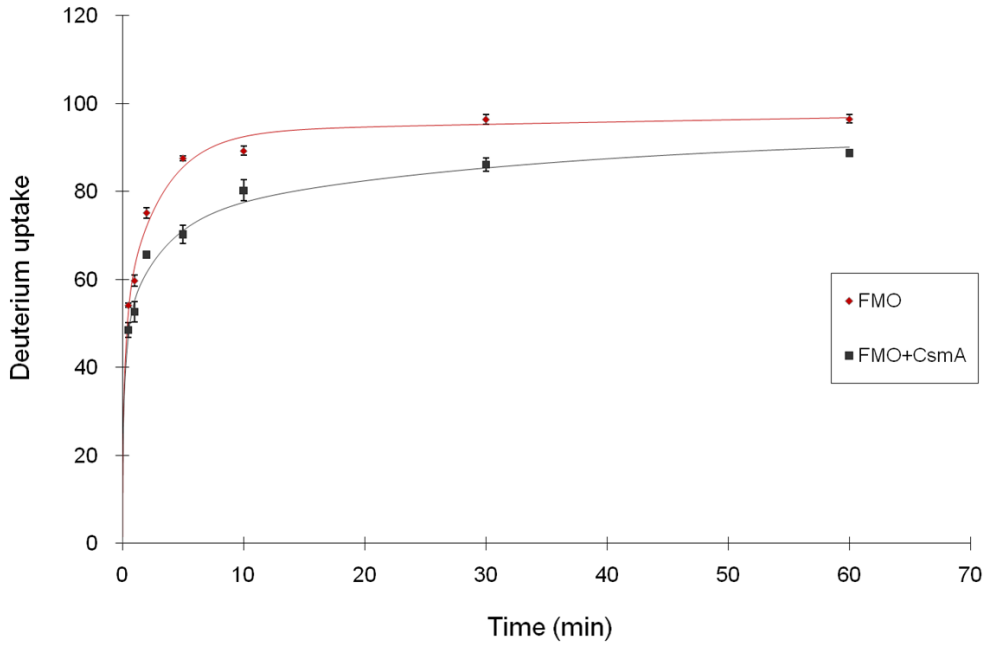

Figure 7-3. H/DX kinetics for FMO from *Chlorobaculum tepidum*. Apo-FMO (diamonds, dark red) shows more extensive D uptake than does holo FMO (CsmA:FMO, 20:1) (squares, black). The fitted curves are shown as solid lines.

Previous SPR studies (*20*) suggest that the interaction between the FMO protein and the chlorosome CsmA protein is primarily on the C-terminal helix of CsmA, especially with the conserved INRNAY residues (*28*). The interaction regions on FMO, however, remain unclear. Given that the protein conformation and the relative solvent accessibilities of FMO will change upon the binding of CsmA, we chose measurements of the H/DX kinetics of FMO alone and as the FMO/CsmA complex to examine globally their interaction and dynamics **(Figure 7-3)**. Given the highly hydrophobic nature of

CsmA, we utilized for interaction a peptide representing the C-terminal region of CsmA, which contains 19 amino acids (MRINRNAYGSMGGGSLRGS) and the highly conserved INRNAY motif.

Each FMO monomer has 348 exchangeable amide protons (excluding 19 prolines). Because the percentage of D_2O in the experiment was 92.5%, the maximum number of observable exchange events was 322. After 10 min of H/DX, the mass of FMO shifted by 89 ± 1 Da, indicating that ~27% of the amides exchanged at this time point. Even after 60 min of H/DX, the extent of exchange had only increased to ~30% (96 ± 1 amides) at a time when the exchange had leveled off and became relatively constant. The small difference is consistent with a compact and stable FMO trimer in solution. Approximately 2/3 of the amides of each monomer are protected because they form hydrogen bonds, or exist inside each monomer, or they are involved in forming a compact trimer. The remaining 1/3 of the amides are solvent-exposed and highly dynamic.

In the presence of CsmA peptide, the number of amides undergoing H/DX decreased to 80 ± 2 after 10 min of exchange, indicating that ~9 amides now exchange more slowly as a consequence of CsmA binding. The number of amides affected by the CsmA binding is relatively small, consistent with the small size of the CsmA peptide and

its limited effect on (i) overall FMO stability, (ii) the extent of hydrogen bonding, and (iii) the solvent accessibility of FMO.

Kinetic Fit	**Number of H's per fixed-rate-constant bin**			
k (min^{-1})	**10**	**1**	**0.1**	**0.01**
apo	**25 ± 3**	**29 ± 4**	**39 ± 3**	**4 ± 1**
holo	**29 ± 2**	**20 ± 2**	**29 ± 1**	**15 ± 1**

Table 7-1. Numbers of amide hydrogen undergoing deuterium exchange for apo and holo FMO. The kinetic modeling used four fixed exchange rate constants and "binned" the number of amides with respect to the rate constants.

To understand better how CsmA binding affects the exchange rate in a quantitative way, we fit the kinetic curve with four exchange rate-constant bins (k = 10, 1, 0.1, 0.01 min^{-1}) (**Table 7-1**). The results show that apo FMO (native FMO trimer without the binding of CsmA) has 25 ± 3 sites that exchange with a rate constant of 10 min^{-1}, whereas after binding with the CsmA peptide (holo FMO), FMO has 29 ± 2 amides that exchange with the same rate constant. Although the number of amides exchanging at this rate constant are similar for the apo and holo states, there are significant differences for those amides that exchange with smaller exchange rate constants. For those exchanging with rate constants of 1 min^{-1} and 0.1 min^{-1}, the numbers of exchangeable amides for holo FMO are lower than for apo by ~10. Some of these sites exchanged with the smallest rate

constant of 0.01 min^{-1} as can be seen for the holo state, for which 15 ± 1 sites exchanged. For the apo state, only 4 ± 1 amides exchanged with this smallest rate constant. These results indicate that CsmA binding slows down the exchange at some sites of the FMO protein with medium exchange rate constants and causes FMO either to form a more rigid secondary structure or to lose solvent accessibility at certain amide sites.

7.4.2 The FMO/CsmA binding interface

Global H/DX of the FMO/CsmA complex shows clear uptake differences compared to apo FMO. To locate the interaction regions, we conducted H/DX at the peptide level by using pepsin digestion and LC/MS analysis. We expected that changes of the peptide-level deuterium uptake of FMO in the presence of CsmA could locate regions implicated in CsmA binding.

We used the same experimental conditions for H/DX as for the global protein measurements. After 10 min of exchange, the H/DX at the protein level had become relatively constant; further, there is a significant difference in D uptake between apo and holo FMO at this time. We were able to identify FMO peptic peptides, as confirmed by accurate mass measurement and tandem-MS sequencing that show sequence coverage of 80% **(Figure 7-4)**. This high coverage ensures that we can localize regional (peptide-level) changes associated with CsmA binding.

Figure 7-4. Sequence coverage (~80%) of peptic peptides from FMO achieved in a peptide-level H/DX study.

There are approximately 10 amides on the FMO protein that are affected by CsmA binding. We found five peptic FMO peptides (123-129, 140-149, 150-162, 191-208, and 224-232) that show decreased deuterium uptake upon the CsmA binding. The level of deuterium uptake difference for each of these five peptides is generally small (~ 2D), which is consistent with the total difference in H/DX measured on the global level. To examine these differences in a comparable way, we converted them to the relative deuterium uptake based on equation 1 and plotted them as a function of peptic peptides **(Figure 7-5)**.

$$\%D = \frac{\text{deuterium uptake}}{(\#aa's - N_{term} - \#Pro)} \qquad (1)$$

In the equation, %D is the relative deuterium uptake for each peptide; #aa's is the total exchangable hydrogens on each peptide; N_{term} is the number of hydrogens on the N-terminus of the peptide.

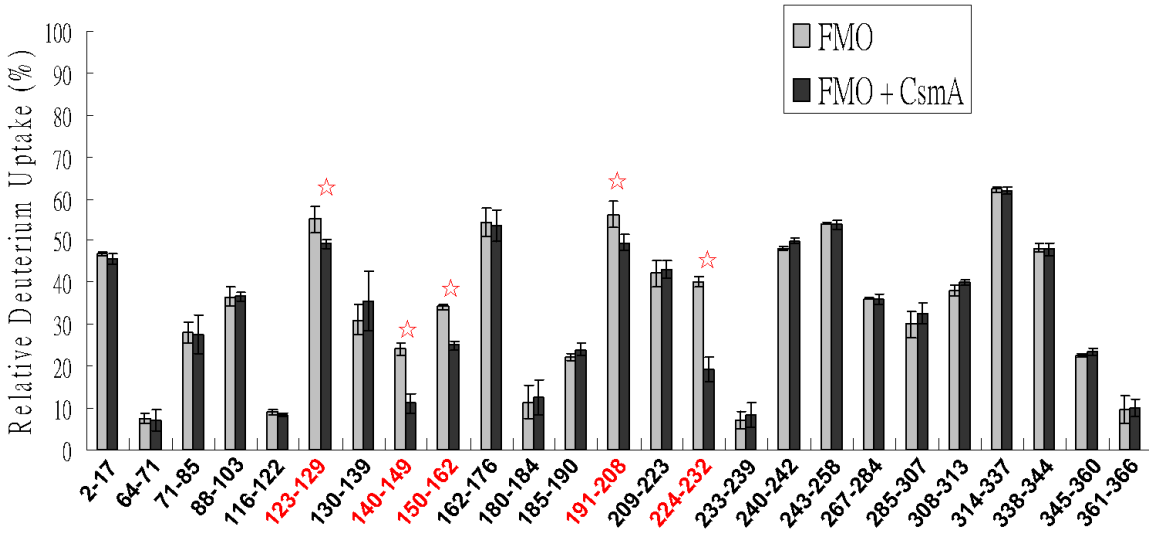

Figure 7-5. Relative deuterium uptakes for peptic peptides from N- to C-terminus of FMO after 10 min of H/DX. Peptide regions showing significant differences in D uptake (>5% difference; a value of $p < 0.05$ was considered significant by Student's t-test) in the presence of CsmA are labeled in red font and marked with red stars.

The plot **(Figure 7-5)** shows that three regions of the FMO represented by peptides 140-149, 150-162, and 224-232 undergo decreased H/DX in the presence of CsmA by at least 10% with respect to the apo state. Two other regions (represented by peptides 123-129 and 191-208) show smaller changes, ~5% differences. All the other detected peptic peptides show virtually no difference with and without CsmA binding. Although we didn't examine the extent of exchange on the CsmA, given that the CsmA

peptide utilized in this study is short and specific, our results conclude that the C-terminal region of CsmA, indeed interacts with FMO.

7.4.3 FMO structural mapping

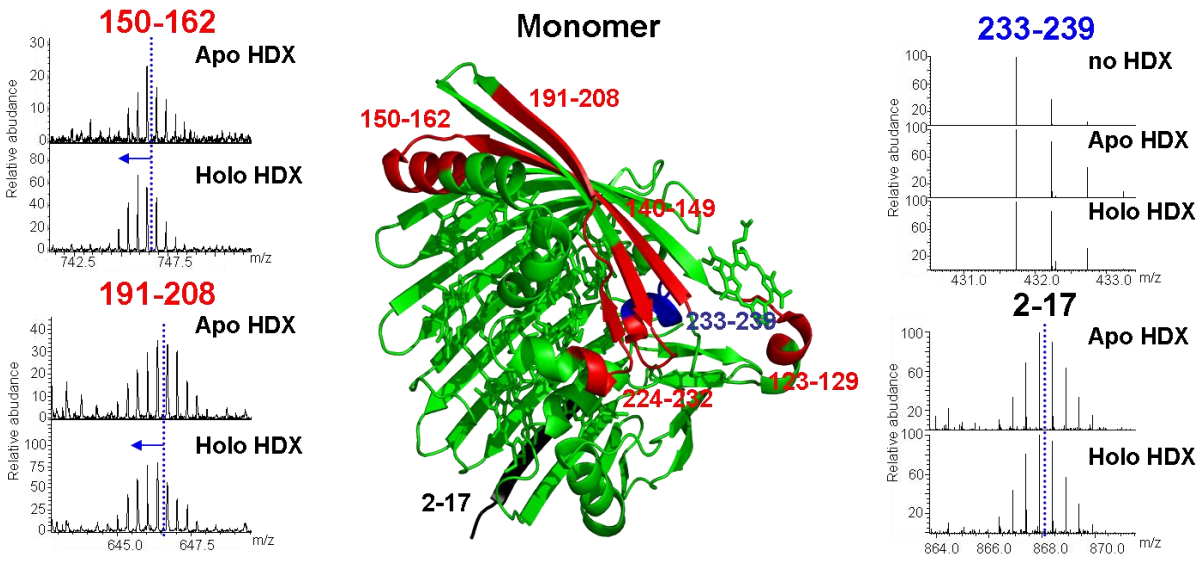

Figure 7-6. FMO monomer structure mapping (PDB: 3ENI) with the deuterium uptake patterns. Peptide regions of FMO undergoing significant D uptake differences between apo and holo states are in red. Peptide 233-239 located in the center of the trimer underwent low D uptake (blue), whereas peptide 2-17 located on the outer shell of the protein underwent relatively extensive D uptake (black).

To locate the regions on FMO that are implicated in binding with CsmA, we mapped the five peptic peptides onto the X-ray crystal structure of FMO from *Chlorobaculum tepidum* (PDB: 3ENI) (*16*) **(Figure 7-6)**. Interestingly, all sites that exchange differently are located on one side of the FMO protein, which is referred to as the Bchl *a* #1 side of the protein (shown in red) (*11*). This finding agrees well with results from a previous study on the membrane orientation of FMO in green-sulfur bacteria (*11*);

those results also show the Bchl *a* #1 side of the FMO interacts with the chlorosome. This study of the peptide-level H/DX further confirms and refines the spatial resolution to a region extending over five peptides of FMO.

On the basis of the relative peptide-level deuterium uptakes, we can identify three categories of deuterium uptake for FMO: (1) regions showing large extents of deuterium uptake (>30%) and significant differences when CsmA binds; (2) regions showing small extents of deuterium uptake (<10%) and no significant differences in the presence and absence of CsmA; and (3) regions showing large extents of deuterium uptake (>30%) but no significant differences in the absence or presence of CsmA. These results, when mapped onto the structure of FMO **(Figure 7-7)**, show that category #3 regions include, for example, peptide 2-17 (shown in black in **Figure 7-6** and **Figure 7-7**), which is located at or near flexible helices or loops mainly on the outer surface of FMO. Those category #2 regions (e.g., peptide 233-239) are located at or near the interface of the FMO trimer (shown in blue in **Figure 7-6** and **Figure 7-7)**.

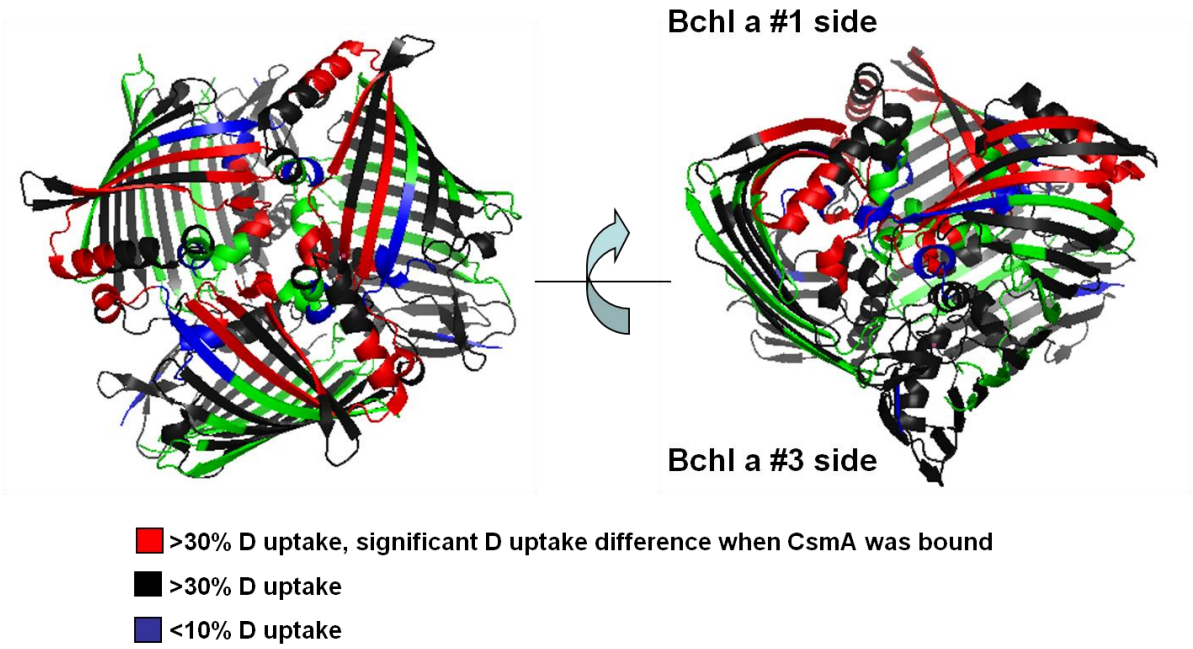

Figure 7-7. Map of H/DX on the FMO trimer structure (PDB: 3ENI). Peptide regions showing relatively extensive H/DX (>30%) and significant differences on D uptake when CsmA was bound are in red. Peptide regions showing relatively low D uptake (<10%) are in blue. Peptide regions undergoing relatively extensive H/DX (>30%) are in black.

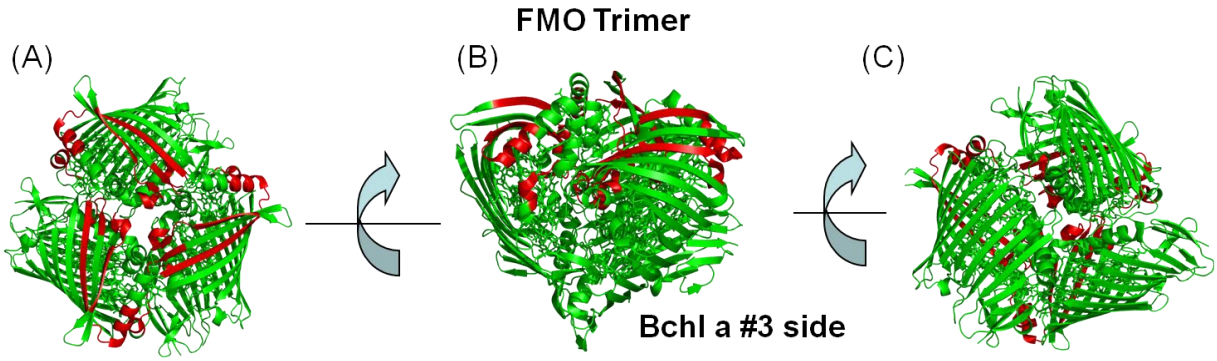

Figure 7-8. Orientation of the FMO trimer structure (PDB: 3ENI). Peptide regions undergoing significantly different D uptake in the presence of CsmA are in red. (A) Top view of the FMO trimer. (B) Side view of FMO trimer. (C) Bottom view of FMO trimer.

7.5 DISCUSSION

One important link in the green-sulfur bacterial photosystem is a light-harvesting chlorosome that absorbs light and transports the energy through a baseplate protein and the FMO protein to the reaction center where energy conversion takes place. A gap existed in our understanding of the interaction between the baseplate and FMO and motivated this study.

CsmA, a major component in the baseplate, contains the putative Bchl *a* binding site in its N-terminal region and may be immersed in the lipid monolayer of the chlorosome, whereas a region near its C-terminal helix protrudes from the membrane and may interact with the FMO protein. A previous SPR study (20) shows that the conserved residues (INRNAY) of the C-terminal region of CsmA interact with the FMO protein.

To investigate this interaction, we chose H/DX because it is a general approach, "marking" all the amino acids except proline and covering nearly the entire protein backbone. H/DX is sensitive to the solution environment surrounding the protein, enabling one to capture even minor changes in protein conformation and solvent accessibility caused by the changes in hydrogen bonding occurring when peptides bind to proteins. In this study, we used a model synthetic peptide of 19 amino acids (MRINRNAYGSMGGGSLRGS) from the C-terminal region of CsmA to probe the

FMO/CsmA interaction. The peptide, which contains the conserved INRNAY region, forms a small alpha helix, as does CsmA itself, and interacts with the FMO protein (*3*). Global-level H/DX shows that only ~10 amides of FMO are affected by the CsmA binding. Although the stoichiometry and the binding affinity between FMO and CsmA are unknown, this small extent of exchange in a large protein makes a determination of the binding affinity by PLIMSTEX (Protein Ligand Interaction by Mass Spectrometry, Titration and H/D Exchange) difficult at the protein level (*26, 27*). Nevertheless, their interaction should be strong *in vivo* possibly because CsmA forms oligomers in the baseplate (*10*), and the oligomeric CsmA interacts more strongly with FMO than does the monomer. In addition, the tail of the 8th Bchl *a* in the FMO protein may play a role *in vivo* by interacting with the carotenoid/Bchl *a* in the CsmA or with hydrophobic regions of CsmA (*17*). The involvement of oligomeric states further complicates determining a relevant affinity by PLIMSTEX or other methods.

Peptide-level H/DX affords further refinement of the binding interfaces between FMO and CsmA. Five regions of FMO, represented by peptides 123-129, 140-149, 150-162, 191-208, and 224-232, show clear decreases of relative deuterium uptake in the presence of CsmA. Interestingly, these regions are all located on the Bchl *a* #1 side of the FMO, and the outcome agrees well with the previous finding that the baseplate interacts

with the Bchl *a* #1 side of the FMO (*11, 18*). Moreover, our results also localize the C-terminal region of CsmA that plays an important role in FMO/CsmA interaction.

7.6 ACKNOWLEDGEMENT

We thank Dr. Henry Rohrs for assistance with the LTQ-FT analysis. Funding was provided by the National Center for Research Resources (NCRR) of the National Institutes of Health (grant no. 2P41RR000954) to M.L.G. and the U.S. Department of Energy Grant DE-FG02-7ER15846 to R.E.B.

7.7 REFERENCES

1. Blankenship, R. E. (2003) *Molecular mechanism of photosynthesis*, Blackwell Science, Oxford, UK.

2. Oostergetel, G., van Amerongen, H., and Boekema, E. (2010) The chlorosome: a prototype for efficient light harvesting in photosynthesis, *Photosynthesis Research 104*, 245-255.

3. Pedersen, M. s., Underhaug, J., Dittmer, J., Miller, M., and Nielsen, N. C. (2008) The three-dimensional structure of CsmA: A small antenna protein from the green sulfur bacterium Chlorobium tepidum, *FEBS letters 582*, 2869-2874.

4. Tronrud, D. E., Schmid, M. F., and Matthews, B. W. (1986) Structure and X-ray amino acid sequence of a bacteriochlorophyll a protein from Prosthecochloris aestuarii refined at 1.9 Å resolution, *Journal of Molecular Biology 188*, 443-454.

5. Beatty, J. T., Overmann, J., Lince, M. T., Manske, A. K., Lang, A. S., Blankenship, R. E., Van Dover, C. L., Martinson, T. A., and Plumley, F. G. (2005) An obligately photosynthetic bacterial anaerobe from a deep-sea hydrothermal vent, *Proceedings of the National Academy of Sciences of the United States of America 102*, 9306-9310.

6. Blankenship, R. E., and Matsuura, K. (2003) Antenna Complexes from Green Photosynthetic Bacteria, In *Light-Harvesting Antennas* (Green, B. R., and Parson, W. W., Eds.), pp 195-217, Kluwer.

7. Ganapathy, S., Oostergetel, G. T., Wawrzyniak, P. K., Reus, M., Gomez Maqueo Chew, A., Buda, F., Boekema, E. J., Bryant, D. A., Holzwarth, A. R., and de Groot, H. J. M. (2009) Alternating syn-anti bacteriochlorophylls form concentric helical nanotubes in chlorosomes, *Proceedings of the National Academy of Sciences 106*, 8525-8530.

8. Furumaki, S., Vacha, F., Habuchi, S., Tsukatani, Y., Bryant, D. A., and Vacha, M. (2011) Absorption Linear Dichroism Measured Directly on a Single Light-Harvesting System: The Role of Disorder in Chlorosomes of Green Photosynthetic Bacteria, *Journal of the American Chemical Society 133*, 6703-6710.

9. Pedersen, M., Linnanto, J., Frigaard, N.-U., Nielsen, N., and Miller, M. (2010) A model of the protein–pigment baseplate complex in chlorosomes of photosynthetic green bacteria, *Photosynthesis Research 104*, 233-243.

10. Li, H., Frigaard, N.-U., and Bryant, D. A. (2006) Molecular Contacts for Chlorosome Envelope Proteins Revealed by Cross-Linking Studies with Chlorosomes from Chlorobium tepidum, *Biochemistry 45*, 9095-9103.

11. Wen, J., Zhang, H., Gross, M. L., and Blankenship, R. E. (2009) Membrane orientation of the FMO antenna protein from Chlorobaculum tepidum as determined by mass spectrometry-based footprinting, *Proceedings of the National Academy of Sciences 106*, 6134-6139.

12. Wen, J., Harada, J., Buyle, K., Yuan, K., Tamiaki, H., Oh-oka, H., Loomis, R. A., and Blankenship, R. E. (2010) Characterization of an FMO Variant of Chlorobaculum tepidum Carrying Bacteriochlorophyll a Esterified by Geranylgeraniol, *Biochemistry 49*, 5455-5463.

13. Larson, C., Seng, C., Lauman, L., Matthies, H., Wen, J., Blankenship, R., and Allen, J. (2011) The three-dimensional structure of the FMO protein from Pelodictyon phaeum and the implications for energy transfer, *Photosynthesis Research 107*, 139-150.

14. Engel, G. S., Calhoun, T. R., Read, E. L., Ahn, T.-K., Mancal, T., Cheng, Y.-C., Blankenship, R. E., and Fleming, G. R. (2007) Evidence for wavelike energy

transfer through quantum coherence in photosynthetic systems, *Nature 446*, 782-786.

15. Panitchayangkoon, G., Hayes, D., Fransted, K. A., Caram, J. R., Harel, E., Wen, J., Blankenship, R. E., and Engel, G. S. (2010) Long-lived quantum coherence in photosynthetic complexes at physiological temperature, *Proceedings of the National Academy of Sciences 107*, 12766-12770.

16. Tronrud, D., Wen, J., Gay, L., and Blankenship, R. (2009) The structural basis for the difference in absorbance spectra for the FMO antenna protein from various green sulfur bacteria, *Photosynthesis Research 100*, 79-87.

17. Wen, J., Zhang, H., Gross, M. L., and Blankenship, R. E. (2011) Native Electrospray Mass Spectrometry Reveals the Nature and Stoichiometry of Pigments in the FMO Photosynthetic Antenna Protein, *Biochemistry 50*, 3502-3511.

18. Wen, J., Tsukatani, Y., Cui, W., Zhang, H., Gross, M. L., Bryant, D. A., and Blankenship, R. E. (2010) Structural model and spectroscopic characteristics of the FMO antenna protein from the aerobic chlorophototroph, Candidatus Chloracidobacterium thermophilum, *Biochimica et Biophysica Acta (BBA) - Bioenergetics 1807*, 157-164.

19. Schmidt am Busch, M., Müh, F., El-Amine Madjet, M., and Renger, T. (2011) The Eighth Bacteriochlorophyll Completes the Excitation Energy Funnel in the FMO Protein, *The Journal of Physical Chemistry Letters 2*, 93-98.

20. Pedersen, M., Borch, J., Højrup, P., Cox, R., and Miller, M. (2006) The light-harvesting antenna of Chlorobium tepidum: Interactions between the FMO protein and the major chlorosome protein CsmA studied by surface plasmon resonance, *Photosynthesis Research 89*, 63-69.

21. Konermann, L., Pan, J., and Liu, Y.-H. (2011) Hydrogen exchange mass spectrometry for studying protein structure and dynamics, *Chemical Society Reviews 40*, 1224-1234.

22. Engen, J. R. (2009) Analysis of Protein Conformation and Dynamics by Hydrogen/Deuterium Exchange MS, *Analytical Chemistry 81*, 7870-7875.

23. Englander, S. (2006) Hydrogen exchange and mass spectrometry: A historical perspective, *Journal of The American Society for Mass Spectrometry 17*, 1481-1489.

24. Chalmers, M. J., Busby, S. A., Pascal, B. D., West, G. M., and Griffin, P. R. (2011) Differential hydrogen/deuterium exchange mass spectrometry analysis of protein-ligand interactions, *Expert Review of Proteomics 8*, 43-59.

25. Weis, D., Engen, J., and Kass, I. (2006) Semi-automated data processing of hydrogen exchange mass spectra using HX-Express, *Journal of The American Society for Mass Spectrometry 17*, 1700-1703.

26. Zhu, M. M., Rempel, D. L., and Gross, M. L. (2004) Modeling data from titration, amide H/D exchange, and mass spectrometry to obtain protein-ligand binding constants, *J. Am. Soc. Mass Spectrom. 15*, 388-397.

27. Zhu, M. M., Chitta, R., and Gross, M. L. (2005) PLIMSTEX: a novel mass spectrometric method for the quantification of protein-ligand interactions in solution, *Int. J. Mass Spectrom. 240*, 213-220.

28. Blankenship, R. E., Olson, J. M., and Miller, M. (1995) Antenna Complexes from Green Photosynthetic Bacteria, In *Anoxygenic Photosynthetic Bacteria* (Blankenship, R. E., Madigan, M. T., and Bauer, C. E., Eds.), pp 399-435.